Parallel-in-Time Simulation of Electromagnetic Energy Converters

Zeitparallele Simulation von elektromagnetischen Energiewandlern
Zur Erlangung des akademischen Grades Doktor-Ingenieur (Dr.-Ing.)
Genehmigte Dissertation von Iryna Kulchytska-Ruchka aus Lemberg, Ukraine
Fachbereich Elektrotechnik und Informationstechnik, Technische Universität Darmstadt
Tag der Einreichung: 11.05.2021, Tag der Prüfung: 22.07.2021

1. Gutachten: Prof. Dr. Sebastian Schöps
2. Gutachten: Prof. Dr. Martin J. Gander
Darmstadt, 2021

TECHNISCHE UNIVERSITÄT DARMSTADT

Fachbereich 18
Computational Electromagnetics Group

Parallel-in-Time Simulation of Electromagnetic Energy Converters
Zeitparallele Simulation von elektromagnetischen Energiewandlern

Genehmigte Dissertation von Iryna Kulchytska-Ruchka aus Lemberg, Ukraine
Fachbereich Elektrotechnik und Informationstechnik, Technische Universität Darmstadt

1. Gutachten: Prof. Dr. Sebastian Schöps
2. Gutachten: Prof. Dr. Martin J. Gander

Tag der Einreichung: 11.05.2021
Tag der Prüfung: 22.07.2021

Darmstadt, Technische Universität Darmstadt
Jahr der Veröffentlichung der Dissertation auf TUprints: 2021

Erklärungen laut Promotionsordnung

§8 Abs. 1 lit. c PromO

Ich versichere hiermit, dass die elektronische Version meiner Dissertation mit der schriftlichen Version übereinstimmt.

§8 Abs. 1 lit. d PromO

Ich versichere hiermit, dass zu einem vorherigen Zeitpunkt noch keine Promotion versucht wurde. In diesem Fall sind nähere Angaben über Zeitpunkt, Hochschule, Dissertationsthema und Ergebnis dieses Versuchs mitzuteilen.

§9 Abs. 1 PromO

Ich versichere hiermit, dass die vorliegende Dissertation selbstständig und nur unter Verwendung der angegebenen Quellen verfasst wurde.

§9 Abs. 2 PromO

Die Arbeit hat bisher noch nicht zu Prüfungszwecken gedient.

Darmstadt, 11.05.2021

Iryna Kulchytska-Ruchka

Zusammenfassung

Computergestützte Simulationen sind in der Industrie weit verbreitet, da sie es ermöglichen, das Design zu optimieren und den Lebenszyklus von Produkten zu verstehen, bevor deren physische Prototypen gebaut werden. Solche Simulationen müssen typischerweise im Zeitbereich durchgeführt werden und sind dann besonders zeitintensiv, wenn lange Zeitintervalle berechnet werden müssen, z.B. bis zum stationären Zustand (Steadystate). Zeitparallele Verfahren wie der Parareal-Algorithmus sind aufgrund ihrer Fähigkeit, die Arbeitslast auf mehrere Recheneinheiten zu verteilen, leistungsfähige Kandidaten für eine Beschleunigung dieser Entwicklungsphasen. In dieser Dissertation werden neuartige effiziente Parareal-basierte Ansätze entwickelt und analysiert, die sich besonders für Anwendungen in der Elektrotechnik eignen, wie pulsweitenmodulierte (PWM) Stromrichter, Elektromotoren oder Transformatoren. Die Hauptbeiträge dieser Doktorarbeit sind die folgenden.

Erstens wird eine Multiraten-Parareal-Methode zur zeitparallelen Lösung von Systemen vorgeschlagen, die mit PWM-Signalen angeregt werden. Die Idee besteht darin, ein Surrogatmodell mit einer glatten Anregung auf der groben Ebene zu lösen, während auf der feinen Ebene die ursprüngliche diskontinuierliche PWM-Anregung benutzt wird. Die Konvergenzanalyse liefert eine Fehlerabschätzung in Form der Abweichung der groben Eingangsfunktion vom PWM-Signal. Die numerische Untersuchung für ein RL-Schaltungsmodell stimmt mit den theoretischen Herleitungen überein. Eine Erweiterung der Methode auf zeitperiodische Probleme wird vorgeschlagen und für ein lineares Modellproblem analysiert. Die Multiraten-Parareal-basierten Methoden werden auf einen Abwärtswandler und eine vierpolige Induktionsmaschine angewendet.

Zweitens wird die zeitliche Parallelisierung mit Parareal in ein industrielles Simulationswerkzeug integriert und für das Design eines Elektrofahrzeugantriebs verwendet. Im Gegensatz zu vielen anderen Verfahren ist Parareal nicht auf bestimmte Betriebspunkte oder Motorkonfigurationen beschränkt und kann aufgrund seiner Nichtinvasivität bereits vorhandene Löser verwenden. Mithilfe einer periodischen Parareal-Methode und 80 Kernen kann der stationäre Zustand des Elektromotors bis zu 28 Mal schneller im Vergleich zur sequentiellen Berechnung erreicht werden. Dies ist eine große Hilfe für die Industrie, da es den Entwurfsablauf erheblich beschleunigt. Eine solch gute Leistung von Parareal für die Simulation von Asynchronmaschinen wird in dieser Arbeit auch anhand einer Eigenwertanalyse zweier Ersatzschaltungen begründet.

Drittens wird ein zeitparalleler Algorithmus für zeitperiodische Probleme vorgestellt, der auf einer multiharmonischen Korrektur auf einem groben Gitter basiert. Er führt eine zusätzliche Parallelisierung auf der groben Ebene durch eine Newton-basierte Linearisierung mit einer blockzyklischen Jacobi-Matrix ein, gefolgt von einer Transformation in den Frequenzbereich. Die Konvergenzanalyse wird für ein nichtlineares Modellproblem durchgeführt und durch eine numerische Studie bestätigt. Die Anwendung auf ein nichtlineares Koaxialkabelmodell und ein nichtlineares Transformatormodell ergibt eine Beschleunigung der sequentiellen Berechnungen bis zu Faktoren von bis zu 175 bei Ausnutzung von 20 Kernen. Schließlich wird in dieser Arbeit ein Parareal-basierter Ansatz für zeitperiodische Probleme mit unbekannter Periode wie, z.B. autonome Evolutionssysteme entwickelt. Die Methode wird an einem Colpitts-Oszillator-Modell getestet.

Abstract

Computer-aided simulations are widely used in industry, as they allow to optimize the design and to understand the life cycle of engineering products, before their physical prototypes are constructed. Such simulations must be typically performed in the time domain and are especially then time consuming, when long time intervals have to be computed, e.g., until the steady state. Parallel-in-time methods such as the Parareal algorithm are powerful candidates for an acceleration of these development stages due to their capability to distribute the workload among multiple processing units. This dissertation develops and analyzes novel efficient Parareal-based approaches, particularly suitable for applications in electrical engineering such as pulse-width modulated (PWM) power converters, electric motors or transformers. The main contributions of this thesis are the following.

First, a multirate Parareal method is proposed for parallel-in-time solution of systems excited with PWM signals. The idea of the approach is to solve a surrogate model with a smooth excitation on the coarse level, while on the fine level the original discontinuous PWM excitation is used. Convergence analysis gives an error estimate in terms of the deviation of the coarse input form the PWM signal. Numerical study for an RL-circuit model is in agreement with the theoretical derivations. An extension of the method to time-periodic problems is proposed and analyzed for a linear model problem. The multirate Parareal-based methods are applied to a buck converter and a four-pole induction machine.

Second, time parallelization with Parareal is incorporated into an industrial simulation tool and used for the design of an electric vehicle drive. In contrast to many other methods Parareal is not limited to particular operating points or motor configurations and can employ already existing solvers due to its non-intrusiveness. By means of a periodic Parareal method and 80 cores, the steady state of the motor can be obtained up to 28 times faster compared to the sequential calculation. This is a great aid to industry as it speeds up the design workflow significantly. Such a good performance of Parareal for induction machine simulations is justified also based on an eigenvalue analysis of two circuit schemes in this thesis.

Third, a parallel-in-time algorithm for time-periodic problems based on a multi-harmonic coarse grid correction is presented. It introduces an additional parallelization on the coarse level due to a Newton-based linearization with a block-cyclic Jacobian matrix, followed by a frequency-domain transformation. Convergence analysis is performed for a model problem and confirmed by a numerical study. Application to a nonlinear coaxial cable model and a nonlinear transformer model yields acceleration of the sequential computations up to factors of 175 when exploiting 20 cores. Finally, this thesis develops a Parareal-based approach for time-periodic problems with unknown period as, e.g., autonomous evolution systems. The method is tested on a Colpitts oscillator model.

Contents

List of figures

1 Introduction and motivation

Electromechanical energy converters such as electric motors are incorporated in a wide range of products such as, e.g., household appliances or electric vehicle drives, as the one shown in Figure 1.1 for an e-bike. Prior to construction of the physical prototypes, designs and performance of the electromagnetic devices are commonly investigated via computer-aided simulations. Within the digital design process, various multi-physical effects (e.g., magnetic, mechanical, thermal, acoustic), losses and costs are optimized. As a result, product development becomes cheaper, faster, and more environmentally friendly due to a reduced consumption of energy and resources such as the rare earth materials.

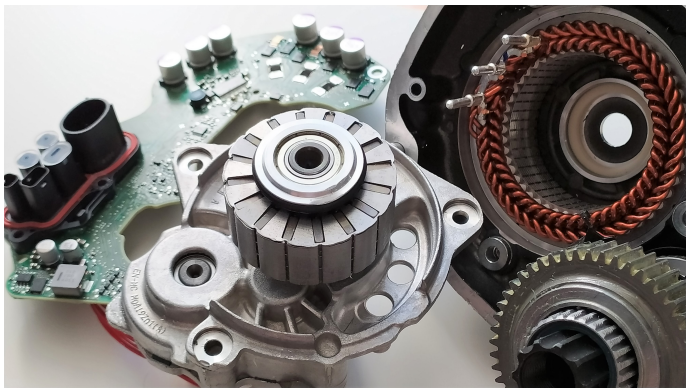

Figure 1.1: An e-bike drive unit, courtesy of Robert Bosch GmbH.

Simulation of a virtual motor prototype provides information about, e.g., the magnetic flux distribution or the produced torque, as illustrated in Figure 1.2 for four-pole induction machine models. To obtain these results, the electromagnetic phenomena taking place in the motor have to be first modeled mathematically, i.e., described by a set of (partial differential) equations. The mathematical model is then discretized in space- and time-domain using numerical methods, which yields a nonlinear system of algebraic equations at each considered time instant [5]. Finally, the quantities of interest like magnetic flux density (Figure 1.2a) and torque (Figure 1.2b) are obtained via post-processing of the calculated system solutions.

In Figure 1.2b we see that the torque evolution has a so-called multirate (or multiscale) behavior: it consists of low-frequency transient oscillations and high-frequency ripples. The transient part gradually fades away and leads to the steady state. The steady-state operating characteristics such as rotational speed and torque are important design criteria, especially during initial design stages. They describe a particular operating point of the induction motor and correspond to a certain driving condition of the electric vehicle. The high-frequency oscillations happen due to the slotting of the motor and require a high resolution and thus a large number of sequential nonlinear system solutions. This results in an extremely time-consuming computation which may last, e.g., a couple of days or even a couple of weeks. Clearly, such a long computing time makes the design process prohibitively slow, since typically tens to hundreds of operating points have to be evaluated to determine technical features and limitations of the electric machine [11]. For this reason, novel efficient numerical algorithms are of paramount importance for further progress in engineering.

Nowadays, in the era of computer systems with multiple processing units, the time-consuming computations can be accelerated via workload distribution and parallelization. Initially, parallelization via decomposition of the space-domain and matching of the solutions at the interfaces was applied [33]. As the number of available cores in the modern computers is increasing, parallelization in space often reaches its saturation limit. This

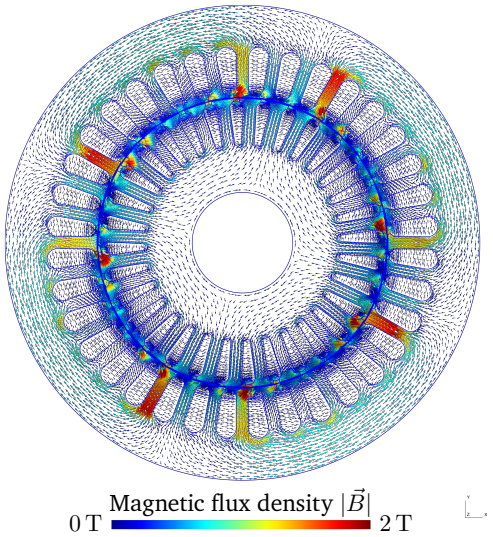

(a) Space-domain solution for a fixed time instant [51][1].

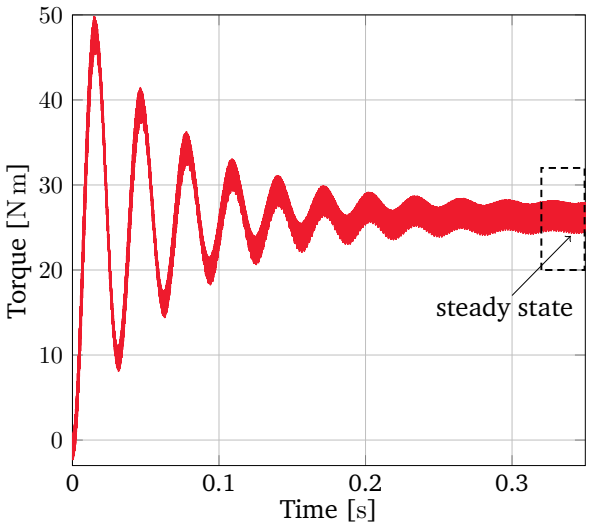

(b) Time-domain solution: transient and steady state [11].

Figure 1.2: Results of electromagnetic simulations of four-pole squirrel cage induction motors.

happens when the communication costs among the cores outweigh the actual gain from the parallelization. As a result, further parallelization direction, namely, parallelization in the time domain, was introduced. At first sight, this seems to contradict the sequential nature of the classical time stepping. However, a rigorous mathematical analysis makes connections to already existing methods and promises high efficiency of the parallel-in-time (PinT) algorithms, see [45].

Parareal is a particular PinT method [88], based on iterative solution on two time grids: it computes a fine and a coarse solution. The cheap coarse solution is calculated sequentially, while the expensive fine solutions are computed in parallel, which is the origin of the speed up. A striking property of the algorithm is that it converges up to the precision of the fine solver in a finite number of iterations [48]. Another important feature is its non-intrusiveness, i.e., existing black-box solvers can be exploited and incorporated easily into the Parareal framework, as it has been presented in [118] for an induction machine model. In this thesis several Parareal-based methods are developed, investigated, and applied to accelerate simulation and steady-state analysis of electromechanical energy converters and electric power converters.

1.1 Related works

There are various approaches which deal with steady-state calculations. In particular, a *suitable initial value* can shorten the transient part of the sequential solution significantly, as it is shown in [12]. There, a method, which computes appropriate initial currents in the rotor bars of an induction motor, is proposed. The disadvantage of the approach is its applicability only to a specific motor type, namely, to an induction motor with squirrel cage rotor, as well as its strong intrusiveness. In [32] 'good' starting conditions for the transient induction machine simulations are calculated by a separate elimination or reduction of the stator and rotor electromagnetic time

[1] ©2019 Society for Industrial and Applied Mathematics.

constants. A non-intrusive method to find a proper initial solution for non-autonomous circuit simulation is described in [29].

Another way to obtain the steady-state solution is time discretization on one period and imposing a time-periodic (TP) constraint [67] instead of the time stepping starting from a prescribed initial condition. This approach corresponds to the well-known multiple shooting method [31, Section 8.2.2] and might lead to a nonlinear system of a very large dimension, whose construction and direct solution might be prohibitive. The discrete TP system can be solved using the Sherman-Morrison-Woodbury formula [89, 119], as it is done in [69] for a three-phase synchronous generator. This approach decouples the discrete time variables and allows to calculate them separately and in parallel.

In [79, 128] the TP framework was used to derive the *simplified TP explicit error correction (TP-EEC) method*. There, after each (half a) period of the time stepping, the solution is updated by the average of the start- and end-values of the (half-)period. This approach is extremely simple and easy to implement, yet its effectiveness seems to be limited to oscillatory systems, whose steady state is located approximately in the middle of the maximal and the minimal deviations of the sequential solution [11]. A parallel variant of the TP-EEC is proposed in [127] and combined with the domain decomposition in space in [126].

An alternative approach to obtain the TP solution is the frequency-domain formulation [94], in particular, the *harmonic balance (HB) method*, proposed in [131]. In terms of the terminology of [8] it is called the *multi-harmonic (MH) approach*. Using the Fourier series expansion, it transforms a differential equation into an algebraic one, which has to be solved with respect to the harmonic coefficients. The method can be interpreted as the Fourier collocation method [30, Section 7.3.3] or the Fourier spectral method [129]. It was applied to circuit simulations, e.g., in [18] and to induction machines in [61]. The disadvantage of the HB approach is that it may require many harmonics, particularly in the case of strong nonlinearities or pulsed excitations [114], and even more for electric machines, e.g., 130 harmonics as in [66]. In either case solution of the resulting nonlinear system becomes cumbersome.

A combination of the time- and frequency-domain representations was proposed in [17]. Due to the special block-cyclic structure of the discrete TP system, application of the Fourier transform can convert it into a block-diagonal form. In this case, similarly to the Sherman-Morrison-Woodbury formula [69], separate and parallel solution for each frequency component becomes possible. Diagonalization using the fast Fourier transform algorithm [129] makes this approach particularly attractive due to its low complexity. The MH diagonalization was recently exploited within the PinT framework in [136, 137]. In [52] a family of PinT methods ParaDIAG, which include system diagonalization, was introduced.

Similarly to induction machines, simulations of pulse-width modulated (PWM) power converters [15, 91] deal with the multirate phenomenon. They commonly exhibit a fast periodic behavior, enveloped by a slowly varying waveform, and thus require a special numerical treatment. The multirate partial differential equation approach [19, 113], allows to resolve the high-frequency ripples and calculate the multirate solution efficiently by introducing two time variables representing the slow and the fast scales. In [87], the envelope-following technique is used within the shooting method to calculate the steady state of nonlinear two-scale circuits.

1.2 Research contributions

This thesis elaborates the PinT principles in order to solve particular problems in electrical engineering such as calculation of the steady-state operation of electric motors or simulation of PWM power converters. The

research contributions are summarized as follows.

1. Development and analysis of Parareal-based methods, suitable for problems with PWM inputs. Testing of the new algorithms for several electromagnetic models: an electric circuit, a power converter, and an induction machine.
2. Demonstration of the fact that Parareal can be easily incorporated into industrial software and that its performance is superior over several other existing approaches like the simplified TP-EEC and the method from [12] for simulation of an induction motor used in an electric vehicle drive.
3. Investigation of possible convergence difficulties of the Parareal algorithm for electric motor computations, as it is the case, e.g., for a magnetomechanical oscillator, due to the beating phenomenon, as stated in [40].
4. Additional parallelization also on the coarse grid within the periodic Parareal framework, based on the MH diagonalization approach [17]. Numerical analysis and comparison to other time-periodic approaches via application to a two-dimensional coaxial cable model and a three-dimensional transformer model.
5. Introduction of a PinT algorithm for TP problems with unknown periods, testing of the proposed approach for a circuit describing the Colpitts oscillator.

1.3 Structure of this treatise

This thesis is organized as follows. Chapter 2 describes the physical principles of electromagnetism with the relevant mathematical tools. In particular, the electromagnetic phenomena are modeled by Maxwell's equations in Section 2.1. The next two sections, namely, Section 2.2 and Section 2.3, provide theory about electric circuits and PWM signals, respectively. Finally, operating principles, governing equations, and equivalent circuit schemes of induction motors are described in Section 2.4.

Chapter 3 deals with numerical solution of the derived mathematical models. In Section 3.1 the fundamentals of functional analysis are provided. Section 3.2 derives the space- and time-discrete models by approximation of the solutions in the finite dimensional spaces. Construction and solution of boundary-value problems in time, particularly, TP problems, is performed in Section 3.3. The family of shooting methods is described in Section 3.3.1, while the MH diagonalization approach is applied to the discrete TP system in Section 3.3.2. Section 3.3.3 extends the multiple shooting method to TP problems with unknown period.

Chapter 4 discusses PinT time-integration methods. The standard Parareal algorithm and two Parareal variants for TP problems (PP-IC and PP-PC) are described in Section 4.1 and Section 4.2, respectively. Section 4.3 introduces a multirate Parareal algorithm, suitable for problems with PWM excitations, analyzes its convergence, and extends it to TP problems. The MH approach is incorporated into the periodic PinT framework in Section 4.4, where a simplified Newton linearization method is used to transform the TP system into a block-cyclic form. The Parareal-based solution of TP problems with unknown period is proposed in Section 4.5.

The developed PinT approaches are exploited to solve multiple problems in electrical engineering in Chapter 5. In particular, the multirate Parareal methods are applied to an RL-circuit, a buck converter, and an induction machine in Section 5.1. Steady-state analysis of an induction motor, developed for an electric

vehicle drive, is performed using the PP-IC algorithm in Section 5.2. The efficiency of the method is compared to that of the simplified TP-EEC and to the approach from [12]. Section 5.3 investigates whether Parareal may possible have convergence difficulties for induction machine simulations. The MH diagonalization is applied to the direct (fine) TP discretization and to the (coarse) PP-PC system for two coaxial cable models and a transformer model in Section 5.4 and Section 5.5, respectively. Section 5.6 solves the Colpitts oscillator model using the PinT approach with unknown period. Finally, the thesis is summarized in Chapter 6.

2 Modeling

The first step towards a computer-aided design of the real-life demands in (electrical) engineering is mathematical modeling. Followed by the numerical solution and analysis it allows for a profound understanding of the underlying physical phenomena. In this way an engineer is able to analyze the behavior and performance of a device before its physical prototype is manufactured.

By a mathematical model we mean a set of equations which describe a complex physical system and its evolution in time. It is commonly constructed from general laws and constitutive relations, whose combination often leads to a system of partial differential equations (PDEs). This chapter focuses on the fundamental laws of electromagnetism represented by the Maxwell equations and coupled to the constitutive relations of the involved physical quantities. Electromagnetic field models are often coupled to electric circuits, which we also characterize in this chapter. A special class of circuit models include discontinuous inputs, used, e.g., in semiconductor devices, present in PWM power converters.

The interaction of electromagnetic fields and circuits forms a basis for operation of electromechanical energy converters such as electric motors or generators. In this chapter we consider three-phase induction (or asynchronous) motors, used in a variety of applications such as household appliances or industrial drives. The corresponding mathematical model is formulated based on the coupling of field, circuit, and motion equations.

2.1 The Maxwell equations

Electromagnetic field theory was originally presented in the work of Maxwell in 1864 [90], although it had started to evolve already earlier through the efforts of several prominent scientists (such as Coulomb, Faraday, Ampère, Gauss and others) of the XIX century. A historical overview of the early stage development is given in [111]. The fundamentals of electromagnetism can be found in a variety of textbooks, e.g., in [58, 68, 75, 76], and are mathematically expressed by the set of Maxwell's equations.

Consider the following physical quantities: the *magnetic flux density* $\vec{B}$, the *magnetic field strength* $\vec{H}$, the *electric flux density* $\vec{D}$, the *electric field strength* $\vec{E}$, and the *electric current density* $\vec{J}$, which are all vector fields as well as the *electric charge density* ϱ, which is a scalar field. All these quantities depend on position $\vec{x} \in \mathbb{R}^3$ and time $t \in \mathbb{R}$. Let $V \subset \mathbb{R}^3$ be a volume with boundary surface ∂V and let $S \subset \mathbb{R}^2$ be a surface with boundary contour ∂S. Both V and S we assume to be compact and have piecewise smooth boundaries. The Maxwell equations are written for a system at rest (i.e., V and S are independent of the time variable t) in the *integral*

form as [7]

$$\int_{\partial S} \vec{E}(\vec{x},t)\cdot \mathrm{d}\vec{s} = -\int_{S} \frac{\partial \vec{B}(\vec{x},t)}{\partial t}\cdot \mathrm{d}\vec{S}, \tag{2.1a}$$

$$\int_{\partial S} \vec{H}(\vec{x},t)\cdot \mathrm{d}\vec{s} = \int_{S} \left(\frac{\partial \vec{D}(\vec{x},t)}{\partial t} + \vec{J}(\vec{x},t)\right)\cdot \mathrm{d}\vec{S}, \tag{2.1b}$$

$$\int_{\partial V} \vec{D}(\vec{x},t)\cdot \mathrm{d}\vec{S} = \int_{V} \varrho(\vec{x},t)\,\mathrm{d}V, \tag{2.1c}$$

$$\int_{\partial V} \vec{B}(\vec{x},t)\cdot \mathrm{d}\vec{S} = 0. \tag{2.1d}$$

The vector $\mathrm{d}\vec{s} = \vec{\tau}\,\mathrm{d}s$ is an infinitesimal curve element, oriented in the direction of the unit vector $\vec{\tau}$, tangent to the contour ∂S. The vector $\mathrm{d}\vec{S} = \vec{n}\,\mathrm{d}S$ is an infinitesimal surface element, directed as the outward unit vector $\vec{n}$, normal to the surface S. When $S = \partial V$ is a closed surface enclosing a volume V as in (2.1c) and (2.1d), then $\vec{n}$ points outward from V. Finally, $\mathrm{d}V$ denotes an infinitesimal volume element [58].

From equation (2.1a) we see that a line integral of the electric field strength $\vec{E}$ along a contour ∂S is determined by the time derivative of the magnetic flux density $\vec{B}$ passing through the surface S enclosed by the contour. This is called the *Faraday law* or the *law of the electromagnetic induction*. Simply formulated, it states that a changing magnetic flux induces a circulating electric field, and as a result an electric current in a wire loop [76]. The minus sign on the right-hand side (RHS) is in accordance with the Lenz law, which states that an induced electric current is directed such that the flux that it produces opposes the change in the inducing magnetic flux.

The *Maxwell-Ampère law* (2.1b) states that a line integral of the magnetic field strength $\vec{H}$ along ∂S is equal to the current passing through S plus the time derivative of the electric flux density $\vec{D}$ through S. Physically it means that the electric current or a changing electric flux give rise to a circulating magnetic field. We note that the original equation of Ampère did not include the change of the electric flux (the first term under the integral on the RHS in (2.1b), called the *displacement current density*), whose addition was a significant contribution of Maxwell.

Equations (2.1c) and (2.1d) are called the *electric* and the *magnetic Gauss laws*, respectively. Due to the electric Gauss law (2.1c) the charge within a volume V is given by the electric flux through the surface ∂V. The magnetic Gauss law (2.1d) states that the total magnetic flux passing through a closed surface ∂V is zero. This corresponds to the fact that there are no magnetic monopoles but only north-south pole pairs in nature.

Applying the following mathematical relations for a smooth vector field $\vec{F}$

$$\int_{\partial S} \vec{F}(\vec{x},t)\cdot \mathrm{d}\vec{s} = \int_{S} \operatorname{curl}\vec{F}(\vec{x},t)\cdot \mathrm{d}\vec{S}, \qquad \int_{\partial V} \vec{F}(\vec{x},t)\cdot \mathrm{d}\vec{S} = \int_{V} \operatorname{div}\vec{F}(\vec{x},t)\,\mathrm{d}V, \tag{2.2}$$

which are given by the Stokes and the Gauss theorems, respectively, one can transform the equations (2.1a)-

(2.1d) into their *differential form*, which reads [7]

$$\operatorname{curl} \vec{E} = -\frac{\partial \vec{B}}{\partial t}, \tag{2.3a}$$

$$\operatorname{curl} \vec{H} = \frac{\partial \vec{D}}{\partial t} + \vec{J}, \tag{2.3b}$$

$$\operatorname{div} \vec{D} = \varrho, \tag{2.3c}$$

$$\operatorname{div} \vec{B} = 0. \tag{2.3d}$$

Although in general the Maxwell equations are valid in the whole space $(\vec{x}, t) \in \mathbb{R}^3 \times \mathbb{R}$, we will consider a finite space-time domain $\Omega \times [0, T]$, with $T > 0$ in the remainder of this thesis. The domain $\Omega \subset \mathbb{R}^3$ is assumed to be open, bounded, and simply connected with Lipschitz boundary. We note that in practice the computational domain Ω might consist of several materials, as illustrated in Figure 2.1, where the subdomains Ω_{Fe}, Ω_{Cu}, and Ω_{Air} represent iron, copper, and air, respectively.

Each of the equations (2.3a)-(2.3d) is a PDE, since they include partial derivatives with respect to space and time. A summary of the PDE theory is presented in Section 2.1.2.

Constitutive relations

The Maxwell equations are complemented with constitutive relations. In particular, we have [7]

$$\vec{D} = \varepsilon \vec{E}, \tag{2.4}$$

$$\vec{J} = \sigma \vec{E} + \vec{J}_{\mathrm{s}}, \tag{2.5}$$

$$\vec{H} = \nu \vec{B}, \tag{2.6}$$

where ε is the *electric permittivity*, σ is the *electric conductivity*, and ν is the *magnetic reluctivity*. These material parameters are in general rank-2 tensors, while in our study we assume them to be scalar fields, as we only consider *isotropic* materials. $\vec{J}_{\mathrm{s}}$ is the *source current density*, which typically comes from a coupled current or voltage supply. It can be expressed as

$$\vec{J}_{\mathrm{s}}(\vec{x}, t) = \sum_{k=1}^{n_{\mathrm{s}}} \vec{\chi}_k(\vec{x}) i_k(t) \tag{2.7}$$

using the *winding functions* $\vec{\chi}_k(\vec{x}) \in \mathbb{R}^3$ [117], which spatially distribute the currents $i_k(t) \in \mathbb{R}$ flowing through n_{s} stranded conductors. Assuming the coils carrying the input currents are represented by the subdomain $\Omega_{\mathrm{Cu}} \subset \Omega$ (see Figure 2.1), we have that $\vec{J}_{\mathrm{s}}(\vec{x}, t) = 0$ for $\vec{x} \in \Omega \setminus \Omega_{\mathrm{Cu}}$ and that $\vec{J}_{\mathrm{s}}(\vec{x}, t) \neq 0$ for $\vec{x} \in \Omega_{\mathrm{Cu}}$.

We assume linear dependencies in (2.4) and (2.5), i.e., $\varepsilon = \varepsilon(\vec{x})$ and $\sigma = \sigma(\vec{x})$. In the multi-material domain Ω from Figure 2.1 the conductivity

$$\sigma(\vec{x}) \quad \text{is} \quad \begin{cases} = 0, & \vec{x} \in \Omega \setminus \Omega_{\mathrm{Fe}}, \\ > 0, & \vec{x} \in \Omega_{\mathrm{Fe}}, \end{cases} \tag{2.8}$$

with the subdomain $\Omega_{\mathrm{Fe}} \subset \Omega$ containing a ferromagnetic material. On the other hand, the relation (2.6) has a nonlinear behavior, i.e., $\nu = \nu(\vec{x}, |\vec{B}|)$, due to the magnetic saturation in ferromagnetic materials.

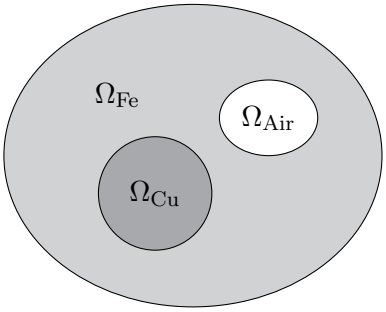

Figure 2.1: Sketch of a multi-material domain $\Omega = \Omega_{\mathrm{Fe}} \cup \Omega_{\mathrm{Cu}} \cup \Omega_{\mathrm{Air}}$.

The reluctivity in (2.6) in the domain Ω from the Figure 2.1 can be modeled, e.g., by

$$\nu(\vec{x}, |\vec{B}|) = \begin{cases} \nu_0, & \vec{x} \in \Omega \setminus \Omega_{\mathrm{Fe}}, \\ \nu(|\vec{B}|), & \vec{x} \in \Omega_{\mathrm{Fe}}, \end{cases} \tag{2.9}$$

where we assume that the materials in $\Omega \setminus \Omega_{\mathrm{Fe}}$ behave like vacuum with reluctivity $\nu_0 = 10^7/(4\pi)\ \mathrm{m/H}$. The properties of the nonlinear reluctivity function $\nu(|\vec{B}|)$ are described in the following Section 2.1.1.

2.1.1 BH-curve and its properties

The theory presented in this section is based on [99, 100]. A BH-curve (or magnetization curve) defines the dependence of the magnetic flux density $\vec{B}$ on the magnetic field strength $\vec{H}$ acting on a ferromagnetic material. In general, it is characterized by *hysteresis* [13], namely, the ability of the ferromagnetic materials to "memorize their magnetic past". This phenomenon is typically represented by a dynamic lag of $\vec{B}$ behind $\vec{H}$ and makes modeling quite challenging.

Within this work we neglect the hysteresis effects and consider a simplified variant of the BH-curve given by a one-to-one correspondence of the experimentally measured magnitudes $B = |\vec{B}|$ and $H = |\vec{H}|$ as it is illustrated in Figure 2.2. In order to reconstruct a monotone continuously differentiable BH-curve from a finite set of measured data points (H_k, B_k), $k \in \mathbb{N}$ one could exploit, e.g., the monotonicity-preserving techniques presented in [42] or [100].

Let the relation between B and H be mathematically given by [77]

$$B = b(H), \quad b\colon \mathbb{R}_0^+ \to \mathbb{R}_0^+, \tag{2.10}$$

where $\mathbb{R}_0^+$ is the set of non-negative real numbers. The physical properties of the BH-curve b are collected in the following assumption.

Assumption 2.1 ([100])**.** *Let $\mu_0 = 1/\nu_0 = 4\pi \cdot 10^{-7}\,\mathrm{H/m}$ denote the permeability of vacuum. For the function b from* (2.10) *it holds:*

1. $b(0) = 0$,
2. $b \in C^1\big(\mathbb{R}_0^+\big)$,
3. $b'(s) \geq \mu_0, \quad s \in \mathbb{R}_0^+$,
4. $\lim\limits_{s\to\infty} b'(s) = \mu_0$.

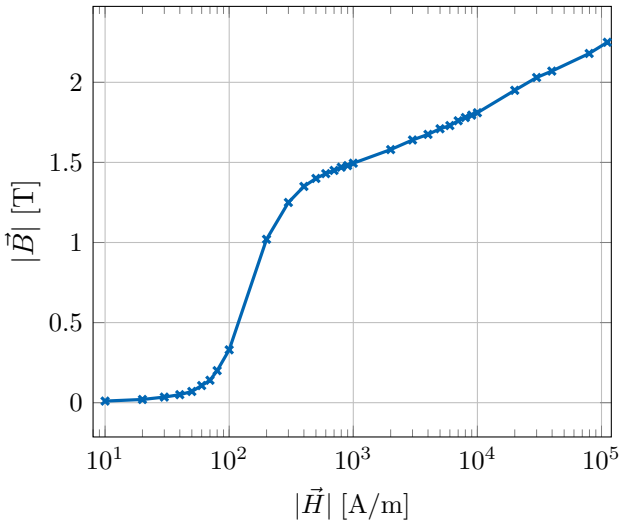

Figure 2.2: An exemplary BH-curve of steel obtained from measurements [82].

Based on the conditions imposed in the Assumption 2.1 on the BH-curve b we can construct a continuous reluctivity function $\nu\colon \mathbb{R}_0^+ \to \mathbb{R}_0^+$ via [70]

$$\nu(s) = \begin{cases} \dfrac{b^{-1}(s)}{s}, & s \in \mathbb{R}^+, \\ (b^{-1})'(0), & s = 0. \end{cases} \tag{2.11}$$

From the Assumption 2.1 one can derive the properties of the reluctivity ν given in (2.11), [99].

Corollary 2.2. *Under the Assumption 2.1 and denoting $f(s) = \nu(s)s$ we have*

B.1 $\nu \in C\left(\mathbb{R}_0^+\right)$, $\lim\limits_{s\to\infty} \nu(s) = \nu_0$ *and* $0 < c_1 \leq \nu(s) \leq \nu_0$, $s \in \mathbb{R}_0^+$,

B.2 $\nu \in C^1(\mathbb{R}^+)$, $\lim\limits_{s\to\infty} \nu'(s) = 0$ *and* $|\nu'(s)| \leq \nu_1 < \infty$, $s \in \mathbb{R}^+$; *if* $\exists\, b''(0)$ *then* $\exists\, \nu'(0)$ *and* $\nu'(0)$ *is bounded,*

B.3 f *is strongly monotone with monotonicity constant* c_1, *i.e.,*

$$(f(s) - f(t))(s - t) \geq c_1(s - t)^2, \quad s, t \in \mathbb{R}_0^+, \tag{2.12}$$

B.4 f *is Lipschitz continuous with Lipschitz constant* ν_0, *i.e.,*

$$|f(s) - f(t)| \leq \nu_0|s - t|, \quad s, t \in \mathbb{R}_0^+. \tag{2.13}$$

Proof. The details can be found in [99]. □

The conditions from the Corollary 2.2 will be exploited for the numerical analysis in Section 3.1.3. Finally, to solve a PDE containing the nonlinearity ν, a linearization method should be applied. For this we define the *differential reluctivity* tensor (see, e.g., [59]) by

$$\boldsymbol{\nu}_{\mathrm{d}}(\vec{B}) = \begin{cases} \nu(B)\mathbf{I} + \dfrac{1}{B}\nu'(B)\vec{B}\vec{B}^\top, & B \in \mathbb{R}^+, \\ \nu(B)\mathbf{I}, & B = 0, \end{cases} \tag{2.14}$$

where $\mathbf{I}$ denotes the identity tensor and $B = |\vec{B}|$. Several linearization methods which use the tensor (2.14) will be discussed in Section 3.2.3.

In the following Section 2.1.2 we provide a summary of basic properties of PDEs, which will allow us to better understand the mathematical formulations of the electromagnetic laws.

2.1.2 Partial differential equations

A PDE defines a relation including an unknown function and its partial derivative. The corresponding theory can be found in numerous books, e.g., [38, 106, 116]. A general form of a PDE of order $k \geq 1$ for a function $u : U \to \mathbb{R}$, with an open bounded domain $U \subset \mathbb{R}^n$, $n \geq 1$ and vector $\vec{x} = [x_1, x_2, \ldots, x_n]^\top$ is

$$F\Big(D^k u(\vec{x}), D^{k-1}u(\vec{x}), \ldots, D^1(\vec{x}), u(\vec{x}), \vec{x}\Big) = 0, \quad \vec{x} \in U, \tag{2.15}$$

where $D^k u(\vec{x})$ denotes the set of all partial derivatives of order k, i.e.,

$$D^k u(\vec{x}) = \left\{ \frac{\partial^{|\alpha|} u(\vec{x})}{\partial x_1^{\alpha_1} \ldots \partial x_n^{\alpha_n}} : \quad |\alpha| = k \right\}, \tag{2.16}$$

with multi-index $\alpha = [\alpha_1, \ldots, \alpha_n]^\top \in \mathbb{R}^n$ of order $|\alpha| = \alpha_1 + \ldots + \alpha_n$, for $\alpha_i \geq 0$ and $i = 1, \ldots, n$. In case of $k = 0$ we set $D^0 u(\vec{x}) := u(\vec{x})$.

As already mentioned, a PDE often originates from a mathematical model describing a physical or an engineering problem. When creating such a model, one has to make sure the posed problem is a solvable PDE, which preferably possesses a unique solution and is stable under small perturbations of the input data. This can be analyzed using the notion of well-posedness by Hadamard, according to which, a problem is called *well-posed* if and only if (iff) each of the following criteria

1. existence: the problem has a solution,
2. uniqueness: there is at most one solution,
3. stability: the solution depends continuously on the input data

holds. To obtain a unique solution *boundary conditions (BCs)* have to be prescribed on the boundary ∂U. There are several types of BCs such as Dirichlet, Neumann, or Robin BCs [106, Section 1.5], given for $\vec{x} \in \partial U$ by

$$u(\vec{x}) = f_1(\vec{x}), \qquad \operatorname{grad} u(\vec{x}) \cdot \vec{n} = f_2(\vec{x}), \quad \text{and} \quad u(\vec{x}) + \beta(\vec{x}) \operatorname{grad} u(\vec{x}) \cdot \vec{n} = f_3(\vec{x}), \tag{2.17}$$

respectively. Here $\vec{n}$ is the outward unit normal vector to ∂U and f_i, $i = 1, 2, 3$, and β are given functions.

By the *classical solution* of the PDE (2.15) of order $k \geq 1$ we call a function $u \in C^k(U)$, i.e., a k times continuously differentiable function, which fulfills (2.15). However, for numerous engineering problems lacking smoothness we might have to allow for weaker properties of the solution in order to still be able to solve the problem and to describe the underlying physics. In this case one speaks of a *weak* or *generalized solution*. Thus, we will consider the well-posedness in a larger class of weak solutions. The corresponding theory is presented in Chapter 3.

Classification of second-order PDEs

We consider the case of $k = 2$ and $n = 2$ in (2.15), which represents a second-order PDE for the function $u = u(\vec{x})$, $\vec{x} = [x_1, x_2]^\top \in U$ in two independent variables. Besides, we assume the equation is linear, i.e., we have

$$a(\vec{x})\frac{\partial^2 u(\vec{x})}{\partial x_1^2} + 2b(\vec{x})\frac{\partial^2 u(\vec{x})}{\partial x_1 \partial x_2} + c(\vec{x})\frac{\partial^2 u(\vec{x})}{\partial x_2^2} + l\left(\frac{\partial u(\vec{x})}{\partial x_1}, \frac{\partial u(\vec{x})}{\partial x_1}, u(\vec{x}), \vec{x}\right) = 0, \tag{2.18}$$

where l is a linear differential operator of first order and a, b, c are given coefficient functions, which do not vanish all simultaneously. Many fundamental properties of (2.18) are determined by the sign of the discriminant [106]

$$\delta(\vec{x}) = \big(b(\vec{x})\big)^2 - a(\vec{x})c(\vec{x}), \quad \vec{x} \in U. \tag{2.19}$$

In particular, the PDE (2.18) is called *hyperbolic* at $\vec{x}$ if $\delta(\vec{x}) > 0$, *parabolic* at $\vec{x}$ if $\delta(\vec{x}) = 0$, and *elliptic* at $\vec{x}$ if $\delta(\vec{x}) < 0$. The equation is hyperbolic, parabolic, or elliptic in the domain U if it is hyperbolic, parabolic, or elliptic at each point $\vec{x} \in U$, respectively.

For the PDE (2.18) one can find a coordinate system $(\xi, \eta) = (\xi(\vec{x}), \eta(\vec{x}))$, which transforms the equation into its *canonical form* [106]. The PDEs

$$u_{\xi\eta} + l_1(u) = g(\xi, \eta), \qquad u_{\xi\xi} + l_1(u) = g(\xi, \eta), \quad \text{and} \quad u_{\xi\xi} + u_{\eta\eta} = g(\xi, \eta) \tag{2.20}$$

are the canonical forms of the hyperbolic, parabolic, and elliptic equations, respectively. Here l_1 denotes a first-order linear differential operator and g is a known function.

The provided brief theory on PDEs will be used in the following Section 2.1.3, where we derive a particular PDE formulation from the Maxwell equations, commonly used for modeling of the electromagnetic fields evolution within low-frequency magnetic applications such as, e.g., electric motors.

2.1.3 Magnetoquasistatic approximation

The magnetoquasistatic (MQS) approximation defines a subset of the Maxwell equations, where some phenomena are assumed to be negligible. In particular, within the MQS setting the magnetic effects and the Joule losses outweigh the electric effects. It means that the variation of the electric flux density $\vec{D}$ in time is small compared to the electric current density $\vec{J}$, i.e.,

$$|\vec{J}| \gg \left|\frac{\partial \vec{D}}{\partial t}\right|. \tag{2.21}$$

Such a scenario is sufficient when one deals with low-frequency applications provided the wavelength is much longer than the size of the problem [75]. This is the case for various electromagnetic devices, like electric motors or transformers, which operate at so-called power frequencies (frequencies below a few tens of kHz). Using (2.21), we can neglect the displacement current in the Maxwell-Ampère law (2.3b), which after insertion of (2.5) and (2.6) becomes

$$\operatorname{curl}\big(\nu\vec{B}\big) = \sigma\vec{E} + \vec{J}_{\mathrm{s}}. \tag{2.22}$$

To define the electromagnetic fields uniquely in the computational domain Ω, conditions on the boundary $\Gamma = \partial\Omega$ are imposed. The common choices of the BCs are the *electric boundary condition (EBC)* and the *magnetic boundary condition (MBC)* given by

$$\vec{n} \times \vec{E} = 0 \quad \text{on } \Gamma_{\mathrm{EBC}} \quad \text{and} \quad \vec{n} \times \vec{H} = 0 \quad \text{on } \Gamma_{\mathrm{MBC}}, \tag{2.23}$$

respectively [3, Section 1.3]. The vector $\vec{n}$ is the outward normal to the boundary $\Gamma = \Gamma_{\mathrm{EBC}} \cup \Gamma_{\mathrm{MBC}}$, where $\Gamma_{\mathrm{EBC}} \cap \Gamma_{\mathrm{MBC}} = \emptyset$. The homogeneous EBC corresponds to the materials with infinite conductivity σ on the boundary (called perfect electric conductors), while the homogeneous MBC defines the materials with infinite permeability $\mu = 1/\nu$ on the boundary (called perfect magnetic conductors).

Potential representations

From the magnetic Gauss law (2.3d) we conclude the existence of the *magnetic vector potential (MVP)* $\vec{A} = \vec{A}(\vec{x}, t)$ [58] such that

$$\vec{B} = \operatorname{curl} \vec{A}, \tag{2.24}$$

since the divergence of the curl operator is equal to zero (for a sufficiently smooth $\vec{A}$-field on the domain Ω). Plugging (2.24) into the Faraday law (2.3a) and using the fact that the curl of any gradient field is zero, we obtain

$$\vec{E} = -\frac{\partial \vec{A}}{\partial t} - \operatorname{grad} \phi, \tag{2.25}$$

where $\phi = \phi(\vec{x}, t)$ is the *electric scalar potential.* We note that the MVP in (2.24) defines the $\vec{B}$-field only up to a gradient field. To ensure uniqueness the notion of *gauge* is used. For instance, one can include $\operatorname{div} \vec{A} = 0$ as an additional equation into the system. The representations (2.24) and (2.25), applied to (2.22), lead to the $\vec{A}$-ϕ*-formulation*

$$\operatorname{curl}\big(\nu \operatorname{curl} \vec{A}\big) = -\sigma \frac{\partial \vec{A}}{\partial t} - \sigma \operatorname{grad} \phi + \vec{J}_{\mathrm{s}}. \tag{2.26}$$

To reduce the number of degrees of freedom (DoFs), we introduce a new unknown

$$\vec{A}^* = \vec{A} + \int_0^t \operatorname{grad} \phi \, \mathrm{d}s, \quad t \in [0, T], \tag{2.27}$$

and obtain the $\vec{A}^*$*-formulation*[2]

$$\operatorname{curl}\big(\nu \operatorname{curl} \vec{A}^*\big) = -\sigma \frac{\partial \vec{A}^*}{\partial t} + \vec{J}_{\mathrm{s}}. \tag{2.28}$$

Equation (2.28) is called the *eddy current equation*, since the first term on the RHS represents the *eddy currents* [75], also called the *Foucault currents* [3, Section 1.2]. According to the first Joule law [3, Section 1.2], they lead to heat generation, which commonly degrades performance of devices, like electric machines. Nevertheless, the eddy current effect is crucial for the applications like induction motors, since it lies in the core of the operation of this motor type, see Section 2.4. The calculation of eddy currents and of the corresponding losses is thus an important part of the electromagnetic device simulations.

The BCs (2.23) are given for each $t \in [0, T]$, $T > 0$, in terms of the MVP by

$$\vec{n} \times \vec{A}^* = 0 \quad \text{on } \Gamma_{\mathrm{EBC}} \quad \text{and} \quad \vec{n} \times (\nu \operatorname{curl} \vec{A}^*) = 0 \quad \text{on } \Gamma_{\mathrm{MBC}}, \tag{2.29}$$

which are the *homogeneous Dirichlet* and the *homogeneous Neumann* BCs, respectively.

[2] In the following we will abuse the notations and will denote the MVP in the $\vec{A}^*$-formulation by $\vec{A}$.

Initial-value and steady-state problems

Additionally to the BCs (2.29) for a unique solvability of the eddy current problem (2.28) on a given time interval $(0, T]$ an *initial condition (IC)*

$$\vec{A}^*(\vec{x}, 0) = \vec{A}_0^*, \quad \vec{x} \in \Omega \tag{2.30}$$

has to be prescribed. The problem (2.28)-(2.30) is called *initial-boundary-value problem (IBVP)*. Typically, the solution of such an IBVP, excited with a periodic signal $\vec{J}_\mathrm{s}$, consists of a transient part and a (periodic) steady state (as in Figure 1.2b).

Alternatively to the sequential solution starting from the IC (2.30), the steady-state solution of (2.28) on $(0, T)$ can be obtained by adding the TP condition

$$\vec{A}^*(\vec{x}, 0) = \vec{A}^*(\vec{x}, T), \quad \vec{x} \in \Omega. \tag{2.31}$$

The problem (2.28), (2.29), (2.31) is called the *TP boundary-value problem (TPBVP)*. In contrast to IVPs, TP problems couple the initial and the end solutions on the period $[0, T]$ and might lead to a higher computational effort compared to the solution of IVPs on the same time interval (see Section 3.3).

Two-dimensional model

In some industrial applications such as electric motors, one commonly assumes that their models are invariant under translation in the axial x_3-direction. In this case two-dimensional (2D) models, which represent the cross-sections of the devices, are sufficient. One then has $\vec{B}(\vec{x}, t) = [B_1(x_1, x_2, t), B_2(x_1, x_2, t), 0]^\top$ and therefore $\vec{J}_\mathrm{s}(\vec{x}, t) = [0, 0, J_{\mathrm{s},3}(x_1, x_2, t)]^\top$ and $\vec{A}(\vec{x}, t) = [0, 0, A_3(x_1, x_2, t)]^\top$. Denoting $u := A_3$ and $f := J_{\mathrm{s},3}$ we transform the equation (2.28) into

$$-\operatorname{div}\big(\nu \operatorname{grad} u\big) = -\sigma \frac{\partial u}{\partial t} + f, \quad (\vec{x}, t) \in \Omega \times (0, T], \tag{2.32}$$

with an open, bounded, simply connected domain $\Omega \subset \mathbb{R}^2$ having Lipschitz boundary, $\vec{x} = [x_1, x_2]^\top$, and $T > 0$. Although in general there is a nonlinearity present in (2.32) we intend to classify the PDE using the theory from Section 2.1.2. Since there is no second-order derivative in t and the second-order derivatives in x_1 and x_2 have the same sign, the PDE (2.32) is of parabolic type for $\sigma > 0$ and of elliptic type for $\sigma = 0$ due to (2.20). We note that within the 2D setting the gauge $\operatorname{div} \vec{A} = 0$ is automatically satisfied.

As already mentioned in Section 2.1.2, in order to obtain the physical (unique) solution of (2.32) one has to fix boundary and initial conditions. In particular, we consider on the boundary $\partial\Omega$ of the domain Ω the homogeneous Dirichlet BC, i.e.,

$$u(\vec{x}, t) = 0, \quad (\vec{x}, t) \in \partial\Omega \times [0, T]. \tag{2.33}$$

It describes the situation, when the normal component of the magnetic flux density is zero. Prescribing an IC at the initial time point $t = 0$

$$u(\vec{x}, 0) = u_0(\vec{x}), \quad \vec{x} \in \Omega \tag{2.34}$$

we obtain an IBVP (2.32)-(2.34). Alternatively, imposing a TP condition

$$u(\vec{x}, 0) = u(\vec{x}, T), \quad \vec{x} \in \Omega \tag{2.35}$$

instead of the IC (2.34), we obtain the TPBVP (2.32) on $\Omega \times (0, T)$ (i.e., with the excluded right limit $t = T$), together with (2.33), (2.35). Theoretical analysis as well as numerical solution approaches for the IBVP (2.32)-(2.34) and for the TPBVP (2.32), (2.33), (2.35) are discussed in Chapter 3.

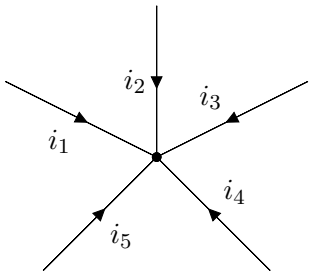

(a) Branches with currents flowing into a node.

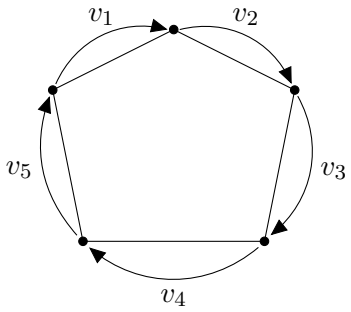

(b) Voltages across the branches in a loop.

Figure 2.3: Visualization of the Kirchhoff current and voltage laws.

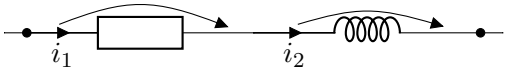

(a) Serial connection.

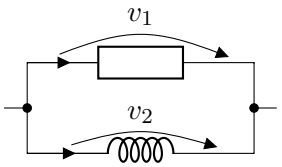

(b) Parallel connection.

Figure 2.4: Two types of connections of two elements in a circuit.

2.2 Electric circuit theory

Electric circuit models are used in a great variety of applications such as, e.g., sensors, microprocessors, or power converters. Mathematical modeling of a circuit is governed by the two Kirchhoff laws: the *Kirchhoff current law (KCL)* and the *Kirchhoff voltage law (KVL)*, [107, Section 2.3]. KCL states that the sum of the currents flowing into any node of the circuit is zero. It shows that electric charge cannot accumulate at a node of the network [107, Section 2.3]. Mathematically this is given by

$$\sum_{k=1}^{N_{\mathrm{bn}}} \pm i_k = 0, \tag{2.36}$$

where N_{bn} denotes the number of branches incident to the node and the signs before the currents i_k are determined by the orientation of the branches. An example with $N_{\mathrm{bn}} = 5$ is visualized in Figure 2.3a.

KVL states that the sum of the voltage drops along the branches in a closed loop is zero. It asserts that the electric potential at any point is independent of the path followed to reach that point [107, Section 2.3]. The mathematical representation is

$$\sum_{k=1}^{N_{\mathrm{bl}}} \pm v_k = 0, \tag{2.37}$$

where N_{bl} denotes the number of branches forming a loop and the signs before the voltages v_k are determined by the orientation of the branches. A loop with $N_{\mathrm{bl}} = 5$ branches is illustrated in Figure 2.3b. The KCL and KVL can be derived from the Maxwell-Ampère law (2.1b) and the Faraday law (2.1a) under the assumptions of statics, i.e., $\partial \vec{D}/\partial t = 0$ and $\partial \vec{B}/\partial t = 0$, respectively.

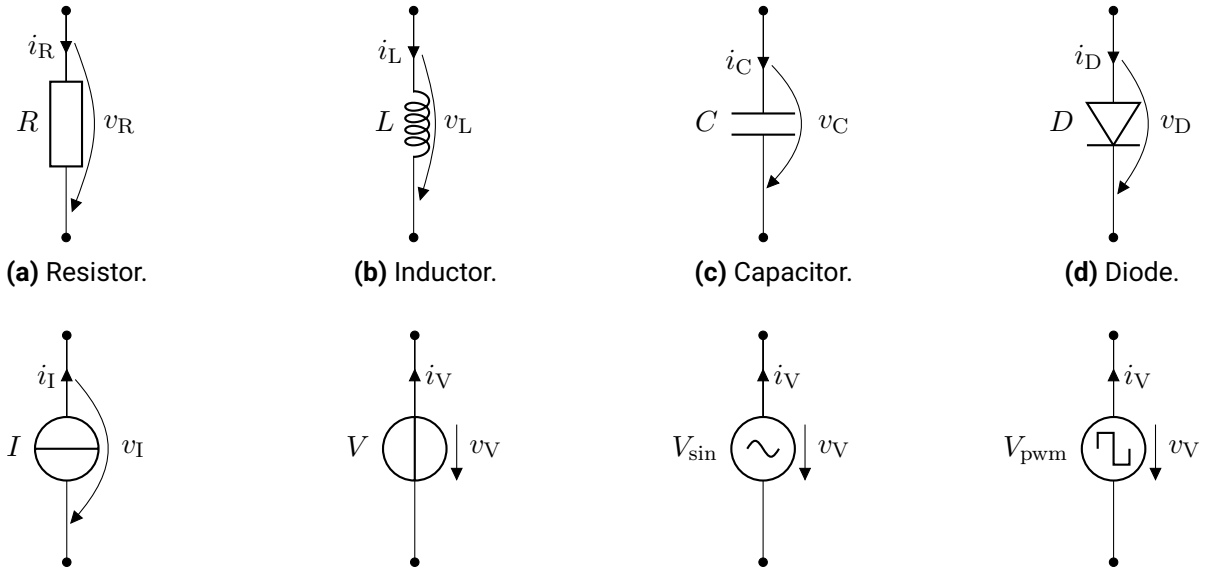

(a) Resistor. **(b)** Inductor. **(c)** Capacitor. **(d)** Diode.

(e) Constant current source. **(f)** Constant voltage source. **(g)** Sinusoidal voltage source. **(h)** PWM voltage source.

Figure 2.5: Typical circuit components.

Elements in a circuit can be connected *in series* or *in parallel* (or in any combination of both) as it is illustrated in Figure 2.4 for $n = 2$ exemplary elements. As a consequence of the Kirchhoff laws we have for the serial connection (Figure 2.4a)

$$i_1 = i_2 = \ldots = i_n, \tag{2.38}$$

and for the parallel connection (Figure 2.4b)

$$v_1 = v_2 = \ldots = v_n, \tag{2.39}$$

where n denotes the number of components in the circuit. The two elements from the Figure 2.4 are called the resistor and the inductor, which we now describe in more detail together with the other typical circuit elements.

The basic components of a circuit are resistors, inductors, capacitors, diodes, current and voltage sources, depicted in Figure 2.5. Additionally to the Kirchhoff laws a circuit model is derived using the following (dynamic) time-dependent constitutive relations of voltages and currents in the circuit elements. In particular, we have

$$v_\mathrm{R}(t) = R i_\mathrm{R}(t), \tag{2.40}$$

$$v_\mathrm{L}(t) = L \frac{\mathrm{d}}{\mathrm{d}t} i_\mathrm{L}(t), \tag{2.41}$$

$$i_\mathrm{C}(t) = C \frac{\mathrm{d}}{\mathrm{d}t} v_\mathrm{C}(t) \tag{2.42}$$

for a (linear) resistor (Figure 2.5a), an inductor (Figure 2.5b), and a capacitor (Figure 2.5c), respectively. These formulas can be derived from the constitutive relations for electromagnetic fields and the Maxwell equations [112]. For example, (2.41) can be obtained by plugging the following relation between the current i_L and the magnetic flux Φ_L passing through the inductor

$$\Phi_\mathrm{L}(t) = L i_\mathrm{L}(t) \tag{2.43}$$

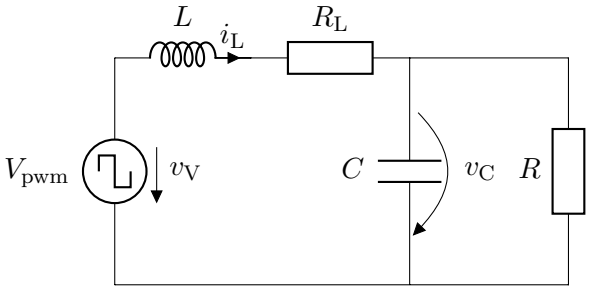

Figure 2.6: A simplified circuit of a buck converter model with a PWM voltage source v_{V} and two state variables: the current i_{L} and the voltage v_{C}.

into the relation between the voltage and the flux

$$v_{\mathrm{L}}(t) = \frac{\mathrm{d}}{\mathrm{d}t}\Phi_{\mathrm{L}}(t), \tag{2.44}$$

which can be derived from the Faraday law (2.1a), [112]. The quantities R, L, and C are called the *resistance*, the *inductance*, and the *capacitance*, respectively. In general, the relations above can be nonlinear, e.g., we may have $L = L\big(i_{\mathrm{L}}(t)\big)$ in (2.43). Additionally to the already mentioned circuit elements also such components as diodes (Figure 2.5d) and transistors play an important role in modern electronics [112]. A diode model can be described by the Shockley diode equation [120]

$$i_{\mathrm{D}}(t) = I_{\mathrm{S}}\big(\exp\big(v_{\mathrm{D}}(t)/U_{\mathrm{T}}\big) - 1\big), \tag{2.45}$$

where I_{S} is the saturation current and U_{T} is the thermal voltage.

Furthermore, circuits can have source elements, which represent the current or voltage supplies. In Figure 2.5e and Figure 2.5f constant current or *direct current (DC)* and constant voltage sources are illustrated, respectively. However, many electric circuits have time-varying input power. In Figure 2.5g and Figure 2.5h we present the sinusoidal and PWM voltage source elements, respectively. Elements representing the sinusoidal current or *alternating current (AC)* and PWM current sources look analogously.

An example of a simple circuit supplied with a PWM voltage source v_{V} is presented in Figure 2.6. This circuit represents a buck (DC-DC) converter model under the assumption of an ideal switch and continuous conduction mode [60]. It is described by two state variables: the current $i_{\mathrm{L}}(t) > 0$ through the inductor and the voltage $v_{\mathrm{C}}(t)$ across the capacitor, which is also the output voltage of the buck converter. We will refer to this circuit model when providing more details on PWM signals in Section 2.3.

Based on the described circuit laws and relations one could formulate an appropriate mathematical model using, e.g., the modified nodal analysis (MNA) [71] or the modified loop analysis [112]. Such circuit models are usually described by (systems of) ordinary differential equations (ODEs) or differential-algebraic equations (DAEs), which we describe in the following sections.

2.2.1 Ordinary differential equations (ODEs)

An ODE of order $n \geq 1$ is an equation of the form

$$F\big(u^{(n)}(t), u^{(n-1)}(t), \ldots, u'(t), u(t), t\big) = 0, \quad t \in (0, T] \tag{2.46}$$

where the superscript (n) denotes the derivative of order n and $T > 0$ is given. As in the case of a PDE, to determine the solution $u(t)$ uniquely we prescribe n ICs at $t = 0$

$$u^{(n-1)}(0) = u_{n,0} \quad \dots \quad u'(0) = u_{2,0} \quad u(0) = u_{1,0}. \tag{2.47}$$

The ODE (2.46) of order n together with the ICs (2.47) can be transformed into an *initial-value problem (IVP)* for the system of first-order ODEs given by

$$\begin{aligned} F\big(u_n'(t), u_n(t), u_{n-1}(t), \dots, u_1(t), t\big) = 0, \qquad & u_n(0) = u_{n,0}, \\ u_{n-1}'(t) = u_n, \qquad & u_{n-1}(0) = u_{n-1,0}, \\ \vdots \qquad & \vdots \\ u_1'(t) = u_2, \qquad & u_1(0) = u_{1,0}. \end{aligned} \tag{2.48}$$

Denoting $\mathbf{u}(t) = [u_1(t), \dots, u_n(t)]^\top \in \mathbb{R}^n$ and $\mathbf{u}_0 = [u_{1,0}, \dots, u_{n,0}]^\top \in \mathbb{R}^n$, we thus consider an IVP for a general system of ODEs

$$\mathbf{u}'(t) = \mathbf{f}(\mathbf{u}(t), t), \quad t \in (0, T], \tag{2.49}$$

$$\mathbf{u}(0) = \mathbf{u}_0. \tag{2.50}$$

According to the Picard-Lindelöf theorem [124, Theorem 7.1.1] the IVP (2.49)-(2.50) possesses a unique solution if the RHS $\mathbf{f}$ is Lipschitz continuous with respect to its first argument, i.e., if there is a constant $L > 0$ such that

$$\|\mathbf{f}(\mathbf{y}, t) - \mathbf{f}(\mathbf{z}, t)\| \leq L\|\mathbf{y} - \mathbf{z}\|, \quad \forall t \in [0, T], \quad \forall\, \mathbf{y}, \mathbf{z} \in \mathbb{R}^n, \tag{2.51}$$

where $\|\cdot\|$ denotes, e.g., the Euclidean norm in $\mathbb{R}^n$. For many simple ODEs one could calculate the solution analytically, e.g., using the method of variation of constants or separation of variables [64]. However, for more complex systems it is often not possible to obtain the analytical solution and one has to compute an approximate solution with the aid of numerical time-integration methods, which will be provided in Section 3.2.2.

We state an intermediate result which gives a bound for the error between an approximate and the exact solutions of (2.49)-(2.50).

Theorem 2.3 (Generalization of the Gronwall lemma, based on [64, Theorem I.10.2])**.** *Let* $\mathbf{u}$ *and* $\mathbf{v}$ *be the exact and approximate solutions to the IVP* (2.49)-(2.50)*, respectively. If*

a) $\|\mathbf{u}(t_0) - \mathbf{v}(t_0)\| \leq \rho$*,*

b) $\|\mathbf{v}_+'(t) - \mathbf{f}(\mathbf{v}(t), t)\| \leq \varepsilon(t)$*, where* $\mathbf{v}_+'(t) = \lim\limits_{s \to t^+} \mathbf{v}'(s)$*,*

c) $\mathbf{f}$ *satisfies the Lipschitz condition* (2.51) *with constant* $L > 0$*,*

then for $t \geq t_0$ *we have the error estimate*

$$\|\mathbf{u}(t) - \mathbf{v}(t)\| \leq \exp\big(L(t - t_0)\big)\left(\rho + \int_{t_0}^{t} \exp\big(-L(s - t_0)\big)\, \varepsilon(s)\, \mathrm{d}s\right), \tag{2.52}$$

where we have set $t_0 = 0$ *for better visibility of the initial time point.*

The estimate (2.52) expresses the influence of the error ρ in the initial values and of the defect $\varepsilon(t), t \in [0, T]$, on the error between the exact and approximate solutions. We will use this result when investigating convergence in Section 4.3.1.

2.2.2 Linear autonomous planar systems of ODEs

There are several classifications of ODEs, e.g., linear and nonlinear, autonomous and non-autonomous, etc. In this section we will focus on linear autonomous systems of ODEs in $\mathbb{R}^2$ (i.e., planar systems), which model, e.g., $(R)LC$-circuits or other oscillators. The system of ODEs (2.49) is called

- *linear* if the RHS $\mathbf{f}$ depends linearly on the unknown function $\mathbf{u}(t)$,
- *autonomous* if the RHS $\mathbf{f}$ does not depend explicitly on the independent variable t, i.e., $\mathbf{f} = \mathbf{f}(\mathbf{u}(t))$.

Consider the 2D linear system of ODEs

$$\mathbf{u}'(t) = \mathbf{A}\mathbf{u}(t) \tag{2.53}$$

with a matrix $\mathbf{A} \in \mathbb{R}^{2\times 2}$. A vector $\tilde{\mathbf{u}} \in \mathbb{R}^2$ is called an *equilibrium* or a *critical point* of (2.53) if $\mathbf{A}\tilde{\mathbf{u}} = \mathbf{0}$. The behavior of the solution around the equilibrium can be characterized by the eigenvalues of the matrix $\mathbf{A}$. In particular, if all eigenvalues have negative real parts, the equilibrium is *stable*. Otherwise, it is *unstable* or given by a *saddle point*. In case $\mathbf{A}$ has at least one zero eigenvalue, i.e., $\det \mathbf{A} = 0$, we speak of a *degenerate equilibrium* [105, Section 1.5]. An equilibrium point is called *hyperbolic* if none of the eigenvalues has zero real part [105, Section 1.9].

The system (2.53) can be reduced to a more convenient linear system by transforming the matrix $\mathbf{A}$ into its Jordan canonical form [105, Section 1.8]. In particular, there exists an invertible matrix $\mathbf{P}$ whose columns consist of the generalized eigenvectors of $\mathbf{A}$ such that the matrix

$$\mathbf{B} = \mathbf{P}^{-1}\mathbf{A}\mathbf{P} \tag{2.54}$$

has one of the following Jordan forms

$$\mathbf{B}_1 = \begin{bmatrix} \lambda & 0 \\ 0 & \mu \end{bmatrix}, \qquad \mathbf{B}_2 = \begin{bmatrix} \lambda & 1 \\ 0 & \lambda \end{bmatrix}, \qquad \mathbf{B}_3 = \begin{bmatrix} a & -b \\ b & a \end{bmatrix}. \tag{2.55}$$

The values $\lambda, \mu, a, b \in \mathbb{R}$ are obtained from the eigenvalues of the matrix $\mathbf{A}$. For example, a and b in $\mathbf{B}_3$ are the real and imaginary parts of the two complex conjugate eigenvalues of $\mathbf{A}$. The solution $\mathbf{u}$ of (2.53) can be obtained from the linear transformation of coordinates

$$\mathbf{u}(t) = \mathbf{P}\mathbf{y}(t) \tag{2.56}$$

where $\mathbf{y}$ denotes the solution of the system

$$\mathbf{y}'(t) = \mathbf{B}\mathbf{y}(t). \tag{2.57}$$

Thus, since the behavior of (2.53) is linearly equivalent to that of (2.57), it suffices to analyze (2.57) with the matrix $\mathbf{B}$ being in one of the Jordan canonical forms (2.55).

The system of ODEs (2.57) with $\mathbf{y}(t) = [y_1(t), y_2(t)]^\top \in \mathbb{R}^2$ can be characterized by its *phase portrait*, which is the set of all solution curves of (2.57) in the *phase space* $\mathbb{R}^2$. In Figure 2.7 we present the phase portraits for the system (2.57) with the system matrix $\mathbf{B} = \mathbf{B}_3$ given in (2.55). This corresponds to the case when $\mathbf{A}$ has a pair of complex conjugate eigenvalues $a \pm \imath b$, with $\imath = \sqrt{-1}$ denoting the imaginary unit. In particular, Figure 2.7a describes the case of $a < 0$, when the equilibrium point is a *stable focus* or *sink*. The arrows indicate the direction of the motion along the solution curves with increasing time t. Note that when $a > 0$ the direction of the arrows is reversed and we have an *unstable focus* or *source* at the origin. Figure 2.7b corresponds to the case when $\mathbf{A}$ has a pair of pure imaginary complex conjugate eigenvalues $\pm \imath b$ (i.e., $a = 0$). The trajectories of the solution curves lie on the circles and the system (2.57) is said to have a *center* at the origin. Additionally to foci and centers, there are also saddle points and nodes, which can take place for the Jordan forms $\mathbf{B}_1$ and $\mathbf{B}_2$ from (2.55). We refer to [105, Section 1.5] for details.

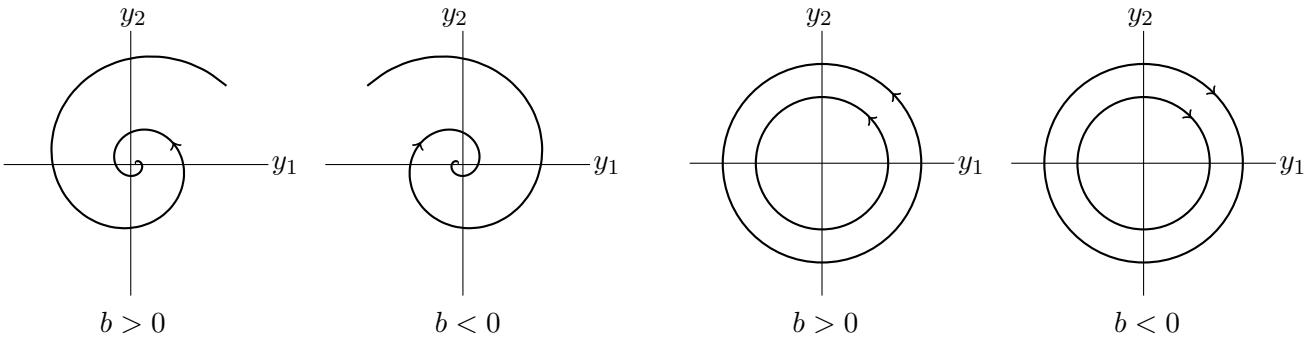

(a) A stable focus at the origin ($a < 0$). **(b)** A center at the origin ($a = 0$).

Figure 2.7: Phase portraits in case of a pair of complex conjugate eigenvalues $a \pm \imath b$.

Periodic orbits and limit cycles

Let $\phi(t, \mathbf{u}_0), t \geq 0$ denote the solution of the system of ODEs (2.53) with a prescribed IC

$$\mathbf{u}(0) = \mathbf{u}_0. \tag{2.58}$$

We consider several possible situations one can face when looking for the solution $\phi(t, \mathbf{u}_0)$. First, consider the case when the system has a stable focus (as in Figure 2.7a). Then for any IC $\mathbf{u}_0$ the solution converges to the *limit point* $\tilde{\mathbf{u}}$ (which is also a critical point of (2.53)), i.e., $\phi(t_n, \mathbf{u}_0) \to \tilde{\mathbf{u}}$ as $t_n \to \infty$, see [105, Section 3.2]. An example of such a system is, e.g., an RLC-circuit where the resistance R inserts the damping into the system.

Second, let the system (2.53) have a center (as in Figure 2.7b). Each closed solution curve which encircles but is not the equilibrium point of the system is called a *cycle* or *periodic orbit* [105, Section 3.3]. Cycles of the system (2.53) correspond to its periodic solutions, i.e., solutions of (2.53) such that

$$\mathbf{u}(0) = \mathbf{u}(T), \tag{2.59}$$

for some $T > 0$. This is due to the fact that $\phi(t, \mathbf{u}_0)$ defines a closed solution curve of (2.53), (2.58) iff for all $t \in \mathbb{R}$

$$\phi(t + T, \mathbf{u}_0) = \phi(t, \mathbf{u}_0). \tag{2.60}$$

It means that one obtains different periodic solutions for different ICs. This happens, e.g., in case of an LC-circuit, whose system represents an ideal oscillator, where no damping is present. The minimal T such that (2.60) holds is called the *period* of the periodic orbit $\phi(t, \mathbf{u}_0)$, [105, Section 3.3]. Although in general the period T varies along the cycles, in the linear case it is the same for each periodic orbit.

Finally, one can have a combination of the two previously described situations. In particular, for any $\mathbf{u}_0$ the solution $\phi(t_n, \mathbf{u}_0)$ of (2.53) might tend to a unique (stable) *limit cycle* Γ_ϕ as $t_n \to \infty$, see [64, Section I.16], [105, Section 3.3]. A limit cycle of the system (2.53) is a periodic orbit, which contains all the limit points of the solution curve $\phi(t, \mathbf{u}_0)$ for any $\mathbf{u}_0$. Such a behavior is characteristic for systems, which possess a unique periodic steady-state solution, typically achieved after a transient phase. Examples of such systems can be an RLC-circuit with a periodic input or the Van der Pol oscillator [64, Section I.16].

The three described scenarios are summarized by an important result from the Poincaré-Bendixson theory [105, Section 3.7] given in the following theorem.

Theorem 2.4 (Poincaré-Bendixson [64, Theorem I.16.1])**.** *Each bounded solution of a 2D system* (2.53) *must tend to a critical point or be a periodic orbit, or tend to a limit cycle.*

Having described the basics of ODE systems and the behavior of the dynamical systems in $\mathbb{R}^2$ we now provide the fundamentals of DAEs.

2.2.3 Differential-algebraic equations

Mathematical models of electric circuits or space-discretizations of the eddy current problem are given by systems of DAEs. For a sufficiently smooth $\mathbf{F}\colon \mathbb{R}^n \times \mathbb{R}^n \times [0,T] \to \mathbb{R}^n$ an implicitly written system

$$\mathbf{F}\big(\mathbf{u}'(t), \mathbf{u}(t), t\big) = \mathbf{0}, \quad t \in (0,T] \tag{2.61}$$

with the unknown $\mathbf{u}\colon [0,T] \to \mathbb{R}^n$, $n \geq 2$ is a system of DAEs if

$$\det\left(\frac{\partial \mathbf{F}}{\partial \mathbf{u}'}\right) = 0, \tag{2.62}$$

as it is stated in [65, Section VII.1]. If the condition (2.62) does not hold, then (2.61) is an implicit system of ODEs. Solvability theory as well as numerical treatment of DAEs is usually more complicated than those of ODEs [21]. In a simple case of a system of linear DAEs with constant coefficients of the form

$$\mathbf{M}\mathbf{u}'(t) + \mathbf{K}\mathbf{u}(t) = \mathbf{f}(t), \tag{2.63}$$

with $\mathbf{M}, \mathbf{K} \in \mathbb{R}^{n\times n}$ and $\mathbf{f}(t) \in \mathbb{R}^n$, the system is solvable iff the *matrix pencil*

$$(\mathbf{M}, \mathbf{K}) := \lambda\mathbf{M} + \mathbf{K} \tag{2.64}$$

is *regular*, i.e., the determinant $\det(\lambda\mathbf{M}+\mathbf{K}) \neq 0$ as a function of $\lambda \in \mathbb{C}$, [21, Theorem 2.3.1]. We note that the condition (2.62) for the explicit DAE system (2.63) corresponds to $\det(\mathbf{M}) = 0$.

To measure "how far away" a DAE is from an ODE we use the notion of the differentiation index, introduced in the following definition.

Definition 2.5 ([65, Definition VII.1.2])**.** *The system* (2.61) *has differentiation index $m \geq 1$ if m is the minimal number of analytical differentiations of* (2.61)*, i.e.,*

$$\frac{\mathrm{d}\mathbf{F}}{\mathrm{d}t}\big(\mathbf{u}'(t), \mathbf{u}(t), t\big) = \mathbf{0} \quad \ldots \quad \frac{\mathrm{d}^m\mathbf{F}}{\mathrm{d}t^m}\big(\mathbf{u}'(t), \mathbf{u}(t), t\big) = \mathbf{0}, \tag{2.65}$$

such that the equations (2.61) *and* (2.65) *possibly after some algebraic manipulations give a system of ODEs* $\mathbf{u}'(t) = \varphi\big(\mathbf{u}(t), t\big)$.

We note that according to this definition a system of ODEs can be classified as a system of DAEs with differential index $m = 0$. From now on we will call the differentiation index of a DAE system simply *index* of the DAE system. We now provide a couple of examples.

An index-1 DAE system is given for $t \in (0,T]$ by

$$\mathbf{u}_\mathrm{d}'(t) = \mathbf{f}(\mathbf{u}_\mathrm{d}, \mathbf{u}_\mathrm{a}, t), \tag{2.66}$$

$$\mathbf{0} = \mathbf{g}(\mathbf{u}_\mathrm{d}, \mathbf{u}_\mathrm{a}, t), \tag{2.67}$$

where the unknown function $\mathbf{u}(t)$ consists of the differential variable $\mathbf{u}_{\mathrm{d}}(t) \in \mathbb{R}^{n_{\mathrm{d}}}$ and the algebraic variable $\mathbf{u}_{\mathrm{a}}(t) \in \mathbb{R}^{n_{\mathrm{a}}}$, i.e.,

$$\mathbf{u}(t) = \left[\mathbf{u}_{\mathrm{d}}(t)^\top, \mathbf{u}_{\mathrm{a}}(t)^\top\right]^\top \in \mathbb{R}^n,$$

with $n = n_{\mathrm{d}} + n_{\mathrm{a}}$. In contrast to the system of ODEs (2.49), where the derivative of $\mathbf{u}$ is present in all of its components, the system of DAEs (2.66)-(2.67) has the part $\mathbf{u}_{\mathrm{a}}$ whose derivative is absent in the system. Equation (2.67) therefore serves only as an *algebraic constraint* for the ODE system (2.66) in $\mathbf{u}_{\mathrm{d}}$. Differentiating (2.67) we obtain

$$\mathbf{u}_{\mathrm{a}}' = -\left[\frac{\partial \mathbf{g}}{\partial \mathbf{u}_{\mathrm{a}}}\right]^{-1} \left(\frac{\partial \mathbf{g}}{\partial \mathbf{u}_{\mathrm{d}}}\,\mathbf{f} + \frac{\partial \mathbf{g}}{\partial t}\right) \tag{2.68}$$

provided the derivative of $\mathbf{g}$ with respect to $\mathbf{u}_{\mathrm{a}}$ is invertible. The system (2.66)-(2.67) is thus an index-1 DAE system.

An index-2 DAE system is given for $t \in (0, T]$ by

$$\mathbf{u}_{\mathrm{d}}'(t) = \mathbf{f}(\mathbf{u}_{\mathrm{d}}, \mathbf{u}_{\mathrm{a}}, t), \tag{2.69}$$

$$\mathbf{0} = \mathbf{g}(\mathbf{u}_{\mathrm{d}}, t). \tag{2.70}$$

We see that in (2.70) not only the derivative of the variable $\mathbf{u}_{\mathrm{a}}$ is missing but also an expression for the variable $\mathbf{u}_{\mathrm{a}}$ itself. This gives after differentiation of (2.70) the *hidden constraint*

$$\mathbf{0} = \frac{\partial \mathbf{g}}{\partial \mathbf{u}_{\mathrm{d}}}\,\mathbf{f} + \frac{\partial \mathbf{g}}{\partial t}. \tag{2.71}$$

In contrast to (2.67), within the differentiation of (2.70) the derivative $\mathbf{u}_{\mathrm{a}}'(t)$ has not appeared yet. After a subsequent differentiation of (2.71), an expression for $\mathbf{u}_{\mathrm{a}}'(t)$ can be obtained provided

$$\frac{\partial \mathbf{g}}{\partial \mathbf{u}_{\mathrm{d}}} \frac{\partial \mathbf{f}}{\partial \mathbf{u}_{\mathrm{a}}} \tag{2.72}$$

is invertible, see [65, Section VII.1]. In this case system (2.69)-(2.70) is an index-2 DAE system.

As we have seen, high-order DAE systems involve differentiation, which in case of high-frequency components might yield a blow-up of the solution. To measure how sensitive the solution of a DAE is with respect to perturbations, a concept of the *perturbation index* is used [65, Section VII.1].

Consistent ICs

An important issue when dealing with DAEs is the choice of consistent ICs. In particular, when solving an IVP for the system (2.66)-(2.67) only the IC $\mathbf{u}_{\mathrm{d}}(0) = \mathbf{u}_{\mathrm{d},0}$ for the differential variable $\mathbf{u}_{\mathrm{d}}$ can be chosen arbitrarily. The IC $\mathbf{u}_{\mathrm{a}}(0) = \mathbf{u}_{\mathrm{a},0}$ for the algebraic variable $\mathbf{u}_{\mathrm{a}}$ has to be calculated by solving the algebraic constraint

$$\mathbf{0} = \mathbf{g}(\mathbf{u}_{\mathrm{d},0}, \mathbf{u}_{\mathrm{a},0}, 0). \tag{2.73}$$

For the index-2 system (2.69)-(2.70) the ICs has to satisfy not only the algebraic constraint (2.70) but also the hidden constraint (2.71), i.e.,

$$\mathbf{0} = \mathbf{g}(\mathbf{u}_{\mathrm{d},0}, 0) \quad \text{and} \tag{2.74}$$

$$\mathbf{0} = \frac{\partial \mathbf{g}}{\partial \mathbf{u}_{\mathrm{d}}}(\mathbf{u}_{\mathrm{d},0}, 0)\,\mathbf{f}(\mathbf{u}_{\mathrm{d},0}, \mathbf{u}_{\mathrm{a},0}, 0) + \frac{\partial \mathbf{g}}{\partial t}(\mathbf{u}_{\mathrm{d},0}, 0). \tag{2.75}$$

Thus, none of the ICs $\mathbf{u}_{\mathrm{d}}(0) = \mathbf{u}_{\mathrm{d},0}$ and $\mathbf{u}_{\mathrm{a}}(0) = \mathbf{u}_{\mathrm{a},0}$ can be chosen freely in this case. A significant contribution to the research on the computation of consistent ICs for index-2 DAEs was made in [35], [36].

Index analysis of the DAE systems stemming from the MNA of electric circuits and an approach to calculate consistent ICs in case of index-2 are presented in [37] and [34], respectively. A structural analysis of field-circuit coupled problems and the underlying systems of DAEs was investigated in [10, 26], [28]. In the remainder of this thesis we will deal only with index-1 DAEs which behave essentially like ODEs.

2.3 Pulse-width modulated (PWM) signals

Pulse-width modulation is a technique used for switching on and off the semiconductor electronic devices used, e.g., in power converters [72]. A PWM signal consists of pulses and is therefore defined by a discontinuous function. We consider PWM signals with the constant switching frequency f_s which can be constructed via

$$p(t) = \operatorname{sgn}\big[r(t) - c(t)\big], \tag{2.76}$$

where $r(t)$ is the *reference signal* and $c(t)$ is the *carrier signal*. For example, a PWM input of $f_s = 20\,\mathrm{kHz}$ is practically relevant in many applications in electrical engineering [51], e.g., for a DC-AC converter from [98]. We refer to [15, 91] for details about common PWM frequencies used for power semiconductor devices.

The choice of the reference signal $r(t)$ depends on the application at hand. In particular, for DC-DC converters a constant signal is used when the converter operates in the steady state, while a time-varying signal is applied within the transient phase [132]. For AC-DC and DC-AC converters the reference signal usually contains a sinusoidal component at the fundamental frequency f_r of the AC input or output [132]. Therefore, the reference signal of the form

$$r(t) = R_0 + R_1 \sin(2\pi f_r t) \tag{2.77}$$

is often considered in (2.76). For the carrier signal $c(t)$, there are several commonly used variants such as the sawtooth carrier, the inverted sawtooth carrier, and the triangle carrier [132, Section 2.1]. In Figure 2.8 we use the *sawtooth carrier* and the two reference signals:

1. the constant (or DC) signal $r_{\mathrm{dc}}(t) = 0.7$ (see Figure 2.8a), which corresponds to $R_0 = 0.7$ and $R_1 = 0$ in (2.77);
2. the sinusoidal (or AC) signal $r_{\mathrm{ac}}(t) = \sin(2\pi 50t)$ (see Figure 2.8b), which corresponds to $R_0 = 0$, $R_1 = 1$, and $f_r = 50$ Hz in (2.77).

The resulting PWM signals are illustrated in Figure 2.8c and Figure 2.8d, respectively. We see that the switching happens at the intersection points of the reference and the carrier signals. The depicted PWM signals attain the values 1 and -1, which correspond to the 'on' and 'off' states of the electronic device.

On the time interval $[0, T_r]$ with $T_r = 0.02$ s the considered sawtooth carrier has $N_s = 10$ teeth (see Figure 2.8a and Figure 2.8b), which leads to the switching frequency $f_s = N_s/T_r = 500$ Hz. Denoting by $\Delta T_{\mathrm{on},n}$ the duration of the 'on'-time on interval $\mathcal{I}_{s,n} = [0, nT_s]$, with $T_s = 1/f_s$ being the switching period and $n = 1, \ldots, N_s$, we define the *duty cycle* $D_{s,n}$ on $\mathcal{I}_{s,n}$ as $D_{s,n} = \Delta T_{\mathrm{on},n}/T_s$. In case of the DC reference signal $r_{\mathrm{dc}}(t)$ we have the same value of $D_{s,n}$ on each interval $\mathcal{I}_{s,n}$, i.e., the duty cycle $D = 0.7$ is constant (see

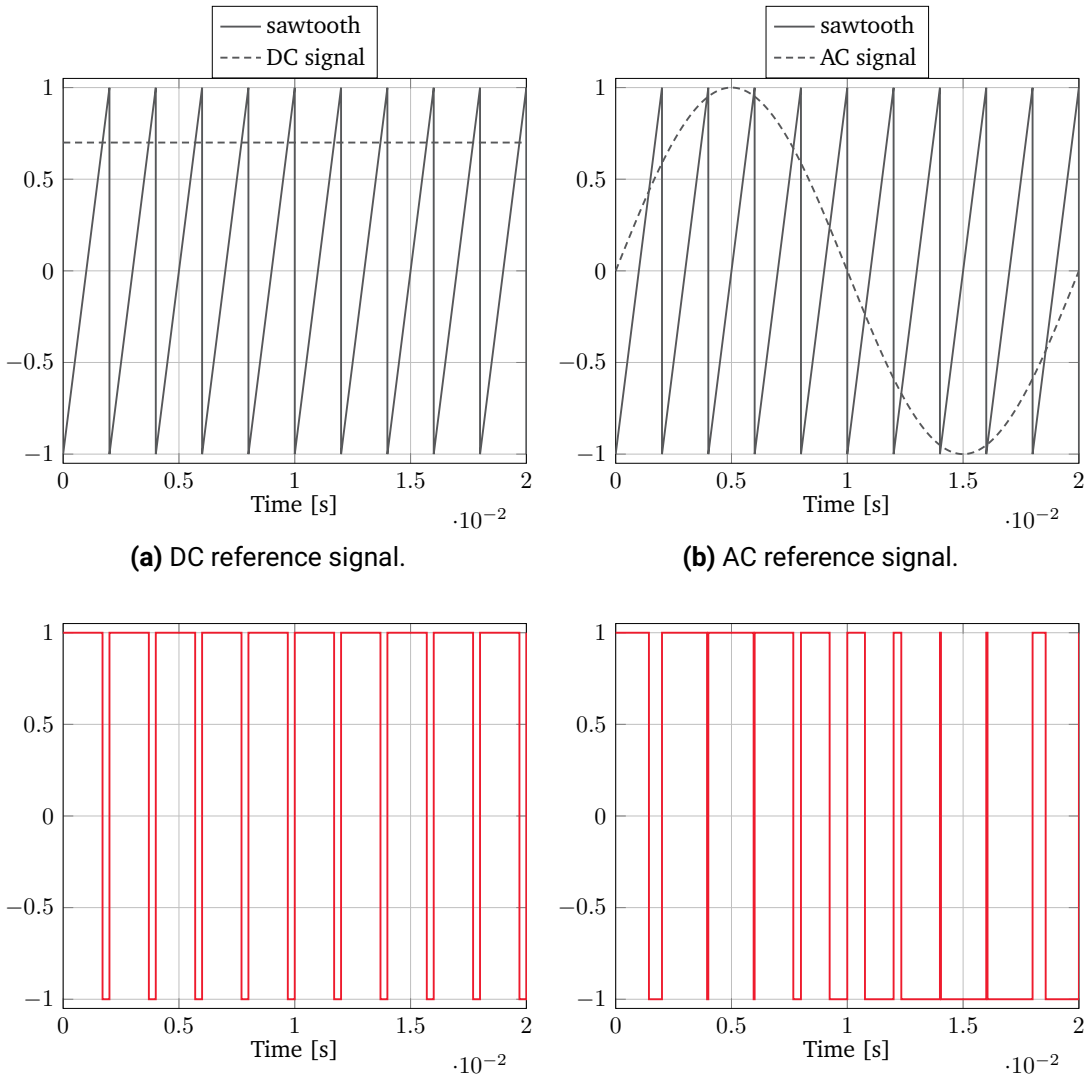

(a) DC reference signal.

(b) AC reference signal.

(c) PWM with constant duty cycle.

(d) PWM with varying duty cycle.

Figure 2.8: Construction of basic PWM signals of frequency $f_s = 500\,\mathrm{Hz}$ using the sawtooth carrier signal.

Figure 2.8c). On the other hand, with the AC reference signal $r_{\mathrm{ac}}(t)$ the duty cycle changes over the intervals $\mathcal{I}_{s,n}$ (see Figure 2.8d).

In order to investigate the (high-frequency) PWM signals in more detail one can use Fourier analysis, which allows to identify the principal components of a signal and their amplitudes. The Fourier theory is presented in the following section.

2.3.1 Fourier series and discrete Fourier transfrom

An analytical model of a PWM signal can be represented by a Fourier series if the PWM waveform is periodic [129, Chapter 2]. The PWM using the reference signal of frequency f_r given in (2.77) and the carrier signal of frequency f_c gives a periodic signal when the ratio f_c/f_r is a rational number. In a special case when f_c is a multiple of f_r the Fourier study can be performed on the period $T_r = 1/f_r$. Note that the Figure 2.8b

describes exactly such a case, since $f_c = 10 f_r$. We now provide the Fourier theory for a periodic (PWM) signal on an interval $[0, T]$.

Let a function $p\colon [0,T] \to \mathbb{C}$ be periodic, i.e., $p(0) = p(T)$, and belong to the Lebesgue space $L^2((0,T))$, i.e., the space of measurable[3] functions p such that $|p(t)|^2$ is Lebesgue integrable, see Section 3.1.1. The function p can then be expanded into the *double-sided Fourier series*, given by the infinite sum

$$p(t) = \sum_{j=-\infty}^{\infty} \hat{p}_j \exp(\imath \omega_j t), \quad t \in [0,T], \tag{2.78}$$

with the imaginary unit $\imath$, the *angular frequencies* $\omega_j = 2\pi j/T$, and the *Fourier coefficients* $\hat{p}_j$ obtained from

$$\hat{p}_j = \frac{1}{T} \int_0^T p(t) \exp(-\imath \omega_j t)\, \mathrm{d}t, \quad j \in \mathbb{Z}. \tag{2.79}$$

Note that the functions $\psi_j(t) = \exp(\imath \omega_j t)$ are called the spectral (orthonormal) basis functions on the interval $[0,T]$ and $\psi_j^*(t) = \exp(-\imath \omega_j t)$ are their complex conjugates.

Since the number of the Fourier coefficients in (2.78) is infinite, in practice, a finite Fourier series approximation with $2M+1$ coefficients, $M \in \mathbb{N}$, is considered. Let $0 = T_0 < T_1 < \ldots < T_{2M} < T$ be a partition of the interval $[0,T]$ and let $p_n = p(T_n)$ denote the discrete values of p at T_n, for $n = 0, \ldots, 2M$. These discrete values can then be calculated via

$$p_n = \sum_{j=-M}^{M} \hat{p}_j \exp(\imath \omega_j T_n), \quad n = 0, \ldots, 2M. \tag{2.80}$$

Clearly, the bigger the value of M is, the more precisely the value p_n is calculated in (2.80). Approximating the integral in (2.79) using the left rectangle quadrature rule, we obtain the expression for the discrete Fourier coefficients

$$\hat{p}_j = \frac{1}{2M+1} \sum_{n=0}^{2M} p_n \exp(-\imath \omega_j T_n), \quad j = -M, \ldots, M. \tag{2.81}$$

The formula (2.81) is called the *discrete Fourier transform (DFT)* which transforms a given vector $\mathbf{p} = [p_0, \ldots, p_{2M}]^\top$ of the discrete values in the time domain into a vector $\hat{\mathbf{p}} = [\hat{p}_{-M}, \ldots, \hat{p}_M]^\top$ of the coefficients in the frequency domain. Conversely, given the vector $\hat{\mathbf{p}}$, the components of the vector $\mathbf{p}$ can be obtained from (2.80), which is called the *inverse DFT*.

2.3.2 Carathéodory differential equations

A system supplied with a PWM signal $\mathbf{p}$ as, e.g., a power converter, can be mathematically described by a system of ODEs in $\mathbb{R}^n$

$$\mathbf{u}'(t) = \mathbf{f}(\mathbf{u}(t), t) := \bar{\mathbf{f}}(\mathbf{u}(t), t) + \mathbf{p}(t), \quad t \in (0,T], \tag{2.82}$$

where $\bar{\mathbf{f}}$ is assumed to be continuous while the total RHS $\mathbf{f}$ contains discontinuities in t due to the PWM input $\mathbf{p}$. In this case the standard Picard-Lindelöf theory for existence and uniqueness of solutions to ODEs cannot be applied. However, systems like (2.82) can be treated using the more general theory of the Carathéodory differential equations [41].

[3] For measurability theory we refer to [4, Section 3.9].

Definition 2.6 ([41, Chapter 1])**.** *The ODE system* (2.82) *is called the Carathéodory equation if on a domain* $U \times (0,T]$ *with* $U \subset \mathbb{R}^n$ *for the RHS* $\mathbf{f}(\mathbf{u},t)$ *it holds:*

C.1 $\mathbf{f}(\mathbf{u},t)$ *is defined and continuous in* $\mathbf{u}$ *for almost every (a.e.)* t*;*

C.2 $\mathbf{f}(\mathbf{u},t)$ *is measurable in* t *for each* $\mathbf{u}$;

C.3 $\|\mathbf{f}(\mathbf{u},t)\| \leq m(t)$*, with* m *being a summable*[4] *function on* $(0,T)$.

The conditions ***C.1****-****C.3*** *are called the Carathéodory conditions.*

A function $\mathbf{u}\colon [0,T] \to \mathbb{R}^n$ is called a solution of the Carathéodory equation (2.82) if it is absolutely continuous (see [4, E3.6]) on each closed subinterval of $[0,T]$ and satisfies the system (2.82) almost everywhere, i.e., outside of zero measure sets.

Theorem 2.7 ([41, Chapter 1])**.** *Let* $\mathbf{f}(\mathbf{u},t)$ *satisfy the Carathéodory conditions* ***C.1****-****C.3*** *on* $U \times (0,T]$ *and let an IC*

$$\mathbf{u}(0) = \mathbf{u}_0 \tag{2.83}$$

be given in U*. Then there exists a solution* $\mathbf{u}(t)$ *to* (2.82)*,* (2.83) *on* $[0,T]$*. Additionally, if there exists a summable function* $l(t)$ *such that for any* $(\mathbf{u},t),(\mathbf{v},t) \in U \times (0,T]$ *it holds*

$$\|\mathbf{f}(\mathbf{u},t) - \mathbf{f}(\mathbf{v},t)\| \leq l(t)\|\mathbf{u}-\mathbf{v}\|, \tag{2.84}$$

then the solution $\mathbf{u}$ *to* (2.82)*,* (2.83) *is unique.*

Clearly, the requirements of the Theorem 2.7 hold for the system of ODEs (2.82) whose RHS $\mathbf{f}$ consists of the continuous part $\bar{\mathbf{f}}$ and the PWM input $\mathbf{p}$. Therefore, the IVP (2.82), (2.83) is uniquely solvable.

2.3.3 Multirate partial differential equations

Consider an IVP for a system of ODEs or DAEs in $\mathbb{R}^n$ of the form

$$\mathbf{M}\mathbf{u}'(t) + \mathbf{K}\big(\mathbf{u}\big)\mathbf{u}(t) = \mathbf{p}(t), \quad t \in (0,T], \tag{2.85}$$

$$\mathbf{u}(0) = \mathbf{u}_0, \tag{2.86}$$

where the matrix pencil $\big(\mathbf{M},\mathbf{K}(\mathbf{u})\big) := \lambda\mathbf{M} + \mathbf{K}(\mathbf{u})$ is regular for any $\mathbf{u} \in \mathbb{R}^n$ and $\lambda \in \mathbb{R}$. In case (2.85) is a system of DAEs, the IC (2.86) is assumed to be consistent.

If the system (2.85) is supplied with the PWM input $\mathbf{p}(t)$, its solution possesses a multirate behavior. For example, in case of the buck converter model from Figure 2.6, excited with a two-level PWM voltage source with constant duty cycle (see Figure 2.8c), the output contains high-frequency periodic ripples and a low-frequency envelope [102]. Figure 2.9 illustrates the PWM voltage input v_{V} of frequency $f_s = 500$ Hz with duty cycle $D = 0.7$ and the two state variables of the buck converter circuit: the voltage v_{C} and the current i_{L}. In order to resolve the ripples and calculate the multirate solution efficiently we consider the *multirate PDE (MPDE) approach* introduced in [19].

[4] A measurable function m is called *summable* if $|m(t)|$ is Lebesgue integrable, i.e., $m \in L^1((0,T))$, see Section 3.1.1.

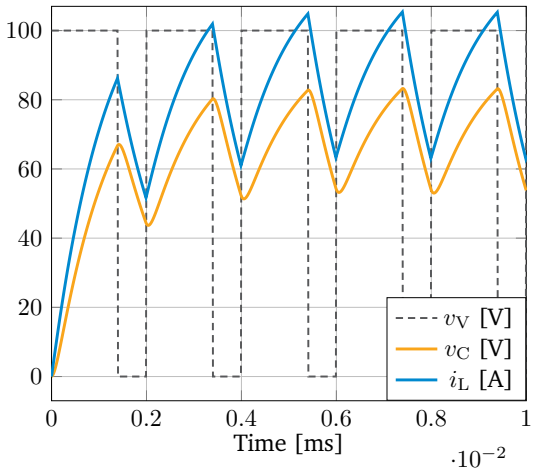

Figure 2.9: Multirate behavior of the state variables v_C and i_L of the buck converter model from Figure 2.6, supplied with a PWM voltage source v_V of $f_s = 500\,\mathrm{Hz}$ with duty cycle $D = 0.7$.

The idea of the MPDE approach lies in the conversion of the system of ODEs/DAEs (2.85) into a system of MPDEs [19, 113]. In particular, introducing $m > 1$ time variables $t_1, t_2, \ldots, t_m$ we obtain

$$\mathbf{M}\left(\frac{\partial \hat{\mathbf{u}}}{\partial t_1} + \frac{\partial \hat{\mathbf{u}}}{\partial t_2} + \ldots + \frac{\partial \hat{\mathbf{u}}}{\partial t_m}\right) + \mathbf{K}(\hat{\mathbf{u}})\hat{\mathbf{u}} = \hat{\mathbf{p}}, \tag{2.87}$$

for $(t_1, \ldots, t_m) \in (0, T_1] \times (0, T_2) \times \ldots \times (0, T_m)$, where $\hat{\mathbf{u}} = \hat{\mathbf{u}}(t_1, t_2, \ldots, t_m)$ and $\hat{\mathbf{p}} = \hat{\mathbf{p}}(t_1, t_2, \ldots, t_m)$ are the multi-variate variants of the solution $\mathbf{u}(t)$ and the excitation $\mathbf{p}(t)$, respectively. The original ODE/DAE system (2.85) and the MPDE system (2.87) are related through the relations:

$$\mathbf{p}(t) = \hat{\mathbf{p}}(t + c_1, t + c_2, \ldots, t + c_m), \tag{2.88}$$

$$\mathbf{u}(t) = \hat{\mathbf{u}}(t + c_1, t + c_2, \ldots, t + c_m), \tag{2.89}$$

where $c_1, c_2, \ldots, c_m \in \mathbb{R}$ are arbitrary constants [113]. It means that, having the solution $\hat{\mathbf{u}}$ of the MPDE system (2.87), whose RHS $\hat{\mathbf{p}}$ satisfies the condition (2.88), we can obtain the solution $\mathbf{u}$ of the original system (2.85) from (2.89).

As for standard ODEs, DAEs and PDEs ICs and/or BCs have to be prescribed for the uniqueness of the solution of the MPDE system (2.87). For example, assuming the solution $\hat{\mathbf{u}}$ represents an envelope-modulated signal along the slowly-changing variable t_1 and is periodic in the variables $t_2, \ldots, t_m$ [113], the mixed initial boundary conditions (IBCs)

$$\hat{\mathbf{u}}(0, t_2, \ldots, t_m) = \hat{\mathbf{u}}_0(t_2, \ldots, t_m), \tag{2.90}$$

$$\hat{\mathbf{u}}(t_1, t_2, \ldots, t_m) = \hat{\mathbf{u}}(t_1, t_2 + T_2 \ldots, t_m + T_m) \tag{2.91}$$

are prescribed with a given function $\hat{\mathbf{u}}_0(t_2, \ldots, t_m)$ on $[0, T_2] \times \ldots \times [0, T_m]$. We note that in case of the buck converter example (see Figure 2.6 and Figure 2.9) we have two scales, i.e., $m = 2$: the envelope in t_1 and the periodic ripples in t_2, [102].

The system (2.87) with the IBCs (2.90)-(2.91) can be solved using numerical methods for PDEs, which will be presented in Section 3.2. In particular, for the two-scale buck converter model one can apply the Galerkin approach with respect to t_2 (see Section 3.2.1) followed by a time-stepping method with respect to t_1 (see Section 3.2.2). For further description of the MPDE approach and its application to the simulation of power converters we refer to [101, 104].

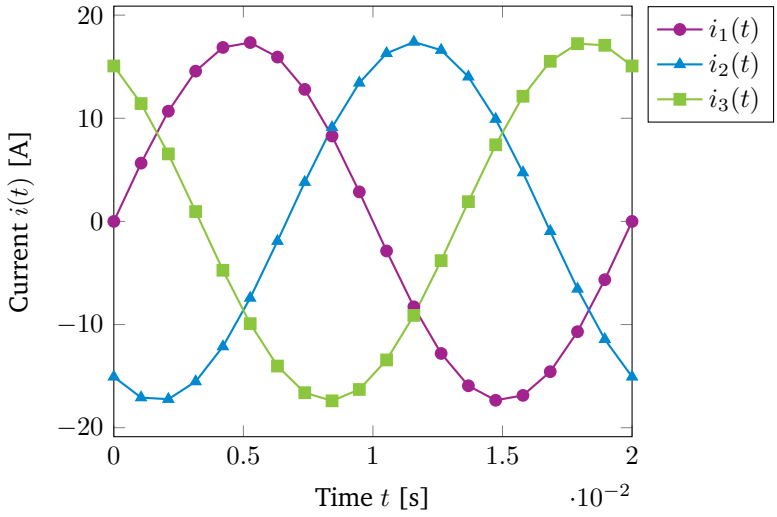

Figure 2.10: Time-variation of a three-phase current system of $f = 50\,\mathrm{Hz}$ and peak current value $I_{\mathrm{peak}} = 17.4\,\mathrm{A}$.

2.4 Induction motors

In contrast to the already mentioned electric power converters (see Section 2.2), which convert electric energy from one form to another, electromechanical energy converters transform electrical energy into mechanical energy (in case of electric motors) and vice versa (in case of generators). In this section we focus on a specific class of electric motors, namely, on *three-phase (3ph) asynchronous* or *induction motors*. Such motors are commonly used in industry and have output power from several hundred watt up to $30\,\mathrm{MW}$ [14]. Especially within the power range under $500\,\mathrm{kW}$ it is the most widespread type of electric motors. An induction motor can operate with constant revolution speed, e.g., in pumps, conveyer bands, saws, or ventilators, while in electric cars, elevators, cranes it is included as a drive with a varying revolution speed.

As we consider induction motors, supplied with a 3ph voltage/current source, we start with the description of the 3ph systems. A 3ph current excitation is given by

$$i_k(t) = I_{\mathrm{peak}} \sin\big(2\pi f t - (k-1)\cdot 2\pi/3\big), \quad k = 1, 2, 3, \tag{2.92}$$

where f is the frequency and I_{peak} is the amplitude or the *peak value* of the AC source. One differentiates the peak value of current (or voltage) from the *effective* or *root mean squared (RMS) value* given by $I_{\mathrm{rms}} = I_{\mathrm{peak}}/\sqrt{2}$. The currents of each phase have the same amplitude but differ in the time phase by $2\pi/3$. The 3ph ACs of frequency $f = 50\,\mathrm{Hz}$ and amplitude $I_{\mathrm{peak}} = 17.4\,\mathrm{A}$ are illustrated in Figure 2.10. A 3ph voltage excitation $u_k(t)$ can be represented analogously to (2.92).

The windings carrying the 3ph AC can be connected in *star* (also called *wye* and denoted by Y) or *delta* (also called *triangle* and denoted by Δ), as illustrated in Figure 2.11. In both cases one distinguishes between *line* voltages/currents (V_{line}, I_{line}) and *phase* voltages/currents (V_{ph}, I_{ph}), whose relations can be derived using the complex calculus (or phasor diagrams [109, Section 1.8]), KVL and KCL.

The 3ph windings are placed into the *stator slots* in the outer part of the motor (called *stator*), as illustrated in Figure 2.12. There, each phase is carried over three consequent slots so that the three-slot bunch of the same

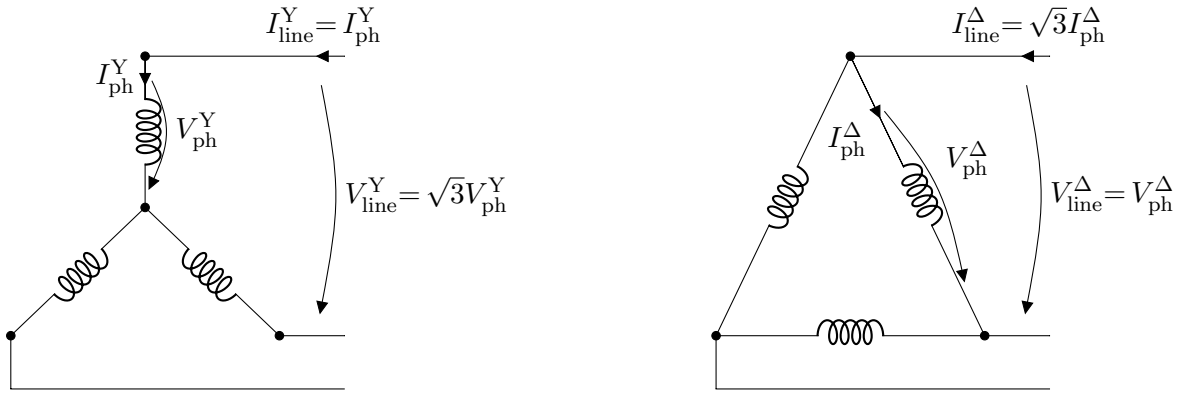

(a) Star connection. **(b)** Delta connection.

Figure 2.11: Two types of connections in three-phase windings.

phase appears four times in the stator (with total number of slots $n_{\mathrm{st}} = 36$). Such a configuration yields a magnetic flux distributed over 4 poles or $p = 2$ north-south pole pairs, i.e., each pole covers a quarter of the motor (9 slots). The mark '$\odot$' corresponds to the superscript '$+$' over the phase voltages u_k, $k = 1, 2, 3$ and describes the positive current flow (i.e., directed, as the x_3-axis, towards us), while '$\otimes$' and the superscript '$-$' represent the negative current flow [109, Section 2.2]. The stator windings in the induction motor model from Figure 2.12 are connected in delta [62].

The inner part of the motor is called *rotor*. We consider a *squirrel-cage rotor*, where the *rotor slots* contain solid conductor bars, connected at both ends of the rotor by the conducting *end rings* [73]. The rotor of the induction motor illustrated in Figure 2.12 has $n_{\mathrm{rt}} = 32$ bars. Rotor bars and end rings are typically made of copper or aluminium. In the majority of induction motors the rotor slots are not parallel to the rotation axis (in case of Figure 2.12 axis x_3) but are skewed along the rotor length. This allows to reduce the harmful high-frequency ripples appearing, e.g., in the torque produced by the motor, and thereby also vibrations and noise. In general, cage motors are relatively cheap to manufacture, they are very robust and reliable [73].

Both stator and rotor cores contain a large number of densely stacked sheets of a ferromagnetic material, e.g., steel. The sheets have a very small thickness ($< 1\,\mathrm{mm}$) and are laminated in order to reduce the eddy current losses. The stator and rotor are separated by the *air gap*, which plays an important role in the operation of the squirrel-cage induction motor. It has to be quite small in order to avoid significant flux leakages in the motor. In the very inner part of the motor a *shaft* is placed, through which the torque is transferred to the mechanical load. In the following Section 2.4.1 we describe the main operation characteristics of induction motors such as, e.g., the revolution speed and the torque production.

2.4.1 Operation principles

According to the Maxwell-Ampère law (2.1b) a wire carrying current produces a magnetic field around it. Let the stator windings be connected in star or delta as in Figure 2.11. When a 3ph current is applied to these special winding arrangements, the produced magnetic field will take different orientations as the AC varies over time. It then looks like a magnetic field of a uniform strength, rotating at *synchronous speed*. For the 3ph AC of frequency f in Hz (which corresponds to the angular frequency $\omega = 2\pi f\ \mathrm{rad/s}$) and a magnetic field

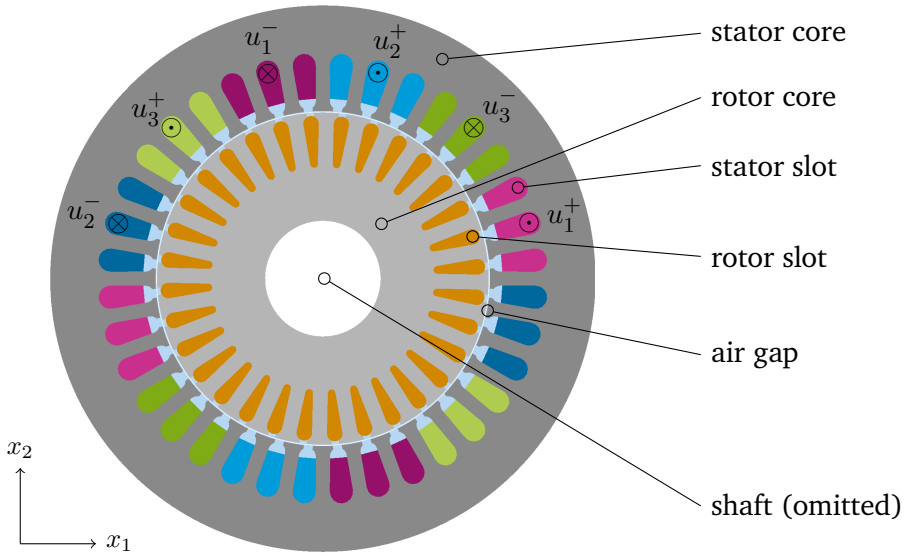

Figure 2.12: A cross section of a four-pole induction machine [62][5].

with p pole pairs, the synchronous speed is given by

$$\omega_{\text{sync}} = \frac{60f}{p} \text{ rpm} \qquad \text{or} \qquad \omega_{\text{sync}} = \frac{\omega}{p} \text{ rad/s} \tag{2.93}$$

in revolutions per minute (rpm) or radians per second (rad/s), respectively. For instance, for $f = 50\,\text{Hz}$ and $p = 2$ pole pairs the synchronous speed ω_{sync} is equal to $1\,500$ rpm or 50π rad/s. The magnetic flux traverses the air gap and passes from the stator core to the rotor and back.

Since the conducting bars of the squirrel cage are short-circuited by the end rings, placing them into the varying magnetic field induces a current flowing in the bars according to the Faraday law (2.1a). As a result, by *the Lorentz force law* there is a force acting on the current-carrying rotor conductors which makes the rotor rotate. The direction of the force can be determined by the right-hand rule: when the thumb points in the direction of the current flow in the conductor, the forefinger indicates the direction of the magnetic flux, then the middle finger shows the direction of the Lorentz force.

The name “induction motor” originates from the fact that the current in the rotor conductors (and thus the rotation) is created by the electromagnetic induction and not by a direct connection to a power supply. Besides, induction motors are inherently self-starting, since no external force is needed to initiate rotation.

Asynchronous operation: slip

Induction motors are also called asynchronous motors, since the rotor revolution speed differs from the speed of the magnetic field induced by the 3ph AC supply. In particular, the rotor revolves with the mechanical speed ω_{mech}, which is usually slightly smaller than the synchronous speed ω_{sync}. The relative difference of the two speed values is expressed by a dimensionless quantity s called *slip* given by

$$s = \frac{\omega_{\text{sync}} - \omega_{\text{mech}}}{\omega_{\text{sync}}}. \tag{2.94}$$

[5]The geometry is given by the ‘im_3kw’ model at `http://onelab.info/`.

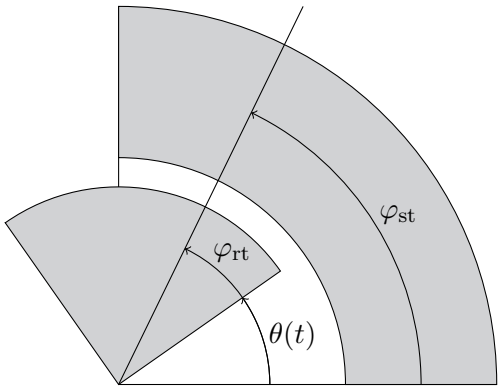

Figure 2.13: Azimuthal coordinates φ_{st} and φ_{rt}, attached to stator and rotor, respectively, related along the rotor angle $\theta(t)$.

If $s = 0$ the rotor rotates with synchronous speed (under the *no-load* operation), which means that there is no change of the magnetic flux experienced by the rotor and therefore no current and no force is produced in the rotor bars. On the other hand, $s = 1$ corresponds to the standstill rotor state (under the *locked rotor* or *short circuit* operation) and thus the maximal force is exerted on the rotor. As we see, the mechanical speed is proportional to the frequency f of the AC input, since

$$\omega_{\mathrm{mech}} = (1 - s)\omega_{\mathrm{sync}} = (1 - s)\omega/p = 2\pi(1 - s)f/p \tag{2.95}$$

due to (2.94) and (2.93). The induction motor speed can therefore be easily controlled using a variable frequency drive supplying the 3ph stator windings [74, Chapter 8], e.g., based on pulse-width modulation.

Air gap field and slip transformation

An ideal air gap field for the input AC frequency f and number of pole pairs p can be mathematically given by a sinusoidal rotating wave, i.e., we have for the radial component of the magnetic flux density

$$B_r(t, \varphi_{\mathrm{st}}) = \hat{B}_r \sin(\omega t - p\varphi_{\mathrm{st}}), \tag{2.96}$$

with time $t \in [0, 1/f]$ and stator azimuthal coordinate $\varphi_{\mathrm{st}} \in [0, 2\pi]$. The magnitude $\hat{B}_r$ of the flux wave depends on the input voltage and frequency as well as on the configuration of the stator windings such as the number of turns per coil, the number of coils per phase and their distribution [74]. In practice, in order to obtain a flux density waveform, close to an ideal sinusoidal wave, a two-layer winding is commonly used [74].

Considering rotation with the constant speed ω_{mech} we can implement the rotation using the coordinate transformation in the air gap

$$\varphi_{\mathrm{st}} = \varphi_{\mathrm{rt}} + \theta(t) = \varphi_{\mathrm{rt}} + \omega_{\mathrm{mech}} t, \tag{2.97}$$

where $\theta(t)$ is the rotor angle and φ_{st} and φ_{rt} are the azimuthal coordinates, attached to stator and rotor, respectively, see Figure 2.13. Plugging (2.97) into (2.96), we obtain the air gap flux density in terms of the rotor coordinate

$$B_r(t, \varphi_{\mathrm{rt}}) = \hat{B}_r \sin\big(\underbrace{(\omega - p\omega_{\mathrm{mech}})}_{=:\omega_{\mathrm{slip}}} t - p\varphi_{\mathrm{rt}}\big). \tag{2.98}$$

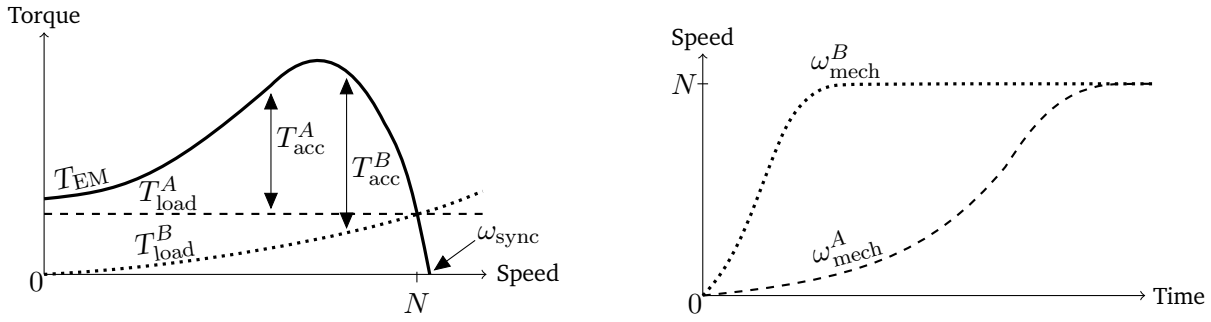

(a) Torque-speed curve and run-up loads.

(b) Speed-time curves for the loads.

Figure 2.14: Steady-state torque and run-up loads with the same steady-state speed N [74, Chapter 6].

Comparing (2.96) and (2.98), we see that the rotor observes the air gap field with the same amplitude $\hat{B}_r$ and pole-pair number p as the stator, but at a modified angular frequency ω_{slip} called the *slip angular frequency*. The procedure of expressing the air gap field in terms of the rotor coordinate system is called the *slip transformation*.

Denoting the speed of the rotating magnetic field observed from the rotor by $\omega_{\mathrm{rt}} = \omega_{\mathrm{slip}}/p$ and using (2.93) and (2.94), we have the relations

$$\omega_{\mathrm{rt}} = \omega_{\mathrm{sync}} - \omega_{\mathrm{mech}} = s\omega_{\mathrm{sync}}. \tag{2.99}$$

Thus, as expected the speed ω_{rt} is smaller than the synchronous speed ω_{sync} exactly by the rotor revolution speed ω_{mech} and can also be calculated multiplying ω_{sync} by the slip.

Electromagnetic torque

The electromagnetic torque induced in the air gap and exerted on the rotor can be calculated using the formula [6], [109, Section 1.5]

$$T_{\mathrm{EM}} = \int_S \vec{r} \times \boldsymbol{\sigma} \cdot \mathrm{d}\vec{S} = \int_S \vec{r} \times (\boldsymbol{\sigma} \cdot \vec{n})\, \mathrm{d}S, \tag{2.100}$$

where S is the surface enclosing the rotor, $\vec{r}$ is the position vector connecting the rotor origin to S, $\vec{n}$ is the unit normal vector to S, and $\boldsymbol{\sigma}$ is *the Maxwell stress tensor* [115, Section 6.3] given by

$$\boldsymbol{\sigma}_{ij} = \nu_0(\vec{B}_i\vec{B}_j - 0.5|\vec{B}|^2\delta_{ij}), \tag{2.101}$$

with the reluctivity in vacuum ν_0, the magnetic flux density $\vec{B}$, the Kronecker delta δ_{ij}, and $i, j = 1, 2, 3$.

To predict the behavior of the motor we need its *torque-speed characteristic*. A typical torque-speed curve of an induction motor is shown in Figure 2.14a. This curve represents the electromagnetic torque, produced by the motor once it has settled down at a particular running speed ω_{mech} [74, Chapter 6]. Figure 2.14a also illustrates two different loads A and B, exerted on the motor shaft. Both loads eventually reach the same steady running speed N, i.e., the speed at which the motor torque T_{EM} is equal to the load torque T_{load}. The load A applies a constant torque T^A_{load} and the load B produces an increasing torque T^B_{load} reaching the value of T^A_{load} at the steady-state speed N. The difference between the torque, produced by the motor, and the torque, required to run the applied loads, is known as the accelerating torque T_{acc} [74, Chapter 6]. We note that

$$T^B_{\mathrm{acc}} = T_{\mathrm{EM}} - T^B_{\mathrm{load}} \;>\; T^A_{\mathrm{acc}} = T_{\mathrm{EM}} - T^A_{\mathrm{load}}$$

for the speed values between 0 and N. Exactly because of this the load B reaches the full speed N much faster than the load A, as it is visualized in Figure 2.14b.

2.4.2 Governing equations

The electromagnetic phenomena taking place in an induction motor can be described by the MVP formulation, i.e., by the eddy current problem (2.28), which for $(\vec{x},t) \in \Omega \times (0,T]$, with $\Omega \subset \mathbb{R}^3$ and $T > 0$, reads

$$\sigma(\vec{x})\frac{\partial \vec{A}}{\partial t} + \operatorname{curl}\big(\nu(\vec{x},|\operatorname{curl}\vec{A}|)\operatorname{curl}\vec{A}\big) = \sum_{k=1}^{3}\vec{\chi}_k(\vec{x})i_k(t), \tag{2.102}$$

where we have included the winding functions representation (2.7). Using the relations (2.40) and (2.44) for the attached electric network on the stator side, we obtain the following equations for the 3ph voltage

$$v_k(t) = R_k i_k(t) + \int_{\Omega}\vec{\chi}_k(\vec{x})\cdot\frac{\partial \vec{A}(\vec{x},t)}{\partial t}\,\mathrm{d}\Omega, \quad k=1,2,3, \tag{2.103}$$

with R_k denoting the DC resistance of the stator stranded conductors. For the mechanical speed ω_{mech} and the angle θ, the motion of the rotor is described by the system of first-order ODEs

$$J\omega'_{\mathrm{mech}}(t) + C\omega_{\mathrm{mech}}(t) = T_{\mathrm{EM}}(t,\theta(t),\vec{A}) - T_{\mathrm{load}}, \tag{2.104}$$

$$\theta'(t) = \omega_{\mathrm{mech}}(t), \tag{2.105}$$

where J is the moment of inertia of the rotor, C is the friction coefficient, T_{EM} is the electromagnetic torque given by (2.100), and T_{load} is the load (or shaft) torque, which may depend on the speed ω_{mech}.

Combining the field and the circuit equations, as well as the equation of motion, one obtains the electromechanical field-circuit coupled model. The coupling is implemented using the formula (2.100) for the electromagnetic torque T_{EM}, which depends on the magnetic flux density $\vec{B} = \operatorname{curl}\vec{A}$ and thus on the MVP $\vec{A}$.

2.4.3 Equivalent schemes

The full model including the field equations coupled to the circuit equations might lead to large systems of equations and thus to a high computational effort. To reduce the system size and the effort one can describe the behavior of an induction motor approximately using simplified models, which use only circuit relations. The common models are the Steinmetz equivalent circuit and the coupled inductance model, both of which are presented in this section, [43, 123].

Steinmetz equivalent circuit

A circuit shown in Figure 2.15 can be used to describe an induction motor [73, Chapter 7], [109, Section 7.1.3]. The phase voltage V_{sin} supplies the stator, whose resistance and leakage inductance are denoted by R_{st} and $L_{\sigma,\mathrm{st}}$, respectively. R_{Fe} is the resistance describing the iron losses of the motor. L_{h} is the magnetizing inductance at the rated point with the voltage V_{h}, induced by the air gap flux linkage. $L_{\sigma,\mathrm{rt}}$ and R_{rt} are the rotor leakage inductance and the rotor resistance referred to the stator, respectively. The term

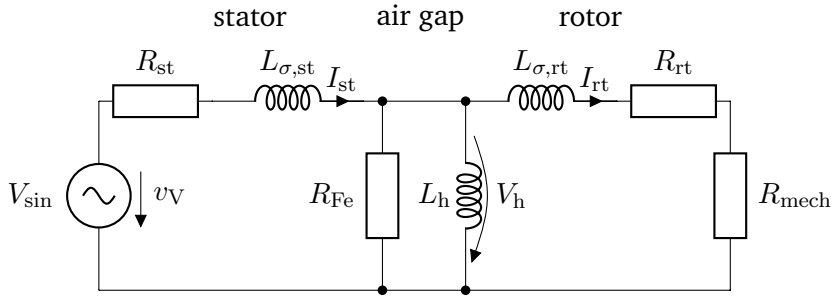

Figure 2.15: Steady-state equivalent circuit of an induction motor per phase [109, Section 7.1.3].

$R_{\mathrm{mech}} = R_{\mathrm{rt}}(1-s)/s$ describes the electromechanical power P_{mech}, produced by the motor, where s is the slip.

Speaking in terms of power, let P_{src} be the power fed to the motor. Some power is consumed in the stator resistance R_{st} and in the iron loss resistance R_{Fe}. The resulting power P_{st} is passed from the stator to the air gap. A part of this power denoted by P_{rt} is lost as heat in the rotor resistance R_{rt} and the remainder is converted into the output power P_{mech} in R_{mech} [109, Section 7.1.3]. These two parts of the power entering the air gap are given by

$$P_{\mathrm{rt}} = 3I_{\mathrm{rt}}^2 R_{\mathrm{rt}}, \tag{2.106}$$

$$P_{\mathrm{mech}} = P_{\mathrm{rt}}(1-s)/s, \tag{2.107}$$

where the factor '3' appears in (2.106), as only one equivalent phase of the AC input is considered in the equivalent circuit. Writing the power balance for the rotor, we have

$$P_{\mathrm{st}} = P_{\mathrm{rt}} + P_{\mathrm{mech}} = P_{\mathrm{rt}}/s, \tag{2.108}$$

which leads to

$$P_{\mathrm{rt}} = sP_{\mathrm{st}}, \tag{2.109}$$

$$P_{\mathrm{mech}} = (1-s)P_{\mathrm{st}}. \tag{2.110}$$

From (2.109) and (2.110) we see that an induction motor operates efficiently only at low values of the slip s. This is also supported by the fact that the efficiency of an induction motor is defined according to [73, Chapter 6] by

$$\eta = (P_{\mathrm{mech}}/P_{\mathrm{st}}) \cdot 100\% = (1-s) \cdot 100\%.$$

Furthermore, using (2.107)-(2.106), and the definition of slip (2.94) we have for the electromagnetic torque

$$T_{\mathrm{EM}}(\omega_{\mathrm{mech}}) = \frac{P_{\mathrm{mech}}}{\omega_{\mathrm{mech}}} = \frac{(1-s)P_{\mathrm{rt}}}{s\omega_{\mathrm{mech}}} = \frac{3I_{\mathrm{rt}}^2 R_{\mathrm{rt}}}{\omega_{\mathrm{sync}} - \omega_{\mathrm{mech}}}. \tag{2.111}$$

The rotation can then be described by the ODE (2.104)-(2.105) with $C = 0$, T_{EM} calculated using (2.111), and

$$T_{\mathrm{load}} = P_{\mathrm{rated}}/\omega_{\mathrm{rated}} \tag{2.112}$$

given at full load. The rotor current $I_{\mathrm{rt}} = V_{\mathrm{h}} Y_{\mathrm{rt}}$ in (2.111) with the rotor admittance Y_{rt} can be calculated using the KCL. As a result, one gets

$$I_{\mathrm{rt}}(\omega_{\mathrm{mech}}) = \frac{Y_{\mathrm{st}} Y_{\mathrm{rt}}(\omega_{\mathrm{mech}})}{Y_{\mathrm{st}} + Y_{\mathrm{h}} + Y_{\mathrm{rt}}(\omega_{\mathrm{mech}})} U_{\mathrm{rms}}, \qquad Y_{\mathrm{rt}}(\omega_{\mathrm{mech}}) = \frac{\omega_{\mathrm{sync}} - \omega_{\mathrm{mech}}}{R_{\mathrm{rt}}\omega_{\mathrm{sync}} + \imath\omega L_{\sigma,\mathrm{rt}}(\omega_{\mathrm{sync}} - \omega_{\mathrm{mech}})},$$

where $U_{\mathrm{rms}} = U_{\mathrm{peak}}/\sqrt{2}$, $\omega_{\mathrm{sync}} = \omega/p$, $\omega = 2\pi f$, $\imath = \sqrt{-1}$, and

$$Y_{\mathrm{st}} = \frac{1}{R_{\mathrm{st}} + \imath\omega L_{\sigma,\mathrm{st}}} \quad \text{and} \quad Y_{\mathrm{h}} = \frac{1}{R_{\mathrm{Fe}}} + \frac{1}{\imath\omega L_{\mathrm{h}}}$$

are the stator and the main admittances [109], respectively.

Coupled inductance model

Another simplified model of an induction machine is the coupled inductance model [43]. It is given by the system of equations

$$\mathbf{u}(t) = \mathbf{R}\mathbf{i}(t) + \big(\mathbf{L}(\theta)\mathbf{i}(t)\big)', \tag{2.113}$$

where

$$\begin{aligned}
\mathbf{u} &= [u_1^{\mathrm{st}}, u_2^{\mathrm{st}}, u_3^{\mathrm{st}}, u_1^{\mathrm{rt}}, u_2^{\mathrm{rt}}, u_3^{\mathrm{rt}}]^\top, \quad \mathbf{i} = [i_1^{\mathrm{st}}, i_2^{\mathrm{st}}, i_3^{\mathrm{st}}, i_1^{\mathrm{rt}}, i_2^{\mathrm{rt}}, i_3^{\mathrm{rt}}]^\top,\\
\mathbf{R} &= \mathrm{diag}\big[R_{\mathrm{st}}, R_{\mathrm{st}}, R_{\mathrm{st}}, R_{\mathrm{rt}}, R_{\mathrm{rt}}, R_{\mathrm{rt}}\big],\\
\mathbf{L}(\theta) &= \begin{bmatrix}
L_{\mathrm{st}} + L_{\sigma,\mathrm{st}} & -0.5L_{\mathrm{st}} & -0.5L_{\mathrm{st}} & L_{\mathrm{h}}\sin(\phi_1) & L_{\mathrm{h}}\sin(\phi_3) & L_{\mathrm{h}}\sin(\phi_2)\\
-0.5L_{\mathrm{st}} & L_{\mathrm{st}} + L_{\sigma,\mathrm{st}} & -0.5L_{\mathrm{st}} & L_{\mathrm{h}}\sin(\phi_2) & L_{\mathrm{h}}\sin(\phi_1) & L_{\mathrm{h}}\sin(\phi_3)\\
-0.5L_{\mathrm{st}} & -0.5L_{\mathrm{st}} & L_{\mathrm{st}} + L_{\sigma,\mathrm{st}} & L_{\mathrm{h}}\sin(\phi_3) & L_{\mathrm{h}}\sin(\phi_2) & L_{\mathrm{h}}\sin(\phi_1)\\
L_{\mathrm{h}}\sin(\phi_1) & L_{\mathrm{h}}\sin(\phi_2) & L_{\mathrm{h}}\sin(\phi_3) & L_{\mathrm{rt}} + L_{\sigma,\mathrm{rt}} & -0.5L_{\mathrm{rt}} & -0.5L_{\mathrm{rt}}\\
L_{\mathrm{h}}\sin(\phi_3) & L_{\mathrm{h}}\sin(\phi_1) & L_{\mathrm{h}}\sin(\phi_2) & -0.5L_{\mathrm{rt}} & L_{\mathrm{rt}} + L_{\sigma,\mathrm{rt}} & -0.5L_{\mathrm{rt}}\\
L_{\mathrm{h}}\sin(\phi_2) & L_{\mathrm{h}}\sin(\phi_3) & L_{\mathrm{h}}\sin(\phi_1) & -0.5L_{\mathrm{rt}} & -0.5L_{\mathrm{rt}} & L_{\mathrm{rt}} + L_{\sigma,\mathrm{rt}}
\end{bmatrix},
\end{aligned}$$

with $\phi_k = p\theta(t) - (k-1)\cdot 2\pi/3$, $k = 1, 2, 3$, the rotor angle $\theta(t)$, and the number of pole pairs p. Pre-multiplying the ODE (2.113) with $\mathbf{i}^\top$, we obtain the power balance equation

$$\mathbf{i}^\top\mathbf{u} = \mathbf{i}^\top\mathbf{R}\mathbf{i} + \mathbf{i}^\top\mathbf{L}\mathbf{i}' + \underbrace{\mathbf{i}^\top\frac{\mathrm{d}\mathbf{L}}{\mathrm{d}\theta}\mathbf{i}\theta'}_{=P_{\mathrm{mech}}}. \tag{2.114}$$

Analogously to (2.111), the electromagnetic torque is given by

$$T_{\mathrm{EM}}(\theta) = \frac{P_{\mathrm{mech}}}{\omega_{\mathrm{mech}}} = \mathbf{i}^\top\frac{\mathrm{d}\mathbf{L}}{\mathrm{d}\theta}\mathbf{i}, \tag{2.115}$$

since $\omega_{\mathrm{mech}} = \theta'$. Introducing the flux linkage

$$\boldsymbol{\psi} = \mathbf{L}(\theta)\mathbf{i} \tag{2.116}$$

we can eliminate the current $\mathbf{i}$ from the torque calculation and obtain

$$T_{\mathrm{EM}}(\theta) = \Big(\big[\mathbf{L}(\theta)\big]^{-1}\boldsymbol{\psi}(t)\Big)^\top\frac{\mathrm{d}\mathbf{L}}{\mathrm{d}\theta}(\theta)\big[\mathbf{L}(\theta)\big]^{-1}\boldsymbol{\psi}(t). \tag{2.117}$$

Similarly, through (2.116), the system (2.113) becomes

$$\boldsymbol{\psi}'(t) = \mathbf{u}(t) - \mathbf{R}\big[\mathbf{L}(\theta)\big]^{-1}\boldsymbol{\psi}(t). \tag{2.118}$$

The ODE (2.118) is coupled to the mechanical ODE system (2.104)-(2.105), with $C = 0$, T_{EM} obtained from (2.115) and T_{load} given in (2.112).

2.5 Conclusion

This chapter described the fundamental concepts of mathematical modeling of electromagnetic phenomena. First, the magnetoquasistatic approximation of the Maxwell (partial differential) equations was derived in terms of the magnetic vector potential. Then, electric circuits, coupled to electromagnetic field models, were modeled by ordinary differential and differential-algebraic equations. Finally, principles of pulse-width modulation and induction motors were discussed. In the following chapter we provide functional analytic basics and derive the variational (or weak) formulation of first-order evolution partial differential equations. There, numerical solution approaches for initial-value problems and boundary-value problems in time are described.

3 Numerical analysis

In order to solve a real-life engineering problem described by PDEs, one typically looks for a numerical solution, as already mentioned in the Section 2.1.2. Using the notion of weak derivatives and appropriate function spaces, one derives a weak formulation of the corresponding PDE, whose solvability and uniqueness of the solution are to be analyzed. The solution is then approximated in a finite dimensional subspace, which allows to solve the problem numerically on a computer.

This chapter provides theoretical basics and numerical solution approaches of first-order evolution problems. First, the fundamentals of functional analysis, necessary for the weak formulations, are summarized in Section 3.1. In particular, the classical and space-time Sobolev spaces are defined in Section 3.1.1 and Section 3.1.2, respectively. The existence and uniqueness results of the weak solutions in the corresponding function spaces are presented in Section 3.1.3 based on the theory from [139, 140]. Discretization methods for approximation of the solution in the space and time domains are described in Section 3.2.1 and Section 3.2.2, respectively. The resulting nonlinear algebraic systems can then be solved with the linearization approaches specified in Section 3.2.3.

Section 3.3 deals with boundary value problems (BVPs) in the time domain. In particular, the class of shooting methods, which solve the BVPs iteratively by the introduction of a sequence of IVPs, is described in Section 3.3.1. In case of a linear TP problem, application of the multiple shooting method leads to a block-cyclic system which can be solved efficiently using a MH diagonalization approach, presented in Section 3.3.2. Finally, some TP problems, e.g., for autonomous systems of ODEs, already described in Section 2.2.2, might not include the period within the problem settings. Solution of the TP problems with unknown period (UP) by means of the shooting methods is discussed in Section 3.3.3.

3.1 Functional analytic preliminaries

We assume in this chapter that the reader is familiar with Banach and Hilbert spaces, the notions of density and separability. The interested reader is referred to [4, Chapter 2].

Let V be a real Banach space with the norm $\|\cdot\|_V$. The space $V^* = \mathcal{L}(V, \mathbb{R})$ of *linear bounded functionals* $u^* : V \to \mathbb{R}$ is called the *dual space* of V. The *duality pairing* of $u^* \in V^*$ and $u \in V$ is denoted by $\langle u^*, u\rangle_{V^*,V} \in \mathbb{R}$.

Let us consider an operator $A\colon V \to V^*$. The norm in V^* is defined by

$$\|A(u)\|_{V^*} = \sup_{\|v\|_V=1} \left|\big\langle A(u), v\big\rangle_{V^*,V}\right|. \tag{3.1}$$

We define several operator properties, which will be used within the solvability and uniqueness theory in Section 3.1.3.

Definition 3.1 (based on [140, Definitions 25.2, 26.1])**.** *Let V denote a real Banach space, equipped with the norm $\|\cdot\|_V$, and $A\colon V \to V^*$ be an operator.*

A.1 *A is monotone iff* $\big\langle A(u) - A(v), u - v\big\rangle_{V^*,V} \geq 0, \quad \forall u, v \in V.$

A.2 *A is strictly monotone iff* $\big\langle A(u) - A(v), u - v\big\rangle_{V^*,V} > 0, \quad \forall u, v \in V\colon\ u \neq v.$

A.3 *A is strongly monotone iff* $\exists\, C > 0\colon\ \big\langle A(u) - A(v), u - v\big\rangle_{V^*,V} \geq C\|u - v\|_V^2, \quad \forall u, v \in V.$

A.4 *A is hemicontinuous iff the mapping $g\colon [0,1] \to \mathbb{R}$ given by $g(t) = \big\langle A(u + ty), v\big\rangle_{V^*,V}$ is continuous $\forall u, v, y \in V$.*

A.5 *A is coercive iff* $\dfrac{\big\langle A(u), u\big\rangle_{V^*,V}}{\|u\|_V} \to \infty,\ \|u\|_V \to \infty.$

A.6 *A is bounded iff* $\exists\, C > 0\colon\ \|A(u)\|_{V^*} \leq C\|u\|_V, \quad \forall u \in V.$

We now head to the definitions of the appropriate functional spaces, which the weak solutions of the PDEs are sought in.

3.1.1 Classical Lebesgue and Sobolev spaces

Let $\Omega \subset \mathbb{R}^d$, $d > 0$ be an open, bounded, simply connected domain with Lipschitz boundary. We denote by $L^p(\Omega)$ for $1 \leq p \leq \infty$ *the Lebesgue space* of measurable functions u with finite norm [1, Chapter 2]

$$\begin{aligned} \|u\|_{L^p(\Omega)} &= \left(\int_\Omega |u(\vec{x})|^p \mathrm{d}\vec{x}\right)^{1/p}, \quad 1 \leq p < \infty, \\ \|u\|_{L^\infty(\Omega)} &= \operatorname*{ess\,sup}_{\vec{x}\in\Omega} |u(\vec{x})|. \end{aligned} \tag{3.2}$$

For the definition of $\operatorname{ess\,sup}$ we refer to [4, Section 3.16], [1, Section 2.5]. Equipped with the norm (3.2) the space $L^p(\Omega)$ is Banach. It is known that the dual space of $L^p(\Omega)$ for $1 \leq p < \infty$ is the space $L^q(\Omega)$ with $1 < q \leq \infty$ such that $1/p + 1/q = 1$. A comprehensive introduction to the Lebesgue spaces can be found, e.g., in [1, Chapter II], [4, Section 3.15], [23, Chapter 4] or [110, Section 1.2].

Definition 3.2 ([1, Definition 1.57])**.** *The weak derivative of order k in space of the function $u \in L^1(\Omega)$ is called the function $y \in L^1(\Omega)$ such that*

$$\int_\Omega D^k\phi(\vec{x})u(\vec{x})\,\mathrm{d}\vec{x} = (-1)^k \int_\Omega y(\vec{x})\phi(\vec{x})\,\mathrm{d}\vec{x}, \quad \forall \phi \in C_0^\infty(\Omega), \tag{3.3}$$

where the derivative $D^k\phi$ is defined in (2.16) *and $C_0^\infty(\Omega)$ denotes the space of infinitely continuously differentiable functions with compact support $\operatorname{supp}(\phi) \subset \Omega$. If such a function y exists, we write $y = D^k u$ to denote the kth weak derivative of the function u.*

Since $L^p(\Omega) \subset L^1(\Omega)$ for $1 < p \leq \infty$ [1, Theorem 2.8], the Definition 3.2 is valid for any $u \in L^p(\Omega)$, $1 \leq p \leq \infty$. The space of the $L^p(\Omega)$-functions, $1 \leq p \leq \infty$, whose weak derivatives up to order $m \geq 0$ also belong to $L^p(\Omega)$, is defined by *the Sobolev space* [1, Chapter 3]

$$W^{m,p}(\Omega) = \left\{ u \in L^p(\Omega) \colon\ D^k u \in L^p(\Omega),\ 0 \leq k \leq m \right\}. \tag{3.4}$$

The space $W^{m,p}(\Omega)$ is Banach space with the norm

$$\begin{aligned} \|u\|_{W^{m,p}(\Omega)} &= \left(\sum_{k=0}^{m} \|D^k u\|^p_{L^p(\Omega)} \right)^{1/p}, \quad 1 \leq p < \infty, \\ \|u\|_{W^{m,\infty}(\Omega)} &= \max_{0 \leq k \leq m} \|D^k u\|_{L^\infty(\Omega)}. \end{aligned} \tag{3.5}$$

We denote by $W_0^{m,p}(\Omega)$ the closure of $C_0^\infty(\Omega)$ in the space $W^{m,p}(\Omega)$ and by $W^{-m,p}(\Omega)$ the dual of $W_0^{m,p}(\Omega)$. For the theory on the Sobolev spaces $W^{m,p}(\Omega)$ we refer to [1, Chapter III], [4, Section 3.27, 3.29], and [110, Section 1.2].

We note that the introduced Lebesgue and Sobolev spaces contain functions, which depend only on the space variable. For investigation of the space- and time-dependent PDEs we need the corresponding function spaces, which we present in the following.

3.1.2 Space-time Lebesgue and Sobolev spaces

We use the notation $V \hookrightarrow Y$ to define a *continuous embedding* of the space V in the space Y, i.e., a continuous, linear, injective mapping $i \colon V \to Y$.

Definition 3.3 ([139, Definition 23.11])**.** *The embedding chain $V \hookrightarrow H \hookrightarrow V^*$ is called an evolution triple if*

- *V is real separable reflexive*[6] *Banach space with the norm $\|\cdot\|_V$,*
- *H is real separable Hilbert space with the inner product $(\cdot,\cdot)_H$ and the norm $\|\cdot\|_H$,*
- *The embedding $V \hookrightarrow H$ is continuous, i.e., $\exists\, C > 0 \colon\ \|v\|_H \leq C\|v\|_V\ \forall v \in V$, and V is dense in H.*

Proposition 3.4 (based on [139, Section 23.4])**.** *For the evolution triple $V \hookrightarrow H \hookrightarrow V^*$ it holds*

- *$\forall h \in H\ \exists\, h^* \in V^*$ such that*
$$\langle h^*, v \rangle_{V^*,V} = (h, v)_H, \quad \forall v \in V. \tag{3.6}$$
- *The embedding $H \hookrightarrow V^*$ is continuous and H is dense in V^*.*

Proof. We refer to [139, Problem 18.6 and Proposition 23.13] for the justification. □

The Proposition 3.4 allows to identify elements $h^* \in V^*$ and $h \in H$ for an evolution triple $V \hookrightarrow H \hookrightarrow V^*$. This will be necessary to match the function spaces when writing down the weak formulation in Section 3.1.3. We now consider particular Lebesgue and Sobolev spaces, needed for treatment of time-dependent problems.

[6] A real Banach space V is called *reflexive* if the canonical injection $J \in \mathcal{L}(V^*, V^{**})$ is surjective, see [23, Sections 1.3, 3.5].

The Lebesgue space $L^p(0,T;V)$

For a Banach space V and a scalar $0 < T < \infty$ we define the Lebesgue space $L^p(0,T;V)$ of functions $u\colon [0,T] \to V$ with the finite norm given by [139, Section 23.2]

$$\begin{aligned} \|u\|_{L^p(0,T;V)} &= \left(\int_0^T \|u(t)\|_V^p \mathrm{d}t \right)^{1/p}, \quad 1 \le p < \infty, \\ \|u\|_{L^\infty(0,T;V)} &= \operatorname*{ess\,sup}_{t\in[0,T]} \|u(t)\|_V. \end{aligned} \tag{3.7}$$

Similarly, by $C([0,T];V)$ we denote the space of continuous functions $u\colon [0,T] \to V$ with the norm defined as

$$\|u\|_{C([0,T];V)} = \max_{t\in[0,T]} \|u(t)\|_V. \tag{3.8}$$

The space $C([0,T];V)$ is dense in $L^p(0,T;V)$, $1 \le p < \infty$, and the embedding $C([0,T];V) \hookrightarrow L^p(0,T;V)$ is continuous (see [139, Proposition 23.2]).

Finally, denoting the dual space of $X = L^p(0,T;V)$ by X^* we can identify $X^* = L^q(0,T;V^*)$, see [139, Convention 23.8], for $1 < p,q < \infty$ such that $1/p+1/q = 1$. We then have the duality pairing

$$\langle v,u\rangle_{X^*,X} = \int_0^T \big\langle v(t),u(t)\big\rangle_{V^*,V} \mathrm{d}t, \quad \forall u \in X, \quad \forall v \in X^*. \tag{3.9}$$

We thus have defined the function spaces $L^p(0,T;V)$, which are candidates to look for weak solutions of PDEs in. However, for the analysis of the evolution PDEs we still need to impose somewhat stronger conditions on the solution, which would take into account also derivatives in time. For this we introduce the notion of the weak derivative and define an appropriate solution space in the following subsection.

Weak derivatives in $L^p(0,T;V)$

Similarly to the Definition 3.2, we provide the definition of the weak derivative in the space-time Lebesgue space $L^p(0,T;V)$.

Definition 3.5 ([139, Definition 23.15])**.** *Let V and Y be two Banach spaces. The weak derivative of order n in time of the function $u \in L^1(0,T;V)$ on $(0,T)$ is called the function $y \in L^1(0,T;Y)$ such that*

$$\int_0^T \phi^{(n)}(t)u(t)\,\mathrm{d}t = (-1)^n \int_0^T y(t)\phi(t),\mathrm{d}t, \quad \forall \phi \in C_0^\infty((0,T)), \tag{3.10}$$

where $C_0^\infty((0,T))$ denotes the space of infinitely continuously differentiable functions with compact support $\operatorname{supp}(\phi) \subset (0,T)$. If such a function y exists, we write $y = u^{(n)}$ to denote the nth weak derivative of the function u.

Since $L^p(0,T;V) \subset L^1(0,T;V)$ for $1 < p \le \infty$ (see [139, Proposition 23.2]), the Definition 3.5 is valid for any $u \in L^p(0,T;V)$, $1 \le p \le \infty$. We now present a uniqueness and existence result for the weak derivative (3.10) in the space $L^p(0,T;V)$.

Proposition 3.6 ([139, Proposition 23.20]). *Let $V \hookrightarrow H \hookrightarrow V^*$ be an evolution triple and $1 \leq p, q \leq \infty$.*

- *(Uniqueness) For a function $u \in L^p(0,T;V)$ the weak derivative $u^{(n)} \in L^q(0,T;V^*)$ is unique.*
- *(Existence) For a function $u \in L^p(0,T;V)$ there exists the weak derivative $u^{(n)} \in L^q(0,T;V^*)$ iff there exists a function $y \in L^q(0,T;V^*)$ such that*

$$\int_0^T \big(u(t),v\big)_H \phi^{(n)}(t)\,\mathrm{d}t = (-1)^{(n)} \int_0^T \big\langle y(t),v\big\rangle_{V^*,V} \phi(t)\,\mathrm{d}t, \quad \forall v \in V, \quad \forall \phi \in C_0^\infty((0,T)). \tag{3.11}$$

Then $y = u^{(n)}$ and we have

$$\frac{\mathrm{d}^n}{\mathrm{d}t^n}\big(u(t),v\big)_H = \big\langle u^{(n)}(t),v\big\rangle_{V^*,V} \quad \forall v \in V, \quad \textit{for a.e. } t \in (0,T). \tag{3.12}$$

The formula (3.12) is very useful for treatment of evolution problems, since one may investigate the weak derivative of the real-valued function $\big(u(t),v\big)_H$ on the left-hand side (LHS) instead of the weak derivative of the function u, whose values are in the Banach space V, on the RHS.

The Sobolev space $W^{1,p}(0,T;V,H)$

Finally, for an evolution triple $V \hookrightarrow H \hookrightarrow V^*$ and $1 < p, q < \infty$, $1/p + 1/q = 1$, we define the space [139]

$$W^{1,p}(0,T;V,H) = \big\{u \in L^p(0,T;V) \colon\ u' \in L^p\big(0,T;V^*\big)\big\}, \tag{3.13}$$

which will be used as the solution space for a weak formulation of a parabolic PDE. In the following proposition we state a couple of useful properties of the space (3.13).

Proposition 3.7 (see [139, Proposition 23.23]). *Let $V \hookrightarrow H \hookrightarrow V^*$ be an evolution triple and $1 < p < \infty$. Then*

- *$W^{1,p}(0,T;V,H)$ from (3.13) is a real Banach space with the norm*

$$\|u\|_{W^{1,p}(0,T;V,H)} = \|u\|_{L^p(0,T;V)} + \|u'\|_{L^p(0,T;V)}, \tag{3.14}$$

- *the embedding $W^{1,p}(0,T;V,H) \hookrightarrow C([0,T];H)$ is continuous.*

We note the continuity of the functions from $W^{1,p}(0,T;V,H)$ with respect to the space H, which often happens to be larger than the space V, [139]. We will see in the following Section 3.1.3 that this continuous embedding will be used to determine the initial condition in the space H.

With these theoretical foundations in mind we are now ready to investigate the existence and uniqueness of the weak solutions to the first-order evolution problems defined by parabolic PDEs.

3.1.3 Theory on first-order evolution problems

Let $V \hookrightarrow H \hookrightarrow V^*$ be an evolution triple and $A\colon X \to X^*$ be an operator, with the space $X = L^p(0,T;V)$ and its dual $X^* = L^q(0,T;V^*)$, where $1 < p,q < \infty$ such that $1/p + 1/q = 1$. We consider a general first-order evolution equation written in an operator form. In particular, we search for $u \in W^{1,p}(0,T;V,H)$, which satisfies

$$u' + A(u) = f \text{ in } X^*, \tag{3.15}$$

where $f \in X^*$ and the derivative u' has to be understood in the weak sense, see Definition 3.5. Additionally, we have an IC or a TP condition, i.e.,

$$u(0) = u_0 \in H \qquad \text{or} \tag{3.16}$$

$$u(0) = u(T) \in H, \tag{3.17}$$

respectively. Note that conditions (3.16) and (3.17) are defined in a larger space H. It is acceptable, since there is a continuous embedding $W^{1,p}(0,T;V,H) \hookrightarrow C([0,T];H)$, see Proposition 3.7. Therefore, a function $u \in W^{1,p}(0,T;V,H)$ is uniquely determined in $C([0,T];H)$ up to zero measure sets. In the following theorem we state the existence and uniqueness results for the IVP (3.15)-(3.16) and TP problem (3.15), (3.17).

Theorem 3.8 (see [140, Theorem 32.D]). *Let $V \hookrightarrow H \hookrightarrow V^*$ denote an evolution triple, $X = L^p(0,T;V)$, with $1 < p < \infty$ and $0 < T < \infty$. Assume that the operator $A\colon X \to X^*$ is monotone, hemicontinuous, coercive and bounded. Then for every $f \in X^*$ and $u_0 \in H$ the IVP* (3.15)- (3.16) *and the TP problem* (3.15), (3.17) *have solutions in $W^{1,p}(0,T;V,H)$. If, in addition, A is strictly monotone, then the corresponding solutions are unique.*

Proof. The proof is based on the proof of Theorem 32.D in [140] and on the fact that monotonicity and hemicontinuity imply pseudomonotonicity (for the definition see [140, Definition 27.5]), as it is stated in [140, Proposition 27.6]. □

Operator equation (3.15) is the most elegant way to write a first-order evolution equation. However, when dealing with concrete parabolic PDEs one rather deals with the formulation

$$u'(t) + \tilde{A}(u(t)) = f(t) \quad \text{for a.e. } t \in (0,T), \tag{3.18}$$

with the operator $\tilde{A}\colon V \to V^*$, the RHS $f \in X^*$, and the sought function $u \in W^{1,p}(0,T;V,H)$. Equivalence of the two formulations when setting $(A(u))(t) = \tilde{A}(u(t))$ can be derived using the formula (3.9) and is proven in the Theorem 30.A in [140]. It is also shown that the operators A and $\tilde{A}$ possess the same properties (such as (strict) monotonicity, hemicontinuity, coercivity and boundedness) in the spaces X and V, respectively. For convenience, we will investigate the operator $\tilde{A}$ in the following, where we apply the provided general theory to the 2D eddy current problem (see Section 2.1.3).

Weak formulation of the eddy current problem

In Section 2.1.3 we have formulated the IBVP and TPBVP for the eddy current equation in a 2D domain Ω. We will now investigate solvability and uniqueness of the weak solution in the appropriate function spaces. For this, we at first provide a weak formulation of the IBVP (2.32)-(2.34) and TPBVP (2.32)-(2.33), (2.35). Taking into account the setting (2.9), we only consider the domain with nonlinear magnetic materials, i.e.,

we have $\nu(\vec{x}, |\operatorname{grad} u|) = \nu(|\operatorname{grad} u|)$. Besides, we assume that in the considered region the conductivity $\sigma > 0$ and thus deal with a parabolic PDE.

For an open, bounded, simply connected domain $\Omega \subset \mathbb{R}^2$ with Lipschitz boundary we define

$$V := W_0^{1,2}(\Omega), \qquad H := L^2(\Omega), \qquad V^* := W^{-1,2}(\Omega), \tag{3.19}$$

with the spaces presented in the Section 3.1.1. By the Sobolev embedding theorem (see [1, Chapter V]) the embedding chain $V \hookrightarrow H \hookrightarrow V^*$ of the spaces from (3.19) defines an evolution triple. Besides, the space $H = L^2(\Omega)$ is a Hilbert space endowed with the scalar product

$$(y, v)_H = \int_\Omega yv \,\mathrm{d}\Omega, \quad \forall y, v \in H, \tag{3.20}$$

see [110, Section 1.2]. For $0 < T < \infty$ we treat the solution u and the input f in (2.32) as functions $u : [0, T] \to V$ and $f : [0, T] \to V^*$ with values in Banach spaces V and V^*, respectively. Exploiting the notations from the Section 3.1.2, we assign

$$X := L^2(0, T; V), \qquad X^* := L^2(0, T; V^*). \tag{3.21}$$

To obtain the weak formulation of the PDE (2.32), we first multiply the PDE by a test function $v \in V$ and integrate the equation with respect to the spatial variable $\vec{x} \in \Omega$, i.e.,

$$\int_\Omega \sigma u'(t) v \,\mathrm{d}\Omega - \int_\Omega \operatorname{div}\big(\nu(|\operatorname{grad} u(t)|) \operatorname{grad} u(t)\big) v \,\mathrm{d}\Omega = \int_\Omega f(t) v \,\mathrm{d}\Omega, \quad \forall v \in V, \quad \text{for a.e. } t \in (0, T). \tag{3.22}$$

The derivative in (3.22) is to be understood in the weak sense as in (3.10). Applying the Green formula (see [110, Section 1.3])

$$\int_\Omega \operatorname{div} \vec{w} v \,\mathrm{d}\Omega = -\int_\Omega \vec{w} \cdot \operatorname{grad} v \,\mathrm{d}\Omega + \int_{\partial\Omega} (\vec{w} \cdot \vec{n}) v \,\mathrm{d}\Gamma, \tag{3.23}$$

where $\vec{w} := \nu(|\operatorname{grad} u(t)|) \operatorname{grad} u(t)$ and $\vec{n}$ denotes the outer unit normal to the boundary $\partial\Omega$, and taking into account that for $v \in V = W_0^{1,2}(\Omega)$ the boundary integral on the RHS in (3.23) vanishes, we obtain the following weak formulation ([140, Definition 30.9]) of the PDE (2.32). For a given $f \in X^*$ find $u \in W^{1,2}(0, T; V, H)$ such that

$$\frac{\mathrm{d}}{\mathrm{d}t}\big(\sigma u(t), v\big)_H + \big\langle \tilde{A}(u(t)), v \big\rangle_{V^*,V} = \big(f(t), v\big)_H \quad \forall v \in V, \quad \text{for a.e. } t \in (0, T), \tag{3.24}$$

where we introduced the operator $\tilde{A} \colon V \to V^*$ such that

$$\big\langle \tilde{A}(y), v \big\rangle_{V^*,V} = \int_\Omega \nu(|\operatorname{grad} y|) \operatorname{grad} y \cdot \operatorname{grad} v \,\mathrm{d}\Omega, \quad \forall y, v \in V \tag{3.25}$$

and used the formula (3.20). Note that the weak derivative in (3.24) is applied to a real-valued function in contrast to the weak derivative of the function u with values in the Banach space V in (3.22).

For a given $f \in X^*$, a function $u \in W^{1,2}(0, T; V, H)$ is called the weak solution to the IBVP (2.32)-(2.34) if it satisfies the equation (3.24) and the initial condition (3.16). Analogously, $u \in W^{1,2}(0, T; V, H)$ is the weak solution to the TPBVP (2.32)-(2.33), (2.35) if it satisfies (3.24) and the TP condition (3.17).

Using the formula (3.12) for the derivate term on the LHS and (3.6) for the term on the RHS, we can transform the equation (3.24) into the functional equation (3.18) if we assume without loss of generality that $\sigma = 1$ (or alternatively divide the equation (3.24) by $\sigma > 0$). This allows us to directly apply the Theorem 3.8 to prove existence and uniqueness of the solutions of the IVP (3.24), (3.16) and the TP problem (3.24), (3.17). For this we need to show that the operator $\tilde{A}$ from (3.25) satisfies the assumptions of the Theorem 3.8, which we do in the following theorem.

Theorem 3.9. *Let the spaces of evolution triple $V \hookrightarrow H \hookrightarrow V^*$ be defined in* (3.19) *and let the reluctivity function ν be given by the BH-curve b via* (2.11)*. If b satisfies the Assumption 2.1, then the operator $\tilde{A}\colon V \to V^*$ in* (3.25) *is strongly monotone, hemicontinuous, coercive and bounded.*

Proof. According to the Corollary 2.2, the conditions **B.1**-**B.4** hold for the reluctivity ν. We will use these conditions to derive the properties of the operator $\tilde{A}$.

- *Strong monotonicity* is shown in [70, 99]. This comes from the strong monotonicity of the mapping $h(p) = \nu(|p|)p$, $p \in \mathbb{R}^2$, which can be derived from the strong monotonicity of the mapping $f(s) = \nu(s)s$, $s \in \mathbb{R}_0^+$ (see Corollary 2.2, **B.3**).
- *Hemicontinuity* is derived from the continuity of ν on $\mathbb{R}_0^+$ (see Corollary 2.2, **B.1**).
- *Coercivity* comes from the boundedness of ν by c_1 from below (see Corollary 2.2, **B.1**). Using the Poincaré inequality [4, Section 6.7] with the constant $C_0 > 0$, we have

$$\frac{\langle \tilde{A}(y), y\rangle_{V^*,V}}{\|y\|_V} \geq \frac{c_1 \|\operatorname{grad} y\|_H^2}{\|y\|_V} \geq \frac{c_1}{1+C_0}\|y\|_V \to \infty, \text{ as } \|y\|_V \to \infty, \tag{3.26}$$

  which implies the coercivity of $\tilde{A}$ (according to the Definition 3.1, **A.5**).
- *Boundedness* comes from the boundedness of ν by ν_0 from above (see Corollary 2.2, **B.1**). Using the Hölder inequality [4, Section 3.18], we obtain from (3.1)

$$\|\tilde{A}(y)\|_{V^*} \leq \nu_0 \sup_{\|v\|_V=1} \left| \int_\Omega \nabla y \nabla v dx \right| \leq \nu_0 \sup_{\|v\|_V=1} \|y\|_H \|v\|_H \leq \nu_0 \|y\|_V, \tag{3.27}$$

  which means that the operator $\tilde{A}$ is bounded (according to the Definition 3.1, **A.6**).

□

We note that strong monotonicity implies strict monotonicity, which in its turn implies monotonicity. Due to the Theorem 30.A in [140] and Theorem 3.9 the operator $A\colon X \to X^*$, defined as $(A(u))(t) = \tilde{A}(u(t))$, has the properties required in Theorem 3.8. Therefore, both the IVP (3.24), (3.16) and the TP problem (3.24), (3.17) have unique solutions in the space $W^{1,2}(0,T;V,H)$. We note that in the linear case when $\nu(\vec{x}, |\operatorname{grad} u|) = \nu_0$ a simpler theory can be applied, see [139, Theorem 23.A] for the details.

Remark 3.10. *In case $\sigma = 0$ the eddy current equation* (2.32) *loses the time derivative and therefore becomes a PDE of the elliptic type, thereby describing the magnetostatic regime. The analysis in this case is based on the theorem of Browder and Minty (see [140, Theorem 26.A]), where the operator $\tilde{A}\colon V \to V^*$ acting on a real Hilbert space V has to be monotone, coercive, and hemicontinuous for the existence, and additionally strictly monotone for the uniqueness of the solution $u \in V$ of the corresponding operator equation $\tilde{A}(u) = f \in V^*$. As we have already seen, the operator $\tilde{A}$ given in* (3.25) *satisfies these requirements, which ensures solvability and uniqueness to the solution of the 2D magnetostatic model. For a more general existence and uniqueness result for a parabolic-elliptic eddy current system in a three-dimensional (3D) domain we refer to [8].*

We now head to the discretization of the weak PDE (3.24) through approximation of the solution $u(t),\ t \in [0,T]$, by a finite set of basis functions in the space V.

3.2 Discretization

In this section we transform the weak PDE (3.24), formulated at the continuous level, to the one defined discretely so that it can be solved on a computer. For this, we apply the *method of lines* [64], which consists of two steps. First, for a fixed $t \in (0,T)$ the sought function $u(t) \in V$ is approximated by a function $u_h(t) \in V_h$ from a finite-dimensional subspace $V_h \subset V$ (using, e.g., the Galerkin method). One then obtains a system of ODEs or DAEs with respect to the time variable t, which is referred to as the space-discrete or the semi-discrete system. Second, the time discretization is performed using a time-integration method (e.g., the standard sequential time stepping). This gives a fully discrete system of algebraic equations, which after a possible linearization by means of, e.g., the Newton method, can be solved using one of the standard linear solvers.

3.2.1 Space discretization

Due to [23, Theorem 5.11] every separable Hilbert space has a countable orthonormal basis. This statement allows to approximate an element of the space by its basis, which is the foundation for the *Galerkin discretization*, presented in this section. Indeed, the space $V = W_0^{1,2}(\Omega)$ is a separable Hilbert space with respect to the scalar product (see [23, Proposition 8.1], [110, Section 1.2])

$$(y,v)_V = (y,v)_H + (D^1 y, D^1 v)_H \quad \forall y, v \in V, \tag{3.28}$$

where the scalar product in H is given in (3.20) and the weak derivative D^1 is defined in (3.2).

Let $h > 0$ denote a discretization parameter, e.g., the mesh size, which is assumed to be small. The main idea of the Galerkin method lies in the approximation of the solution $u \in W^{1,2}(0,T;V,H)$ by the finite sum

$$u(t) \approx u_h(t) = \sum_{j=1}^{N_\mathrm{d}} \mathbf{u}_j(t)\phi_j, \quad t \in [0,T], \tag{3.29}$$

where $\{\phi_j,\ j = 1,\dots,N_\mathrm{d}\}$ form a basis of the finite-dimensional subspace $V_h \subset V$ and $\mathbf{u}_j : [0,T] \to \mathbb{R}$ are the time-dependent coefficients. Plugging (3.29) into the weak formulation (3.24) and setting $v := \phi_i$, $i = 1,\dots,N_\mathrm{d}$, we obtain the *semi-discrete problem*, given by the finite-dimensional system of nonlinear ODEs/DAEs

$$\mathbf{M}_\sigma \mathbf{u}'(t) + \mathbf{K}_\nu\big(\mathbf{u}(t)\big)\mathbf{u}(t) = \mathbf{f}(t), \quad t \in (0,T), \tag{3.30}$$

where we used the notation $\mathbf{u}(t) = \big[\mathbf{u}_1(t),\dots,\mathbf{u}_{N_\mathrm{d}}(t)\big]^\top \in \mathbb{R}^{N_\mathrm{d}}$ and

$$(\mathbf{M}_\sigma)_{ij} = \int_\Omega \sigma\phi_j\phi_i \,\mathrm{d}\Omega, \qquad \big(\mathbf{f}(t)\big)_i = \int_\Omega f(t)\phi_i \,\mathrm{d}\Omega, \tag{3.31}$$

$$\big(\mathbf{K}_\nu(\mathbf{u})\big)_{ij} = \int_\Omega \nu\Big(\Big|\sum_{k=1}^{N_\mathrm{d}} \mathbf{u}_k \operatorname{grad}\phi_k\Big|\Big) \operatorname{grad}\phi_j \cdot \operatorname{grad}\phi_i \,\mathrm{d}\Omega, \tag{3.32}$$

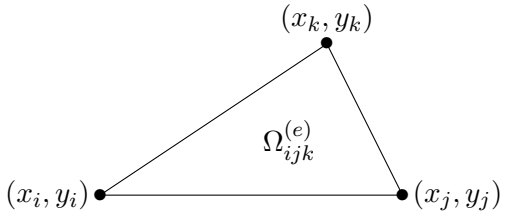

Figure 3.1: An exemplary linear triangular element.

for $i, j = 1, \ldots, N_\mathrm{d}$, the RHS vector $\mathbf{f} \in \mathbb{R}^{N_\mathrm{d}}$ and matrices $\mathbf{M}_\sigma, \mathbf{K}_\nu(\mathbf{u}) \in \mathbb{R}^{N_\mathrm{d} \times N_\mathrm{d}}$, called the *mass* and the *stiffness matrices*, respectively. We point out that the matrix $\mathbf{M}_\sigma$ is singular when the domain Ω contains non-conductive regions where $\sigma = 0$. In this case (3.30) is a system of index-1 DAEs [96]. For solvability of the system we require that the matrix pencil $(\mathbf{M}_\sigma, \mathbf{K}_\nu(\mathbf{u})) := \lambda \mathbf{M}_\sigma + \mathbf{K}_\nu(\mathbf{u})$, with $\lambda \in \mathbb{R}$, is regular for any $\mathbf{u} \in \mathbb{R}^{N_\mathrm{d}}$. We note that the matrix $\mathbf{K}_\nu$ depends nonlinearly on the vector $\mathbf{u}$ due to the nonlinearity of the reluctivity ν.

The initial value $u_0 \in H$ from (3.16) is also represented using the basis functions $\phi_j \in V_h$, $j = 1, \ldots, N_\mathrm{d}$, i.e.,

$$u_0 \approx \sum_{j=1}^{N_\mathrm{d}} (\mathbf{u}_0)_j \phi_j, \quad \text{with } (\mathbf{u}_0)_j = (u_0, \phi_j)_H. \tag{3.33}$$

The IC (3.16) and the TP condition (3.17) in the infinite-dimensional Hilbert space H are given in the finite-dimensional space $\mathbb{R}^{N_\mathrm{d}}$ by

$$\mathbf{u}(0) = \mathbf{u}_0 \in \mathbb{R}^{N_\mathrm{d}} \qquad \text{and} \tag{3.34}$$

$$\mathbf{u}(0) = \mathbf{u}(T) \in \mathbb{R}^{N_\mathrm{d}}, \tag{3.35}$$

respectively. We point out that the prescribed values have to be consistent for a system of DAEs, see Section 2.2.3. It is shown in [140, Theorem 30.A] that the finite-dimensional solution u_h given in (3.29) converges to the weak solution u of the problem (3.24) in the sense that

$$u_h \rightharpoonup u \text{ in } X,\ h \to 0, \quad \text{i.e.,} \quad \langle F, u_h \rangle_{X^*,X} \to \langle F, u \rangle_{X^*,X},\ h \to 0, \quad \forall\, F \in X^*,$$
$$\text{and} \quad \|u_h - u\|_{C([0,T];H)} \to 0,\ h \to 0$$

with the spaces X and X^* defined in (3.21) and the norm in $C([0,T];H)$ from (3.8).

First-order finite elements

The idea of the *finite element method (FEM)* in the 2D computational domain Ω lies in the partition of Ω into *elements* and introduction of the *shape functions* on each element [22]. We consider here triangular elements and first-order nodal functions. In this case the solution is approximated by a linear combination of piecewise-linear "hat" functions

$$\phi_i^{(e)}(x, y) = \frac{1}{2|\Omega_{ijk}^{(e)}|} \left[a_i^{(e)} + b_i^{(e)} x + c_i^{(e)} y \right], \quad (x, y) \in \Omega_{ijk}^{(e)} \tag{3.36}$$

given on an element $\Omega_{ijk}^{(e)}$. The area of the element is denoted by $|\Omega_{ijk}^{(e)}|$ and the coordinates of its vertices are (x_i, y_i), (x_j, y_j), and (x_k, y_k), see Figure 3.1. The coefficients in (3.36) are defined by [121, Section 2.2.]

$$a_i^{(e)} = x_j y_k - x_k y_j, \tag{3.37}$$

$$b_i^{(e)} = y_j - y_k, \tag{3.38}$$

$$c_i^{(e)} = x_k - x_j. \tag{3.39}$$

The function $\phi_i^{(e)}$ is linear in each element, which has a vertex at the node (x_i, y_i). It attains the value 1 at (x_i, y_i) and the value 0 at the other nodes, i.e.,

$$\phi_i^{(e)}(x_j, y_j) = \begin{cases} 0, & i \neq j, \\ 1, & i = j. \end{cases} \tag{3.40}$$

Basis functions with the property (3.40) are called *nodal basis functions* [22, Chapter 3]. The total number of nodes obtained from the *triangulation* of the domain Ω is equal to N_d (the number of DoFs). The global $(N_\mathrm{d} \times N_\mathrm{d})$-dimensional matrices $\mathbf{M}_\sigma$, $\mathbf{K}_\nu$ and the N_d-dimensional vector $\mathbf{f}$ in (3.30) are obtained by summing up the local (3×3)-dimensional FEM matrices $\mathbf{M}_\sigma^{(e)}$, $\mathbf{K}_\nu^{(e)}$ and the 3-dimensional vector $\mathbf{f}^{(e)}$, constructed by integrating over the corresponding elements $\Omega_{ijk}^{(e)}$ with $\phi_i^{(e)}$ as the basis functions. For the details about the matrix assembly see, e.g., [121]. Finally, for the generalization to the 3D setting using the Hilbert space $\mathbf{H}(\mathrm{curl}; \Omega)$ and the (Nédélec) edge elements [95] we refer to [16, 92].

Remark 3.11. *The spatial discretization can be also performed using the finite integration technique (FIT), introduced in [133]. It solves the Maxwell equations in the integral from* (2.1a)-(2.1d) *and is based on the time-domain approach from [138]. As within FEM, the resulting discrete FIT system attains the form of* (3.30). *For the detailed explanation of FIT we refer to [134].*

To attain a fully discrete system of algebraic equations, the time-dependent system of ODEs/DAEs (3.30) has to be discretized in time. In the following Section 3.2.2 we provide basics of time-discretization.

3.2.2 Time discretization

Consider an IVP for a system of ODEs (see Section 2.2.1) with the unknown $\mathbf{u}\colon [0, T] \to \mathbb{R}^{N_\mathrm{d}}$ and the RHS $\mathbf{f}\colon \mathbb{R}^{N_\mathrm{d}} \times [0, T] \to \mathbb{R}^{N_\mathrm{d}}$ given by

$$\mathbf{u}'(t) = \mathbf{f}(\mathbf{u}(t), t), \quad t \in (0, T], \tag{3.41}$$

$$\mathbf{u}(0) = \mathbf{u}_0. \tag{3.42}$$

For simplicity, consider an equidistant partition of the time interval $[0, T]$ with the step size $\Delta T := T/N$

$$0 =: t_0 < t_1 < \ldots < t_N := T, \quad \text{where } t_n = t_{n-1} + \Delta T,\ n = 1, \ldots, N. \tag{3.43}$$

Note that in general the time-domain discretization can be performed adaptively. We denote by $\mathbf{u}_n$ an approximate solution of the system (3.41) at $t = t_n$, obtained from the application of a numerical time-integration method, starting from the initial exact solution $\mathbf{u}(t_{n-1})$ at $t = t_{n-1}$. The difference between the

exact solution $\mathbf{u}(t_n)$ and the approximate solution $\mathbf{u}_n$ is called the *local truncation error (LTE)* [25], which we denote by

$$l_n = \mathbf{u}(t_n) - \mathbf{u}_n. \tag{3.44}$$

The *order* of a time-integration method is the number $p \geq 1$ such that $l_n = \mathcal{O}(\Delta T^{p+1})$. For the equidistant partition (3.43), the θ-method [64, Section II.7] is given by

$$\mathbf{u}_n = \mathbf{u}_{n-1} + \Delta T\big[\theta \mathbf{f}(\mathbf{u}_n, t_n) + (1-\theta)\mathbf{f}(\mathbf{u}_{n-1}, t_{n-1})\big], \quad n = 1, \ldots, N, \tag{3.45}$$

with $0 \leq \theta \leq 1$. Different choices of the parameter θ yield different one-step time-integration schemes. In particular, we have

$$\theta = \begin{cases} 0, & \text{for explicit Euler (EE),} \\ 1, & \text{for implicit Euler (IE),} \\ 0.5, & \text{for trapezoidal rule (TR).} \end{cases} \tag{3.46}$$

The EE and IE methods have order $p = 1$ and the TR is of order $p = 2$, provided $\mathbf{f}$ is sufficiently smooth.

Stability

We now discuss the stability of numerical time-integration methods. For this, consider the Dahlquist test equation [65]

$$u'(t) = \lambda u(t), \quad \lambda \in \mathbb{C}. \tag{3.47}$$

A one-step scheme applied to the ODE (3.47) on the equidistant partition (3.43) reads

$$u_n = R(z)u_{n-1}, \quad \text{with } z = \lambda \Delta T. \tag{3.48}$$

Definition 3.12 ([65, Section IV.2])**.** *The function $R(z)$ in* (3.48) *is called the stability function of the one-step method applied to* (3.47)*. The stability domain of the method is defined by the set*

$$S = \big\{z \in \mathbb{C}\colon \quad |R(z)| \leq 1\big\}. \tag{3.49}$$

Note that the stability functions for the EE and IE methods, and TR are

$$R_1(z) = 1 + z, \quad R_2(z) = \frac{1}{1-z}, \quad \text{and} \quad R_3(z) = \frac{1 + 0.5z}{1 - 0.5z}, \tag{3.50}$$

respectively, [65, Table 3.1]. There are several classifications of methods regarding their stability properties, a couple of which we mention in the following.

Definition 3.13 ([65, Section IV.3])**.** *A time-integration method is said to be A-stable if the stability region S contains the entire complex left half-plane, i.e.,*

$$\mathbb{C}^- := \big\{z \in \mathbb{C}\colon \quad \mathrm{Re}(z) \leq 0\big\} \subseteq S.$$

Both IE and TR are A-stable [65], while the EE method is not A-stable. A stronger stability notion is L-stability, presented in the following definition.

Definition 3.14 ([65, Section IV.3])**.** *A method is called L-stable if it is A-stable and*

$$\lim_{z \to \infty} R(z) = 0. \tag{3.51}$$

It can be seen that the IE method is L-stable, since it is A-stable and the condition (3.51) holds for R_2 from (3.50). The TR is however not L-stable. For further stability concepts we refer to [31, Section 6.1.3].

We see that the stability domain of the EE method is bounded to $z \in \mathbb{C}$ such that $|R_1(z)| = |1 + z| \leq 1$, which might lead to stability difficulties. This is especially critical for stiff problems, which we describe in the following.

Stiffness

Although there is no rigorous definition, vaguely speaking, an ODE is considered to be *stiff* if an applied explicit numerical time-integration scheme has stability problems. It is known that explicit time-integration methods (as, e.g., EE) might lead to numerical oscillations in the solution of stiff equations, especially when the step size is not small enough. In contrast to this, implicit methods (as IE or TR) are known to deliver a stable solution independent of the step size. We refer to [65, Section IV.1] for examples of stiff problems and performance of explicit and implicit numerical methods.

A criterion for the definition of stiffness can be the following. According to [25], if $\mathbf{f}$ is Lipschitz continuous with Lipschitz constant $L > 0$, see (2.51), then for two solutions $\mathbf{y}$ and $\mathbf{z}$ of (3.41), which satisfy different ICs, it holds

$$\|\mathbf{y}(t_2) - \mathbf{z}(t_2)\| \leq \exp\big(L(t_2 - t_1)\big)\|\mathbf{y}(t_1) - \mathbf{z}(t_1)\|, \quad t_2 > t_1. \tag{3.52}$$

A problem is said to be stiff if the value of LT is large [25]. In case when the RHS in (3.41) has the form $\mathbf{f}(\mathbf{u}(t), t) = \mathbf{A}\mathbf{u}(t)$, where $\mathbf{A} \in \mathbb{R}^{N_\mathrm{d} \times N_\mathrm{d}}$ is a diagonalizable matrix with eigenvalues $\lambda_1, \ldots, \lambda_{N_\mathrm{d}} \in \mathbb{C}$, the constant L is given by the spectral radius $\rho(\mathbf{A}) = \max\{|\lambda_1|, \ldots, |\lambda_{N_\mathrm{d}}|\}$. However, in practice it might be difficult to calculate L a priori. Thus, one could intend to deduce whether the problem is stiff considering the nature of the underlying physical system. For example, if the system has components with widely varying time constants, then the model will often lead to a stiff system of ODEs [25, Section 2.2].

In the following we use the IE method and the TR, suitable for stiff problems. They belong to the family of implicit Runge-Kutta methods, which also includes higher-order time-integration schemes, e.g., the diagonal implicit Runge-Kutta or Radau methods [65].

Application to the semi-discrete eddy current problem

The IE discretization of the semi-discrete eddy current system (3.30) with the IC (3.34) on the equidistant partition (3.43) gives for $n = 1, 2, \ldots, N$

$$\frac{1}{\Delta T}\mathbf{M}_\sigma\big[\mathbf{u}_n - \mathbf{u}_{n-1}\big] + \mathbf{K}_\nu(\mathbf{u}_n)\mathbf{u}_n = \mathbf{f}_n, \tag{3.53}$$

where $\mathbf{u}(t_0) = \mathbf{u}_0$ and $\mathbf{f}_n = \mathbf{f}(t_n)$. In general, the IC $\mathbf{u}_0$ has to be chosen such that the algebraic constraints in the system (3.30) are satisfied. However, after one step of the IE method, applied to this index-1 DAE system, a consistent IC is obtained [118].

Similarly, the TR for (3.30), (3.34) and $n = 1, 2, \ldots, N$ reads

$$\frac{1}{\Delta T}\mathbf{M}_\sigma\big[\mathbf{u}_n - \mathbf{u}_{n-1}\big] + 0.5\big[\mathbf{K}_\nu(\mathbf{u}_n)\mathbf{u}_n + \mathbf{K}_\nu(\mathbf{u}_{n-1})\mathbf{u}_{n-1}\big] = 0.5\big[\mathbf{f}_n + \mathbf{f}_{n-1}\big]. \tag{3.54}$$

As a result of the application of the time-stepping methods, we have obtained the fully discrete systems of nonlinear algebraic equations. Thus, at each step a linearization approach has to be applied. We discuss several common linearization methods in the following Section 3.2.3.

3.2.3 Solution of nonlinear systems

Consider a nonlinear operator equation

$$\mathbf{F}(\mathbf{x}) = \mathbf{0}, \tag{3.55}$$

with operator $\mathbf{F}\colon X \to Y$ and Banach spaces X, Y. One of the common approaches to solve such nonlinear problems are the Newton-type methods, whose large variety is briefly described in [30, Section 1.3]. The *ordinary Newton method* reads: for a given $\mathbf{x}^{(0)}$ and for $k = 0, 1, \ldots$ calculate

$$\mathbf{J}_{\mathbf{F}}(\mathbf{x}^{(k)})\Delta\mathbf{x}^{(k)} = -\mathbf{F}(\mathbf{x}^{(k)}), \quad \mathbf{x}^{(k+1)} = \mathbf{x}^{(k)} + \Delta\mathbf{x}^{(k)}, \tag{3.56}$$

where $\mathbf{J}_{\mathbf{F}}(\mathbf{x})\colon X \to Y$ and $\mathbf{J}_{\mathbf{F}}(\mathbf{x})\mathbf{w}$ denotes the *directional derivative* of $\mathbf{F}$ in the direction of $\mathbf{w}$ at $\mathbf{x}$, see [4, Section 3.5] for the definition. In case $X = Y = \mathbb{R}^{N_\mathrm{d}}$, $\mathbf{J}_{\mathbf{F}}(\mathbf{x})$ is simply the Jacobian matrix of $\mathbf{F}$ evaluated at $\mathbf{x} \in \mathbb{R}^{N_\mathrm{d}}$. In the following theorem we state the convergence result of the Newton method in Banach spaces.

Theorem 3.15 (Newton-Kantorovich [30, Theorem 2.1])**.** *Let $\mathbf{F}: D \subset X \to Y$ be a continuously Fréchet differentiable [7] mapping with open and convex subspace D and Banach spaces X, Y. Assume that for a given $\mathbf{x}^{(0)} \in D$ there exists $\mathbf{J}_{\mathbf{F}}^{-1}(\mathbf{x}^{(0)})$ and that*

$$\left\| \left[\mathbf{J}_{\mathbf{F}}(\mathbf{x}^{(0)})\right]^{-1} \mathbf{F}(\mathbf{x}^{(0)}) \right\| \leq \alpha, \tag{3.57}$$

$$\left\| \left[\mathbf{J}_{\mathbf{F}}(\mathbf{x}^{(0)})\right]^{-1} \big(\mathbf{J}_{\mathbf{F}}(\mathbf{x}) - \mathbf{J}_{\mathbf{F}}(\mathbf{y})\big) \right\| \leq \delta_0 \|\mathbf{x} - \mathbf{y}\|, \quad \forall \mathbf{x}, \mathbf{y} \in D. \tag{3.58}$$

If $h_0 = \alpha\delta_0 \leq 0.5$ and $\bar{S}(\mathbf{x}^{(0)}, \rho) \subset D$, with $\rho = (1 - \sqrt{1 - 2h_0})/\delta_0$, then the sequence $\mathbf{x}^{(k)}$ for $k \geq 0$, obtained from the Newton iteration (3.56)*, is well defined, remains in the ball $\bar{S}(\mathbf{x}^{(0)}, \rho)$, and converges to some $\mathbf{x}^*$ such that $\mathbf{F}(\mathbf{x}^*) = \mathbf{0}$. For $h_0 < 0.5$ the convergence is quadratic.*

Application to the discrete eddy current problem

It can be shown that the operator $\tilde{A}\colon V \to V^*$ from (3.25) is Fréchet differentiable [99]. For an arbitrary $u \in V$ the derivative operator $\tilde{A}'(u)\colon V \to V^*$ is given by

$$\big\langle \tilde{A}'(u)y, v \big\rangle_{V^*,V} = \int_\Omega (\operatorname{grad} y)^\top \boldsymbol{\nu}_\mathrm{d}(\operatorname{grad} u) \cdot \operatorname{grad} v \,\mathrm{d}\Omega, \quad \forall y, v \in V, \tag{3.59}$$

with the differential reluctivity tensor $\boldsymbol{\nu}_\mathrm{d}$ defined in (2.14). Using this definition one could prove that the conditions (3.57) and (3.58) hold for the operator $\tilde{A}'(u)$ for all $u \in V_h \subset V$, [99].

We now apply the Newton method (3.56) to solve the nonlinear fully discrete system (3.53), obtained with the IE method. At each time step $n = 1, 2, \ldots, N$ we search for the root $\mathbf{x} \in \mathbb{R}^{N_\mathrm{d}}$ of the mapping $\mathbf{F}_n\colon \mathbb{R}^{N_\mathrm{d}} \to \mathbb{R}^{N_\mathrm{d}}$ defined by

$$\mathbf{F}_n(\mathbf{x}) := \frac{1}{\Delta T}\mathbf{M}_\sigma\big[\mathbf{x} - \mathbf{u}_{n-1}\big] + \mathbf{K}_\nu(\mathbf{x})\mathbf{x} - \mathbf{f}_n = \mathbf{0}. \tag{3.60}$$

[7] For the definition of Fréchet differentiability see, e.g., [4, Section 5.4].

The Jacobian matrix of $\mathbf{F}_n$ is given by

$$\mathbf{J}_{\mathbf{F}_n}(\mathbf{x}) = \frac{1}{\Delta T}\mathbf{M}_\sigma + \mathbf{K}_{\nu,\mathrm{d}}(\mathbf{x}) \tag{3.61}$$

where

$$\big(\mathbf{K}_{\nu,\mathrm{d}}(\mathbf{x})\big)_{ij} = \int_\Omega (\operatorname{grad}\phi_j)^\top \boldsymbol{\nu}_\mathrm{d}\Big(\sum_{k=1}^{N_\mathrm{d}} \mathbf{x}_k \operatorname{grad}\phi_k\Big)\cdot \operatorname{grad}\phi_i \,\mathrm{d}\Omega. \tag{3.62}$$

For a given $\mathbf{x}^{(n,0)}$, e.g., $\mathbf{x}^{(n,0)} = \mathbf{u}_{n-1}$, after the Newton procedure

$$\mathbf{J}_{\mathbf{F}_n}(\mathbf{x}^{(n,k)})\Delta\mathbf{x}^{(n,k)} = -\mathbf{F}_n(\mathbf{x}^{(n,k)}), \quad \mathbf{x}^{(n,k+1)} = \mathbf{x}^{(n,k)} + \Delta\mathbf{x}^{(n,k)} \tag{3.63}$$

has converged after K iterations, we obtain the solution $\mathbf{u}_n = \mathbf{x}^{(n,K)}$ of (3.53) at the time step n.

In case of the TR (3.54) we have

$$\mathbf{F}_n(\mathbf{x}) := \frac{1}{\Delta T}\mathbf{M}_\sigma\big[\mathbf{x} - \mathbf{u}_{n-1}\big] + 0.5\big[\mathbf{K}_\nu(\mathbf{x})\mathbf{x} + \mathbf{K}_\nu(\mathbf{u}_{n-1})\mathbf{u}_{n-1}\big] - 0.5\big[\mathbf{f}_n + \mathbf{f}_{n-1}\big] = \mathbf{0}, \tag{3.64}$$

whose Jacobian matrix is then given by

$$\mathbf{J}_{\mathbf{F}_n}(\mathbf{x}) = \frac{1}{\Delta T}\mathbf{M}_\sigma + 0.5\mathbf{K}_{\nu,\mathrm{d}}(\mathbf{x}), \tag{3.65}$$

with matrix $\mathbf{K}_{\nu,\mathrm{d}}(\mathbf{x})$ defined in (3.62). As before, the solution $\mathbf{u}_n$ is calculated applying the Newton iteration (3.63).

Simplified Newton method

Another Newton-based method, which we will exploit in Section 4.4.1, is *the simplified Newton method*. Its iteration reads: for a given $\mathbf{x}^{(0)}$ and $k = 0, 1, \ldots$ calculate

$$\mathbf{J}_\mathbf{F}(\mathbf{x}^{(0)})\Delta\mathbf{x}^{(k)} = -\mathbf{F}(\mathbf{x}^{(k)}), \quad \mathbf{x}^{(k+1)} = \mathbf{x}^{(k)} + \Delta\mathbf{x}^{(k)}, \tag{3.66}$$

where $\mathbf{J}_\mathbf{F}$ denotes the Jacobian matrix of the mapping $\mathbf{F}$. The advantage of the simplified Newton method (3.66), compared to the ordinary Newton method (3.56), is that the Jacobian $\mathbf{J}_\mathbf{F}$ has to be evaluated only once, namely, at the initial approximation $\mathbf{x}^{(0)}$. The system matrix therefore remains fixed over the iterations, which saves computational cost per iteration. However, the number of iterations might increase due to the applied approximation. We state the convergence result for the simplified Newton method in the following theorem.

Theorem 3.16 ([30, Theorem 2.5])**.** *Let $\mathbf{F}\colon D \subset \mathbb{R}^{N_\mathrm{d}} \to \mathbb{R}^{N_\mathrm{d}}$ be a continuously differentiable mapping with open and convex subset D. Assume that for a given $\mathbf{x}^{(0)} \in D$ there exists $\mathbf{J}_\mathbf{F}^{-1}(\mathbf{x}^{(0)})$ and that the affine covariant Lipschitz condition*

$$\big\|\big[\mathbf{J}_\mathbf{F}(\mathbf{x}^{(0)})\big]^{-1}\big(\mathbf{J}_\mathbf{F}(\mathbf{x}) - \mathbf{J}_\mathbf{F}(\mathbf{x}^{(0)})\big)\big\| \le \delta_0\big\|\mathbf{x} - \mathbf{x}^{(0)}\big\| \tag{3.67}$$

holds $\forall \mathbf{x} \in D$. If $h_0 = \delta_0\|\mathbf{x}^{(1)} - \mathbf{x}^{(0)}\| \le 0.5$ and $\bar{S}(\mathbf{x}^{(0)}, \rho) \subset D$, with $\rho = (1 - \sqrt{1 - 2h_0})/\delta_0$, then the sequence $\mathbf{x}^{(k)}$ for $k \ge 0$, obtained from the simplified Newton iteration (3.66)*, remains in the ball $\bar{S}(\mathbf{x}^{(0)}, \rho)$ and converges to some $\mathbf{x}^*$ such that $\mathbf{F}(\mathbf{x}^*) = \mathbf{0}$.*

The local convergence rate of the simplified Newton method is in general smaller than the one of the ordinary Newton method [30].

Fixed point iteration

Finally, the nonlinear system (3.55) can be solved using an arbitrary *fixed point iteration* method [124]. For this, we introduce $\mathbf{\Phi}(\mathbf{x}) := \mathbf{F}(\mathbf{x}) + \mathbf{x}$ and then search for the fixed point of $\mathbf{\Phi}$, i.e., for $\mathbf{x} = \mathbf{\Phi}(\mathbf{x})$. The classical (Jacobi-type) fixed point iteration for $\mathbf{\Phi}$ reads: for a given $\mathbf{x}^{(0)}$ and $k = 0, 1, \dots$ calculate

$$\mathbf{x}^{(k+1)} = \mathbf{\Phi}(\mathbf{x}^{(k)}). \tag{3.68}$$

The convergence result of the fixed point iteration is formulated in the following theorem.

Theorem 3.17 ([124, Theorem 5.2.3])**.** *Consider a function $\mathbf{\Phi}\colon \mathbb{R}^{N_\mathrm{d}} \to \mathbb{R}^{N_\mathrm{d}}$ and the starting point $\mathbf{x}^{(0)}$ of the iteration* (3.68)*. Let $S(\mathbf{x}^{(0)}, r)$ be an open ball of the radius r with the center in $\mathbf{x}^{(0)}$ and $\exists\, K \in (0,1)$ such that*

$$\|\mathbf{\Phi}(\mathbf{x}) - \mathbf{\Phi}(\mathbf{y})\| \le K\|\mathbf{x} - \mathbf{y}\| \quad \forall \mathbf{x}, \mathbf{y} \in \bar{S}(\mathbf{x}^{(0)}, r), \tag{3.69}$$

$$\|\mathbf{x}^{(1)} - \mathbf{x}^{(0)}\| \le (1 - K)r < r. \tag{3.70}$$

Then the function $\mathbf{\Phi}$ has a unique fixed point $\mathbf{x}^*$. The sequence $\mathbf{x}^{(k)}$ for $k \ge 0$, obtained from the fixed point iteration (3.68)*, remains in the ball $S(\mathbf{x}^{(0)}, r)$ and converges to $\mathbf{x}^*$. Besides, we have $\|\mathbf{x}^{(k+1)} - \mathbf{x}^*\| \le K\|\mathbf{x}^{(k)} - \mathbf{x}^*\|$ for $k \ge 0$, i.e., the convergence of the fixed point iteration is linear.*

3.3 Solution of timelike boundary value problems

Consider a BVP for a system of ODEs with the unknown $\mathbf{u}\colon [0,T] \to \mathbb{R}^{N_\mathrm{d}}$ and the RHS $\mathbf{f}\colon \mathbb{R}^{N_\mathrm{d}} \times [0,T] \to \mathbb{R}^{N_\mathrm{d}}$ given by

$$\mathbf{u}'(t) = \mathbf{f}(\mathbf{u}(t), t), \quad t \in (0,T), \tag{3.71}$$

$$\mathbf{r}(\mathbf{u}(0), \mathbf{u}(T)) = \mathbf{0}, \tag{3.72}$$

where $\mathbf{r}\colon \mathbb{R}^{2N_\mathrm{d}} \to \mathbb{R}^{N_\mathrm{d}}$ defines a BC. Often a linear BC of the type

$$\mathbf{A}\mathbf{u}(0) + \mathbf{B}\mathbf{u}(T) = \mathbf{c}, \tag{3.73}$$

with given matrices $\mathbf{A}, \mathbf{B} \in \mathbb{R}^{N_\mathrm{d} \times N_\mathrm{d}}$ and vector $\mathbf{c} \in \mathbb{R}^{N_\mathrm{d}}$. To solve the problem (3.71)-(3.72) we consider *initial-value-based methods*, particularly, the *single shooting method* and the *multiple shooting method* in Section 3.3.1. These methods transform the BVP into a sequence of IVPs which are then solved using the numerical time integrators described in Section 3.2.2. Such solution approaches are preferred for the *timelike BVPs*, where the independent variable t represents time or a time-related variable. The theory on the initial-value methods for the timelike BVPs can be found in [31, Section 8.2], [30, Section 7.1], and [124, Section 7.3].

3.3.1 Shooting methods

The nomenclature "shooting methods" originates from the problem of aiming at a target in martial artillery [31, Section 8.2.1]. The *single shooting method* searches for the initial value $\boldsymbol{\xi} \in \mathbb{R}^{N_\mathrm{d}}$ such that the solution $\mathbf{u}(t) = \mathcal{F}(t, 0, \boldsymbol{\xi})$ of the IVP

$$\mathbf{u}'(t) = \mathbf{f}(\mathbf{u}(t), t), \quad t \in (0,T], \tag{3.74}$$

$$\mathbf{u}(0) = \boldsymbol{\xi} \tag{3.75}$$

satisfies the BC

$$\mathbf{r}\big(\boldsymbol{\xi}, \mathcal{F}(T, 0, \boldsymbol{\xi})\big) = \mathbf{0}. \tag{3.76}$$

We have introduced the solution operator $\mathcal{F}$, which gives the solution of the ODE (3.74) at time t, obtained by time integration starting from the initial value ξ at time $t = 0$. The root $\boldsymbol{\xi}$ of (3.76) can be found applying the Newton method (see Section 3.2.3). In particular, considering the linear BC (3.73), i.e.,

$$\mathbf{r}\big(\boldsymbol{\xi}, \mathcal{F}(T, 0, \boldsymbol{\xi})\big) = \mathbf{A}\boldsymbol{\xi} + \mathbf{B}\mathcal{F}(T, 0, \boldsymbol{\xi}) - \mathbf{c} = \mathbf{0}, \tag{3.77}$$

we have the Jacobian matrix

$$\mathbf{J}_{\mathbf{r}}(\boldsymbol{\xi}) = \frac{\mathrm{d}\mathbf{r}}{\mathrm{d}\boldsymbol{\xi}}\big(\boldsymbol{\xi}, \mathcal{F}(T, 0, \boldsymbol{\xi})\big) = \mathbf{A} + \mathbf{B}\frac{\partial}{\partial \boldsymbol{\xi}}\mathcal{F}(T, 0, \boldsymbol{\xi}). \tag{3.78}$$

We note that the derivative of the solution with respect to the initial value on the RHS in (3.78) is typically unknown in practice. For a given $\boldsymbol{\xi}^{(0)}$ and $k = 0, 1, \ldots$ the Newton iteration reads

$$\mathbf{J}_{\mathbf{r}}(\boldsymbol{\xi}^{(k)})\Delta\boldsymbol{\xi}^{(k)} = -\mathbf{r}(\boldsymbol{\xi}^{(k)}), \quad \boldsymbol{\xi}^{(k+1)} = \boldsymbol{\xi}^{(k)} + \Delta\boldsymbol{\xi}^{(k)}. \tag{3.79}$$

The iteration (3.79) requires solution of the IVP (3.74)-(3.75) with an initial value $\mathbf{u}(0) = \boldsymbol{\xi}^{(k)}$ at each iteration k. Although the idea of the shooting method is quite simple and the convergence is well understood (see Section 3.2.3), there are some applicability limits of the approach, e.g., in case of movable singularities [31, Section 8.2.1]. Such limitations can be avoided with the multiple shooting method, which we describe in the following.

Multiple shooting method

The multiple shooting method was introduced already in 1962 by Morrison et al. [93], analyzed in 1968 by Keller [80], and formalized in 1971 by Bulirsch [24]. It considers the partition (3.43) and solves for $n = 1, \ldots, N$ an IVP

$$\mathbf{u}'(t) = \mathbf{f}(\mathbf{u}(t), t), \quad t \in (t_{n-1}, t_n], \tag{3.80}$$

$$\mathbf{u}(t_{n-1}) = \boldsymbol{\xi}_{n-1}, \tag{3.81}$$

with a given initial value $\boldsymbol{\xi}_{n-1}$. The goal of the multiple shooting is to eliminate the jumps arising at the *synchronization points* t_n, $n = 1, \ldots, N-1$, as it is visualized in Figure 3.2.

Let the solution to (3.80)-(3.81) be denoted by $\mathcal{F}(t, t_{n-1}, \boldsymbol{\xi}_{n-1})$ for $t \in (t_{n-1}, t_n]$. We then impose the continuity conditions

$$\Delta\mathbf{F}_j(\boldsymbol{\xi}_j, \boldsymbol{\xi}_{j-1}) = \mathcal{F}(t_j, t_{j-1}, \boldsymbol{\xi}_{j-1}) - \boldsymbol{\xi}_j = \mathbf{0}, \quad j = 1, \ldots, N-1, \tag{3.82}$$

which are complemented with the BC

$$\mathbf{r}(\boldsymbol{\xi}_0, \boldsymbol{\xi}_{N-1}) = \mathbf{A}\boldsymbol{\xi}_0 + \mathbf{B}\mathcal{F}(t_N, t_{N-1}, \boldsymbol{\xi}_{N-1}) - \mathbf{c} = \mathbf{0}. \tag{3.83}$$

We thus search for the root $\mathbf{x} = \big[\boldsymbol{\xi}_0^\top, \ldots, \boldsymbol{\xi}_{N-1}^\top\big]^\top \in \mathbb{R}^{N_\mathrm{d}N}$ of mapping $\mathbf{F}$: $\mathbb{R}^{N_\mathrm{d}N} \to \mathbb{R}^{N_\mathrm{d}N}$ given by

$$\mathbf{F}(\mathbf{x}) = \begin{bmatrix} \mathbf{r}(\xi_0, \xi_{N-1}) \\ \Delta\mathbf{F}_1(\xi_1, \xi_0) \\ \vdots \\ \Delta\mathbf{F}_{N-1}(\xi_{N-1}, \xi_{N-2}) \end{bmatrix} = \mathbf{0}. \tag{3.84}$$

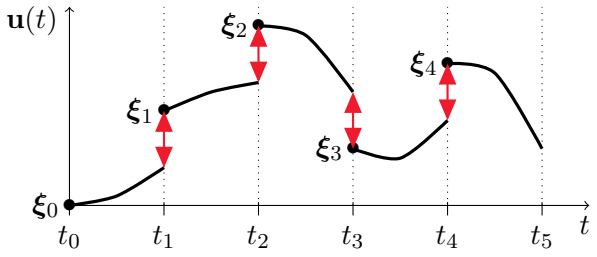

Figure 3.2: Jumps arising at the synchronization points t_n within the multiple shooting method.

Introducing the notation

$$\mathbf{G}_{j-1} = \frac{\partial}{\partial \boldsymbol{\xi}_{j-1}} \mathcal{F}(t_j, t_{j-1}, \boldsymbol{\xi}_{j-1}), \quad j = 1, \dots, N, \tag{3.85}$$

we define the Jacobian matrix of $\mathbf{F}$ through

$$\mathbf{J}_{\mathbf{F}}(\mathbf{x}) = \begin{bmatrix} \mathbf{A} & & & \mathbf{B}\mathbf{G}_{N-1} \\ \mathbf{G}_0 & -\mathbf{I} & & \\ & \ddots & \ddots & \\ & & \mathbf{G}_{N-2} & -\mathbf{I} \end{bmatrix} \tag{3.86}$$

with the identity matrix $\mathbf{I} \in \mathbb{R}^{N_\mathrm{d} \times N_\mathrm{d}}$. Equation (3.84) can then be solved using the standard Newton iteration (3.56) with the Jacobian matrix (3.86), i.e.,

$$\mathbf{A}\boldsymbol{\xi}_0^{(k+1)} = -\mathbf{B}\mathcal{F}\big(T_N, T_{N-1}, \boldsymbol{\xi}_{N-1}^{(k)}\big) - \mathbf{B}\frac{\partial \mathcal{F}\big(T_N, T_{N-1}, \boldsymbol{\xi}_{N-1}^{(k)}\big)}{\partial \boldsymbol{\xi}_{N-1}} \Big[\boldsymbol{\xi}_{N-1}^{(k+1)} - \boldsymbol{\xi}_{N-1}^{(k)}\Big] + \mathbf{c}, \tag{3.87}$$

$$\boldsymbol{\xi}_n^{(k+1)} = \mathcal{F}\big(T_n, T_{n-1}, \boldsymbol{\xi}_{n-1}^{(k)}\big) + \frac{\partial \mathcal{F}\big(T_n, T_{n-1}, \boldsymbol{\xi}_{n-1}^{(k)}\big)}{\partial \boldsymbol{\xi}_{n-1}} \Big[\boldsymbol{\xi}_{n-1}^{(k+1)} - \boldsymbol{\xi}_{n-1}^{(k)}\Big], \quad n = 1, \dots, N-1. \tag{3.88}$$

We point out the large size $(N_\mathrm{d}N \times N_\mathrm{d}N)$ and the block structure of the matrix in (3.86). One way to solve a linear system with such a matrix is the *block Gaussian elimination* or the *condensing approach* [31, Section 8.3], where a system with a "condensed" matrix

$$\mathbf{E}(\mathbf{x}) = \mathbf{A} + \mathbf{B}\mathbf{G}_{N-1} \dots \mathbf{G}_0 \in \mathbb{R}^{N_\mathrm{d} \times N_\mathrm{d}}$$

is solved, thereby reducing the size of the system. The disadvantage of this method is the need of multiplication and storage of N matrices of the size $N_\mathrm{d} \times N_\mathrm{d}$, which might have a high computational cost.

Remark 3.18. *We note that the BC* (3.73) *with the setting*

$$\mathbf{A} = -\mathbf{I}, \quad \mathbf{B} = \mathbf{I}, \quad \mathbf{c} = \mathbf{0} \tag{3.89}$$

becomes the TP condition (3.35)*. Solution of the TP problem is demonstrated in detail for the semi-discrete eddy current equation* (3.30) *in the following subsection.*

Besides, the multiple shooting method can be also applied to the solution of an IVP with a prescribed IC (3.34) *through the setting*

$$\mathbf{A} = \mathbf{I}, \quad \mathbf{B} = \mathbf{0}, \quad \mathbf{c} = \mathbf{u}_0 \tag{3.90}$$

in the BC (3.73)*. In contrast to the BVP, where all the discrete values $\boldsymbol{\xi}_j$, $j = 0, \dots, N-1$ are interconnected, in case of an IVP only the two neighboring values $\boldsymbol{\xi}_{j-1}$ and $\boldsymbol{\xi}_j$, $j = 1, \dots, N-1$ are coupled. Therefore, there is no coupled block system arising when dealing with IVPs.*

Application to the TP eddy current problem

Consider the system (3.30) complemented with the TP condition (3.35). Setting (3.89) in (3.83) we obtain

$$\mathbf{r}(\boldsymbol{\xi}_0, \boldsymbol{\xi}_{N-1}) = -\boldsymbol{\xi}_0 + \mathcal{F}(t_N, t_{N-1}, \boldsymbol{\xi}_{N-1}) = \mathbf{0}. \tag{3.91}$$

Let the system (3.30) be solved on the interval $(t_{n-1}, t_n]$ by the IE method, i.e., $\mathbf{u}_n = \mathcal{F}(t_n, t_{n-1}, \mathbf{u}_{n-1})$ is obtained from the equation (3.53) for $n = 1, \dots, N$. The derivative (3.85) can then be expressed using the *implicit function theorem* as

$$\mathbf{G}_{j-1} = \Big[\mathbf{C} + \mathbf{K}_{\nu,\mathrm{d}}\big(\mathcal{F}(t_j, t_{j-1}, \boldsymbol{\xi}_{j-1})\big)\Big]^{-1}\mathbf{C}, \quad j = 1, \dots, N, \tag{3.92}$$

where $\mathbf{C} = (1/\Delta T)\mathbf{M}_\sigma$ and $\mathbf{K}_{\nu,\mathrm{d}}(\mathbf{x})$ is given in (3.62). Using the continuity conditions (3.82) and the BC (3.91), we have

$$\mathbf{G}_{j-1} = \begin{cases} \big[\mathbf{C} + \mathbf{K}_{\nu,\mathrm{d}}(\boldsymbol{\xi}_j)\big]^{-1}\mathbf{C}, & j = 1, \dots, N-1, \\ \big[\mathbf{C} + \mathbf{K}_{\nu,\mathrm{d}}(\boldsymbol{\xi}_0)\big]^{-1}\mathbf{C}, & j = N. \end{cases} \tag{3.93}$$

Finally, denoting $\mathbf{Q}_\mathrm{d}(\boldsymbol{\xi}_j) = \mathbf{C} + \mathbf{K}_{\nu,\mathrm{d}}(\boldsymbol{\xi}_j)$ for $j = 0, \dots, N-1$ and applying the multiple shooting method, we obtain the linear TP block system

$$\begin{bmatrix} \mathbf{Q}_\mathrm{d}(\boldsymbol{\xi}_0^{(k)}) & & & -\mathbf{C} \\ -\mathbf{C} & \mathbf{Q}_\mathrm{d}(\boldsymbol{\xi}_1^{(k)}) & & \\ & \ddots & \ddots & \\ & & -\mathbf{C} & \mathbf{Q}_\mathrm{d}(\boldsymbol{\xi}_{N-1}^{(k)}) \end{bmatrix} \begin{bmatrix} \Delta\boldsymbol{\xi}_0^{(k)} \\ \Delta\boldsymbol{\xi}_1^{(k)} \\ \vdots \\ \Delta\boldsymbol{\xi}_{N-1}^{(k)} \end{bmatrix} = \begin{bmatrix} \mathbf{Q}_\mathrm{d}(\boldsymbol{\xi}_0^{(k)})\Big[\mathcal{F}(t_N, t_{N-1}, \boldsymbol{\xi}_{N-1}^{(k)}) - \boldsymbol{\xi}_0^{(k)}\Big] \\ \mathbf{Q}_\mathrm{d}(\boldsymbol{\xi}_1^{(k)})\Big[\mathcal{F}(t_1, t_0, \boldsymbol{\xi}_0^{(k)}) - \boldsymbol{\xi}_1^{(k)}\Big] \\ \vdots \\ \mathbf{Q}_\mathrm{d}(\boldsymbol{\xi}_{N-1}^{(k)})\Big[\mathcal{F}(t_{N-1}, t_{N-2}, \boldsymbol{\xi}_{N-2}^{(k)}) - \boldsymbol{\xi}_{N-1}^{(k)}\Big] \end{bmatrix} \tag{3.94}$$

with $\Delta\boldsymbol{\xi}_j^{(k)} = \boldsymbol{\xi}_j^{(k+1)} - \boldsymbol{\xi}_j^{(k)}$, $j = 0, \dots, N-1$, at Newton iteration k. In practice, the iteration (3.94) is stopped once the jumps $\Delta\mathbf{F}(\boldsymbol{\xi}_j, \boldsymbol{\xi}_{j-1})$ at the synchronization points t_j, $j = 1, \dots, N-1$, defined in (3.82), as well as the periodicity jump $\mathbf{r}(\boldsymbol{\xi}_0, \boldsymbol{\xi}_{N-1})$ from (3.91) vanish up to a prescribed tolerance.

Equivalently to the multiple shooting iteration (3.94), the TP problem (3.30), (3.35) can be solved by first constructing the nonlinear TP block system

$$\begin{bmatrix} \mathbf{Q}(\mathbf{u}_0) & & & -\mathbf{C} \\ -\mathbf{C} & \mathbf{Q}(\mathbf{u}_1) & & \\ & \ddots & \ddots & \\ & & -\mathbf{C} & \mathbf{Q}(\mathbf{u}_{N-1}) \end{bmatrix} \begin{bmatrix} \mathbf{u}_0 \\ \mathbf{u}_1 \\ \vdots \\ \mathbf{u}_{N-1} \end{bmatrix} = \begin{bmatrix} \mathbf{f}_N \\ \mathbf{f}_1 \\ \vdots \\ \mathbf{f}_{N-1} \end{bmatrix} \tag{3.95}$$

with $\mathbf{Q}(\mathbf{u}_n) = \mathbf{C} + \mathbf{K}_\nu(\mathbf{u}_n)$ for $n = 0, \dots, N-1$ coming from the IE discretization, followed by the Newton linearization of (3.95). This approach is known in the engineering literature as TP-FEM [67], as it stems from the direct TP (fine) discretization using the FEM matrices from (3.30).

Analogously, in case of the TR (3.54) we have a nonlinear TP block system

$$\begin{bmatrix} \mathbf{Q}(\mathbf{u}_0) & & & -\mathbf{C}(\mathbf{u}_{N-1}) \\ -\mathbf{C}(\mathbf{u}_0) & \mathbf{Q}(\mathbf{u}_1) & & \\ & \ddots & \ddots & \\ & & -\mathbf{C}(\mathbf{u}_{N-2}) & \mathbf{Q}(\mathbf{u}_{N-1}) \end{bmatrix} \begin{bmatrix} \mathbf{u}_0 \\ \mathbf{u}_1 \\ \vdots \\ \mathbf{u}_{N-1} \end{bmatrix} = \begin{bmatrix} 0.5\big[\mathbf{f}_N + \mathbf{f}_{N-1}\big] \\ 0.5\big[\mathbf{f}_1 + \mathbf{f}_0\big] \\ \vdots \\ 0.5\big[\mathbf{f}_{N-1} + \mathbf{f}_{N-2}\big] \end{bmatrix} \tag{3.96}$$

where $\mathbf{C}(\mathbf{u}_n) = (1/\Delta T)\mathbf{M}_\sigma - 0.5\mathbf{K}_\nu(\mathbf{u}_n)$ and $\mathbf{Q}(\mathbf{u}_n) = \mathbf{C}(\mathbf{u}_n) + \mathbf{K}_\nu(\mathbf{u}_n)$ for $n = 0, \ldots, N-1$.

Note that in the linear case the matrices $\mathbf{C}$, $\mathbf{Q}$, and $\mathbf{Q}_\mathrm{d}$ in (3.94), (3.95) and (3.96) are constant. In the following Section 3.3.2 we discuss a diagonalization approach for linear block-cyclic systems, which is based on the transformation into the frequency domain.

3.3.2 Multi-harmonic (MH) diagonalization

In this section we describe an efficient solution approach for linear TP problems using the MH representation from Section 2.3.1. Let us assume that the TP system (3.95) is linear with respect to $\mathbf{u}$, i.e., it is given by

$$\underbrace{\begin{bmatrix} \mathbf{Q} & & & -\mathbf{C} \\ -\mathbf{C} & \mathbf{Q} & & \\ & \ddots & \ddots & \\ & & -\mathbf{C} & \mathbf{Q} \end{bmatrix}}_{=:\mathbf{G}} \underbrace{\begin{bmatrix} \mathbf{u}_0 \\ \mathbf{u}_1 \\ \vdots \\ \mathbf{u}_{N-1} \end{bmatrix}}_{=:\mathbf{u}_\mathrm{tot}} = \underbrace{\begin{bmatrix} \mathbf{f}_N \\ \mathbf{f}_1 \\ \vdots \\ \mathbf{f}_{N-1} \end{bmatrix}}_{=:\mathbf{f}_\mathrm{tot}} \tag{3.97}$$

with the constant matrices $\mathbf{C} = 1/\Delta T \cdot \mathbf{M}_\sigma$ and $\mathbf{Q} = \mathbf{C} + \mathbf{K}_\nu$. The system (3.97) has a possibly large size of $N_\mathrm{d}N$ and its system matrix is of a special block-cyclic structure, whose naive solution might have a large computational effort. To overcome this difficulty we apply the diagonalization approach introduced in [17].

According to [17], the system (3.97) can be transformed into an equivalent system in the frequency domain

$$\underbrace{\begin{bmatrix} \hat{\mathbf{G}}_0 & & & \\ & \hat{\mathbf{G}}_1 & & \\ & & \ddots & \\ & & & \hat{\mathbf{G}}_{N-1} \end{bmatrix}}_{=:\hat{\mathbf{G}}} \underbrace{\begin{bmatrix} \hat{\mathbf{u}}_0 \\ \hat{\mathbf{u}}_1 \\ \vdots \\ \hat{\mathbf{u}}_{N-1} \end{bmatrix}}_{=:\hat{\mathbf{u}}_\mathrm{tot}} = \underbrace{\begin{bmatrix} \hat{\mathbf{f}}_N \\ \hat{\mathbf{f}}_1 \\ \vdots \\ \hat{\mathbf{f}}_{N-1} \end{bmatrix}}_{=:\hat{\mathbf{f}}_\mathrm{tot}} \tag{3.98}$$

related to (3.97) through

$$\hat{\mathbf{G}} = (\mathbf{F} \otimes \mathbf{I})\mathbf{G}(\mathbf{F}^\mathrm{H} \otimes \mathbf{I}), \qquad \hat{\mathbf{u}}_\mathrm{tot} = (\mathbf{F} \otimes \mathbf{I})\mathbf{u}_\mathrm{tot}, \qquad \hat{\mathbf{f}}_\mathrm{tot} = (\mathbf{F} \otimes \mathbf{I})\mathbf{f}_\mathrm{tot}. \tag{3.99}$$

The matrix $\mathbf{F}$ is the DFT matrix, which is obtained from a *one-sided Fourier series*, and whose elements are

$$\mathbf{F}_{jn} = \frac{1}{\sqrt{N}} \exp(-\imath\omega_{j-1}t_{n-1}), \qquad j, n = 1, \ldots, N, \tag{3.100}$$

with the angular frequencies $\omega_j = 2\pi j/T$, $j = 0, \ldots, N-1$ and time points $t_n = n\Delta T$, $n = 0, \ldots, N-1$. The matrix $\mathbf{I}$ is the $(N_\mathrm{d} \times N_\mathrm{d})$-dimensional identity matrix, '$\otimes$' denotes the Kronecker product of two matrices, and $\mathbf{F}^\mathrm{H}$ is the Hermite conjugate matrix of $\mathbf{F}$. We have the representations

$$\hat{\mathbf{G}}_j = \mathbf{Q} - \mathbf{C}\exp(-\imath\omega_j\Delta T), \qquad \hat{\mathbf{u}}_j = \frac{1}{\sqrt{N}} \sum_{n=0}^{N-1} \mathbf{u}_n \exp(-\imath\omega_j t_n), \quad j = 0, \ldots, N-1, \tag{3.101}$$

$$\hat{\mathbf{f}}_N = \frac{1}{\sqrt{N}} \sum_{n=0}^{N-1} \mathbf{f}_n \exp(-\imath\omega_0 t_n), \qquad \hat{\mathbf{f}}_j = \frac{1}{\sqrt{N}} \sum_{n=0}^{N-1} \mathbf{f}_n \exp(-\imath\omega_j t_n), \quad j = 1, \ldots, N-1. \tag{3.102}$$

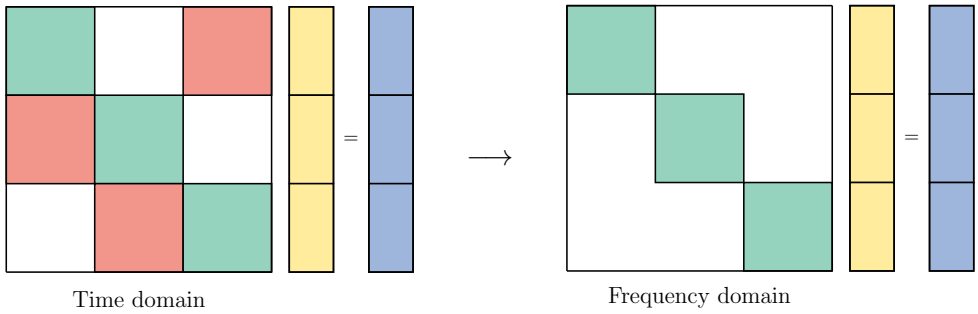

Figure 3.3: Sketch visualizing the transformation from the time domain into the frequency domain.

As we see the block-cyclic system (3.97) is now converted into a block-diagonal system (3.98), as it is sketched in Figure 3.3. Therefore, having the RHS $\hat{\mathbf{f}}_j$, $j = 1, \dots, N$ from (3.102), we can calculate the harmonic components $\hat{\mathbf{u}}_j$ separately by solving

$$\hat{\mathbf{G}}_0 \hat{\mathbf{u}}_0 = \hat{\mathbf{f}}_N, \qquad \hat{\mathbf{G}}_j \hat{\mathbf{u}}_j = \hat{\mathbf{f}}_j, \quad j = 1, \dots, N-1. \tag{3.103}$$

The solution of each N_d-dimensional linear system in (3.103) as well as the construction of the blocks $\hat{\mathbf{f}}_j$ can be performed in parallel. Finally, the solution in the time domain can be obtained by application of the inverse DFT to the calculated solution vector $\hat{\mathbf{u}}_\mathrm{tot}$, i.e.,

$$\mathbf{u}_\mathrm{tot} = (\mathbf{F}^\mathrm{H} \otimes \mathbf{I}) \hat{\mathbf{u}}_\mathrm{tot}, \qquad \mathbf{u}_n = \frac{1}{\sqrt{N}} \sum_{j=0}^{N-1} \hat{\mathbf{u}}_j \exp(\imath \omega_j t_n), \quad n = 0, \dots, N-1. \tag{3.104}$$

Note that the DFT and its inverse can be efficiently applied using the *fast Fourier transform (FFT)* algorithm [129], thereby further reducing the complexity of the transformation. The MH approach, applied to the standard TP discretization (3.97), allows for optimal scaling, i.e., N times speed up provided N parallel processing units are available.

Remark 3.19. *Note that when $\Delta T \to 0$, the diagonalization of the TP linear system* (3.97) *using the FT is equivalent to application of the HB method to the semi-discrete system* (3.30) *in case the matrix $\mathbf{K}_\nu$ is constant and the RHS $\mathbf{f}$ is periodic. In particular, the HB method with N frequencies reads*

$$\big[\imath \omega_j \mathbf{M}_\sigma + \mathbf{K}_\nu\big] \hat{\mathbf{u}}_j = \hat{\mathbf{f}}_j, \tag{3.105}$$

where $\omega_j = 2\pi j / T$ and $j = 0, \dots, N-1$. For the matrices $\hat{\mathbf{G}}_j$ given in (3.101) *we have*

$$\lim_{\Delta T \to 0} \hat{\mathbf{G}}_j = \lim_{\Delta T \to 0} \Big[\mathbf{M}_\sigma \big(1 - \exp(-\imath \omega_j \Delta T)\big) / \Delta T + \mathbf{K}_\nu\Big] = \imath \omega_j \mathbf{M}_\sigma + \mathbf{K}_\nu.$$

Therefore, provided $\mathbf{f}_N = \mathbf{f}_0$ the system matrices in (3.103) *head to the system matrices in* (3.105) *for all $j = 0, \dots, N-1$ as $\Delta T \to 0$.*

3.3.3 Time-periodic problems with unknown period

We now consider TP problems where the period T is not given in the problem setting. This can happen when searching for periodic orbits of autonomous systems of ODEs (see Section 2.2.2). Consider a TP problem

for a system of autonomous ODEs with the unknown function $\mathbf{u}\colon [0,T] \to \mathbb{R}^{N_\mathrm{d}}$, the UP $T > 0$, and the RHS $\mathbf{f}\colon \mathbb{R}^{N_\mathrm{d}} \to \mathbb{R}^{N_\mathrm{d}}$, given by

$$\mathbf{u}'(t) = \mathbf{f}(\mathbf{u}(t)), \quad t \in (0,T), \tag{3.106}$$

$$\mathbf{u}(T) = \mathbf{u}(0). \tag{3.107}$$

Based on [30, Section 7.3], we apply the shooting methods, presented in Section 3.3.1, to (3.106)-(3.107).

Single shooting method with UP

Similarly to (3.77), we use the operator $\mathcal{F}$, which solves the IVP (3.74)-(3.75), and obtain the TP condition

$$\mathbf{r}(\boldsymbol{\xi}, T) = \mathcal{F}(T, 0, \boldsymbol{\xi}) - \boldsymbol{\xi} = 0. \tag{3.108}$$

The Jacobian matrix of $\mathbf{r}$ reads

$$\mathbf{J}_\mathbf{r}(\boldsymbol{\xi}, T) = \left[\frac{\partial}{\partial \boldsymbol{\xi}}\mathcal{F}(T,0,\boldsymbol{\xi}) - \mathbf{I} \quad \frac{\partial}{\partial T}\mathcal{F}(T,0,\boldsymbol{\xi})\right] = \left[\frac{\partial}{\partial \boldsymbol{\xi}}\mathcal{F}(T,0,\boldsymbol{\xi}) - \mathbf{I} \quad \mathbf{f}(\boldsymbol{\xi})\right], \tag{3.109}$$

since integrating (3.106) and using (3.108), we have

$$\frac{\partial}{\partial T}\mathcal{F}(T,0,\boldsymbol{\xi}) = \frac{\partial}{\partial T}\left(\boldsymbol{\xi} + \int_0^T \mathbf{f}(\mathbf{u}(t))\mathrm{d}t\right) = \mathbf{f}\big(\mathcal{F}(T,0,\boldsymbol{\xi})\big) = \mathbf{f}(\boldsymbol{\xi}).$$

Note that the Jacobian matrix $\mathbf{J}_\mathbf{r}(\boldsymbol{\xi}, T) \in \mathbb{R}^{N_\mathrm{d} \times (N_\mathrm{d}+1)}$ in (3.109) is not quadratic in contrast to the matrix $\mathbf{J}_\mathbf{r}(\boldsymbol{\xi}) \in \mathbb{R}^{N_\mathrm{d} \times N_\mathrm{d}}$ in (3.78). For this reason, the ordinary Newton method with the Jacobian inversion cannot be applied. Instead, *the Gauss-Newton method* [30, Chapter 4] can be used. In particular, denoting $\mathbf{x} = [\boldsymbol{\xi}^\top, T]^\top \in \mathbb{R}^{N_\mathrm{d}}$ we have for a given $\mathbf{x}^{(0)}$ and $k = 0, 1, \ldots$ the Gauss-Newton iteration

$$\Delta\mathbf{x}^{(k)} = -\mathbf{J}_\mathbf{r}^+(\mathbf{x}^{(k)})\mathbf{r}(\mathbf{x}^{(k)}), \quad \mathbf{x}^{(k+1)} = \mathbf{x}^{(k)} + \Delta\mathbf{x}^{(k)}, \tag{3.110}$$

where $\mathbf{J}_\mathbf{r}^+(\mathbf{x})$ denotes *the Moore-Penrose pseudoinverse* matrix [124, Section 4.8.5] of the matrix $\mathbf{J}_\mathbf{r}(\mathbf{x}) = \mathbf{J}_\mathbf{r}(\boldsymbol{\xi}, T)$ from (3.109) and has a full column rank [30, Section 7.3.1].

Multiple shooting method with UP

The multiple shooting method is based on the partition of the considered time interval $[t_0, t_N] = [0, T]$, solution of the corresponding IVPs on each subinterval $(t_{n-1}, t_n]$, and iterative reduction of the jumps at the synchronization points t_n, $n = 1, \ldots, N-1$. In case the upper boundary (or the period) T is an additional unknown, its value might change within the iteration, which would urge the need to introduce a new partition and to approximate in some way the solution at the updated synchronization points. In order to avoid these complications we introduce, following [30, Section 7.3], the dimensionless variable τ through scaling the time variable $t \in [0, T]$ by the UP T, i.e.,

$$\tau = \tau(t) = t/T \in [0, 1].$$

The problem (3.106)-(3.107) is then equivalent to

$$\tilde{\mathbf{u}}'(\tau) = T\mathbf{f}(\tilde{\mathbf{u}}(\tau)), \quad \tau \in (0,1), \tag{3.111}$$

$$\tilde{\mathbf{u}}(1) = \tilde{\mathbf{u}}(0). \tag{3.112}$$

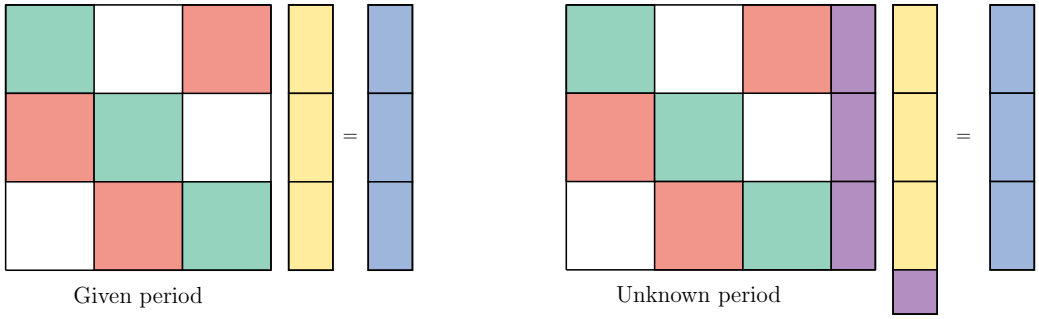

Figure 3.4: Sketch comparing time-periodic systems with a given and with an unknown period.

Consider the equidistant partition $0 = \tau_0 < \tau_1 < \ldots < \tau_N = 1$ of the unit interval $[0, 1]$, where $\tau_n = n\Delta\tau$, $n = 0, \ldots, N$. Note that $\tau_n = t_n/T$ for t_n given in (3.43). Let $\mathcal{F}(\tau, \tau_{n-1}, \tilde{\boldsymbol{\xi}}_{n-1}, T)$ denote the solution to the IVP

$$\tilde{\mathbf{u}}'(\tau) = T\mathbf{f}(\tilde{\mathbf{u}}(\tau)), \quad \tau \in (\tau_{n-1}, \tau_n], \tag{3.113}$$

$$\tilde{\mathbf{u}}(\tau_{n-1}) = \tilde{\boldsymbol{\xi}}_{n-1}, \tag{3.114}$$

for $n = 1, \ldots, N$. We then impose the TP and the continuity conditions

$$\mathbf{F}(\mathbf{x}) = \begin{cases} \mathcal{F}(\tau_N, \tau_{N-1}, \tilde{\boldsymbol{\xi}}_{N-1}, T) - \boldsymbol{\xi}_0 = \mathbf{0}, \\ \mathcal{F}(\tau_j, \tau_{j-1}, \tilde{\boldsymbol{\xi}}_{j-1}, T) - \tilde{\boldsymbol{\xi}}_j = \mathbf{0}, \quad j = 1, \ldots, N-1 \end{cases} \tag{3.115}$$

where $\mathbf{x} = \left[\tilde{\boldsymbol{\xi}}_0^\top, \ldots, \tilde{\boldsymbol{\xi}}_{N-1}^\top, T\right]^\top \in \mathbb{R}^{N_\mathrm{d}N+1}$. With the notation

$$\mathbf{G}_{j-1} = \frac{\partial}{\partial \boldsymbol{\xi}_{j-1}} \mathcal{F}(\tau_j, \tau_{j-1}, \tilde{\boldsymbol{\xi}}_{j-1}, T), \qquad \mathbf{g}_{j-1} = \frac{\partial}{\partial T} \mathcal{F}(\tau_j, \tau_{j-1}, \tilde{\boldsymbol{\xi}}_{j-1}, T), \tag{3.116}$$

for $j = 1, \ldots, N$, the Jacobian matrix of $\mathbf{F}(\mathbf{x})$ is given by

$$\mathbf{J}_\mathbf{F}(\mathbf{x}) = \begin{bmatrix} -\mathbf{I} & & & \mathbf{G}_{N-1} & \mathbf{g}_{N-1} \\ \mathbf{G}_0 & -\mathbf{I} & & & \mathbf{g}_0 \\ & \ddots & \ddots & & \vdots \\ & & \mathbf{G}_{N-2} & -\mathbf{I} & \mathbf{g}_{N-2} \end{bmatrix} \tag{3.117}$$

with the identity matrix $\mathbf{I} \in \mathbb{R}^{N_\mathrm{d} \times N_\mathrm{d}}$ and

$$\mathbf{g}_{j-1} = \frac{\partial}{\partial T}\left(\tilde{\boldsymbol{\xi}}_{j-1} + \int_{\tau_{j-1}}^{\tau_j} T\mathbf{f}(\tilde{\mathbf{u}}(\tau))\mathrm{d}\tau\right) = \int_{\tau_{j-1}}^{\tau_j} \mathbf{f}\big(\tilde{\mathbf{u}}(\tau)\big)\mathrm{d}\tau \approx \Delta\tau\mathbf{f}\big(\mathcal{F}(\tau_j, \tau_{j-1}, \tilde{\boldsymbol{\xi}}_{j-1}, T)\big) = \Delta\tau\mathbf{f}(\tilde{\boldsymbol{\xi}}_j). \tag{3.118}$$

As in the case of (3.109), the Jacobian matrix $\mathbf{J}_\mathbf{F}(\mathbf{x})$ has one row less than columns. Hence, to find a root of $\mathbf{F}(\mathbf{x})$ we again apply the Gauss-Newton method, where the Moore-Penrose pseudoinverse $\mathbf{J}_\mathbf{F}^+(\mathbf{x})$ has to be calculated. Comparison of the underlying system with the given and the unknown period T is visualized in Figure 3.4.

Similarly to the multiple shooting method for problems with a given boundary T, the Gauss-Newton system with the Jacobian matrix from (3.117) can be solved using Gaussian elimination [30, Section 7.3.1]. In particular, a system with a "condensed" matrix

$$\mathbf{E}(\mathbf{x}) = \begin{bmatrix} \mathbf{G}_{N-1} \dots \mathbf{G}_0 - \mathbf{I} & \mathbf{g} \end{bmatrix} \in \mathbb{R}^{N_\mathrm{d} \times (N_\mathrm{d}+1)}$$

where $\mathbf{g} = \mathbf{g}_{N-1} + \mathbf{G}_{N-1}\mathbf{g}_{N-2} + \ldots + \mathbf{G}_{N-1} \dots \mathbf{G}_1 \mathbf{g}_0$, is solved. This is then as in the case of the single shooting method, applied to the TP problem with unknown period, described above.

3.4 Conclusion

This chapter provided theoretical fundamentals for the numerical solution of initial-value and boundary-value problems in time. First, existence and uniqueness results were stated in the corresponding Sobolev spaces. The spatial discretization was then performed using the finite element method, while the time discretization used one-step implicit time integrators. Shooting methods were applied for the solution of timelike boundary-value problems such as time-periodic problems. A multi-harmonic representation was used for the diagonalization of block-cyclic systems, stemming from the time-periodic discretization. Finally, the solution of periodic problems with an unknown period was described based on the multiple shooting method. The following chapter deals with the parallel-in-time solution of initial-value and time-periodic problems (with unknown period).

4 Parallel-in-time time integration

A recent overview of the existing PinT approaches and their development can be found in [45]. There, time-parallel methods are classified into four groups: methods based on multiple shooting [97], methods based on domain decomposition and waveform relaxation [86], space-time multigrid methods [63], and direct time-parallel methods [135]. In this chapter we focus on the first group, in particular, on the Parareal algorithm [88].

Parareal is an arguably most well-known PinT method, which accelerates the time integration using two propagators: the fine one and the coarse one. The fine solution is very accurate and therefore expensive to calculate. However, the fine solver can be applied in parallel, thereby exploiting the available computing capacity. In contrast to this, the coarse solver gives a rough solution, which has to be calculated sequentially. Nevertheless, the coarse solution requires a low computational effort, as it is typically quite cheap, e.g., due to low resolution. Apart from the parallelization potential, another important property of Parareal is its non-intrusiveness. It means that possibly existing black-box solvers can be used and integrated easily into the Parareal framework as the fine and the coarse propagators. This is particularly relevant for many engineering applications.

The convergence analysis of the Parareal algorithm for nonlinear problems was performed in [48], where it was shown that the method always converges to the fine solution in a finite number of iterations. As this theory was valid only for problems with smooth RHSs, we proposed in [51] a multirate Parareal method, applicable for problems with discontinuous excitations such as PWM signals described in Section 2.3. The idea of the approach is to use a smooth surrogate of the discontinuous input on the coarse level, while the original input is maintained on the fine level. We proved convergence and derived estimates, which implied a possible reduction of the convergence order due to the introduction of the surrogate coarse model. In [103] we proposed another version of the Parareal method for problems with PWM inputs, which uses the MPDE approach (see Section 2.3.3).

TP problems can also be solved using two Parareal-based approaches, proposed in [50], i.e., *periodic Parareal with initial-value coarse problem* (PP-IC) and *periodic Parareal with periodic coarse problem* (PP-PC). For systems with PWM inputs, we introduced a natural extension of the multirate Parareal to TP problems, namely the multirate PP-IC method, in [52]. Since a TP block system arises on the coarse level within PP-PC, the diagonalization approach from the Section 3.3.2 can be applied in the linear case [81]. We extended the method to nonlinear problems using the simplified Newton method in [82]. Similar approaches, where the coarse grid correction was parallelized due to diagonalization, were derived in [49, 137]. Such parallel methods are nowadays classified as a family of ParaDIAG methods [53]. Finally, TP problems with unknown period (see Section 3.3.3) can be solved using a PP-PC-based approach according to [83].

4.1 Initial-value problems: Parareal method

Consider an IVP for a system of ODEs with the unknown $\mathbf{u}(t) \in \mathbb{R}^d$ and the RHS $\mathbf{f}\colon \mathbb{R}^d \times [0,T] \to \mathbb{R}^d$, where $T > 0$ and $d \geq 1$, such that

$$\mathbf{u}'(t) = \mathbf{f}(\mathbf{u}(t), t), \quad t \in (0,T], \tag{4.1}$$
$$\mathbf{u}(0) = \mathbf{u}_0. \tag{4.2}$$

Introducing a partition of the time interval $[0,T]$

$$0 =: T_0 < T_1 < \ldots < T_N := T \tag{4.3}$$

and the ICs $\mathbf{U}_{n-1}$ at T_{n-1}, we consider N IVPs

$$\mathbf{u}_n'(t) = \mathbf{f}(\mathbf{u}_n(t), t), \quad t \in (T_{n-1}, T_n], \tag{4.4}$$
$$\mathbf{u}_n(T_{n-1}) = \mathbf{U}_{n-1}, \tag{4.5}$$

for $n = 1, \ldots, N$. Due to the Remark 3.18, the IVP (4.1)-(4.2) can be solved using the multiple shooting method (3.87)-(3.88) through the setting (3.90), i.e., for $k = 0, 1, \ldots$

$$\mathbf{U}_0^{(k+1)} = \mathbf{u}_0, \tag{4.6}$$
$$\mathbf{U}_n^{(k+1)} = \mathcal{F}\big(T_n, T_{n-1}, \mathbf{U}_{n-1}^{(k)}\big) + \frac{\partial \mathcal{F}\big(T_n, T_{n-1}, \mathbf{U}_{n-1}^{(k)}\big)}{\partial \mathbf{U}_{n-1}} \Big[\mathbf{U}_{n-1}^{(k+1)} - \mathbf{U}_{n-1}^{(k)}\Big], \quad n = 1, \ldots, N, \tag{4.7}$$

where we have included also the solution $\mathbf{U}_N^{(k+1)}$ at the end point T_N. Here $\mathcal{F}$ is the *fine propagator*, which solves the IVP (4.4)-(4.5) and delivers a very accurate and thus quite expensive solution. It is typically obtained using a time-stepping scheme with a small step size $\delta T > 0$.

The Parareal algorithm can be derived from the multiple shooting iteration (4.6)-(4.7) using a finite-difference-based approximation of the derivative [44]

$$\frac{\partial \mathcal{F}\big(T_n, T_{n-1}, \mathbf{U}_{n-1}^{(k)}\big)}{\partial \mathbf{U}_{n-1}} \Big[\mathbf{U}_{n-1}^{(k+1)} - \mathbf{U}_{n-1}^{(k)}\Big] \approx \mathcal{G}\big(T_n, T_{n-1}, \mathbf{U}_{n-1}^{(k+1)}\big) - \mathcal{G}\big(T_n, T_{n-1}, \mathbf{U}_{n-1}^{(k)}\big), \tag{4.8}$$

for $n = 1, \ldots, N$. Here $\mathcal{G}$ is another solution operator applied to the IVP (4.4)-(4.5), which is less accurate and thus computationally cheaper than $\mathcal{F}$. It is called the *coarse propagator* and can, e.g., be the same time-integration scheme as $\mathcal{F}$, but use a larger step size $\Delta T \gg \delta T$. Inserting the approximation (4.8) into (4.7) yields the Parareal iteration: for $k = 0, 1, \ldots$

$$\mathbf{U}_0^{(k+1)} = \mathbf{u}_0, \tag{4.9}$$
$$\mathbf{U}_n^{(k+1)} = \mathcal{F}\big(T_n, T_{n-1}, \mathbf{U}_{n-1}^{(k)}\big) + \mathcal{G}\big(T_n, T_{n-1}, \mathbf{U}_{n-1}^{(k+1)}\big) - \mathcal{G}\big(T_n, T_{n-1}, \mathbf{U}_{n-1}^{(k)}\big), \quad n = 1, \ldots, N. \tag{4.10}$$

The initial approximations $\mathbf{U}_n^{(0)}$ can be obtained, e.g., by applying the coarse solver sequentially starting from $\mathbf{U}_0^{(0)} = \mathbf{u}_0$, i.e.,

$$\mathbf{U}_n^{(0)} = \mathcal{G}\big(T_n, T_{n-1}, \mathbf{U}_{n-1}^{(0)}\big), \quad n = 1, \ldots, N. \tag{4.11}$$

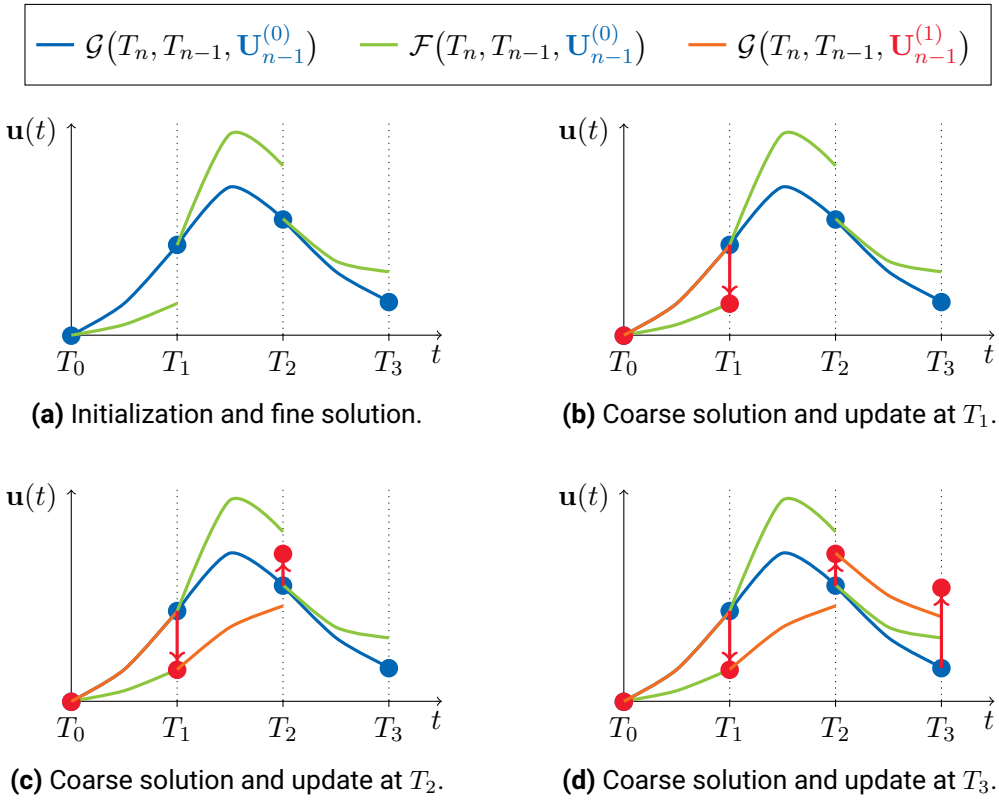

(a) Initialization and fine solution.

(b) Coarse solution and update at T_1.

(c) Coarse solution and update at T_2.

(d) Coarse solution and update at T_3.

Figure 4.1: Visualization of the Parareal algorithm for $N = 3$ and $k = 0$.

We note from (4.10) that at iteration $k+1$ the fine solution $\mathcal{F}(T_n, T_{n-1}, \mathbf{U}_{n-1}^{(k)})$ depends only on the solution at the previous iteration k. This allows to apply the fine propagator on each subinterval in parallel, thereby reducing the computational cost. On the other hand, the coarse solution $\mathcal{G}(T_n, T_{n-1}, \mathbf{U}_{n-1}^{(k+1)})$ depends on the solution at the same iteration $k+1$ and therefore has to be calculated sequentially. However, as the coarse propagator is cheaper to apply, this shall not affect the computational effort significantly.

One iteration of the Parareal algorithm (4.9)-(4.10) for $N = 4$ is visualized in Figure 4.1. At first, the values $\mathbf{U}_n^{(0)}$, $n = 1, \dots, N$ are initialized via (4.11) and the fine solution is calculated in parallel (see Figure 4.1a). The update (4.10) is performed at each synchronization point T_n, $n = 1, \dots, N$ (see Figure 4.1b-4.1d), once the coarse solutions are calculated sequentially. We note that after the first update the very accurate (fine) solution is obtained on the first subinterval $[T_0, T_1]$. This is due to the special property of the Parareal method, which we describe by the convergence result based on [48] in the following theorem.

Theorem 4.1 (Convergence of the Parareal method [48])**.** *Let RHS* $\mathbf{f}$ *in* (4.1) *be sufficiently smooth and let the partition* (4.3) *of the interval* $[0, T]$ *be equidistant with the step size* $\Delta T = T/N$*. We additionally assume:*

- $\mathcal{F}(T_n, T_{n-1}, \mathbf{U}_{n-1})$ *and* $\mathcal{G}(T_n, T_{n-1}, \mathbf{U}_{n-1})$ *are the exact and an approximate solutions to the IVP* (4.4)-(4.5) *at* T_n*, respectively.*
- *The LTE is bounded by* $C_3 \Delta T^{p+1}$ *with* $p \geq 1$ *and can be expanded for small step size* ΔT *and an initial value* $\mathbf{U}$ *as*

$$\mathcal{F}(T_n, T_{n-1}, \mathbf{U}) - \mathcal{G}(T_n, T_{n-1}, \mathbf{U}) = c_{p+1}(\mathbf{U})\Delta T^{p+1} + c_{p+2}(\mathbf{U})\Delta T^{p+2} + \dots, \tag{4.12}$$

where functions c_i, $i = p+1, p+2, \dots$, *are continuously differentiable.*

- *$\mathcal{G}$ satisfies the Lipschitz condition*

$$\|\mathcal{G}\big(t+\Delta T,\, t, \mathbf{U}\big) - \mathcal{G}\big(t+\Delta T,\, t, \mathbf{V}\big)\| \leq (1 + C_2 \Delta T)\|\mathbf{U} - \mathbf{V}\|, \tag{4.13}$$

for $t \in [0, T]$, for all $\mathbf{U}, \mathbf{V}$, and a constant C_2.

Then at the Parareal iteration $k = 0, 1, \ldots$ (4.9)-(4.10) we have for a constant $C_1 > 0$ the error bound

$$\big\|\mathbf{u}(T_n) - \mathbf{U}_n^{(k)}\big\| \leq C_1^k C_3 \left(\Delta T^{p+1}\right)^{k+1} \frac{(1 + C_2 \Delta T)^{n-k-1}}{(k+1)!} \prod_{j=0}^{k} (n - j). \tag{4.14}$$

We see from the estimate (4.14) that the error of the Parareal method at T_n vanishes at iteration $k = n$ for $n = 1, \ldots, N$ due to the product on the RHS in (4.14). It means that at the Parareal iteration k, the exact solution is obtained on all the subintervals $[T_{n-1}, T_n]$ for $n \leq k$. We point out that application of n Parareal iterations requires the same computational time as the standard sequential time stepping on $[0, T_n]$, when neglecting the time for the coarse solutions. In practice it can be expected that the method reaches a required tolerance earlier in order to obtain a maximal possible speed up through the parallelization of the fine solutions.

As the termination criterion of the Parareal method we consider the maximum among the jumps at the synchronization points T_n, $n = 1, \ldots, N-1$, and define the error at iteration k by [82]

$$\varepsilon_{\mathrm{PR},\times}^{(k)} = \max_{1 \leq n \leq N-1} \big\|\mathbf{U}_n^{(k)} - \mathcal{F}\big(T_n, T_{n-1}, \mathbf{U}_{n-1}^{(k)}\big)\big\|_{\times}, \tag{4.15}$$

with $\|\cdot\|_{\times}$ being a norm in a d-dimensional real space. The Parareal iteration (4.9)-(4.10) is considered to have converged up to a prescribed tolerance $\varepsilon_{\mathrm{tol}}$ when the error $\varepsilon_{\mathrm{PR},\times}^{(k)}$ becomes smaller than $\varepsilon_{\mathrm{tol}}$.

4.2 Two Parareal variants for time-periodic problems: PP-IC and PP-PC

Consider a TP for a system of ODEs with the unknown $\mathbf{u}(t) \in \mathbb{R}^d$ and the RHS $\mathbf{f} \colon \mathbb{R}^d \times [0, T] \to \mathbb{R}^d$, where $T > 0$ and $d \geq 1$, such that

$$\mathbf{u}'(t) = \mathbf{f}(\mathbf{u}(t), t), \quad t \in (0, T), \tag{4.16}$$

$$\mathbf{u}(0) = \mathbf{u}(T). \tag{4.17}$$

Based on the Parareal method for IVPs, two PinT algorithms for TP problems were proposed in [50], namely PP-IC and PP-PC. The first approach, PP-IC, is a natural extension of Parareal to TP problems obtained via introduction of a relaxed TP condition. As Parareal, PP-IC is non-intrusive and is given by the iteration: for $k = 0, 1, \ldots$

$$\mathbf{U}_0^{(k+1)} = \mathbf{U}_N^{(k)}, \tag{4.18}$$

$$\mathbf{U}_n^{(k+1)} = \mathcal{F}\big(T_n, T_{n-1}, \mathbf{U}_{n-1}^{(k)}\big) + \mathcal{G}\big(T_n, T_{n-1}, \mathbf{U}_{n-1}^{(k+1)}\big) - \mathcal{G}\big(T_n, T_{n-1}, \mathbf{U}_{n-1}^{(k)}\big), \quad n = 1, \ldots, N. \tag{4.19}$$

We see that the only difference between PP-IC and Parareal is the update of the IC $\mathbf{U}_0^{(k+1)}$ in (4.18) with the end value from the previous iteration, while the IC remains fixed in (4.9). Since PP-IC imposes a relaxed

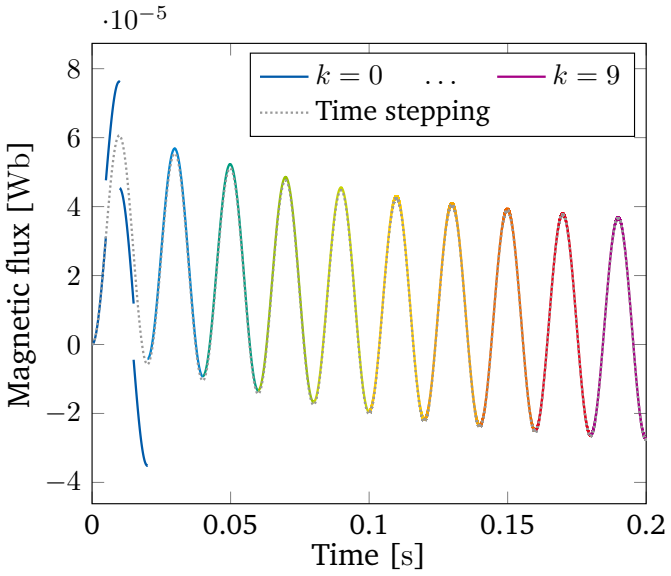

Figure 4.2: Fine solution at the PP-IC iteration k, visualized on each time interval $[T_0 + kT,\ T_0 + (k+1)T]$ with $k = 0, \ldots, 9$, $T_0 = 0\,\mathrm{s}$, and $T = 0.02\,\mathrm{s}$, and compared to the sequential time-stepping solution. Illustrated data is based on the solution of a linear RL-circuit model, excited with a $50\,\mathrm{Hz}$ AC source [11] ©2019 IEEE.

periodicity constraint one may expect a rather slow convergence to the periodic solution, especially when the underlying dynamical system possesses a very long settling time [50, 82].

According to [11], PP-IC can be interpreted as a "forward-in-time Parareal iteration", i.e., as a subsequent application of a single Parareal iteration on each period $[T_0 + kT, T_0 + (k+1)T]$ using initial guess $\mathbf{U}_N^{(k)}$, $k = 0, 1, 2, \ldots$, as illustrated in Figure 4.2 for $T_0 = 0\,\mathrm{s}$, $T = 0.02\,\mathrm{s}$, $N = 4$, and $k = 0, \ldots, 9$. It is visible that the fine solution on the first period $[0, T]$ contains jumps at the synchronization points T_n, $n = 1, \ldots, N-1$, as well as the periodicity jump between the solution at T_0 and at $T_N = T$. The discontinuities at the synchronization points decrease already after the next PP-IC update for $k = 1$ and the obtained solution nearly replicates the classical time-stepping solution on the second period $[T, 2T]$. However, as we see, the solution is still not periodic. The iterative procedure is thus continued until the periodicity jump becomes smaller than a prescribed tolerance $\varepsilon_{\mathrm{tol}}$.

The error at PP-IC iteration $k = 0, 1, \ldots$ is given by the maximum among the jumps at the synchronization points T_n, $n = 1, \ldots, N-1$, as in (4.15), and the periodicity jump of the solution at T_0 and T_N [82], i.e.,

$$\varepsilon_{\mathrm{IC},\times}^{(k)} = \max\Big\{\varepsilon_{\mathrm{PR},\times}^{(k)},\ \big\|\mathbf{U}_0^{(k)} - \mathcal{F}\big(T_N, T_{N-1}, \mathbf{U}_{N-1}^{(k)}\big)\big\|_\times\Big\}, \tag{4.20}$$

with $\|\cdot\|_\times$ as before being a norm in a d-dimensional space.

The second approach, PP-PC, is obtained by plugging (3.89) into the multiple shooting method (3.87)-(3.88) and applying the approximation (4.8), [50]. The PP-PC iteration reads: for $k = 0, 1, \ldots$

$$\mathbf{U}_0^{(k+1)} = \mathcal{F}\big(T_N, T_{N-1}, \mathbf{U}_{N-1}^{(k)}\big) + \mathcal{G}\big(T_N, T_{N-1}, \mathbf{U}_{N-1}^{(k+1)}\big) - \mathcal{G}\big(T_N, T_{N-1}, \mathbf{U}_{N-1}^{(k)}\big), \tag{4.21}$$

$$\mathbf{U}_n^{(k+1)} = \mathcal{F}\big(T_n, T_{n-1}, \mathbf{U}_{n-1}^{(k)}\big) + \mathcal{G}\big(T_n, T_{n-1}, \mathbf{U}_{n-1}^{(k+1)}\big) - \mathcal{G}\big(T_n, T_{n-1}, \mathbf{U}_{n-1}^{(k)}\big), \quad n = 1, \ldots, N-1. \tag{4.22}$$

In contrast to PP-IC, the PP-PC method introduces a direct periodic coupling on the coarse level in (4.21), which shows its intrusiveness. The PP-PC scheme (4.21)-(4.22) can be written in the matrix-vector operator form

$$\begin{bmatrix} \mathbf{I} & & & -\mathcal{G}\left(T_N, T_{N-1}, \cdot\right) \\ -\mathcal{G}\left(T_1, T_0, \cdot\right) & \mathbf{I} & & \\ & \ddots & \ddots & \\ & & -\mathcal{G}\left(T_{N-1}, T_{N-2}, \cdot\right) & \mathbf{I} \end{bmatrix} \begin{bmatrix} \mathbf{U}_0^{(k+1)} \\ \mathbf{U}_1^{(k+1)} \\ \vdots \\ \mathbf{U}_{N-1}^{(k+1)} \end{bmatrix} = \begin{bmatrix} \mathbf{b}_N^{(k)} \\ \mathbf{b}_1^{(k)} \\ \vdots \\ \mathbf{b}_{N-1}^{(k)} \end{bmatrix} \tag{4.23}$$

with the notation

$$\mathbf{b}_n^{(k)} = \mathcal{F}\big(T_n, T_{n-1}, \mathbf{U}_{n-1}^{(k)}\big) - \mathcal{G}\big(T_n, T_{n-1}, \mathbf{U}_{n-1}^{(k)}\big), \quad n = 1, \ldots, N. \tag{4.24}$$

Since the system (4.16) is in general nonlinear, an additional linearization of the PP-PC system (4.23) has to be performed. For example, in [52] the fixed point (Jacobi-type) iteration of the form (3.68) was applied at each PP-PC iteration $k+1$, i.e., for $s = 0, 1, \ldots$ calculate

$$\begin{bmatrix} \mathbf{U}_0^{(k+1,s+1)} \\ \mathbf{U}_1^{(k+1,s+1)} \\ \vdots \\ \mathbf{U}_{N-1}^{(k+1,s+1)} \end{bmatrix} = \begin{bmatrix} \mathbf{0} & & & \mathcal{G}\left(T_N, T_{N-1}, \cdot\right) \\ \mathcal{G}\left(T_1, T_0, \cdot\right) & \mathbf{0} & & \\ & \ddots & \ddots & \\ & & \mathcal{G}\left(T_{N-1}, T_{N-2}, \cdot\right) & \mathbf{0} \end{bmatrix} \begin{bmatrix} \mathbf{U}_0^{(k+1,s)} \\ \mathbf{U}_1^{(k+1,s)} \\ \vdots \\ \mathbf{U}_{N-1}^{(k+1,s)} \end{bmatrix} + \begin{bmatrix} \mathbf{b}_N^{(k)} \\ \mathbf{b}_1^{(k)} \\ \vdots \\ \mathbf{b}_{N-1}^{(k)} \end{bmatrix}. \tag{4.25}$$

We see that the iteration (4.25) decouples the calculation of the discrete solution values $\mathbf{U}_n^{(k+1,s+1)}$ for $n = 0, \ldots, N-1$ completely, thereby allowing parallel solution also the coarse level and making the algorithm non-intrusive. On the other hand, such a lineariazation relaxes the periodicity constraint similarly to PP-IC and thus a loss of efficiency must be expected [82]. Moreover, this iterative method is not exact for linear problems (i.e., it does not necessarily converge in one iteration), and thus requires more computational effort than the solution of the PP-PC system (4.23), which is possible in the linear case.

For the termination of the PP-PC method, the error at the iteration k can be calculated as

$$\varepsilon_{\mathrm{PP}}^{(k)} = \frac{\varepsilon_{\mathrm{IC},2}^{(k)}}{\varepsilon_{\mathrm{tol}} + \big\|\mathbf{U}_{\mathrm{tot}}^{(k)}\big\|_*}, \tag{4.26}$$

where

$$\mathbf{U}_{\mathrm{tot}}^{(k)} = \Big[\big(\mathbf{U}_0^{(k)}\big)^\top, \big(\mathbf{U}_1^{(k)}\big)^\top, \ldots, \big(\mathbf{U}_{N-1}^{(k)}\big)^\top\Big]^\top \tag{4.27}$$

and for a vector $\mathbf{u} = \left[\mathbf{u}_1^\top, \ldots, \mathbf{u}_N^\top\right]^\top \in \mathbb{R}^{Nd}$ the norm $\|\cdot\|_*$ is given by

$$\|\mathbf{u}\|_* = \max_{1 \le n \le N} \|\mathbf{u}_n\|_2, \tag{4.28}$$

with the error $\varepsilon_{\mathrm{IC},2}^{(k)}$ defined in (4.20) using the l_2-norm $\|\cdot\|_2$. The error of the inner iteration (4.25) at PP-PC iteration $k+1$ is calculated as the relative difference of the solution vectors at the two subsequent iterations $s+1$ and s for $s = 0, 1, \ldots$ [82], i.e.,

$$\varepsilon_{\mathrm{PC,\,it}}^{(k+1,s+1)} = \frac{\big\|\mathbf{U}_{\mathrm{tot}}^{(k+1,s+1)} - \mathbf{U}_{\mathrm{tot}}^{(k+1,s)}\big\|_*}{\varepsilon_{\mathrm{tol}} + \big\|\mathbf{U}_{\mathrm{tot}}^{(k+1,s+1)}\big\|_*}, \tag{4.29}$$

with the $\|\cdot\|_*$-norm defined in (4.28). The iterative methods terminate once the corresponding errors become smaller than a prescribed tolerance $\varepsilon_{\mathrm{tol}}$.

4.3 Multirate Parareal for problems with PWM excitations

We now consider problems, which include discontinuous signals on the RHSs such as, e.g., PWM excitations described in Section 2.3. In those cases, acceleration of time stepping using PinT approaches is especially important due to the need to resolve the high-frequency pulses with a very small time step. The imposition of smoothness assumptions on the RHS $\mathbf{f}$ (see Theorem 4.1) makes the analysis of the Parareal algorithm impossible for problems with discontinuous inputs. Besides, the coarse propagator $\mathcal{G}$ will most probably not capture the high-frequency dynamics, which might lead to a slow convergence of Parareal. Therefore, in order to solve problems with discontinuous inputs we propose a multirate Parareal method, which uses a modified coarse solver $\bar{\mathcal{G}}$, in [51]. There, a surrogate model with a smooth low-frequency excitation is considered on the coarse level. Exploiting the multirate Parareal, the MPDE approach from Section 2.3.3 is used in [103] as the coarse solver.

We assume that the RHS in (4.1) can be expressed as a sum

$$\mathbf{f}(\mathbf{u}(t), t) = \bar{\mathbf{f}}(\mathbf{u}(t), t) + \tilde{\mathbf{f}}(t), \tag{4.30}$$

where $\bar{\mathbf{f}}$ and $\tilde{\mathbf{f}}$ satisfy the following assumption.

Assumption 4.2. *Assume for functions $\bar{\mathbf{f}}$ and $\tilde{\mathbf{f}}$ from* (4.30) *it holds that*

- $\bar{\mathbf{f}}$ *is bounded, sufficiently smooth in both arguments, and Lipschitz continuous in the first argument with Lipschitz constant L, see* (2.51)*;*
- $\tilde{\mathbf{f}} \in \mathbf{L}^\gamma([0,T], \mathbb{R}^d)$, $\gamma \geq 1$, *(see Section 3.1.2) with a bounded norm* (3.7)

$$C_\gamma = \|\tilde{\mathbf{f}}\|_{\mathbf{L}^\gamma([0,T],\mathbb{R}^d)} < \infty. \tag{4.31}$$

The idea of the multirate Parareal algorithm for systems with discontinuous inputs [51] is the introduction of a simplified coarse propagator $\bar{\mathcal{G}}$, which solves the IVP with a smooth RHS $\bar{\mathbf{f}}$ instead of the original RHS $\mathbf{f}$, i.e., $\bar{\mathcal{G}}(t, T_{n-1}, \mathbf{U}_{n-1})$ is the solution to

$$\bar{\mathbf{u}}_n'(t) = \bar{\mathbf{f}}(\mathbf{u}_n(t), t), \quad t \in (T_{n-1}, T_n], \tag{4.32}$$

$$\bar{\mathbf{u}}_n(T_{n-1}) = \mathbf{U}_{n-1}, \tag{4.33}$$

for $n = 1, \ldots, N$. The fine propagator $\mathcal{F}$ solves the IVP (4.4)-(4.5) with the discontinuous RHS $\mathbf{f}$, as within the standard Parareal method. The proposed multirate Parareal [51] differs from the classical Parareal by replacing $\mathcal{G}$ by the simplified coarse solver $\bar{\mathcal{G}}$, i.e., for $k = 0, 1, \ldots$

$$\mathbf{U}_0^{(k+1)} = \mathbf{u}_0, \tag{4.34}$$

$$\mathbf{U}_n^{(k+1)} = \mathcal{F}\big(T_n, T_{n-1}, \mathbf{U}_{n-1}^{(k)}\big) + \bar{\mathcal{G}}\big(T_n, T_{n-1}, \mathbf{U}_{n-1}^{(k+1)}\big) - \bar{\mathcal{G}}\big(T_n, T_{n-1}, \mathbf{U}_{n-1}^{(k)}\big), \quad n = 1, \ldots, N-1. \tag{4.35}$$

The smooth part of a PWM input can be obtained from Fourier analysis (see Section 2.3.1), i.e., by extracting the principal frequency component(s). For example, in case of the PWM signal with varying duty cycle depicted in the Figure 2.8d, the natural choice is the AC reference signal r_{ac} from the Figure 2.8b.

4.3.1 Convergence analysis

We analyze the convergence of the multirate Parareal algorithm (4.34)-(4.35) based on [51]. We first provide an auxiliary result, necessary for the derivation of the error estimate for the multirate Parareal.

Lemma 4.3 ([51]). *Let Assumption 4.2 hold, and let the subinterval size $\Delta T = T_n - T_{n-1}$ be small. We denote by $\mathbf{u}_n = \mathcal{F}(T_n, T_{n-1}, \mathbf{U}_{n-1})$ and $\bar{\mathbf{u}}_n = \bar{\mathcal{F}}(T_n, T_{n-1}, \mathbf{U}_{n-1})$ the solutions to* (4.4)-(4.5) *and* (4.32)-(4.33)*, respectively. Then there exists $C_4 > 0$ such that*

$$\big\|\mathbf{u}_n(T_n) - \bar{\mathbf{u}}_n(T_n)\big\| \leq C_4 C_\gamma \Delta T^{1/\zeta}, \tag{4.36}$$

with the integer $\zeta \geq 1$ such that $1/\gamma + 1/\zeta = 1$ and constant C_γ defined in (4.31).

Proof. It can be seen that $\mathbf{u}_n$ and $\bar{\mathbf{u}}_n$ satisfy the assumptions of the Theorem 2.3 with $\rho = 0$ and $\varepsilon(t) = \|\tilde{\mathbf{f}}(t)\|$ from the space $\mathbf{L}^\gamma((0,T))$, $\gamma \geq 1$, [51]. We then have for $1 \leq \gamma < \infty$, using Hölder's inequality and Taylor's expansion for small ΔT, the bound

$$\begin{aligned}
\big\|\mathbf{u}_n(T_n) - \bar{\mathbf{u}}_n(T_n)\big\| &\leq \exp(L\Delta T) \int_{T_{n-1}}^{T_n} \Big|\exp\big(-L(s - T_{n-1})\big)\varepsilon(s)\Big| \mathrm{d}s \\
&\leq \exp(L\Delta T)\bigg(\int_{T_{n-1}}^{T_n} \Big|\exp\big(-L(s - T_{n-1})\big)\Big|^\zeta \mathrm{d}s\bigg)^{1/\zeta} \bigg(\int_{T_{n-1}}^{T_n} |\varepsilon(s)|^\gamma \mathrm{d}s\bigg)^{1/\gamma} \\
&= \big(1 + L\Delta T + \mathcal{O}(\Delta T^2)\big)\big(\Delta T + \mathcal{O}(\Delta T^2)\big)^{1/\zeta} \|\varepsilon\|_{L^\gamma((T_{n-1},T_n))} \leq C_\gamma \Delta T^{1/\zeta} + \mathcal{O}(\Delta T^{2/\zeta}) \\
&\leq C_4 C_\gamma \Delta T^{1/\zeta},
\end{aligned}$$

with the integer $\zeta > 1$ such that $1/\gamma + 1/\zeta = 1$ and the constant C_4 coming from the definition of the Landau symbol "big $\mathcal{O}$". Similar result is obtained for $\gamma = \infty$, $\zeta = 1$, [51]. In this case, Theorem 2.3 with $\rho = 0$ and $\varepsilon(t) = \|\tilde{\mathbf{f}}(t)\| \leq C_\infty$ and Taylor's expansion for small ΔT give

$$\big\|\mathbf{u}_n(T_n) - \bar{\mathbf{u}}_n(T_n)\big\| \leq C_\infty\big(\exp(L\Delta T) - 1\big)/L = C_\infty\big(1 + L\Delta T + \mathcal{O}(\Delta T^2) - 1\big)/L \leq C_4 C_\infty \Delta T.$$

We then obtain the bound (4.36) for $\zeta \geq 1$. □

Theorem 4.4 (Convergence of the multirate Parareal method [51]). *Let RHS $\mathbf{f}$ in* (4.1) *be expressed by* (4.30) *fulfilling the Assumption 4.2 and let the partition* (4.3) *of the interval $[0, T]$ be equidistant with the step size $\Delta T = T/N$. We additionally assume:*

- *$\mathcal{F}(T_n, T_{n-1}, \mathbf{U}_{n-1})$ is the exact solution to the IVP* (4.4)-(4.5) *at T_n.*
- *$\bar{\mathcal{F}}(T_n, T_{n-1}, \mathbf{U}_{n-1})$ and $\bar{\mathcal{G}}(T_n, T_{n-1}, \mathbf{U}_{n-1})$ are the exact and an approximate solution to* (4.32)-(4.33) *at T_n, respectively.*
- *The LTE is bounded by $\bar{C}_3 \Delta T^{p+1}$ with $p \geq 1$ and can be expanded for small step size ΔT and an initial value $\mathbf{U}$ as*

$$\bar{\mathcal{F}}(T_n, T_{n-1}, \mathbf{U}) - \bar{\mathcal{G}}(T_n, T_{n-1}, \mathbf{U}) = \bar{c}_{p+1}(\mathbf{U})\Delta T^{p+1} + \bar{c}_{p+2}(\mathbf{U})\Delta T^{p+2} + \ldots, \tag{4.37}$$

where functions $\bar{c}_i$, $i = p+1, p+2, \ldots$, are continuously differentiable.

- *$\bar{\mathcal{G}}$ satisfies the Lipschitz condition*

$$\|\bar{\mathcal{G}}\big(t+\Delta T,\, t, \mathbf{U}\big) - \bar{\mathcal{G}}\big(t+\Delta T,\, t, \mathbf{V}\big)\| \leq (1 + C_2 \Delta T)\|\mathbf{U} - \mathbf{V}\|, \tag{4.38}$$

for $t \in [0, T]$, for all $\mathbf{U}, \mathbf{V}$, and a constant C_2.

Then at the multirate Parareal iteration $k = 0, 1, \ldots$ (4.34)-(4.35) we have for the constants $\bar{C}_1 > 0$ and $C_4 > 0$ the error bound

$$\big\|\mathbf{u}(T_n) - \mathbf{U}_n^{(k)}\big\| \leq \bar{C}_1^k \left[C_4 C_\gamma \Delta T^{(p+1)k+1/\zeta} + \bar{C}_3 \left(\Delta T^{p+1}\right)^{k+1}\right] \frac{(1 + C_2\Delta T)^{n-k-1}}{(k+1)!} \prod_{j=0}^{k} (n-j), \tag{4.39}$$

with the integer $\zeta \geq 1$ such that $1/\gamma + 1/\zeta = 1$ and constant C_γ defined in (4.31).

Proof. By adding and subtracting several terms, we obtain from the multirate Parareal update formula (4.35)

$$\begin{aligned}
\mathbf{u}(T_n) - \mathbf{U}_n^{(k+1)} &= \mathcal{F}\big(T_n, T_{n-1}, \mathbf{u}(T_{n-1})\big) - \mathcal{F}\big(T_n, T_{n-1}, \mathbf{U}_{n-1}^{(k)}\big) + \bar{\mathcal{G}}\big(T_n, T_{n-1}, \mathbf{U}_{n-1}^{(k)}\big) - \bar{\mathcal{G}}\big(T_n, T_{n-1}, \mathbf{U}_{n-1}^{(k+1)}\big) \\
&\pm \bar{\mathcal{F}}\big(T_n, T_{n-1}, \mathbf{u}(T_{n-1})\big) \pm \bar{\mathcal{G}}\big(T_n, T_{n-1}, \mathbf{u}(T_{n-1})\big) \pm \bar{\mathcal{F}}\big(T_n, T_{n-1}, \mathbf{U}_{n-1}^{(k)}\big) \\
&= \underbrace{\bar{\mathcal{F}}\big(T_n, T_{n-1}, \mathbf{u}(T_{n-1})\big) - \bar{\mathcal{G}}\big(T_n, T_{n-1}, \mathbf{u}(T_{n-1})\big)}_{= \bar{c}_{p+1}\left(\mathbf{u}(T_{n-1})\right)\Delta T^{p+1} + \ldots} - \Big(\underbrace{\bar{\mathcal{F}}\big(T_n, T_{n-1}, \mathbf{U}_{n-1}^{(k)}\big) - \bar{\mathcal{G}}\big(T_n, T_{n-1}, \mathbf{U}_{n-1}^{(k)}\big)}_{= \bar{c}_{p+1}\left(\mathbf{U}_{n-1}^{(k)}\right)\Delta T^{p+1} + \ldots}\Big) \\
&+ \underbrace{\mathcal{F}\big(T_n, T_{n-1}, \mathbf{u}(T_{n-1})\big) - \bar{\mathcal{F}}\big(T_n, T_{n-1}, \mathbf{u}(T_{n-1})\big) - \Big(\mathcal{F}\big(T_n, T_{n-1}, \mathbf{U}_{n-1}^{(k)}\big) - \bar{\mathcal{F}}\big(T_n, T_{n-1}, \mathbf{U}_{n-1}^{(k)}\big)\Big)}_{= \mathbf{0}} \\
&+ \bar{\mathcal{G}}\big(T_n, T_{n-1}, \mathbf{u}(T_{n-1})\big) - \bar{\mathcal{G}}\big(T_n, T_{n-1}, \mathbf{U}_{n-1}^{(k+1)}\big).
\end{aligned} \tag{4.40}$$

Using the Lipschitz continuity of $\bar{c}_{p+1}$ and the Lipschitz condition (4.38), we obtain the bound

$$\big\|\mathbf{u}(T_n) - \mathbf{U}_n^{(k+1)}\big\| \leq \underbrace{\bar{C}_1 \Delta T^{p+1}}_{=:\alpha} \big\|\mathbf{u}(T_n) - \mathbf{U}_{n-1}^{(k)}\big\| + \underbrace{(1 + C_2\Delta T)}_{=:\beta} \big\|\mathbf{u}(T_{n-1}) - \mathbf{U}_{n-1}^{(k+1)}\big\|, \tag{4.41}$$

with a constant $\bar{C}_1 > 0$. Following [48] and [51] we consider the bounding recurrence relation for the errors

$$e_n^{(k+1)} = \alpha e_{n-1}^{(k)} + \beta e_{n-1}^{(k+1)}. \tag{4.42}$$

Applying the initialization (4.11) and the Lemma 4.3, we have an estimate of the initial error

$$\begin{aligned}
\big\|\mathbf{u}(T_n) - \mathbf{U}_n^{(0)}\big\| &= \big\|\mathcal{F}\big(T_n, T_{n-1}, \mathbf{u}(T_{n-1})\big) - \bar{\mathcal{G}}\big(T_n, T_{n-1}, \mathbf{U}_{n-1}^{(0)}\big)\big\| \\
&\leq \big\|\mathcal{F}\big(T_n, T_{n-1}, \mathbf{u}(T_{n-1})\big) - \bar{\mathcal{G}}\big(T_n, T_{n-1}, \mathbf{u}(T_{n-1})\big)\big\| + \big\|\bar{\mathcal{G}}\big(T_n, T_{n-1}, \mathbf{u}(T_{n-1})\big) - \bar{\mathcal{G}}\big(T_n, T_{n-1}, \mathbf{U}_{n-1}^{(0)}\big)\big\| \\
&\leq \underbrace{C_4 C_\gamma \Delta T^{1/\zeta} + \bar{C}_3 \Delta T^{p+1}}_{=:\eta} + \beta \big\|\mathbf{u}(T_n) - \mathbf{U}_{n-1}^{(0)}\big\|,
\end{aligned}$$

for $n = 1, \ldots, N$. We thus obtain for the bounding recurrence relation for the initial error

$$e_n^{(0)} = \eta + \beta e_{n-1}^{(0)}. \tag{4.43}$$

Multiplying the equations (4.42) and (4.43) by μ^n and summing over $n \geq 1$, we obtain that the generating function

$$\rho_k(\mu) = \sum_{n \geq 1} e_n^{(k)} \mu^n \tag{4.44}$$

satisfies the recurrence relation

$$\rho_{k+1}(\mu) = \alpha\mu\rho_k(\mu) + \beta\mu\rho_{k+1}(\mu), \quad \text{with } \rho_0(\mu) = \eta\frac{\mu}{1-\mu} + \beta\mu\rho_0(\mu).$$

Solving for $\rho_k(\mu)$, we get by induction

$$\rho_k(\mu) = \eta\alpha^k \frac{\mu^{k+1}}{(1-\mu)} \frac{1}{(1-\beta\mu)^{k+1}}. \tag{4.45}$$

Coefficients in the power series in (4.44) will increase, when the factor $1-\mu$ in the denominator of (4.45) is replaced by $1-\beta\mu$. Then, using the binomial series expansion

$$\frac{1}{(1-\beta\mu)^{k+2}} = \sum_{j\geq 0} \binom{k+1+j}{j} \beta^j \mu^j,$$

we derive from $\rho_k(\mu)$ the following bound

$$e_n^{(k)} \leq \eta\alpha^k \beta^{n-k-1} \binom{n}{k+1},$$

which leads to the estimate (4.39) after the insertion of the definitions for the constants η, α, and β, [51]. □

We see that the estimate (4.39) of the multirate Parareal has an additional term of order $(p+1)k + 1/\zeta$, compared to the estimate (4.14) of the standard Parareal, where only the term of order $(p+1)(k+1)$ is present. This amendment might lead to a reduction of the convergence order. Indeed, for $p \geq 1$ and $\zeta \geq 1$ we have for the powers of the two terms in (4.39)

$$(p+1)k + 1/\zeta < (p+1)(k+1),$$

since $1/\zeta < p+1$. This happens even in the best case when we have order $(p+1)k+1$ and $\zeta = 1$, which corresponds to $\gamma = \infty$. However, if the value C_γ of the norm $\tilde{\mathbf{f}}$ in (4.31) is small enough, the second term in the estimate (4.39) dominates pre-asymptotically (i.e., for not too small ΔT) over the first term [51]. In this case, the convergence rate of order $(p+1)(k+1)$ as within the standard Parareal is maintained, which is also observed through numerical experiments in [51]. We thus conclude that the closer the surrogate model (4.32) is to the original model (4.4), the closer the convergence rate of the multirate Parareal (4.34)-(4.35) is to the convergence rate of the original Parareal (4.9)-(4.10). Finally, the convergence result of Theorem 4.4 can be considered as a generalization of the standard result from Theorem 4.1 when setting $\tilde{\mathbf{f}}(t) = \mathbf{0}$ in (4.30), [51].

4.3.2 Time-periodic extension: multirate PP-IC

A natural extension of the multirate Parareal method to TP problems was developed based on the PP-IC algorithm in [52]. In particular, the mutlirate PP-IC iteration: for $k = 0, 1, \ldots$

$$\mathbf{U}_0^{(k+1)} = \mathbf{U}_N^{(k)}, \tag{4.46}$$

$$\mathbf{U}_n^{(k+1)} = \mathcal{F}(T_n, T_{n-1}, \mathbf{U}_{n-1}^{(k)}) + \bar{\mathcal{G}}(T_n, T_{n-1}, \mathbf{U}_{n-1}^{(k+1)}) - \bar{\mathcal{G}}(T_n, T_{n-1}, \mathbf{U}_{n-1}^{(k)}), \quad n = 1, \ldots, N, \tag{4.47}$$

was introduced. As within the multirate Parareal iteration (4.34)-(4.35), the fine propagator $\mathcal{F}$ solves the original problem (4.4)-(4.5) with a discontinuous (high-frequency) RHS, while the coarse propagator $\bar{\mathcal{G}}$ solves the surrogate problem (4.32)-(4.33) with a smooth RHS and a reduced dynamics. In [52] it is shown that the convergence estimate for the standard PP-IC algorithm (4.18)-(4.19) from [50] can be also used for the multirate PP-IC variant (4.46)-(4.47), which we describe in the following.

4.3.2.1 Convergence analysis for a model problem

Following the analysis of the original PP-IC algorithm in [50], we analyze the convergence of the proposed multirate PP-IC method [52] for a TP linear model problem of a single ODE

$$u'(t) + \nu u(t) = f(t), \quad t \in (0, T), \tag{4.48}$$

$$u(0) = u(T), \tag{4.49}$$

with a T-periodic discontinuous RHS $f : [0, T] \to \mathbb{R}$, a positive constant $\nu \in \mathbb{R}$, and the sought solution $u \colon [0, T] \to \mathbb{R}$, $T > 0$. We consider the partition (4.3) of the interval $[0, T]$. As within the multirate Parareal algorithm, the fine propagator $\mathcal{F}$ solves the IVP for the original ODE

$$\begin{aligned} u_n'(t) + \nu u_n(t) &= f(t), \quad t \in (T_{n-1}, T_n], \\ u_n(T_{n-1}) &= U_{n-1}, \end{aligned} \tag{4.50}$$

while the coarse propagator $\bar{\mathcal{G}}$ solves the IVP for the modified ODE

$$\begin{aligned} \bar{u}_n'(t) + \nu \bar{u}_n(t) &= \bar{f}(t), \quad t \in (T_{n-1}, T_n], \\ \bar{u}_n(T_{n-1}) &= U_{n-1}, \end{aligned} \tag{4.51}$$

with a smooth slowly-varying RHS $\bar{f}$ such that $f = \bar{f} + \tilde{f}$. We denote the error at the iteration $k = 0, 1, \ldots$ of the mutlirate PP-IC algorithm (4.46)-(4.47) by

$$\mathbf{e}^{(k)} = \left[e_0^{(k)}, e_1^{(k)}, \ldots, e_N^{(k)}\right]^\top, \qquad \text{with} \quad e_n^{(k)} = u(T_n) - U_n^{(k)}, \quad n = 0, 1, \ldots, N, \tag{4.52}$$

where $u(T_n)$ is the exact solution to the ODE in (4.50) at T_n, expressed by

$$u(T_n) = \exp(-\nu \Delta T) u(T_{n-1}) + \int_{T_{n-1}}^{T_n} \exp\big(-\nu(T_n - s)\big) f(s) \, \mathrm{d}s, \tag{4.53}$$

with $u(T_{n-1})$ denoting the exact solution at T_{n-1}.

Theorem 4.5 (Convergence of the multirate PP-IC method [52])**.** *Let RHS f in* (4.48) *be expressed by $f = \bar{f} + \tilde{f}$, with a smooth low-frequency function $\bar{f}$, and let the partition* (4.3) *of the interval $[0, T]$ be equidistant with the step size $\Delta T = T/N$. We additionally assume:*

- *$\mathcal{F}(T_n, T_{n-1}, U_{n-1})$ is the exact solution to* (4.50) *at T_n, expressed by*

$$\mathcal{F}(T_n, T_{n-1}, U_{n-1}) = \exp(-\nu \Delta T) U_{n-1} + \int_{T_{n-1}}^{T_n} \exp\big(-\nu(T_n - s)\big) f(s) \, \mathrm{d}s. \tag{4.54}$$

- *$\bar{\mathcal{G}}(T_n, T_{n-1}, U_{n-1})$ is an approximate solution to* (4.51) *at T_n, obtained by a one-step method with the stability function $\mathcal{R}(\nu \Delta T)$ (see Definition 3.12), i.e.,*

$$\bar{\mathcal{G}}\big(T_n, T_{n-1}, U_{n-1}\big) = \mathcal{R}(\nu \Delta T) \, U_{n-1} + \xi_n\left(\bar{f}, \nu \Delta T\right), \tag{4.55}$$

  where the function ξ_n corresponds to the RHS $\bar{f}$ discretized on $[T_n, T_{n-1}]$ with the one-step method.

- *The stability condition*

$$\big|\mathcal{R}(\nu\Delta T)\big| + \underbrace{\big|\exp(-\nu\Delta T) - \mathcal{R}(\nu\Delta T)\big|}_{=:r(\nu\Delta T)} < 1. \tag{4.56}$$

Then the errors (4.52) *of the multirate PP-IC iteration* (4.46)-(4.47) *are defined by the following fixed-point iteration*

$$\mathbf{e}^{(k+1)} = S\mathbf{e}^{(k)}, \tag{4.57}$$

with the matrix S *given by*

$$S = \begin{bmatrix} 1 & & & \\ -\mathcal{R}(\nu\Delta T) & 1 & & \\ & \ddots & \ddots & \\ & & -\mathcal{R}(\nu\Delta T) & 1 \end{bmatrix}^{-1} \begin{bmatrix} 0 & & & 1 \\ r(\nu\Delta T) & 0 & & \\ & \ddots & \ddots & \\ & & r(\nu\Delta T) & 0 \end{bmatrix}. \tag{4.58}$$

Furthermore, the asymptotic convergence factor

$$\rho_{\text{asym}}(S) = \lim_{k\to\infty} \Big(\big\|\mathbf{e}^{(k)}\big\| / \big\|\mathbf{e}^{(0)}\big\| \Big)^{1/k} \tag{4.59}$$

of the multirate PP-IC algorithm (4.46)-(4.47) *is bounded by the sequence* x_l *given by*

$$x_l = \Big(\big|\mathcal{R}(\nu\Delta T)\big| x_{l-1} + \big|r(\nu\Delta T)\big| \Big)^{\frac{N}{N+1}}, \quad l \geq 1, \qquad x_0 = 1. \tag{4.60}$$

Proof. Using (4.53)-(4.55) and following [50], we have for the error at the iteration $k+1$

$$\begin{aligned} e_n^{(k+1)} &= u(T_n) - \mathcal{F}\big(T_n, T_{n-1}, U_{n-1}^{(k)}\big) - \bar{\mathcal{G}}\big(T_n, T_{n-1}, U_{n-1}^{(k+1)}\big) + \bar{\mathcal{G}}\big(T_n, T_{n-1}, U_{n-1}^{(k)}\big) \\ &= \mathcal{R}\left(\nu\Delta T\right) e_{n-1}^{(k+1)} + r(\nu\Delta T) e_{n-1}^{(k)}, \quad n = 1, 2, \ldots, N. \end{aligned} \tag{4.61}$$

Additionally, the initial error satisfies $e_0^{(k+1)} = e_N^{(k)}$. Due to the definition of the matrix S in (4.58) we obtain directly the fixed point iteration (4.57) for the errors, which is the same as in [50]. The bound (4.60) is then obtained due to [50, Theorem 3.7]. □

We note that under the assumption (4.56), the fixed point operator S from (4.58) is a contraction [50], which ensures convergence of the mutlirate PP-IC algorithm (4.46)-(4.47).

4.4 PP-PC with MH coarse grid correction

We now consider the PP-PC method (4.21)-(4.22), written in the matrix-vector operator form (4.23). For the efficient solution of the PP-PC system (4.23) the MH diagonalization approach from [17] described in Section 3.3.2 can be applied. The method can be easily used in the linear case as it was proposed by the author in [81]. Let the linear TP eddy current problem

$$\mathbf{M}_\sigma \mathbf{u}'(t) + \mathbf{K}_\nu \mathbf{u}(t) = \mathbf{f}(t), \quad t \in (0, T), \tag{4.62}$$

$$\mathbf{u}(0) = \mathbf{u}(T), \tag{4.63}$$

be discretized on the coarse level using the equidistant partition (4.3) with the step size $\Delta T = T/N$. Assuming the coarse propagator $\mathcal{G}$ is the IE method, i.e., $\bar{\mathbf{U}}_n^{(k+1)} = \mathcal{G}\big(T_n, T_{n-1}, \mathbf{U}_{n-1}^{(k+1)}\big)$ solves

$$\mathbf{Q}\bar{\mathbf{U}}_n^{(k+1)} - \mathbf{C}\mathbf{U}_{n-1}^{(k+1)} = \mathbf{f}_n, \quad n = 1, \ldots, N, \tag{4.64}$$

with $\mathbf{C} = (1/\Delta T)\mathbf{M}_\sigma$, we obtain for the joint vector $\mathbf{U}_{\mathrm{tot}}^{(k+1)}$ defined as in (4.27) the block-cyclic system

$$\mathbf{G}\,\mathbf{U}_{\mathrm{tot}}^{(k+1)} = \mathbf{r}_{\mathrm{tot}}^{(k)} \tag{4.65}$$

at the PP-PC iteration $k+1$. The matrix $\mathbf{G}$ is defined in (3.97) and the RHS is given by

$$\mathbf{r}_{\mathrm{tot}}^{(k)} = \Big[\big(\mathbf{r}_N^{(k)}\big)^\top, \big(\mathbf{r}_1^{(k)}\big)^\top, \ldots, \big(\mathbf{r}_{N-1}^{(k)}\big)^\top\Big]^\top, \qquad \text{with} \quad \mathbf{r}_n^{(k)} = \mathbf{Q}\mathbf{b}_n^{(k)} + \mathbf{f}_n, \quad n = 1, \ldots, N, \tag{4.66}$$

with $\mathbf{Q} = \mathbf{C} + \mathbf{K}_\nu$ and $\mathbf{b}_n^{(k)}$ defined in (4.24). The system (4.65) has the same structure as the system (3.97) and can therefore be transformed into the block-diagonal system of the form (3.98) using the MH approach from Section 3.3.2. In contrast to the MH approach applied to the standard TP discretization (3.97), the MH coarse grid correction of the PP-PC system does not lead to optimal scaling (provided N parallel processing units are available), since PP-PC is an iterative method. Besides, the difference between the two approaches is that the direct TP discretization has to use a fine discretization, e.g., using the fine step size δT, while a coarse step size $\Delta T \gg \delta T$ is used within PP-PC. It means that the number of variables $N = N_{\mathrm{f}} = T/\delta T$ is significantly larger within the TP MH method compared to PP-PC MH, where $N = T/\Delta T$ variables on the coarse level are used.

In the nonlinear case the MH diagonalization can be exploited within an applied linearization method, provided the system matrix at each iteration possesses the block-cyclic structure (3.97). For this purpose we apply the simplified Newton method (see Section 3.2.3) based on [82].

4.4.1 Linearization using the simplified Newton method

Consider the nonlinear TP eddy current problem (3.30), (3.35), where the stiffness matrix $\mathbf{K}_\nu\big(\mathbf{u}(t)\big)$ depends on the solution. The coarse discretization using the IE method with the step size $\Delta T = T/N$, i.e., setting $\bar{\mathbf{U}}_n^{(k+1)} = \mathcal{G}\big(T_n, T_{n-1}, \mathbf{U}_{n-1}^{(k+1)}\big)$ such that

$$\mathbf{Q}\big(\bar{\mathbf{U}}_n^{(k+1)}\big)\bar{\mathbf{U}}_n^{(k+1)} - \mathbf{C}\mathbf{U}_{n-1}^{(k+1)} = \mathbf{f}_n, \quad n = 1, \ldots, N, \tag{4.67}$$

leads to the block system of the form (3.95) at the PP-PC iteration $k+1$

$$\begin{bmatrix} \mathbf{Q}\big(\bar{\mathbf{U}}_N^{(k+1)}\big) & & & -\mathbf{C} \\ -\mathbf{C} & \mathbf{Q}\big(\bar{\mathbf{U}}_1^{(k+1)}\big) & & \\ & \ddots & \ddots & \\ & & -\mathbf{C} & \mathbf{Q}\big(\bar{\mathbf{U}}_{N-1}^{(k+1)}\big) \end{bmatrix} \begin{bmatrix} \mathbf{U}_0^{(k+1)} \\ \mathbf{U}_1^{(k+1)} \\ \vdots \\ \mathbf{U}_{N-1}^{(k+1)} \end{bmatrix} = \begin{bmatrix} \mathbf{r}_N^{(k)}\big(\bar{\mathbf{U}}_N^{(k+1)}\big) \\ \mathbf{r}_1^{(k)}\big(\bar{\mathbf{U}}_1^{(k+1)}\big) \\ \vdots \\ \mathbf{r}_{N-1}^{(k)}\big(\bar{\mathbf{U}}_{N-1}^{(k+1)}\big) \end{bmatrix} \tag{4.68}$$

with

$$\mathbf{C} = \frac{1}{\Delta T}\mathbf{M}_\sigma, \qquad \mathbf{Q}(\mathbf{X}) = \mathbf{C} + \mathbf{K}_\nu(\mathbf{X}), \qquad \mathbf{r}_n^{(k)}(\mathbf{X}) = \mathbf{Q}(\mathbf{X})\mathbf{b}_n^{(k)} + \mathbf{f}_n, \tag{4.69}$$

for a vector $\mathbf{X} \in \mathbb{R}^{N_\mathrm{d}}$ and $\mathbf{b}_n^{(k)}$ given by (4.24), $n = 1, \ldots, N$. We point out the dependence on the coarse solution $\bar{\mathbf{U}}_n$ in (4.68) in contrast to the standard TP discretization (3.95), where the dependence directly on the unknown variable $\mathbf{u}_n$ is present. This is due to the application of the coarse propagator $\mathcal{G}$ within PP-PC, as it can be seen in the operator system (4.23). Expressing the coarse solution $\bar{\mathbf{U}}_n^{(k+1)}$ from the PP-PC iteration (4.21)-(4.22) as

$$\bar{\mathbf{U}}_n^{(k+1)} = \mathbf{U}_n^{(k+1)} - \mathbf{b}_n^{(k)}, \quad n = 1, \ldots, N-1, \qquad \bar{\mathbf{U}}_N^{(k+1)} = \mathbf{U}_0^{(k+1)} - \mathbf{b}_N^{(k)} \tag{4.70}$$

and substituting it into (4.68), one can obtain a nonlinear system in terms of the unknown variable $\mathbf{U}_\mathrm{tot}^{(k+1)}$. To solve the system (4.68) at PP-PC iteration $k+1$, we search for the root $\mathbf{U}_\mathrm{tot}^{(k+1)}$ of the mapping $\mathbf{F}$: $\mathbb{R}^{N_\mathrm{d}N} \to \mathbb{R}^{N_\mathrm{d}N}$ given by

$$\mathbf{F}\big(\mathbf{U}_\mathrm{tot}^{(k+1)}\big) = \begin{bmatrix} \mathbf{Q}\big(\bar{\mathbf{U}}_N^{(k+1)}\big)\bar{\mathbf{U}}_N^{(k+1)} - \mathbf{C}\mathbf{U}_{N-1}^{(k+1)} - \mathbf{f}_N \\ \mathbf{Q}\big(\bar{\mathbf{U}}_1^{(k+1)}\big)\bar{\mathbf{U}}_1^{(k)} - \mathbf{C}\mathbf{U}_0^{(k+1)} - \mathbf{f}_1 \\ \vdots \\ \mathbf{Q}\big(\bar{\mathbf{U}}_{N-1}^{(k+1)}\big)\bar{\mathbf{U}}_{N-1}^{(k+1)} - \mathbf{C}\mathbf{U}_{N-2}^{(k+1)} - \mathbf{f}_{N-1} \end{bmatrix} = \mathbf{0}, \tag{4.71}$$

where $\bar{\mathbf{U}}_n^{(k+1)}$ for $n = 1, \ldots, N$ are defined in (4.70). The root can be computed by the simplified Newton iteration (see Section 3.2.3 and [30]), i.e., for $s = 0, 1, \ldots$ calculating $\mathbf{U}^{(k+1,s+1)}$ from

$$\mathbf{J}_\mathbf{F}\big(\mathbf{U}_\mathrm{tot}^{(k+1,0)}\big)\mathbf{U}_\mathrm{tot}^{(k+1,s+1)} = -\Big[\mathbf{F}\big(\mathbf{U}_\mathrm{tot}^{(k+1,s)}\big) - \mathbf{J}_\mathbf{F}\big(\mathbf{U}_\mathrm{tot}^{(k+1,0)}\big)\mathbf{U}_\mathrm{tot}^{(k+1,s)}\Big], \tag{4.72}$$

with a given initial approximation $\mathbf{U}^{(k+1,0)}$ and Jacobian matrix $\mathbf{J}_\mathbf{F}$ defined by

$$\mathbf{J}_\mathbf{F}\big(\mathbf{U}_\mathrm{tot}^{(k+1)}\big) = \begin{bmatrix} \mathbf{Q}_\mathrm{d}\big(\bar{\mathbf{U}}_N^{(k+1)}\big) & & & -\mathbf{C} \\ -\mathbf{C} & \mathbf{Q}_\mathrm{d}\big(\bar{\mathbf{U}}_1^{(k+1)}\big) & & \\ & \ddots & \ddots & \\ & & -\mathbf{C} & \mathbf{Q}_\mathrm{d}\big(\bar{\mathbf{U}}_{N-1}^{(k+1)}\big) \end{bmatrix}, \tag{4.73}$$

where each component of $\bar{\mathbf{U}}_\mathrm{tot}^{(k+1)}$ is obtained from $\mathbf{U}_\mathrm{tot}^{(k+1)}$ according to (4.70), the matrices $\mathbf{Q}_\mathrm{d}(\cdot)$ on the diagonal are given by

$$\mathbf{Q}_\mathrm{d}(\mathbf{X}) = \mathbf{C} + \mathbf{K}_{\nu,\mathrm{d}}(\mathbf{X}), \tag{4.74}$$

and matrix $\mathbf{K}_{\nu,\mathrm{d}}(\mathbf{X})$ is defined in (3.62), $\mathbf{X} \in \mathbb{R}^{N_\mathrm{d}}$. In order to apply the MH diagonalization to the Jacobian matrix in (4.73), the block matrices $\mathbf{Q}_\mathrm{d}(\cdot)$ on the diagonal have to be all equal. This can be achieved by choosing the initial approximation $\mathbf{U}_\mathrm{tot}^{(k+1,0)}$ for the simplified Newton iteration (4.72) at PP-PC iteration $k+1$ as [82]

$$\mathbf{U}_\mathrm{tot}^{(k+1,0)} = \Big[\big(\mathbf{Z}^{(k)} + \mathbf{b}_N^{(k)}\big)^\top, \big(\mathbf{Z}^{(k)} + \mathbf{b}_1^{(k)}\big)^\top, \ldots, \big(\mathbf{Z}^{(k)} + \mathbf{b}_{N-1}^{(k)}\big)^\top\Big]^\top, \tag{4.75}$$

which due to (4.70) corresponds to

$$\bar{\mathbf{U}}_\mathrm{tot}^{(k+1,0)} = \Big[\big(\mathbf{Z}^{(k)}\big)^\top, \big(\mathbf{Z}^{(k)}\big)^\top, \ldots, \big(\mathbf{Z}^{(k)}\big)^\top\Big]^\top, \tag{4.76}$$

for a given vector $\mathbf{Z}^{(k)} \in \mathbb{R}^{N_\mathrm{d}}$. The system (4.72) is then transformed for $s = 0, 1, \ldots$ into

$$\mathbf{G}_\mathrm{d}^{(k)}\mathbf{U}_\mathrm{tot}^{(k+1,s+1)} = \mathbf{h}_\mathrm{tot}^{(k+1,s)}, \tag{4.77}$$

with the RHS vector $\mathbf{h}_{\mathrm{tot}}^{(k+1,s)} = \Big[\big(\mathbf{h}_N^{(k+1,s)}\big)^\top, \big(\mathbf{h}_1^{(k+1,s)}\big)^\top, \ldots, \big(\mathbf{h}_{N-1}^{(k+1,s)}\big)^\top\Big]^\top$ given by

$$\begin{aligned}
\mathbf{h}_n^{(k+1,s)} &= \Big[\mathbf{Q}_{\mathrm{d}}\big(\mathbf{Z}^{(k)}\big) - \mathbf{Q}\big(\bar{\mathbf{U}}_n^{(k+1,s)}\big)\Big]\mathbf{U}_n^{(k+1,s)} + \mathbf{r}_n^{(k)}\big(\bar{\mathbf{U}}_n^{(k+1,s)}\big), \quad n = 1, \ldots, N-1, \\
\mathbf{h}_N^{(k+1,s)} &= \Big[\mathbf{Q}_{\mathrm{d}}\big(\mathbf{Z}^{(k)}\big) - \mathbf{Q}\big(\bar{\mathbf{U}}_N^{(k+1,s)}\big)\Big]\mathbf{U}_0^{(k+1,s)} + \mathbf{r}_N^{(k)}\big(\bar{\mathbf{U}}_N^{(k+1,s)}\big),
\end{aligned} \tag{4.78}$$

where $\bar{\mathbf{U}}_n^{(k+1,s)}$ is determined by (4.70) via replacing superscript $(k+1)$ by $(k+1,s)$, and the block-cyclic system matrix is given by

$$\mathbf{G}_{\mathrm{d}}^{(k)} = \begin{bmatrix} \mathbf{Q}_{\mathrm{d}}\big(\mathbf{Z}^{(k)}\big) & & & -\mathbf{C} \\ -\mathbf{C} & \mathbf{Q}_{\mathrm{d}}\big(\mathbf{Z}^{(k)}\big) & & \\ & \ddots & \ddots & \\ & & -\mathbf{C} & \mathbf{Q}_{\mathrm{d}}\big(\mathbf{Z}^{(k)}\big) \end{bmatrix}. \tag{4.79}$$

A possible choice of the vector $\mathbf{Z}^{(k)}$ could be the average of the solution at PP-PC iteration k [82], i.e.,

$$\mathbf{Z}^{(k)} = \frac{1}{N}\sum_{n=0}^{N-1} \mathbf{U}_n^{(k)}. \tag{4.80}$$

As a result, at PP-PC iteration $k+1$, the MH diagonalization from Section 3.3.2 can be applied to the Newton system (4.77) with the matrix $\mathbf{G}_{\mathrm{d}}^{(k)}$ defined in (4.79). In particular, a block-diagonal system of the form (3.98), or equivalently, separate systems for each frequency component $\hat{\mathbf{U}}_j^{(k+1,s+1)}$

$$\big(\hat{\mathbf{G}}_{\mathrm{d}}^{(k)}\big)_0 \hat{\mathbf{U}}_0^{(k+1,s+1)} = \hat{\mathbf{h}}_N^{(k+1,s)}, \qquad \big(\hat{\mathbf{G}}_{\mathrm{d}}^{(k)}\big)_j \hat{\mathbf{U}}_j^{(k+1,s+1)} = \hat{\mathbf{h}}_j^{(k+1,s)}, \quad j = 1, \ldots, N-1, \tag{4.81}$$

can be obtained, using the DFT matrix $\mathbf{F}$ from (3.100) and its Hermite conjugate matrix $\mathbf{F}^{\mathrm{H}}$. The system matrices are given by

$$\big(\hat{\mathbf{G}}_{\mathrm{d}}^{(k)}\big)_j = \mathbf{Q}_{\mathrm{d}}\big(\mathbf{Z}^{(k)}\big) - \mathbf{C}\exp(-\imath\omega_j \Delta T), \quad j = 0, \ldots, N-1. \tag{4.82}$$

The single frequency components $\hat{\mathbf{U}}_j^{(k+1,s+1)}$ are stored in the joint vector $\hat{\mathbf{U}}_{\mathrm{tot}}^{(k+1,s+1)}$, which can be transformed into the vector $\mathbf{U}_{\mathrm{tot}}^{(k+1,s+1)}$ in time domain by applying the inverse DFT as in (3.104).

As the termination criterion of the simplified Newton iteration (4.77) at PP-PC iteration $k+1$ the error $\varepsilon_{\mathrm{PC,\,it}}^{(k+1,s+1)}$ from (4.29) is used, while the error at the PP-PC iteration k is given by $\varepsilon_{\mathrm{PP}}^{(k)}$ in (4.26). Summarizing the described methodology, we provide the pseudocode of the PP-PC MH method for nonlinear TP problems based on [82] in Algorithm 1.

Remark 4.6 ([82])**.** *Note that the simplified Newton iteration* (4.72) *could be also interpreted as a linear iterative method based on an additive splitting of the system matrix in* (4.68)*. Indeed, using any constant matrix* $\mathbf{H}^{(k)} \in \mathbb{R}^{N_{\mathrm{d}}N \times N_{\mathrm{d}}N}$ *we can introduce at PP-PC iteration* $k+1$ *a linear iteration for* $s = 0, 1, \ldots$

$$\mathbf{H}^{(k)}\mathbf{U}_{\mathrm{tot}}^{(k+1,s+1)} = -\Big[\mathbf{F}\big(\mathbf{U}_{\mathrm{tot}}^{(k+1,s)}\big) - \mathbf{H}^{(k)}\mathbf{U}_{\mathrm{tot}}^{(k+1,s)}\Big], \tag{4.83}$$

which in case of $\mathbf{H}^{(k)} = \mathbf{J}_{\mathbf{F}}\big(\mathbf{U}^{(k+1,0)}\big)$ *becomes exactly the simplified Newton iteration* (4.72)*. Besides, the choice*

$$\mathbf{H}^{(k)}\big(\mathbf{U}_{\mathrm{tot}}^{(k+1)}\big) = \mathrm{diag}\Big[\mathbf{Q}_{\mathrm{d}}\big(\bar{\mathbf{U}}_N^{(k+1)}\big), \mathbf{Q}_{\mathrm{d}}\big(\bar{\mathbf{U}}_1^{(k+1)}\big), \ldots, \mathbf{Q}_{\mathrm{d}}\big(\bar{\mathbf{U}}_{N-1}^{(k+1)}\big)\Big],$$

with $\bar{\mathbf{U}}_n^{(k+1)}$, $n = 1, \ldots, N$, *defined in* (4.70) *from* $\mathbf{U}_{\mathrm{tot}}^{(k+1)}$, *yields the Jacobi-like fixed-point iteration* (4.25)*, [82].*

Algorithm 1 PP-PC MH algorithm [82].

initialize: $\tilde{\mathbf{U}}_j^{(0)}, \bar{\mathbf{U}}_j^{(0)}, \mathbf{U}_{j-1}^{(0)} \leftarrow \mathbf{0}$, $\varepsilon_{\mathrm{PP}}^{(0)} \leftarrow \varepsilon_{\mathrm{tol}}$, set counter: $k \leftarrow 0$;
while $k \leq K$ **and** $\varepsilon_{\mathrm{PP}}^{(k)} \geq \mathrm{Tol}$ **do**
  calculate: $\mathbf{b}_j^{(k)} \leftarrow \tilde{\mathbf{U}}_j^{(k)} - \bar{\mathbf{U}}_j^{(k)}$, choose $\mathbf{Z}^{(k)}$, e.g., by (4.80), assign $\big(\hat{\mathbf{G}}_{\mathrm{d}}^{(k)}\big)_j$ by (4.82);
  initialize: $\mathbf{U}^{(k+1,0)}$ by (4.75), $\varepsilon_{\mathrm{PC,\ it}}^{(k+1,0)} \leftarrow \varepsilon_{\mathrm{tol}}$, set counter: $s \leftarrow 0$;
  while $s \leq S$ **and** $\varepsilon_{\mathrm{PC,\ it}}^{(k+1,s)} \geq \varepsilon_{\mathrm{tol}}$ **do**
    FFT of the RHS in (4.77): $\hat{\mathbf{h}}_{\mathrm{tot}}^{(k+1,s)} \leftarrow (\mathbf{F} \otimes \mathbf{I})\mathbf{h}_{\mathrm{tot}}^{(k+1,s)}$;
    parfor $j \leftarrow 1, N$ **do**
      solve (4.81) for each frequency component $\hat{\mathbf{U}}_{j-1}^{(k+1,s+1)}$;
    end parfor
    inverse FFT of the solution: $\mathbf{U}_{\mathrm{tot}}^{(k+1,s+1)} \leftarrow (\mathbf{F}^{\mathrm{H}} \otimes \mathbf{I})\hat{\mathbf{U}}_{\mathrm{tot}}^{(k+1,s+1)}$;
    update $\varepsilon_{\mathrm{PC,\ it}}^{(k+1,s+1)}$ by (4.29), increment counter: $s \leftarrow s + 1$;
  end while
  assign $\mathbf{U}_j^{(k+1)} := \mathbf{U}_j^{(k+1,s)}$;
  parfor $j \leftarrow 1, N$ **do**
    solve fine problem: $\tilde{\mathbf{U}}_j^{(k+1)} \leftarrow \mathcal{F}\big(T_j, T_{j-1}, \mathbf{U}_{j-1}^{(k+1)}\big)$;
    solve coarse problem: $\bar{\mathbf{U}}_j^{(k+1)} \leftarrow \mathcal{G}\big(T_j, T_{j-1}, \mathbf{U}_{j-1}^{(k+1)}\big)$;
  end parfor
  update $\varepsilon_{\mathrm{PP}}^{(k+1)}$ by (4.26), increment counter: $k \leftarrow k + 1$;
end while

Remark 4.7. *Clearly, the simplified Newton iteration* (4.72) *followed by the MH diagonalization can be applied also to the direct TP discretization* (3.95)*. In this case the error like* (4.29)

$$\varepsilon_{\mathrm{it}}^{(s+1)} = \frac{\big\|\mathbf{u}_{\mathrm{tot}}^{(s+1)} - \mathbf{u}_{\mathrm{tot}}^{(s)}\big\|_*}{\varepsilon_{\mathrm{tol}} + \big\|\mathbf{u}_{\mathrm{tot}}^{(s+1)}\big\|_*} \tag{4.84}$$

is used in the termination criterion, where $\|\cdot\|_*$ *is defined in* (4.28)*. When nearly as many processing units as the (fine) time steps within the TP discretization are available, one may expect this to outperform the speed up provided by the PinT solution on the fine grid in PP-PC. However, we note that the application of the MH solver to the PP-PC system and not to the direct TP discretization* (3.95) *is especially beneficial when the number of processors* N *is limited, i.e., smaller than the number of variables* N_{f} *within the TP MH approach. We refer to Section 5.4 for a numerical convergence and speed up study.*

4.4.2 Convergence analysis for a model problem

We analyze the convergence of the simplified Newton iteration (4.72), based on the result from Theorem 3.16 following [82]. Motivated by the result of the Theorem 3.9, where the properties of the operator $\tilde{A}$ given in (3.25) are derived from the properties of the reluctivity ν, we consider the following TP model problem for a nonlinear ODE

$$\begin{aligned} mu'(t) + \nu(|u|)u(t) &= f(t), \quad t \in (0,T), \\ u(0) &= u(T), \end{aligned} \tag{4.85}$$

with $m \in \mathbb{R}_0^+$, function $\nu\colon \mathbb{R}_0^+ \to \mathbb{R}_0^+$, unknown $u\colon [0,T] \to \mathbb{R}$, and T-periodic input f, i.e., $f(0) = f(T), T > 0$. We assume that the nonlinear function ν satisfies the conditions **B.1**-**B.4** of the Corollary 2.2. We now apply the simplified Newton iteration (4.72) to (4.85). Analogously to (4.73) the Jacobian matrix for the problem (4.85) is determined for $\mathbf{U} = [U_0, U_1, \ldots, U_{N-1}]^\top$, at PP-PC iteration $k+1$ by

$$\mathbf{J_F}(\mathbf{U}) = \begin{bmatrix} q_\mathrm{d}(\bar{U}_N) & & & -c \\ -c & q_\mathrm{d}(\bar{U}_1) & & \\ & \ddots & \ddots & \\ & & -c & q_\mathrm{d}(\bar{U}_{N-1}) \end{bmatrix}, \tag{4.86}$$

where $c = m/\Delta T$, $q_\mathrm{d}(x) = c + \nu_\mathrm{d}(x)$, $\nu_\mathrm{d}\colon \mathbb{R} \mapsto \mathbb{R}_0^+$ is given by

$$\nu_\mathrm{d}(x) = \nu'(|x|)|x| + \nu(|x|), \quad x \in \mathbb{R}, \tag{4.87}$$

and $\bar{U}_n$ is defined by $\mathbf{U}$ via

$$\bar{U}_n = U_n - b_n^{(k)}, \quad n = 1, \ldots, N-1, \qquad \bar{U}_N = U_0 - b_N^{(k)}, \tag{4.88}$$

with $b_n^{(k)} = \mathcal{F}\big(T_n, T_{n-1}, U_{n-1}^{(k)}\big) - \mathcal{G}\big(T_n, T_{n-1}, U_{n-1}^{(k)}\big)$. As in (4.75), choosing a fixed value $z^{(k)} \in \mathbb{R}$ we define the initial approximation for the simplified Newton algorithm at PP-PC iteration $k+1$ by

$$\mathbf{U}_\mathrm{tot}^{(k+1,0)} = \Big[z^{(k)} + b_N^{(k)}, z^{(k)} + b_1^{(k)} \ldots, z^{(k)} + b_{N-1}^{(k)}\Big]^\top. \tag{4.89}$$

Analogously to (4.79), the matrix $\mathbf{G}_\mathrm{d}^{(k)} = \mathbf{J_F}\big(\mathbf{U}_\mathrm{tot}^{(k+1,0)}\big)$ is given by

$$\mathbf{G}_\mathrm{d}^{(k)} = \begin{bmatrix} q_\mathrm{d}\big(z^{(k)}\big) & & & -c \\ -c & q_\mathrm{d}\big(z\big) & & \\ & \ddots & \ddots & \\ & & -c & q_\mathrm{d}\big(z\big) \end{bmatrix}. \tag{4.90}$$

Before demonstrating the convergence results based on the Theorem 3.16 we derive some properties of the function ν_d in the following lemma.

Lemma 4.8 ([82]). *If the nonlinear function ν in* (4.85) *satisfies the conditions **B.2**-**B.3** in Corollary 2.2 and the function $g(s) = \nu'(s)s$, $s \in \mathbb{R}_0^+$, is Lipschitz continuous with Lipschitz constant ν_0', we have that the function ν_d from* (4.87) *is*

1) bounded from below by c_1, i.e.,

$$\nu_\mathrm{d}(x) \geq c_1 \quad \forall x \in \mathbb{R}, \tag{4.91}$$

2) Lipschitz continuous with Lipschitz constant $\nu_2 = \nu_0' + \nu_1$, i.e.,

$$|\nu_\mathrm{d}(x) - \nu_\mathrm{d}(y)| \leq \nu_2 |x - y| \quad \forall x, y \in \mathbb{R}, \tag{4.92}$$

where we assume there exists $\nu_1 = \sup_{t \in \mathbb{R}_0^+} |\nu'(t)| < \infty$.

Proof. The proof is based on [70, 99].

1) Based on the proof in [99, Lemma 2.8], strong monotonicity of $f(s) = \nu(s)s$, $s \in \mathbb{R}_0^+$, with constant c_1 given in **B.3** implies strong monotonicity of $f_{\text{abs}}(s) = \nu(|s|)s$, $s \in \mathbb{R}$, with the same constant c_1. This yields the condition (4.91), since $\nu_{\text{d}}(s) = f'_{\text{abs}}(s)$, $s \in \mathbb{R}$.

2) Due to the boundedness $|\nu'(s)| \leq \nu_1$, $s \in \mathbb{R}_0^+$, which we assume to hold in **B.2**, and the mean value theorem we obtain that ν is Lipschitz continuous with Lipschitz constant ν_1, since for some $\xi \in \mathbb{R}_0^+$

$$|\nu(t) - \nu(s)| = |\nu'(\xi)(t-s)| \leq \nu_1 |t-s|, \quad t, s \in \mathbb{R}_0^+. \tag{4.93}$$

The assumption on $g(s) = \nu'(s)s$ and the Lipschitz condition (4.93) yield for $\nu_{\text{d}}(x) = g(|x|) + \nu(|x|)$, $x \in \mathbb{R}$,

$$|\nu_{\text{d}}(x) - \nu_{\text{d}}(y)| = \big|g(|x|) - g(|y|) + \nu(|x|) - \nu(|y|)\big| \leq (\nu_0' + \nu_1)|x-y|, \quad x, y \in \mathbb{R},$$

which then gives (4.92) with $\nu_2 = \nu_1 + \nu_0'$.

□

Theorem 4.9 ([82])**.** *If the assumptions of the Lemma 4.8 hold, then the affine covariant Lipschitz condition* (3.67) *holds with constant* $\delta_0 = \nu_2/c_1$*, where* c_1 *and* ν_2 *are given in* (4.91) *and* (4.92)*, respectively.*

Proof. We first decompose the cyclic matrix $\mathbf{G}_{\text{d}}^{(k)}$ from (4.90) as

$$\mathbf{G}_{\text{d}}^{(k)} = \mathbf{F}^{\text{H}} \hat{\mathbf{G}}_{\text{d}}^{(k)} \mathbf{F}, \tag{4.94}$$

with the unitary DFT matrix $\mathbf{F}$ defined in (3.100), its Hermite conjugate matrix $\mathbf{F}^{\text{H}}$, and diagonal matrix $\hat{\mathbf{G}}_{\text{d}}^{(k)}$ with the elements

$$\big(\hat{\mathbf{G}}_{\text{d}}^{(k)}\big)_j = \nu_{\text{d}}\big(z^{(k)}\big) + \big(1 - \exp(-\imath\omega_j \Delta T)\big)c, \quad j = 0, \ldots, N-1,$$

which are also the eigenvalues of $\mathbf{G}_{\text{d}}^{(k)}$. Let $\|\cdot\|_2 = \sigma_{\max}(\cdot)$ denote the largest singular value of a matrix, which for a normal matrix such as $\big(\mathbf{G}_{\text{d}}^{(k)}\big)^{-1}$ is equal to its spectral radius. We then have due to (4.91) and since $c \in \mathbb{R}_0^+$ the estimate

$$\begin{aligned}
\big\|\big(\mathbf{G}_{\text{d}}^{(k)}\big)^{-1}\big\|_2 = \big\|\big(\mathbf{F}^{\text{H}} \hat{\mathbf{G}}_{\text{d}} \mathbf{F}\big)^{-1}\big\|_2 = \big\|\big(\hat{\mathbf{G}}_{\text{d}}^{(k)}\big)^{-1}\big\|_2 &= \max_{0 \leq j \leq N-1} \Big|\Big[\nu_{\text{d}}\big(z^{(k)}\big) + \big(1 - \exp(-\imath\omega_j \Delta T)\big)c\Big]^{-1}\Big| \\
&\leq \max_{0 \leq j \leq N-1} \Big[\operatorname{Re}\Big(\nu_{\text{d}}\left(z\right) + \big(1 - \exp(-\imath\omega_j \Delta T)\big)c\Big)\Big]^{-1} = \max_{0 \leq j \leq N-1} \Big[\nu_{\text{d}}\left(z\right) + \big(1 - \cos\left(\Delta T \omega_j\right)\big)c\Big]^{-1} \\
&\leq \big(\nu_{\text{d}}(z)\big)^{-1} \leq 1/c_1.
\end{aligned} \tag{4.95}$$

Using (4.95), the Lipschitz condition (4.92), and the definition (4.88), we obtain the affine covariant Lipschitz condition (3.67) with $\delta_0 = \nu_2/c_1$

$$\begin{aligned}
&\Big\|\Big[\mathbf{J}_{\mathbf{F}}\big(\mathbf{U}_{\text{tot}}^{(k+1,0)}\big)\Big]^{-1}\Big(\mathbf{J}_{\mathbf{F}}(\mathbf{U}) - \mathbf{J}_{\mathbf{F}}\big(\mathbf{U}_{\text{tot}}^{(k+1,0)}\big)\Big)\Big\|_2 \leq \big\|\big(\mathbf{G}_{\text{d}}^{(k)}\big)^{-1}\big\|_2 \big\|\mathbf{J}_{\mathbf{F}}(\mathbf{U}) - \mathbf{G}_{\text{d}}^{(k)}\big\|_2 \\
&\leq \max_{1 \leq n \leq N} \big|\nu_{\text{d}}(\bar{U}_n) - \nu_{\text{d}}\big(z^{(k)}\big)\big|/c_1 \leq \nu_2/c_1 \max_{1 \leq n \leq N} \big|\bar{U}_n - z^{(k)}\big| \leq \delta_0 \big\|\mathbf{U} - \mathbf{U}_{\text{tot}}^{(k+1,0)}\big\|_2.
\end{aligned}$$

□

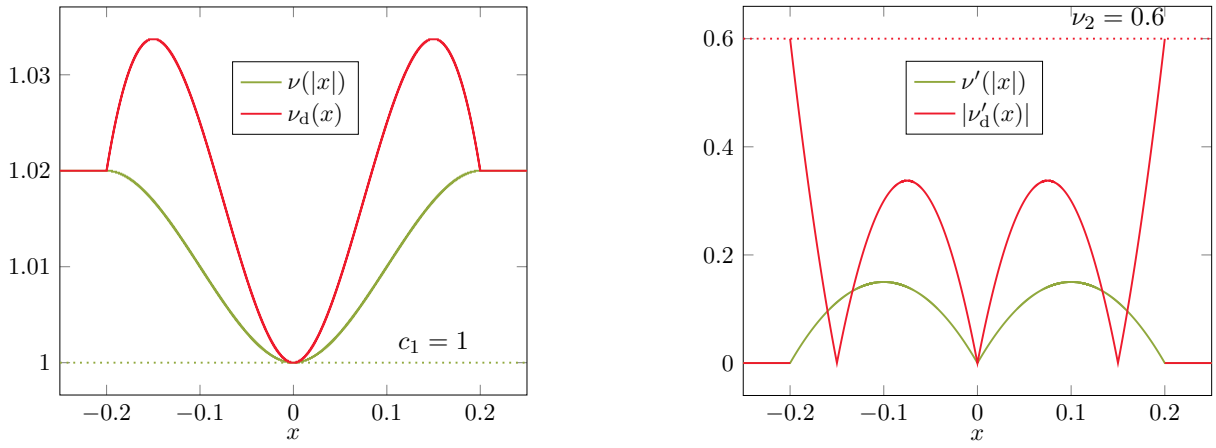

Figure 4.3: Nonlinearity of the model problem [82] ©2021 Society for Industrial and Applied Mathematics.

By the Theorem 3.16, the Lipschitz condition (3.67) with constant δ_0 implies the convergence of the simplified Newton method (4.77), provided that the bound

$$h_0 = \delta_0 \underbrace{\left\| \mathbf{U}^{(k+1,1)} - \mathbf{U}^{(k+1,0)} \right\|}_{=:\rho_1} \leq 0.5 \tag{4.96}$$

holds for the selected initial approximation $\mathbf{U}^{(k+1,0)}$. However, one should be aware of the fact that it may not always be possible to find an initial guess $\mathbf{U}_{\mathrm{tot}}^{(k+1,0)}$ which at the same time ensures the convergence of the simplified Newton iteration and has the form (4.75) for applicability of the MH solver to the system (4.77) with the block-cyclic matrix $\mathbf{G}_{\mathrm{d}}^{(k)}$ from (4.79).

4.4.3 Numerical study of a model problem

We discuss convergence of the simplified Newton method applied to a model problem (4.85) with $m = 0.1$, RHS $f(t) = 10^{-3}\sin(2\pi t/T)$, $T = 0.02\,\mathrm{s}$, and nonlinearity ν defined by a piecewise polynomial [82]

$$\nu(|x|) = \begin{cases} -5|x|^3 + 1.5|x|^2 + 1, & 0 \leq |x| < 0.1, \\ -5(|x| - 0.1)^3 + 0.15(|x| - 0.1) + 1.01, & 0.1 \leq |x| < 0.2, \\ 1.02, & 0.2 \leq |x|. \end{cases} \tag{4.97}$$

Such a problem can be interpreted as a nonlinear RL-circuit model with unknown magnetic flux x as in [51]. The nonlinear functions ν and ν_{d} are depicted in Figure 4.3 (left). This shows that the lower bound for both $\nu(|x|)$ and $\nu_{\mathrm{d}}(x)$, $x \in \mathbb{R}$ is $c_1 = 1$. Figure 4.3 (right) depicts the corresponding derivatives $\nu'(|x|)$ and $|\nu'_{\mathrm{d}}(x)|$, $x \in \mathbb{R}$. Based on the observed characteristics of ν one can deduce that the assumptions of the Lemma 4.8 and thus the Lipschitz condition (4.92) hold. We estimate the Lipschitz constant ν_2 as the upper bound for $|\nu'_{\mathrm{d}}(x)| \leq \nu_2 = 0.6$. Based on Theorem 4.9 we have $\delta_0 = \nu_2/c_1 = 0.6$, [82].

We now describe the performance of the simplified Newton algorithm for the TP discretization of the model problem depending on the choice of the initial approximation $\mathbf{U}^{(0)} = [z, z, \ldots, z]^\top \in D = (-0.25, 0.25)^N \subset \mathbb{R}^N$ with $N = 10$ [82]. In Figure 4.4a we show the number of iterations required until convergence with respect to the error (4.84). We observed that in the neighborhood of $z = 0$ as well as for $|z| \geq 0.2$ the algorithm converged in 2 iterations, while for $0.1 < |z| < 0.2$ the number of iterations was between 3 and 5. This shows that for the

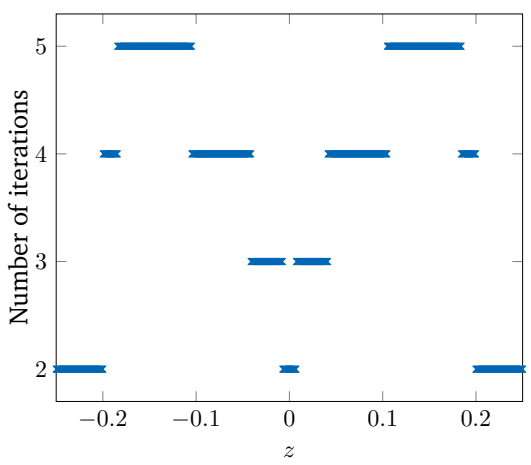

(a) Convergence for different choices of z.

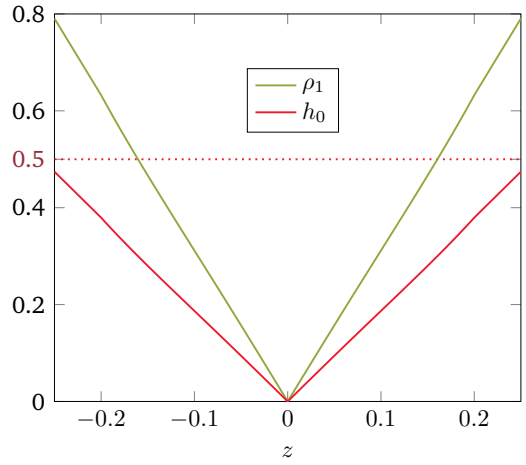

(b) Constants ρ_1 and h_0 from (4.96).

Figure 4.4: Convergence of the simplified Newton iteration [82] ©2021 Society for Industrial and Applied Mathematics.

considered example the simplified Newton method is convergent for all the considered initial approximations $\mathbf{U}^{(0)}$. The calculated periodic solution is $\mathbf{U}^* \approx 10^{-5} \cdot [-3.02, -1.8, 0.1, 1.9, 3.07, 3.01, 1.8, -0.1, -1.96, -3.07]^\top$ in all cases.

For each $\mathbf{U}^{(0)}$ the calculated values of $h_0 = \delta_0 \rho_1 = 0.6\rho_1$ from (4.96) together with ρ_1, are depicted in Figure 4.4b. We see that condition (4.96) holds, since for all cases $h_0 < 0.5$. Then by Theorem 3.16 the iterates $\mathbf{U}^{(s)}$ remain in the ball $\bar{S}(\mathbf{U}^{(0)}, \rho)$ of radius $\rho = (1 - \sqrt{1 - 2h_0})/\delta_0$, as is also observed numerically [82].

4.5 Time-periodic problems with unknown period

We now consider a TP ODE system with an UP $T > 0$, as in Section 3.3.3. In particular, we want to solve the problem (3.111)-(3.112) in d variables on the unit interval using the multiple shooting method with UP. For this, on the equidistant partition $0 = \tau_0 < \tau_1 < \ldots < \tau_N = 1$ of the unit interval $[0, 1]$, where $\tau_n = n\Delta\tau$, $n = 0, \ldots, N$, we solve the IVP

$$\tilde{\mathbf{u}}_n'(\tau) = T\mathbf{f}(\tilde{\mathbf{u}}_n(\tau)), \quad \tau \in (\tau_{n-1}, \tau_n], \tag{4.98}$$

$$\tilde{\mathbf{u}}_n(\tau_{n-1}) = \mathbf{U}_{n-1}, \tag{4.99}$$

for $n = 1, \ldots, N$. Let $\mathcal{F}(\tau, \tau_{n-1}, \mathbf{U}_{n-1}, T)$ denote the fine (exact) solution to (4.98)-(4.99). As described in the Section 3.3.3, the shooting method with UP reads for $k = 0, 1, \ldots$

$$\mathbf{U}_0^{(k+1)} = \mathcal{F}\big(\tau_N, \tau_{N-1}, \mathbf{U}_{n-1}^{(k)}, T^{(k)}\big) + \mathbf{G}_{N-1}^{(k)}\big[\mathbf{U}_{N-1}^{(k+1)} - \mathbf{U}_{N-1}^{(k)}\big] + \mathbf{g}_{N-1}^{(k)}\big[T^{(k+1)} - T^{(k)}\big], \tag{4.100}$$

$$\mathbf{U}_n^{(k+1)} = \mathcal{F}\big(\tau_n, \tau_{n-1}, \mathbf{U}_{n-1}^{(k)}, T^{(k)}\big) + \mathbf{G}_{n-1}^{(k)}\big[\mathbf{U}_{n-1}^{(k+1)} - \mathbf{U}_{n-1}^{(k)}\big] + \mathbf{g}_{n-1}^{(k)}\big[T^{(k+1)} - T^{(k)}\big], \tag{4.101}$$

with $n = 1, \ldots, N$ and

$$\mathbf{G}_{n-1}^{(k)} = \frac{\partial \mathcal{F}(\tau_n, \tau_{n-1}, \mathbf{U}_{n-1}^{(k)}, T^{(k)})}{\partial \mathbf{U}_{n-1}}, \qquad \mathbf{g}_{n-1}^{(k)} = \frac{\partial \mathcal{F}(\tau_n, \tau_{n-1}, \mathbf{U}_{n-1}^{(k)}, T^{(k)})}{\partial T}. \tag{4.102}$$

As in (3.118) we calculate $\mathbf{g}_{n-1}^{(k)} = \Delta\tau \mathbf{f}(\mathbf{U}_n^{(k)})$. Inheriting the idea of the Parareal we approximate $\mathbf{G}_{n-1}^{(k)}$ using a coarse propagator $\mathcal{G}$, i.e.,

$$\mathbf{G}_{n-1}^{(k)}\big[\mathbf{U}_{n-1}^{(k+1)} - \mathbf{U}_{n-1}^{(k)}\big] \approx \mathcal{G}\big(\tau_n, \tau_{n-1}, \mathbf{U}_{n-1}^{(k+1)}, T^{(k)}\big) - \mathcal{G}\big(\tau_n, \tau_{n-1}, \mathbf{U}_{n-1}^{(k)}, T^{(k)}\big). \tag{4.103}$$

Following [83], we substitute (4.103) into (4.100)-(4.101) and obtain the PP-PC algorithm with UP (PP-PC UP):

$$\begin{bmatrix} \mathbf{I} & & & -\mathcal{G}_N\left(\cdot, T^{(k)}\right) & -\mathbf{g}_{N-1}^{(k)} \\ -\mathcal{G}_1\left(\cdot, T^{(k)}\right) & \mathbf{I} & & & -\mathbf{g}_0^{(k)} \\ & \ddots & \ddots & & \\ & & -\mathcal{G}_{N-1}\left(\cdot, T^{(k)}\right) & \mathbf{I} & -\mathbf{g}_{N-2}^{(k)} \end{bmatrix} \begin{bmatrix} \mathbf{U}_0^{(k+1)} \\ \mathbf{U}_1^{(k+1)} \\ \vdots \\ \mathbf{U}_{N-1}^{(k+1)} \\ T^{(k+1)} \end{bmatrix} = \begin{bmatrix} \mathbf{b}_N^{(k)} \\ \mathbf{b}_1^{(k)} \\ \vdots \\ \mathbf{b}_{N-1}^{(k)} \end{bmatrix}, \tag{4.104}$$

where $\mathcal{G}_n\left(\cdot, T^{(k)}\right) = \mathcal{G}\big(\tau_n, \tau_{n-1}, \cdot, T^{(k)}\big)$ and

$$\mathbf{b}_n^{(k)} = -\mathbf{g}_{n-1}^{(k)} T^{(k)} + \mathcal{F}\big(\tau_n, \tau_{n-1}, \mathbf{U}_{n-1}^{(k)}, T^{(k)}\big) - \mathcal{G}\big(\tau_n, \tau_{n-1}, \mathbf{U}_{n-1}^{(k)}, T^{(k)}\big), \quad n = 1, \ldots, N. \tag{4.105}$$

In the general case, the system of equations (4.104) is nonlinear and implicit, which requires an additional linearization. Building upon the ideas presented in Section 4.4.1, we incorporate an additive splitting of the system matrix in (4.104) according to the Remark 4.6. For this, we introduce a modified coarse propagator $\bar{\mathcal{G}}$, which instead of (4.98)-(4.99) solves an approximate model with a linear function $\bar{\mathbf{f}}(\mathbf{u}) = \mathbf{A}\mathbf{u} + \mathbf{c}$ on the RHS, [83], i.e.,

$$\begin{aligned} \tilde{\mathbf{u}}_n'(\tau) &= T\bar{\mathbf{f}}(\tilde{\mathbf{u}}_n(\tau)) = T[\mathbf{A}\tilde{\mathbf{u}}_n(\tau) + \mathbf{c}_n], \quad \tau \in (\tau_{n-1}, \tau_n] \\ \tilde{\mathbf{u}}_n(\tau_{n-1}) &= \mathbf{U}_{n-1}, \end{aligned} \tag{4.106}$$

with a given matrix $\mathbf{A} \in \mathbb{R}^{d\times d}$ (which can be, e.g., the Jacobian matrix of $\mathbf{f}$) and a vector $\mathbf{c} \in \mathbb{R}^d$. Having the linear coarse model we construct a fixed point iteration at PP-PC UP iteration $k+1$: for $s = 0, 1, \ldots$

$$\begin{bmatrix} \mathbf{I} & & & -\bar{\mathcal{G}}_N\left(\cdot, T^{(k)}\right) & -\mathbf{g}_N^{(k)} \\ -\bar{\mathcal{G}}_1\left(\cdot, T^{(k)}\right) & \mathbf{I} & & & -\mathbf{g}_1^{(k)} \\ & \ddots & \ddots & & \\ & & -\bar{\mathcal{G}}_{N-1}\left(\cdot, T^{(k)}\right) & \mathbf{I} & -\mathbf{g}_{N-1}^{(k)} \end{bmatrix} \begin{bmatrix} \mathbf{U}_0^{(k+1,s+1)} \\ \mathbf{U}_1^{(k+1,s+1)} \\ \vdots \\ \mathbf{U}_{N-1}^{(k+1,s+1)} \\ T^{(k+1)} \end{bmatrix} = \begin{bmatrix} \mathbf{h}_N^{(k+1,s)} \\ \mathbf{h}_1^{(k+1,s)} \\ \vdots \\ \mathbf{h}_{N-1}^{(k+1,s)} \end{bmatrix}, \tag{4.107}$$

where $\bar{\mathcal{G}}_n\left(\cdot, T^{(k)}\right) = \bar{\mathcal{G}}\big(\tau_n, \tau_{n-1}, \cdot, T^{(k)}\big)$ and

$$\mathbf{h}_n^{(k+1,s)} = \mathbf{b}_n^{(k)} + \mathcal{G}\big(\tau_n, \tau_{n-1}, \mathbf{U}_{n-1}^{(k+1,s)}, T^{(k)}\big) - \bar{\mathcal{G}}\big(\tau_n, \tau_{n-1}, \mathbf{U}_{n-1}^{(k+1,s)}, T^{(k)}\big), \quad n = 1, \ldots, N. \tag{4.108}$$

We assume the coarse propagator $\bar{\mathcal{G}}$ is the IE method with the step size $\Delta\tau$, i.e., $\bar{\mathbf{U}}_{n-1}^{(k+1,s)} = \bar{\mathcal{G}}_n\big(\mathbf{U}_{n-1}^{(k+1,s)}, T^{(k)}\big)$ solves

$$\mathbf{Q}^{(k)}\bar{\mathbf{U}}_{n-1}^{(k+1,s)} - \mathbf{C}\mathbf{U}_{n-1}^{(k+1,s)} = T^{(k)}\mathbf{c}_n, \quad n = 1, \ldots, N, \tag{4.109}$$

where $\mathbf{C} = (1/\Delta\tau)\mathbf{I}$, $\mathbf{Q}^{(k)} = \mathbf{C} - T^{(k)}\mathbf{A}$, $\mathbf{c}_n = \mathbf{c}(\tau_n)$, and $\mathbf{I} \in \mathbb{R}^{d\times d}$ is the identity matrix. Plugging (4.109) into the system (4.107) we obtain [83]

$$\begin{bmatrix} -\mathbf{Q}^{(k)} & & & \mathbf{C} & -\mathbf{Q}^{(k)}\mathbf{g}_N^k \\ \mathbf{C} & -\mathbf{Q}^{(k)} & & & -\mathbf{Q}^{(k)}\mathbf{g}_1^k \\ & \ddots & \ddots & & \vdots \\ & & \mathbf{C} & -\mathbf{Q}^{(k)} & -\mathbf{Q}^{(k)}\mathbf{g}_{N-1}^k \end{bmatrix} \begin{bmatrix} \mathbf{U}_0^{(k+1,s+1)} \\ \mathbf{U}_1^{(k+1,s+1)} \\ \vdots \\ \mathbf{U}_{N-1}^{(k+1,s+1)} \\ T^{(k+1)} \end{bmatrix} = \left(\mathbf{I} \otimes \mathbf{Q}^{(k)}\right) \begin{bmatrix} \mathbf{h}_N^{(k+1,s)} \\ \mathbf{h}_1^{(k+1,s)} \\ \vdots \\ \mathbf{h}_{N-1}^{(k+1,s)} \end{bmatrix} + T^{(k)} \begin{bmatrix} \mathbf{c}_N \\ \mathbf{c}_1 \\ \vdots \\ \mathbf{c}_{N-1} \end{bmatrix}.$$

This is again an underdetermined system at each iteration but only on the coarse level in contrast to the one from the Section 3.3.3, which is based on a fine TP discretization.

4.6 Conclusion

In this chapter we described the Parareal algorithm for the parallel-in-time solution of initial-value problems and two Parareal variants for time-periodic problems: PP-IC and PP-PC. To solve problems with pulse-width modulated inputs, multirate Parareal and multirate PP-IC methods were proposed and analyzed. A simplified Newton-based linearization, which transforms the PP-PC system into a block-cyclic form, was introduced. This enabled the application of the multi-harmonic diagonalization and additional parallelization on the coarse grid. Convergence of the proposed PP-PC MH method was analyzed and studied numerically for a nonlinear model problem. Finally, a Parareal-based approach for the solution of time-periodic problems with unknown period, called PP-PC UP, was proposed. In the following chapter the parallel-in-time methods considered are exploited for different electromagnetic applications such as power converters, induction motors, and transformers.

5 Applications and numerical results

Having set a solid theoretical basis in the previous chapters, we apply the numerical methods considered to diverse applications from electrical engineering such as electric circuits, power converters, induction motors, and transformers. First, in Section 5.1 an RL-circuit model is used for numerical convergence studies of the multirate Parareal and multirate PP-IC algorithms, proposed in Section 4.3 for problems with PWM inputs. The performance of the two methods is illustrated through their application to a four-pole induction machine under no-load operation. Several choices of the surrogate coarse solver, in particular, a low-frequency input and the MPDE approach, within the multirate Parareal algorithm are investigated for a buck converter model.

Non-intrusiveness of the PP-IC algorithm allows its incorporation into an industrial solver, which is demonstrated in Section 5.2 for the solver EDYSON of the Robert Bosch GmbH. The application to several operating points of an induction motor built into an electric vehicle drive confirms the significant potential of the method to accelerate the steady-state analysis of the dynamical systems in engineering. Good performance of Parareal(-based) method(s) is not assured for all problems at hand. In particular, it is known that Parareal converges quite slowly for hyperbolic problems and linear oscillatory systems described by second-order ODEs, barely giving any speed up compared to the sequential time stepping [9, 40]. These convergence difficulties were analyzed in [44, 46] for hyperbolic problems and in [47] for Hamiltonian systems of ODEs like the harmonic oscillator and Keppler's equation of motion. In Section 5.3 we perform eigenvalue studies of several rotating electromagnetic devices to indicate whether the application of the Parareal method is reasonable.

The calculation of the steady-state solution of a 2D coaxial cable model is performed in Section 5.4 using the PinT approaches considered, namely, PP-IC, PP-PC with a Jacobi-like linearization [50], PP-PC with MH coarse grid correction [82] (see Section 4.4), as well as the fine TP discretization with MH diagonalization (see Remark rem:TP-MH). The PP-PC MH and TP MH approaches are also applied to a 3D transformer model in Section 5.5. Finally, PP-PC method with an UP, introduced in the Section 4.5 is tested on the Colpitts oscillator circuit in Section 5.6. The efficiency of the considered algorithms, which calculate TP solutions, is estimated in comparison to the sequential time stepping with the IE method starting from an IC $\mathbf{u}_0$ until the steady state. On each period $[(k-1)T, kT]$, $k \geq 1$, the periodicity error of the sequential solution $\mathbf{u}(t) \in \mathbb{R}^{N_\mathrm{d}}$ given by

$$\varepsilon_{\mathrm{seq}}(k) = \|\mathbf{u}(kT) - \mathbf{u}\big((k-1)T\big)\|_\times \tag{5.1}$$

is calculated, where $\|\cdot\|_\times$ is a norm in an N_d-dimensional space. The time stepping is terminated once the error (5.1) has become smaller than a prescribed relative tolerance $\varepsilon_{\mathrm{tol}}$ on a period $[(k^*-1)T, k^*T]$. The precision (or the step size δT) of the obtained steady-state solution is the same as that of the fine solver of an applied PinT method.

The efficiency of the algorithms is evaluated in terms of the number of *effective linear systems solutions* (ELSS) or *effective (nonlinear) time steps*, which is the total number of solution processes executed sequentially. In case of parallel computations this corresponds to the maximum number of system solutions performed

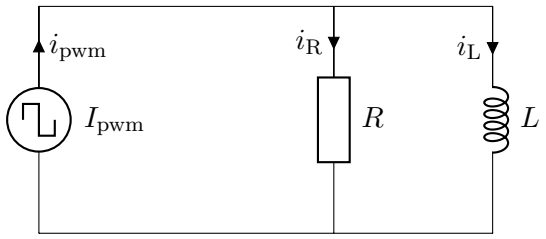

Figure 5.1: RL-circuit with PWM current source i_{pwm}.

by a single core. This is a convenient and easily reproducible measure because of its independence of the software implementation. Besides, for all the PinT methods it is assumed that the number of subintervals N is equal to the number of available processing units, i.e., one processor governs exactly one subinterval.

The considered methods are implemented in GNU Octave version 3.8.2 using the 'parallel' package[8] for parallelization. We use Octave's Fourier analysis implemented by the parallel version of FFTW3[9] using 80 threads. The code is executed on an Intel Xeon cluster with $80 \times 2.00\,\mathrm{GHz}$ cores, i.e., $8\times$E7-8850 and 1TB DDR3 memory.

5.1 Problems with PWM excitations

In this section we consider several problems from electrical engineering, which include PWM inputs described in Section 2.3. For these examples the performance of the multirate Parareal and the multirate PP-IC is investigated and compared to the standard Parareal and the sequential time-stepping computation.

5.1.1 RL-circuit: numerical study

Based on [51], we study the convergence of the multirate Parareal algorithm (4.34)-(4.35) in terms of Theorem 4.4 for an ODE of the form (4.48), which models an RL-circuit shown in Figure 5.1. The RL-circuit model can be derived from the KCL (see Section 2.2) and is written for the unknown magnetic flux ϕ as [51]

$$R^{-1}\phi'(t) + L^{-1}\phi(t) = i_{\mathrm{pwm}}(t), \quad t \in (0, T], \tag{5.2}$$

with resistance $R = 10^{-2}\,\Omega$, inductance $L = 10^{-3}\,\mathrm{H}$, period $T = 2 \cdot 10^{-2}\,\mathrm{s}$, and PWM current source i_{pwm} (see Section 2.3) of switching frequency $f_s = 20\,\mathrm{kHz}$, defined by [51]

$$i_{\mathrm{pwm}}(t) = \begin{cases} \operatorname{sign}\big[\sin(2\pi f_r t)\big], & \big(f_s t - \lfloor f_s t \rfloor\big) - \big|\sin(2\pi f_r t)\big| < 0, \\ 0, & \text{otherwise}, \end{cases} \tag{5.3}$$

where $f_r = 50\,\mathrm{Hz}$ is the frequency of the reference signal. Figure 5.2a illustrates an example of such a PWM signal i_{pwm} of $5\,\mathrm{kHz}$.

[8] `http://octave.sourceforge.io/parallel`.
[9] `http://www.fftw.org/parallel`.

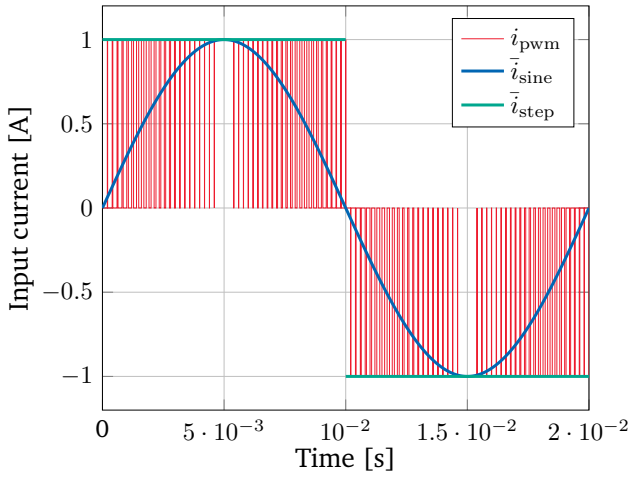

(a) PWM input of frequency $f_s = 5\,\text{kHz}$ and two coarse inputs [52] ©Springer Nature Switzerland AG 2020.

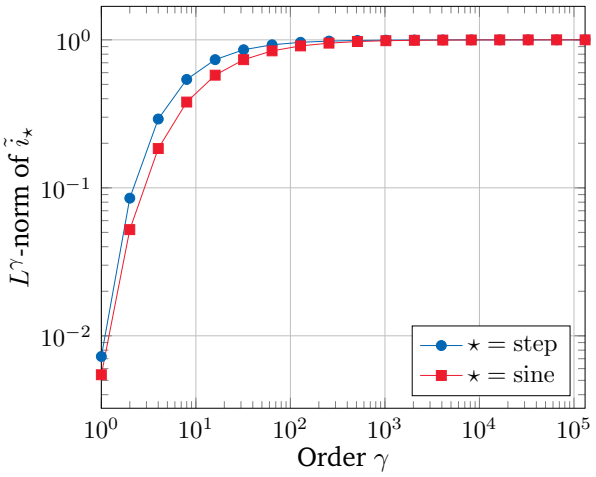

(b) L^γ-norm of $\tilde{i}_\star$ from (5.6), $\star \in \{\text{sine}, \text{step}\}$ [52] ©2019 Society for Industrial and Applied Mathematics.

Figure 5.2: Fine PWM input, two coarse inputs and their difference from the fine input.

We choose $n = 4$ and $T_4 = 4\Delta T$, in the estimates (4.14) and (4.39), and apply the standard and the multirate Parareal methods to the ODE (5.2) with a prescribed IC $\phi(0) = 0$. The fine step size is chosen $\delta T = T/2^{17} \approx 1.5 \cdot 10^{-7}\,\text{s}$. The coarse step size is $\Delta T = T/N$, with $N = 2^2, \ldots, 2^q$, $2 \leq q \leq 17$.

5.1.1.1 Standard Parareal algorithm

We first consider the standard Parareal method (4.9)-(4.10), where both fine and coarse problem solve the ODE (5.2) with the PWM excitation of $f_s = 20\,\text{kHz}$. In this case, for a small number of processors, $N \ll m = Tf_s$, where m denotes the number of pulses, the coarse propagator does not resolve the dynamics of the excitation. However, for N large enough, when the coarse propagator resolves all the pulses and the function is locally smooth, one can expect the high convergence rate of the Parareal algorithm to be maintained according to Theorem 4.1, [51].

For the IE method (of order $p = 1$) being the fine and the coarse solver, Figure 5.3a illustrates the error at iterations $k = 1$ and $k = 2$. There, we see that for large N we obtain 4th order convergence for $k = 1$, which matches the prediction $(p + 1)(k + 1) = 4$ in (4.14). However, for small N ($N < 20$), the convergence order is much lower. Convergence deceleration is even more evident for $k = 2$, where the order reduction remains even for larger N [51]. In Figure 5.3b, the results for the TR (of order $p = 2$) and $k = 1$ are shown. There, the asymptotic order is reduced to 5 instead of the order $(p + 1)(k + 1) = 6$, predicted by the standard Parareal's estimate in (4.14), [51].

5.1.1.2 Multirate Parareal algorithm

We now apply the multirate Parareal method (4.34)-(4.35) for the ODE (5.2). We consider two choices for the surrogate coarse excitation: the sinusoidal function $\bar{i}_{\text{sine}}$ and the step function $\bar{i}_{\text{step}}$, illustrated in Figure 5.2a

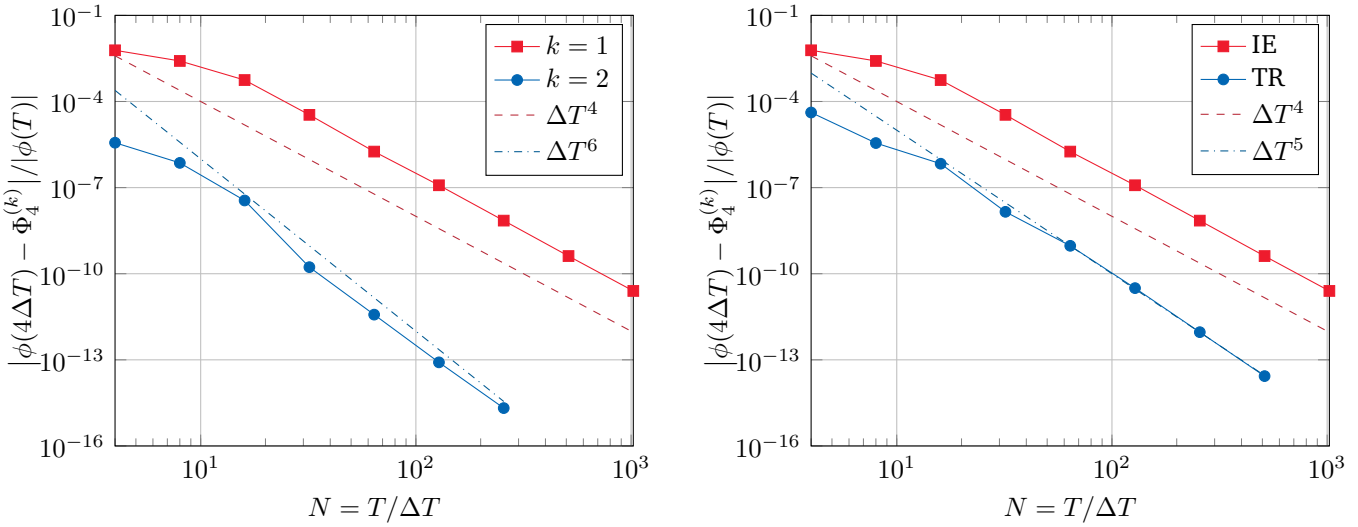

(a) IE method, $k = 1, 2$.

(b) IE method and TR, $k = 1$.

Figure 5.3: Convergence of the standard Parareal algorithm [51] ©2019 Society for Industrial and Applied Mathematics.

and given by

$$\bar{i}_{\text{sine}}(t) = \sin(2\pi f_r t), \quad t \in [0, T], \tag{5.4}$$

$$\bar{i}_{\text{step}}(t) = \begin{cases} 1, & t \in [0, T/2], \\ -1, & t \in (T/2, T], \end{cases} \tag{5.5}$$

with $f_r = 50\,\text{Hz}$. We note that the step function (5.5) is discontinuous only at $t = T/2$. This does not cause any difficulties, since we choose the discontinuity to be located exactly at a synchronization point [52]. The coarse propagator $\bar{\mathcal{G}}$ then solves the RL-circuit model (5.2) with one of the inputs $\bar{i}_{\text{sine}}$ or $\bar{i}_{\text{step}}$ instead of i_{pwm}, while the fine propagator $\mathcal{F}$ solves the ODE (5.2) with the PWM input (5.3) of switching frequency $f_s = 20\,\text{kHz}$. The non-smooth part of the PWM input is given by

$$\tilde{i}_\star(t) = i_{\text{pwm}}(t) - \bar{i}_\star(t), \quad t \in [0, T], \tag{5.6}$$

where $\star = \text{sine}$ and $\star = \text{step}$ for the sinusoidal input (5.4) and the step input (5.5), respectively. Clearly, $\tilde{i}_\star \in L^\infty((0, T))$ for both sinusoidal and step coarse inputs. This leads to the freedom in the choice of $\gamma \geq 1$ in the L^γ-norm of $\tilde{i}_\star$, which influences the convergence rate due to the estimate (4.39), [51]. In fact, it could be seen that for both choices of the coarse input

$$\|\tilde{i}_\star\|_{L^\infty((0,T))} = 1, \quad \star \in \{\text{sine}, \text{step}\}.$$

However, based on the calculated values of the norms presented in Figure 5.2b we can conclude that for any $1 \leq \gamma < \infty$ the L^γ-norm of $\tilde{i}_{\text{sine}}$ is smaller than that of $\tilde{i}_{\text{step}}$. This implies that the sinusoidal waveform is a superior candidate for the coarse input than the step function, and therefore could lead to a higher convergence rate.

Figure 5.4a and Figure 5.4b illustrate the convergence of the multirate Parareal algorithm using IE on both fine and coarse levels for iteration $k = 1$ and $k = 2$, respectively. When the step function $\bar{i}_{\text{step}}$ from (5.5) is

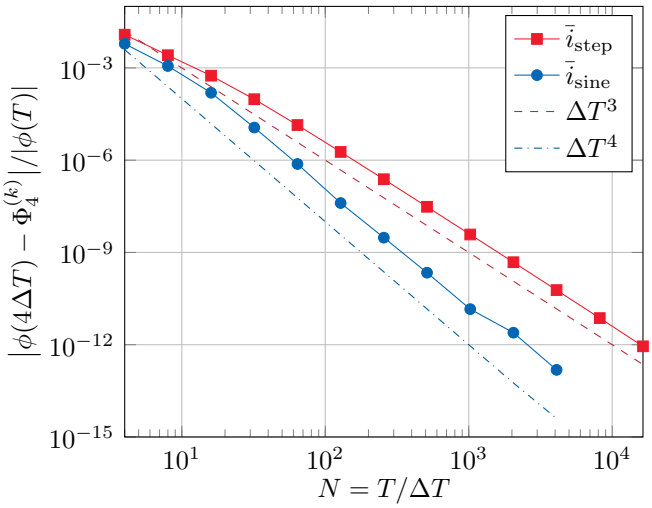

(a) IE method, $k = 1$.

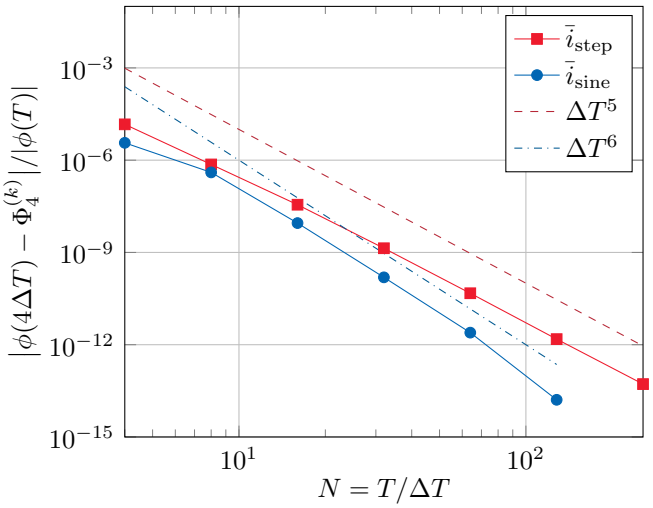

(b) IE method, $k = 2$.

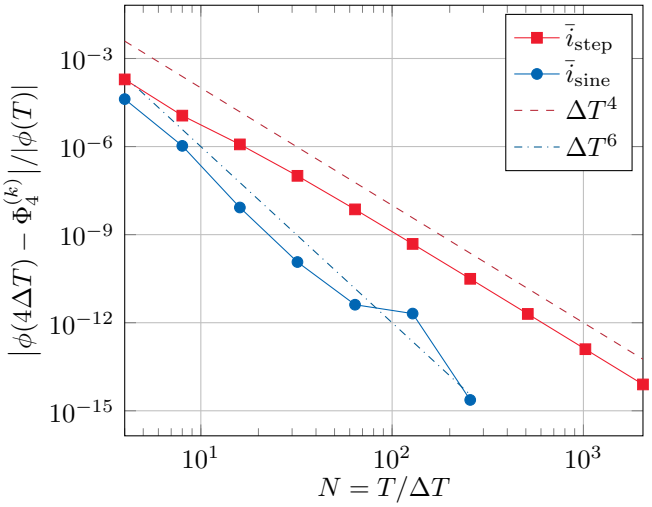

(c) TR scheme, $k = 1$.

Figure 5.4: Convergence of the multirate Parareal algorithm [51] ©2019 Society for Industrial and Applied Mathematics.

used for the coarse propagator, we observe an order reduction, which matches the theoretical predictions. In particular, we get orders $(p+1)k+1 = 3$ and $(p+1)k+1 = 5$, which are the maximal orders of the lowest-order term in (4.39) for $k = 1$ and $k = 2$, respectively, [51]. On the other hand, in case of the sinusoidal excitation $\bar{i}_{\text{sine}}$ from (5.4) applied for the coarse problem, the highest-order term in the estimate (4.39) is dominant over the lowest-order term. Indeed, convergence of orders $(p+1)(k+1) = 4$ and $(p+1)(k+1) = 6$ are obtained for $k = 1$ and $k = 2$, respectively, [51]. Hence, the sinusoidal function is shown to be a good choice of the coarse input, since in this case the multirate Parareal has the same convergence rate $(p+1)(k+1)$, as the standard Parareal. This happens also when using the TR and $k = 1$, as illustrated in Figure 5.4c. There, the step input function $\bar{i}_{\text{step}}$ leads to the convergence order $(p+1)k+1 = 4$, while the sinusoidal input $\bar{i}_{\text{sine}}$ gives order $(p+1)(k+1) = 6$, which are lowest- and the highest-order terms in (4.39), respectively, [51].

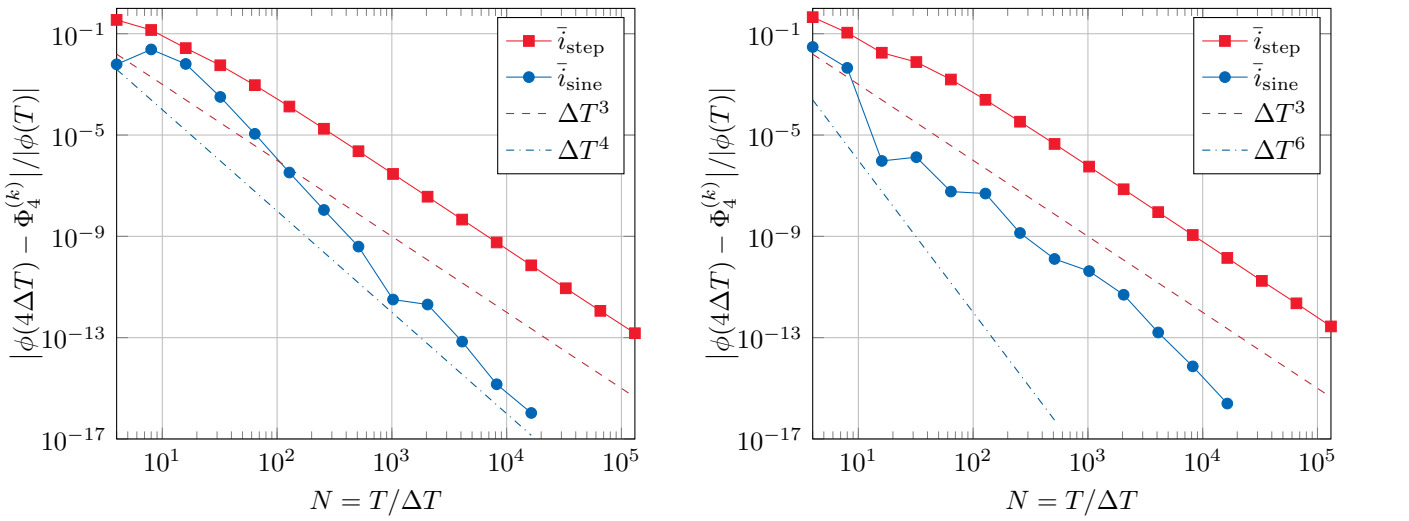

(a) IE method.

(b) TR.

Figure 5.5: Convergence of the multirate Parareal algorithm for the nonlinear model and $k = 1$ [51] ©2019 Society for Industrial and Applied Mathematics.

Nonlinear model

We now investigate the performance of the multirate Parareal method for a nonlinear counterpart of the RL-circuit model (5.2), given by [51]

$$R^{-1}\phi'(t) + L^{-1}(|\phi|)\phi(t) = i_{\text{pwm}}(t), \quad t \in (0, T], \tag{5.7}$$

with a flux-dependent inverse of the inductance $L^{-1}(|\phi|) = k_{\text{L}}|\phi(t)|$, where $k_{\text{L}} = 10^3\,\text{A/Wb}^2$. As in (5.2), $R = 10^{-2}\,\Omega$, $T = 2 \cdot 10^{-2}\,\text{s}$, i_{pwm} is given in (5.3) with $f_s = 20\,\text{kHz}$ and $f_r = 50\,\text{Hz}$, and the IC $\phi(0) = 0$ is prescribed.

Convergence of the multirate Parareal method for $k = 1$ using the IE method and TR is illustrated in Figure 5.5a and Figure 5.5b, respectively. Also in the nonlinear case the sinusoidal coarse excitation $\bar{i}_{\text{sine}}$ (5.4) gives a higer convergence order compared to the step input $\bar{i}_{\text{step}}$ (5.5). In particular, with the IE method as the coarse and the fine time integrator, the sine coarse input gives order close to 5, which is even higher than $(p+1)(k+1) = 4$ for almost all the values of N, whereas the step coarse input leads to the low order $(p+1)k+1 = 3$, [51]. A similar situation is observed in the case of the TR: using the sinusoidal signal the multirate Parareal converges with the order close to $(p+1)(k+1) = 6$, while the step signal leads to the converges order $(p+1)k = 3$, which is the lowest possible convergence rate due to the estimate (4.39), [51].

5.1.1.3 Multirate PP-IC algorithm

Based on [52], we illustrate the convergence of the multirate PP-IC algorithm (4.46)-(4.47) for the RL-circuit model (5.2) with a prescribed TP condition $\phi(0) = \phi(T)$. According to the Theorem 4.5, we intend to calculate the upper bound x_l (4.60) for the numerical convergence factor

$$\rho_{\text{num}} = \left(\|\mathbf{e}^{(K)}\|/\|\mathbf{e}^{(0)}\|\right)^{1/K} \quad \text{with} \quad \|\mathbf{e}^{(k)}\| = \max_{0\le n\le N}\left|\phi(T_n) - \Phi_n^{(k)}\right|, \quad 0 \le k \le K. \tag{5.8}$$

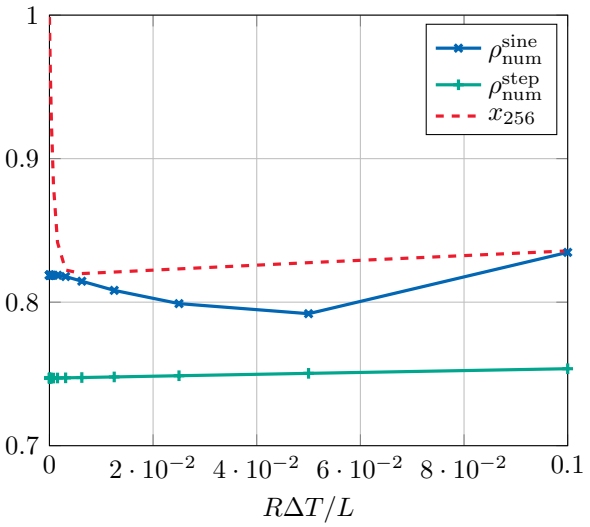

Figure 5.6: Convergence of the multirate PP-IC algorithm [52] ©Springer Nature Switzerland AG 2020.

Here $\phi(T_n)$ denotes the TP solution at $t = T_n$, obtained by the time stepping using the IE method until the steady state, when the relative periodicity error (5.1) with $\|u - v\|_\times = |u - v|/v$ for $u, v \in \mathbb{R}$, has reached the tolerance $\varepsilon_{\text{tol}} = 10^{-6}$ after calculating over $k^* = 50$ periods. The same $\|\cdot\|_\times$-norm and tolerance ε_{tol} are used in the termination criterion of the multirate PP-IC (4.46)-(4.47) in terms of the error (4.20), [52]. Both fine and coarse solutions are calculated using the IE method. The fine step size is $\delta T = T/2^{18} \approx 7.63^{-8}\,\text{s}$, while the coarse step size is $\Delta T = T/N$, with $N = 2^1, \ldots, 2^{17}$. The stability function of the IE method applied to (5.2) with time step ΔT is $1/(1 + R\Delta T/L)$, see (3.50).

In Figure 5.6, the measured convergence factor $\rho_{\text{num}}^\star$ is shown, where $\star \in \{\text{sine}, \text{step}\}$ represents the two choices of the coarse excitation: the sinusoidal input (5.4) and the step input (5.5), respectively. The figure also illustrates the values of x_{256} from (4.60) for the considered coarse step sizes ΔT. The graphs confirm that the theoretical estimate x_l is an upper bound for the numerical convergence factor $\rho_{\text{num}}^\star$, with $\star \in \{\text{sine}, \text{step}\}$ for the chosen coarse inputs (sine and step), [52]. We observe that the value of x_{256} is a sharper estimate in the case of the sinusoidal input $\bar{i}_{\text{sine}}$ compared to the step input $\bar{i}_{\text{step}}$. The number of iterations required until convergence of the multirate PP-IC algorithm is the same for both choices of the coarse input ($K = 9$ iterations on average for the considered values of ΔT), while the initial error $\|\mathbf{e}^{(0)}\|$ is bigger in case of the step function (5.5) than for the sinusoidal waveform (5.4). This explains that the convergence factor $\rho_{\text{num}}^{\text{step}}$ is slightly smaller than $\rho_{\text{num}}^{\text{sine}}$ due to the definition of ρ_{num} in (5.8) (since $\|\mathbf{e}^{(0)}\|$ is located in the denominator).

5.1.2 Buck converter

We now consider the buck converter model supplied with a PWM voltage source v_{pwm} shown in Figure 2.6. The model can be derived from the KVL (see Section 2.2) and is described in terms of the two variables: the current $i_{\text{L}}(t)$ and the voltage $v_{\text{C}}(t)$ by the IVP

$$\begin{bmatrix} L & 0 \\ 0 & C \end{bmatrix} \begin{bmatrix} i'_{\text{L}}(t) \\ v'_{\text{C}}(t) \end{bmatrix} + \begin{bmatrix} R_{\text{L}} & 1 \\ -1 & R^{-1} \end{bmatrix} \begin{bmatrix} i_{\text{L}}(t) \\ v_{\text{C}}(t) \end{bmatrix} = \begin{bmatrix} v_{\text{pwm}}(t) \\ 0 \end{bmatrix}, \quad t \in (0, T], \qquad \begin{bmatrix} i_{\text{L}}(0) \\ v_{\text{C}}(0) \end{bmatrix} = \mathbf{0}, \tag{5.9}$$

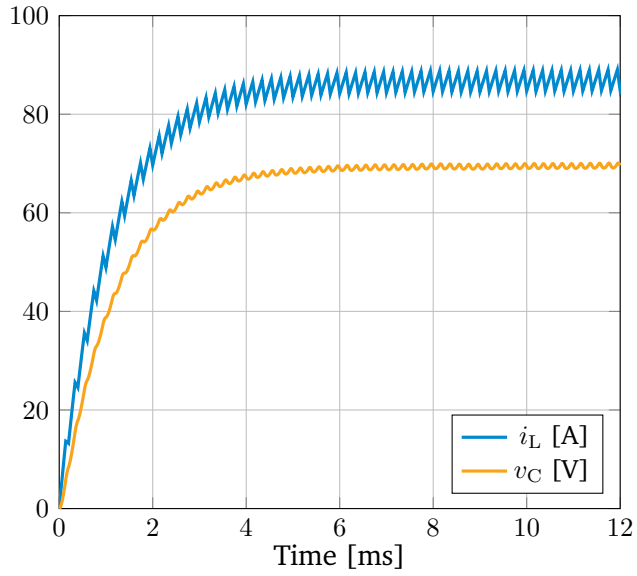

(a) Sequential solution with the IE method.

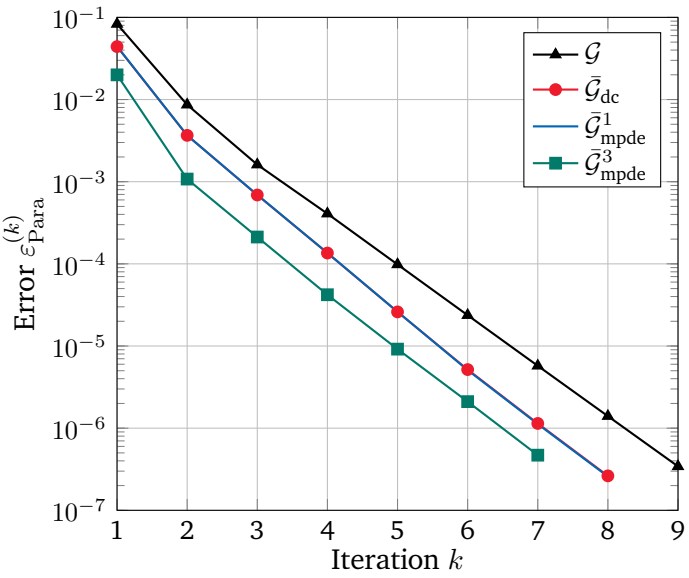

(b) Convergence of the Parareal algorithm.

Figure 5.7: Results for the buck converter model supplied with the PWM input of frequency $f_s = 5\,\mathrm{kHz}$ [103].

with end time point $T = 12\,\mathrm{ms}$, inductance $L = 10^{-3}\,\mathrm{H}$, capacitance $C = 10^{-4}\,\mathrm{F}$, resistances $R_{\mathrm{L}} = 10^{-2}\,\Omega$ and $R = 8 \cdot 10^{-1}\,\Omega$. The PWM voltage input $v_{\mathrm{pwm}}(t)$ is given by

$$v_{\mathrm{pwm}}(t) = V_{\mathrm{pwm}}\Big(\mathrm{sgn}\big(r(t) - s(t)\big)+1\Big)/2, \tag{5.10}$$

and has the amplitude of $V_{\mathrm{pwm}} = 100\,\mathrm{V}$. It is generated by a sawtooth carrier signal $s(t) = tf_s \bmod 1$ with switching frequency of $f_s = 5\,\mathrm{kHz}$ and the reference signal $r(t) = 0.7$. The described PWM signal has the form illustrated in Figure 2.8c. The sequential solution obtained using the IE method with the step size $\delta T = 10^{-6}\,\mathrm{s}$ is depicted in Figure 5.7a.

We split the time interval $[0, T] = [0, 12]\,\mathrm{ms}$ into $N = 40$ windows. The coarse time step size is $\Delta T = T/N = 3 \cdot 10^{-4}\,\mathrm{s}$ and the fine propagator uses the time step $\delta T = 10^{-6}\,\mathrm{s}$. Both coarse and fine solvers use the IE discretization. Based on [103], we apply the multirate Parareal method (4.34)-(4.35) with the two choices of the surrogate coarse solver $\bar{\mathcal{G}}$:

1. $\bar{\mathcal{G}}_{\mathrm{dc}}$ which solves the system (5.9) using the low-frequency input $v_{dc} = 0.7$, containing only the DC component, instead of the PWM input v_{pwm} (similarly to Section 5.1.1);
2. $\bar{\mathcal{G}}^{N_{\mathrm{p}}}_{\mathrm{mpde}}$ solves the system (5.9) using the MPDE approach (described in Section 2.3.3), i.e., it decomposes the solution as [102]

$$\hat{i}_{\mathrm{L}}(t_1, t_2) = \sum_{k=1}^{N_{\mathrm{p}}} y_{L,k}(t_1) w_k(\tau(t_2)), \qquad \hat{v}_{\mathrm{C}}(t_1, t_2) = \sum_{k=1}^{N_{\mathrm{p}}} y_{C,k}(t_1) w_k(\tau(t_2)), \tag{5.11}$$

where $y_{\star,k}(t_1)$, $\star \in \{L, C\}$, are slowly varying coefficients and $w_k(\tau(t_2))$ are basis functions with the relative time variable $\tau(t_2) = t_2 f_s \bmod 1$.

The expansion (5.11) splits the solution into a slowly varying envelope in t_1 and fast periodically varying ripples in t_2, which leads to the MPDE (2.87) with the RHS $\hat{\mathbf{p}}(t_1, t_2) = \mathbf{p}(t_2)$, where we denote $\mathbf{p}(t) = [v_{\mathrm{pwm}}(t), 0]^{\top}$,

[103]. Applying the Galerkin approach with respect to the fast variable t_2, one obtains an ODE system in terms of the slow variable t_1 of a bigger size $2N_\mathrm{p}$, [102, 103]. We choose $N_\mathrm{p} = 1$ and $N_\mathrm{p} = 3$, and apply the propagators $\bar{\mathcal{G}}^1_{\mathrm{mpde}}$ and $\bar{\mathcal{G}}^3_{\mathrm{mpde}}$.

The multirate Parareal with different choices of the coarse solver is compared to the classical Parareal method (4.9)-(4.10), where both fine and coarse propagators solve the original system (5.9) with the PWM input. In each case, convergence up to the tolerance $\varepsilon_\mathrm{tol} = 10^{-6}$ is considered in terms of the error (4.15) and the $\|\cdot\|_\times$-norm given by

$$\|\mathbf{u} - \mathbf{v}\|_\times = \frac{\|\mathbf{u} - \mathbf{v}\|_2}{\|\mathbf{u}\|_2}, \quad \mathbf{u}, \mathbf{v} \in \mathbb{R}^{N_\mathrm{d}}; \tag{5.12}$$

where $N_\mathrm{d} = 2$ and $\|\cdot\|_2$ denotes the l_2- or Euclidean norm in the 2D real space. An iterative algorithm is terminated once the error (4.15) with the norm (5.12) becomes smaller than the prescribed tolerance.

The error (4.15), calculated at each iteration k, is depicted in Figure 5.7b for all the considered Parareal variants. The standard Parareal method converges in 9 iterations, which corresponds to $2\,700$ and 360 ELSS of linear algebraic systems of size 2 on the fine and the coarse levels, respectively, or $3\,060$ linear systems in total, [103]. The multirate Parareal with the coarse solvers $\bar{\mathcal{G}}_\mathrm{dc}$ and $\bar{\mathcal{G}}^1_{\mathrm{mpde}}$ required 8 iterations ($2\,400$ fine and 320 ELSS, or in total $2\,720$ solutions of linear systems in two variables) in both cases. Finally, Parareal with the coarse solver $\bar{\mathcal{G}}^3_{\mathrm{mpde}}$ converged after 7 iterations, thereby solving $2\,100$ linear systems of size 2 on the fine level and 280 linear systems of size $2N_\mathrm{p} = 6$ on the coarse level. Furthermore, from Figure 5.7b we see that multirate Parareal with coarse propagators $\bar{\mathcal{G}}^1_{\mathrm{mpde}}$ and $\bar{\mathcal{G}}_\mathrm{dc}$ perform very similarly (if not identically). This resemblance is not surprising, since $\bar{\mathcal{G}}^1_{\mathrm{mpde}}$ computes only the envelope of the solution, which is conceptually similar to the solution obtained with $\bar{\mathcal{G}}_\mathrm{dc}$, where the constant input is used. Finally, we have observed that the exploitation of more basis functions ($N_\mathrm{p} > 3$) does not improve the convergence of Parareal, which is similar to the case of $N_\mathrm{p} = 3$.

5.1.3 Induction machine

We now apply the Parareal-based time-integration methods to the four-pole induction motor, whose 2D model is depicted in Figure 2.12. We consider one-pole (one-quarter) model, which consists of $n_\mathrm{st} = 9$ stator slots and $n_\mathrm{rt} = 8$ rotor bars. The electromagnetic phenomena in the motor are described by the governing equations from Section 2.4.2. In particular, the model is solved using a 2D MVP formulation coupled to circuit equations [61, 62], and the motion is modeled with the moving band technique. We assume the machine is excited with a 3ph PWM voltage source of $f_s = 20\,\mathrm{kHz}$ given by

$$v_{\mathrm{pwm},k}(t) = \mathrm{sgn}\big[r_{\mathrm{ac},k}(t) - c(t)\big], \quad k = 1, 2, 3. \tag{5.13}$$

The reference signal $r_{\mathrm{ac},k}$ of the phase k is given by the 3ph AC signal and the modulation factor $m_\mathrm{f} = 0.8$, i.e.,

$$r_{\mathrm{ac},k}(t) = m_\mathrm{f} U_\mathrm{peak} \sin\big(2\pi f_r t - (k-1)\cdot 2\pi/3\big), \quad f_r = 50\,\mathrm{Hz}, \quad k = 1, 2, 3. \tag{5.14}$$

The sawtooth carrier signal c is given by

$$c(t) = U_\mathrm{peak}\Big[2\big(f_s t - \lfloor f_s t \rfloor\big) - 1\Big], \quad f_s = 20\,\mathrm{kHz}, \tag{5.15}$$

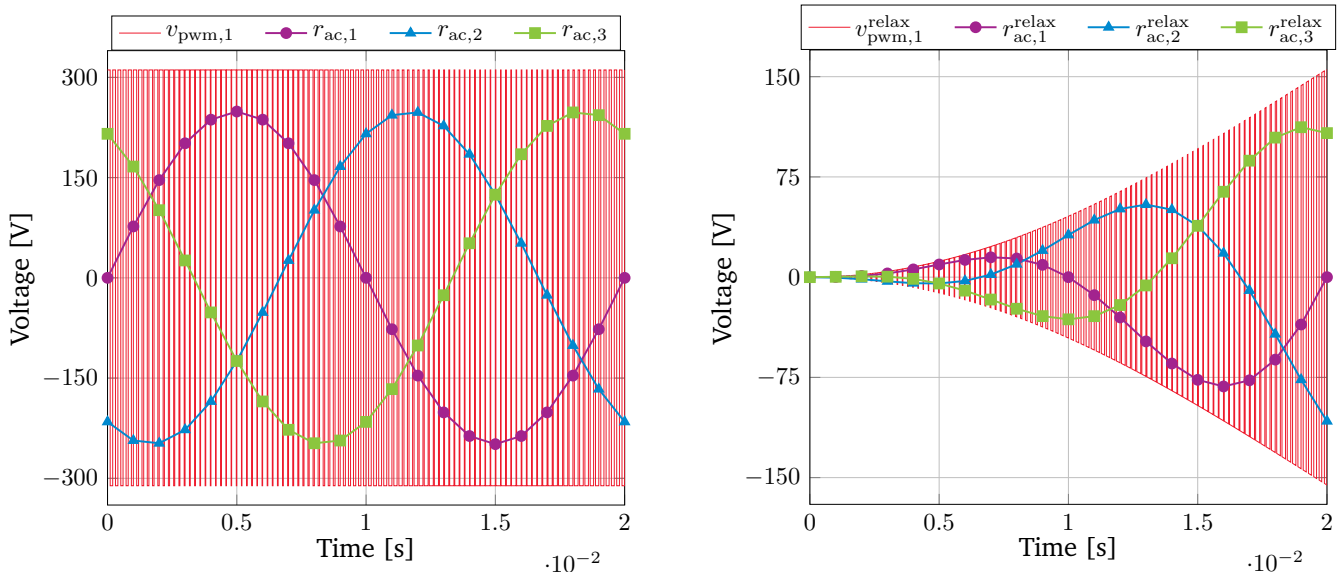

(a) No relaxation.

(b) Relaxation.

Figure 5.8: One phase of the PWM voltage source of $f_s = 5\,\mathrm{kHz}$ and 3ph AC reference signals [51, 52].

and obtained from a bipolar trailing-edge modulation [125]. The peak value U_{peak} in (5.14) and (5.15) is $U_{\mathrm{peak}} = 220\sqrt{2} \approx 311.13\,\mathrm{V}$. An example of the PWM voltage input $v_{\mathrm{pwm},1}$ of switching frequency $f_s = 5\,\mathrm{kHz}$ together with the underlying 3ph AC reference signal $r_{\mathrm{ac},k}$, $k = 1, 2, 3$ on the period $[0, T]$, $T = 1/f_r = 2 \cdot 10^{-2}\,\mathrm{s}$ is illustrated in Figure 5.8a. The MVP formulation defined on $\Omega \times (0, T]$ is completed with the BC and the IC

$$\vec{n} \times \vec{A}(\vec{x}, t) = 0, \quad (\vec{x}, t) \in \partial\Omega \times [0, T], \qquad \vec{A}(\vec{x}, 0) = 0, \quad \vec{x} \in \Omega. \tag{5.16}$$

The FEM discretization in space with $N_{\mathrm{d}} = 4\,400$ DoFs and solution of a resulting time-dependent system of DAEs is done in the GetDP library [56] under the no-load operation. The errors of the multirate Parareal and multirate PP-IC approaches are calculated using the definitions (4.15) and (4.20), respectively, with the $\|\cdot\|_{\times}$-norm defined according to [64, Chapter II.4], [51] by

$$\|\mathbf{u} - \mathbf{v}\|_{\times} = \sqrt{\frac{1}{N_{\mathrm{d}}} \sum_{i=1}^{N_{\mathrm{d}}} \frac{|u_i - v_i|^2}{(1 + |v_i|)^2}}, \quad \mathbf{u}, \mathbf{v} \in \mathbb{R}^{N_{\mathrm{d}}} \tag{5.17}$$

The prescribed tolerance $\varepsilon_{\mathrm{tol}} = 1.5 \cdot 10^{-5}$ is used for the errors in the termination criterion of the applied PinT methods.

5.1.3.1 Multirate Parareal algorithm

According to [51], the multirate Parareal algorithm (4.34)-(4.35), applied to one period $[0, T]$, uses the 3ph voltage inputs

$$v^{\mathrm{relax}}_{\mathrm{pwm},k} = f_{\mathrm{relax}}(t) v_{\mathrm{pwm},k}(t), \qquad r^{\mathrm{relax}}_{\mathrm{ac},k} = f_{\mathrm{relax}}(t) r_{\mathrm{ac},k}(t), \qquad k = 1, 2, 3 \tag{5.18}$$

on the fine and on the coarse levels, respectively. The function

$$f_{\mathrm{relax}}(t) = 0.5\big(1 - \cos(0.5\pi f_r t)\big), \quad f_r = 50\,\mathrm{Hz}, \tag{5.19}$$

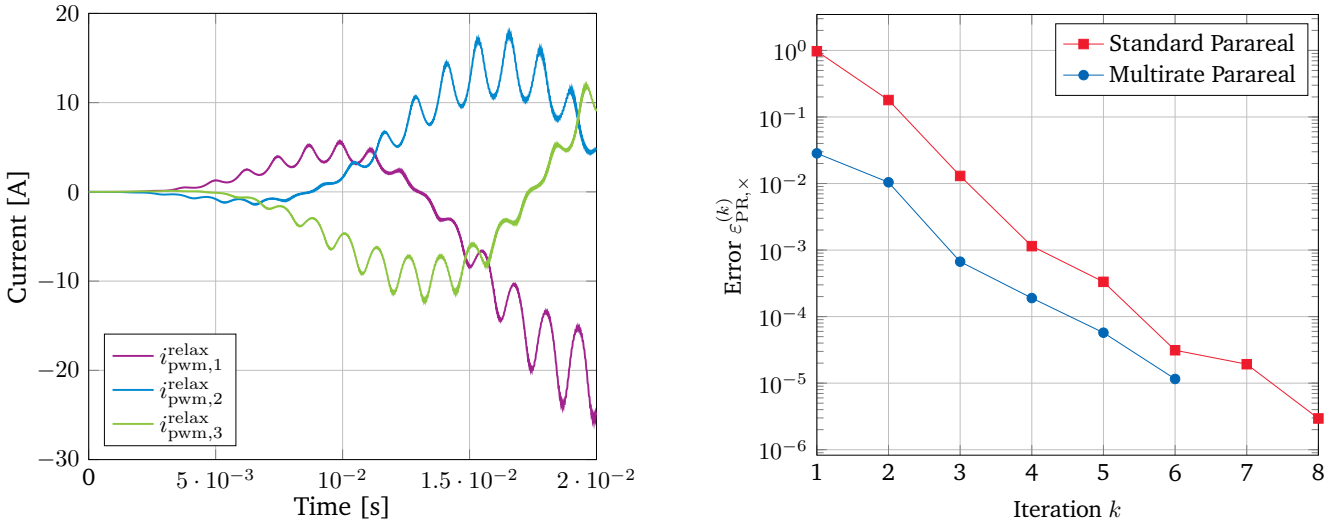

(a) 3ph currents in stator.

(b) Convergence of Parareal.

Figure 5.9: Application of Parareal to the induction motor model excited with 3ph PWM voltage supply of $f_s = 20\,\text{kHz}$ [51] ©2019 Society for Industrial and Applied Mathematics.

introduces a smooth relaxation of the applied voltages and is used for reduction of the transient part [56]. One phase of the ramped up PWM signal of $f_s = 5\,\text{kHz}$ and 3ph AC signals defined in (5.18) are depicted in Figure 5.8b. The fine propagator $\mathcal{F}$ uses the time step size $\delta T = 10^{-6}\,\text{s}$, while the coarse propagator $\bar{\mathcal{G}}$ uses $\Delta T = 10^{-3}\,\text{s}$. The considered time interval $[0, T] = [0, 2 \cdot 10^{-2}]\,\text{s}$ is partitioned into $N = 20$ subintervals, i.e., one coarse step is done per subinterval. Both fine and coarse solvers use the IE method. We provide the Octave-code for simulation of this GetDP induction machine model using multirate Parareal in [84].

Figure 5.9a illustrates the induced 3ph stator currents calculated according to the relation (2.103). In [51] a comparison of the standard Parareal (4.9)-(4.10), where the 3ph PWM voltage source $v^{\text{relax}}_{\text{pwm},k}$, $k = 1, 2, 3$, is used on both fine and coarse levels, and the multirate Parareal (4.34)-(4.35) is investigated. The errors (4.15) with the norm $\|\cdot\|_\times$ from (5.17) at each iteration k of both approaches are illustrated in Figure 5.9b. It shows that the multirate Parareal requires a quarter of iterations fewer than the standard Parareal to obtain the solution up to the prescribed tolerance ε_{tol}. In terms of the ELSS, the multirate Parareal calculates $121\,264$ ELSS (in 6 iterations), the standard Parareal requires $156\,309$ ELSS (in 8 iterations), while the classical sequential IE time-stepping on $[0, 2 \cdot 10^{-2}]\,\text{s}$ with the fine step size $\delta T = 10^{-6}\,\text{s}$ needs $244\,104$ ELSS, [51]. Thus, the multirate and the standard Parareal methods require about 50% and 64% of the ELSS, calculated within the IE time integration, respectively.

5.1.3.2 Multirate PP-IC algorithm

Based on [52], we calculate the TP solution of the induction machine model, supplied with the 3ph PWM voltage input $v_{\text{pwm},k}$, $k = 1, 2, 3$, of $f_s = 20\,\text{kHz}$, defined in (5.13). The reference steady-state solution is obtained through the IE time stepping with the step size $\delta T = 10^{-6}\,\text{s}$ over $k^* = 9$ periods, i.e., over $[0, k^*T] = [0, 1.8 \cdot 10^{-1}]\,\text{s}$, which requires $2\,176\,179$ ELSS. The sequential calculation is compared to the multirate Parareal and multirate PP-IC, whose fine and coarse solvers use the IE method. The coarse solver

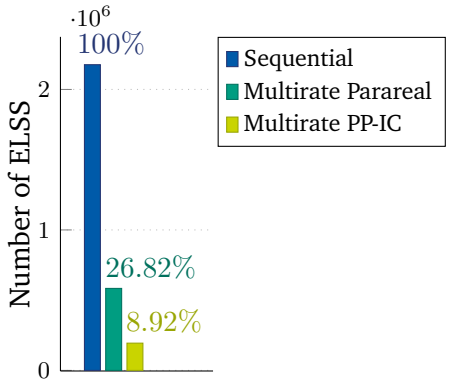

Figure 5.10: Number of ELSS for the induction machine model with the 3ph PWM voltage supply of $f_s = 20\,\mathrm{kHz}$, [52].

uses the 3ph AC input $r_{\mathrm{ac},k}$, $k = 1, 2, 3$, given in (5.14), while the fine propagator uses the original PWM excitation of $f_s = 20\,\mathrm{kHz}$ from (5.13).

The multirate Parareal algorithm is applied on $k^* = 9$ periods, i.e., on $[0, 9T] = [0, 1.8 \cdot 10^{-1}]\,\mathrm{s}$, split into $N = 20$ subintervals. The coarse step size is $\Delta T = 9T/N = 1.8 \cdot 10^{-1}/20\,\mathrm{s} = 9 \cdot 10^{-3}\,\mathrm{s}$, and the fine step size is $\delta T = 10^{-6}\,\mathrm{s}$, [52]. The multirate Parareal calculates $583\,707$ ELSS, which amount to 26.82% of the sequential time stepping. On the other hand, the multirate PP-IC method is applied on one period $[0, T] = [0, 2 \cdot 10^{-2}]\,\mathrm{s}$ with $N = 20$ subintervals, the coarse step $\Delta T = T/N = 10^{-3}\,\mathrm{s}$, and the fine step $\delta T = 10^{-6}\,\mathrm{s}$, [52]. The multirate PP-IC needs $194\,038$ ELSS, 8.92% of the sequential calculation. Computational costs in terms of the ELSS and the corresponding percentages are summarized in Figure 5.10.

We see that multirate Parareal and multirate PP-IC reduce the computational effort significantly compared to the sequential time stepping until the steady state. We differentiate between speed up due to the parallelization and due to the method. In particular, as the classical time stepping, Parareal calculates the solution on the whole interval $[0, k^*T]$, $k^* \geq 1$, until the steady state is reached. Therefore, the reduction of the computational time within Parareal occurs only due to the workload distribution among parallel processing units. In contrast, PP-IC is applied on a shorter interval, namely on the period $[0, T]$, thereby accelerating the computations not only due to parallelization but also due to the approach itself.

5.2 Industrial application: electric vehicle drive

Based on [11], we apply the PP-IC algorithm to simulate an induction motor used in an electric vehicle drive. It is a four-pole squirrel cage motor with $n_{\mathrm{st}} = 48$ stator slots and $n_{\mathrm{rt}} = 36$ rotor bars [2]. We consider a 2D two-pole model, which we discretize with FEM using $N_{\mathrm{d}} = 4\,459$ DoFs, see Figure 5.11a. Figure 5.11b illustrates the torque-speed characteristic of the motor, obtained by evaluation of tens to hundreds of operating points (OPs), which correspond to certain driving conditions of the electric vehicle. For example, OP1 describes the operation limit at maximum speed, while OP2 corresponds to the maximum acceleration at low speed. To apply the PP-IC method, the period T has to be defined. This is not a trivial task in case of an induction machine due to the presence of the slip (see Section 2.4.1), [109]. We calculate the periodic solution up to a prescribed tolerance $\varepsilon_{\mathrm{tol}}$ choosing the period T empirically depending on the type of the excitation [11]. For this, we consider two current-driven examples (OP1 and OP2) and a voltage-driven case (OP3) in the following sections.

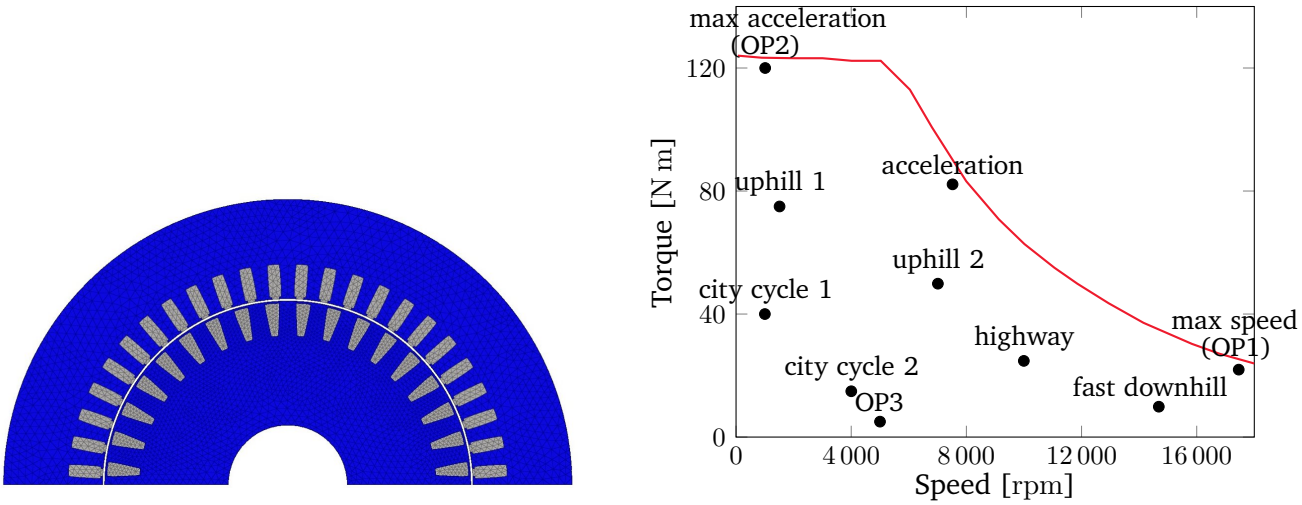

(a) FEM model with $N_{\mathrm{d}} = 4\,459$.

(b) Torque-speed characteristic.

Figure 5.11: Induction motor of an electric vehicle drive [11] ©2019 IEEE.

5.2.1 Operating point 1

This OP is characterized by the revolution speed of $18\,000\,\mathrm{rpm}$ and a 3ph AC input with the amplitude $I_{\mathrm{peak}} = 751\,\mathrm{A}$ and frequency $f = 632\,\mathrm{Hz}$. In [11] PP-IC is applied on one electric period in rotor $[0, 0.0311]\,\mathrm{s}$ using $N = 80$ parallel processors and fine step $\delta T = 4.6 \cdot 10^{-6}\,\mathrm{s}$. Computation over 12 PP-IC iterations requires $1\,968$ effective time steps and produces the torque, periodic up to tolerance $\varepsilon_{\mathrm{tol}} = 1.6 \cdot 10^{-2}$. The steady-state solution of the same precision, obtained from the time stepping on 9 periods, calculated $56\,160$ time steps of size δT. The number of the effective time steps calculated within the PP-IC algorithm thus amounts to only 3.5% of the sequential time steps calculated until the steady state. Both sequential solution until the steady state and the PP-IC solution, replicated over various periods, are illustrated in Figure 5.12a. We see that the PP-IC solution calculated using the fine step size $\delta T = 4.6 \cdot 10^{-6}\,\mathrm{s}$ still contains a residual oscillation, while the sequential steady-state solution eventually flattens out [11]. The deviation by $0.5\,\mathrm{N\,m}$, however, does not exceed 2% of the mean torque of $25\,\mathrm{N\,m}$ and is therefore acceptable, also since it is in a quite good agreement with the chosen periodicity tolerance $\varepsilon_{\mathrm{tol}} = 1.6\%$. Nevertheless, the residual oscillation can be eliminated through the refinement of the fine step size. In particular, using $\delta T = 4.6 \cdot 10^{-7}\,\mathrm{s}$, we obtain the expected flat steady-state solution, see Figure 5.12b.

We apply the simplified TP-EEC method [128], where the sequential solution $\mathbf{u}$ is corrected at every half a period $T/2 = 0.016\,\mathrm{s}$. In particular, $\mathbf{u}(t + T/2)$ is updated by the average $\big[\mathbf{u}(t) + \mathbf{u}(t + T/2)\big]/2$,$t = kT/2$, $k = 0, 1, \ldots$ until the steady state is reached, as it is shown in Figure 5.12c. Already after two corrections the relative periodicity error of $2.5 \cdot 10^{-2}$ is reached. The simplified TP-EEC method requires the calculation of $13\,435$ time steps, which corresponds to about 24% of the standard sequential time stepping. We also apply the approach from [12], where a suitable IC is computed, to this OP, see Figure 5.12d. This requires $26\,033$ time steps and corresponds to 46% of the sequential calculation. Clearly, a combination of the approach from [12] and the TP-EEC method can be considered for even faster attainment of the steady-state solution.

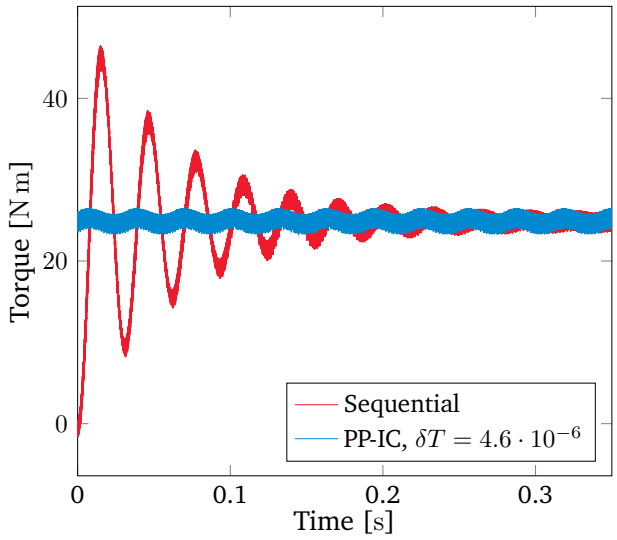

(a) Sequential solution and PP-IC solution replicated.

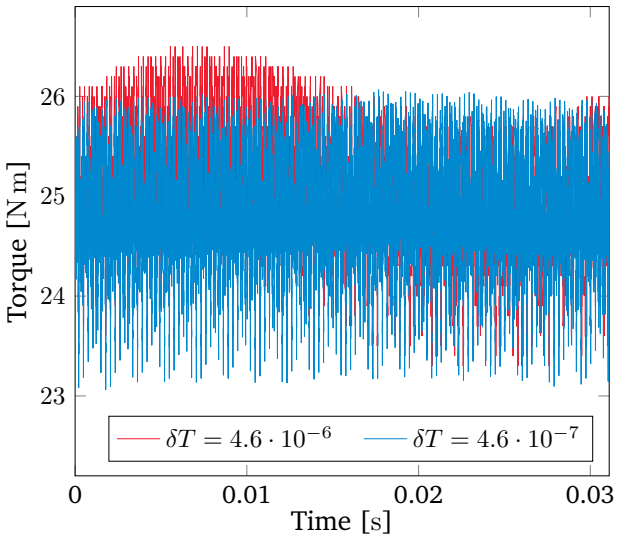

(b) PP-IC on one period with two fine step sizes.

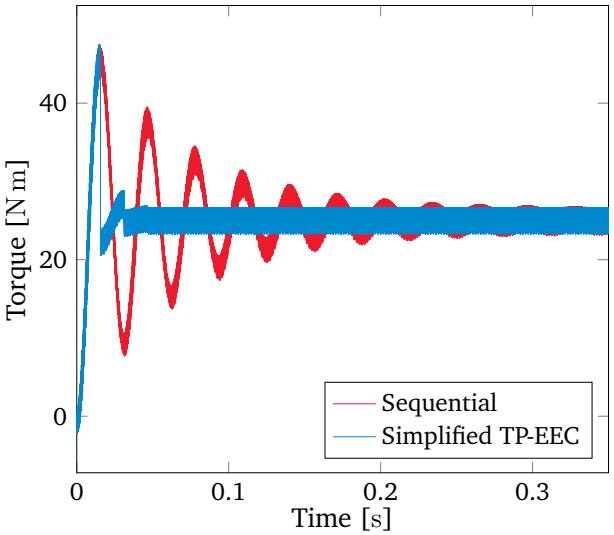

(c) Sequential and simplified TP-EEC solution.

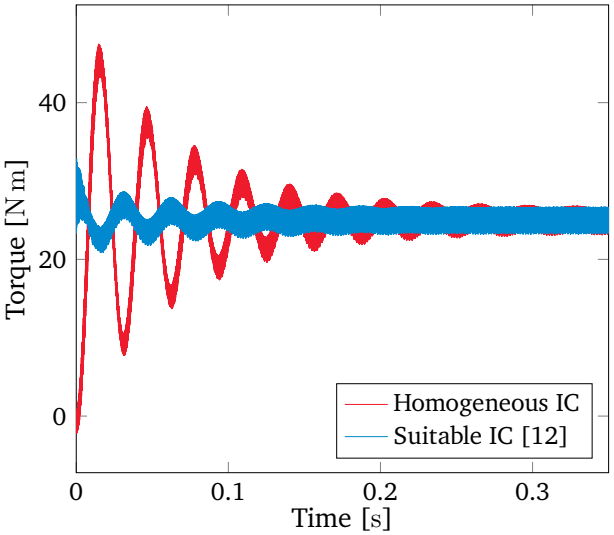

(d) Sequential solution starting from different ICs [12].

Figure 5.12: Torque calculation of OP1 [11] ©2019 IEEE.

5.2.2 Operating point 2

At OP2 the rotational speed is $1\,000$ rpm, peak value and frequency of the 3ph current is $I_{\mathrm{peak}} = 954.6\,\mathrm{A}$ and $f = 42.1\,\mathrm{Hz}$, respectively. In contrast to OP1, where an oscillatory transient behavior is observed, within OP2 there is no significant overshoot of the mean torque (see Figure 5.13a). The torque, periodic up to the relative tolerance $\varepsilon_{\mathrm{tol}} = 2 \cdot 10^{-3}$, is obtained after 4 iterations of PP-IC, applied on one rotor period $[0, 0.114]\,\mathrm{s}$ with $N = 154$ processors and fine step size $\delta T = 4.6 \cdot 10^{-6}\,\mathrm{s}$. This requires the calculation of $1\,256$ effective time steps, while the classical time stepping with the fine step size δT, applied on $[0, 0.12]\,\mathrm{s}$, computes $25\,920$ time steps, thereby giving the torque with relative periodicity error $\varepsilon_{\mathrm{tol}} < 10^{-2}$ on the second rotor period

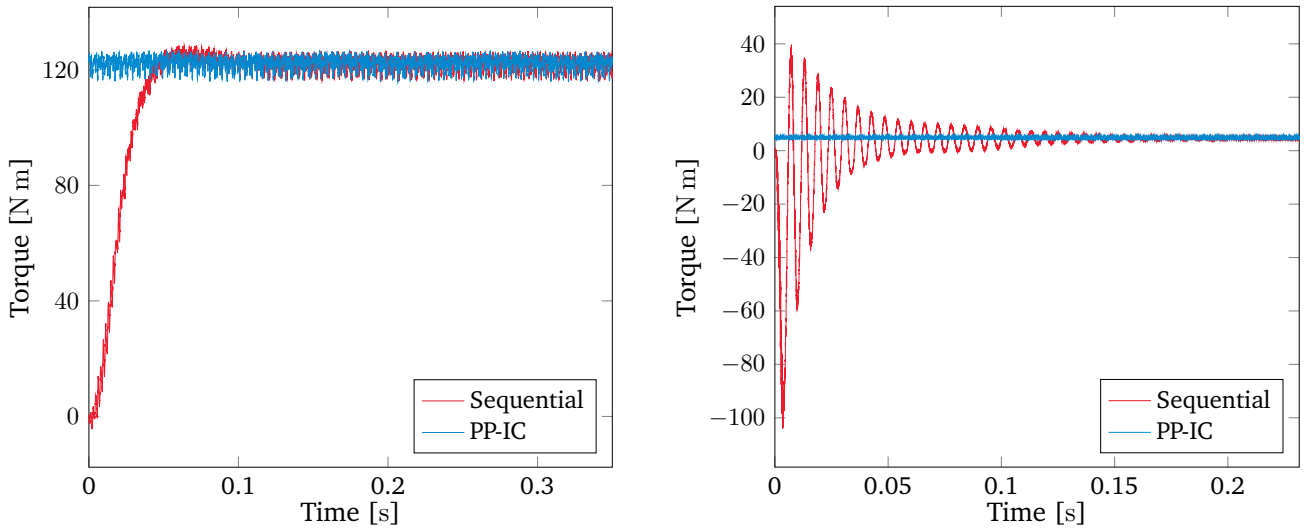

(a) OP2. **(b)** OP3.

Figure 5.13: Torque calculation of OP2 and OP3 [11] ©2019 IEEE.

[11]. The PP-IC method therefore calculated only about 5% of the time steps calculated within the standard time stepping. The periodic PP-IC solution, replicated over various periods, is illustrated in Figure 5.13a. The application of the approach from [12] to OP2 leads to $13\,299$ time steps, i.e., 51% of the standard time stepping until the steady state.

An attempt to apply the simplified TP-EEC to OP2 was not successful, since the correction at every half a period $T/2 = 0.057\,\mathrm{s}$ set the transient solution even further apart from reaching the steady state [11]. This observation is in agreement with [128], where it is stated that the simplified TP-EEC approach is suitable only for problems possessing a large time constant. Indeed, the successful application of the method is defined by the relation between the time constant τ of the underlying system and the value of $T/2$, used for the error correction [11]. The time constant can be estimated from a first-order circuit model via $\tau = L_{\mathrm{rt}}/R_{\mathrm{rt}}$, with the rotor resistance R_{rt} and self-inductance of a rotor bar L_{rt}. In particular, for OP2 we have the time constant $\tau_{\mathrm{OP2}} = 0.0072\,\mathrm{s}$. This value is one order of magnitude smaller than the considered half-period $T_{\mathrm{OP2}}/2 = 0.057\,\mathrm{s}$. The ratio $r = T/(2\tau)$ for this OP is then equal to $r_{\mathrm{OP2}} = 7.92$. On the other hand, for OP1 the time constant $\tau_{\mathrm{OP1}} = 0.182\,\mathrm{s}$ is about 10 times bigger than $T_{\mathrm{OP1}}/2 = 0.016\,\mathrm{s}$, which gives $r_{\mathrm{OP1}} = 0.086$. The value of r_{OP1} is clearly closer to zero than r_{OP2}. One can then conclude that ratio $r = T/(2\tau)$ can be considered an estimator for applicability of the simplified TP-EEC method [11].

5.2.3 Operating point 3

This OP represents a voltage-driven case and prescribes the rotational speed of $5\,000\ \mathrm{rpm}$, a sinusoidal 3ph voltage source of $U_{\mathrm{peak}} = 94\,\mathrm{V}$ and frequency $f = 171.2\,\mathrm{Hz}$. In contrast to the current-driven examples (OP1 and OP2), where the electric period in the rotor is used for PP-IC, in the voltage-driven case the electrical period in the stator coils, i.e., $T = 1/f = 5.84 \cdot 10^{-3}\,\mathrm{s}$ is chosen [11]. The sequential time stepping with the time step size $\delta T = 4.6 \cdot 10^{-6}\,\mathrm{s}$ requires $50\,000$ steps until the steady state is achieved up to the relative tolerance $\varepsilon_{\mathrm{tol}} = 7.5 \cdot 10^{-3}$ [11]. The PP-IC computation over 43 iterations with $N = 20$ processors and the fine step size $\delta T = 4.6 \cdot 10^{-6}\,\mathrm{s}$ amounts to $3\,569$ effective time steps, which is 7% of the sequential time stepping. The torque, obtained with PP-IC and with the sequential solution, is shown in Figure 5.13b.

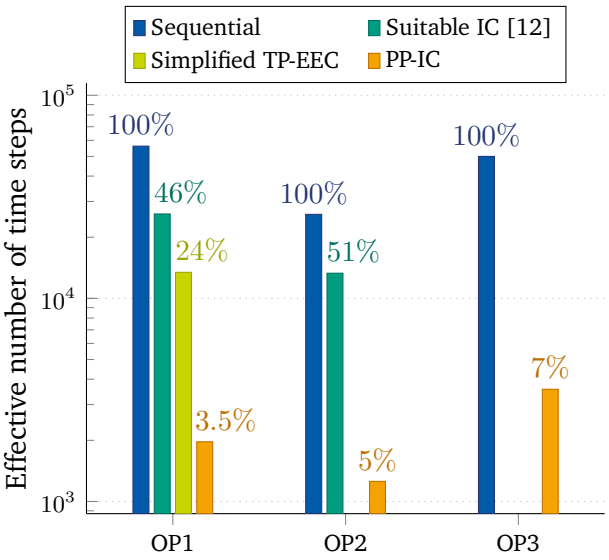

Figure 5.14: Number of effective time steps within several approaches (presented in a logarithmic scale), in contrast to the sequential time stepping [11]. Note that the simplified TP-EEC method and the approach from [12] are not tested for OP3, while the simplified TP-EEC is not applicable to OP2.

Conclusion

The computational costs of the considered solution approaches (PP-IC, simplified TP-EEC, suitable IC [12]) are summarized in Figure 5.14 in terms of the number of the computed effective time steps. These approaches are opposed to the standard sequential time stepping until the steady state, whose computational cost is considered as 100%. We see that the PP-IC method needs to compute the least number of time steps (up to 7%), provided a sufficient number of parallel processing units is available. Note that for OP1 and OP2 the numbers of processors N are optimized for maximal performance for each case. It means that for other choices, the cost may be bigger, e.g., 10% for OP1 and 20% for OP2 when using $N = 20$ [11]. The number of processors for the voltage-driven case OP3 ($N = 20$) has not been optimized, i.e., for more processors even lower costs may be expected. The simplified TP-EEC method is also a quite good alternative to the classical time stepping, especially taking into account that it is not a parallel approach. However, its applicability is limited and therefore can only be considered for some cases. Speaking of the approach from [12], although the method finds a suitable IC quite precisely, it reduces the total cost only by about 50% for the considered OPs. Besides, the approach seems to be very technical and needs a direct access to the model at hand, while the PP-IC and the simplified TP-EEC methods can operate on existing (black-box) time-domain solvers.

5.3 Numerical eigenvalue-based performance study

As it shown in [9, 39, 40], the Parareal method is very effective for first-order ODEs, e.g., stemming from parabolic PDEs, but does not have the same potential for second-order ODEs, e.g., originating from hyperbolic PDEs. The analysis of hyperbolic problems such as, e.g., the wave equation, in [44, 46] shows that the algorithm has difficulties in convergence and barely gives any acceleration of the time-domain computations. This is observed also for some oscillatory systems such as the harmonic oscillator or other Hamiltonian systems [47]. The inefficiency of the algorithm for such linear second-order ODEs is caused by a beating

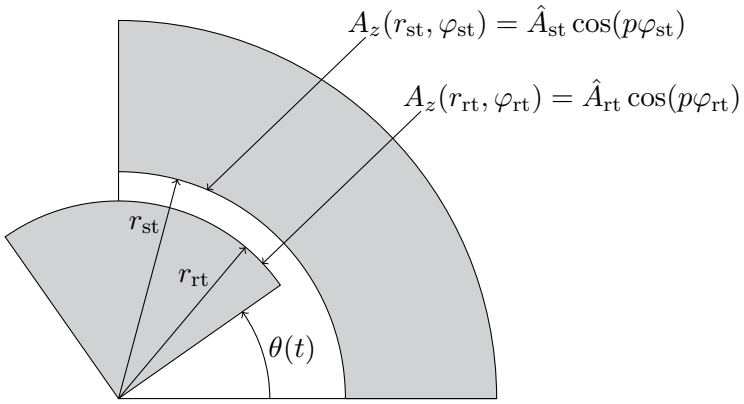

Figure 5.15: A quarter of a magnetomechanical oscillator model, whose air gap has inner radius r_{rt} and outer radius r_{st}. The angle θ relates the azimuthal coordinates φ_{rt} and φ_{st}, attached to rotor and stator, respectively, as in Figure 2.13.

phenomenon, since the propagation of the jumps on the coarse grid generates an artificial resonance leading to large-amplitude oscillations in the solution, as explained in [40, 55].

In this section we investigate whether Parareal may possibly face convergence problems for simulation of rotating electromagnetic devices based on a numerical eigenvalue study. We first apply Parareal to a magnetomechanical oscillator and analyze its convergence for the linear and nonlinear oscillator models in Section 5.3.1. Then in Section 5.3.2, we solve two equivalent schemes of an induction motor, already described in Section 2.4.3, using Parareal. For all the examples in this section we calculate at Parareal iteration k the error

$$\varepsilon_{\mathrm{Para}}^{(k)} = \frac{\varepsilon_{\mathrm{PR},2}^{(k)}}{1 + \left\| \mathbf{U}_{\mathrm{tot}}^{(k)} \right\|_*}, \tag{5.20}$$

with the joint solution vector $\mathbf{U}_{\mathrm{tot}}^{(k)}$ defined in (4.27), the error $\varepsilon_{\mathrm{PR},2}^{(k)}$ from (4.15), and the $\|\cdot\|_*$-norm given in (4.28). The calculations are terminated once the error in (5.20) becomes smaller than a prescribed tolerance $\varepsilon_{\mathrm{tol}}$.

5.3.1 Cylindrical magnetomechanical oscillator

In this section we describe the motion of a magnetomechanical oscillator[10], a quarter of whose cross section is illustrated in Figure 5.15, based on its air gap field. The air gap has inner radius $r_{\mathrm{rt}} = 3.5\,\mathrm{mm}$, outer radius $r_{\mathrm{st}} = 4\,\mathrm{mm}$, and length $\ell_z = 5\,\mathrm{mm}$ in cylindrical coordinates (r, φ, z). Let p denote the pole-pair number, θ be the rotor angle, which relates the azimuthal coordinates φ_{rt} and φ_{st}, attached to rotor and stator, respectively, as in Figure 2.13. Besides, let $\hat{A}_{\mathrm{rt}}$ and $\hat{A}_{\mathrm{st}}$ denote the real-valued amplitudes of the z-component A_z of the MVP at the inner and the outer circles, respectively, see Figure 5.15. The motion of the oscillator is described by the equation

$$J\theta''(t) = T_{\mathrm{EM}}(\theta, A_z), \tag{5.21}$$

[10]This example can be considered as a special case of a stripped permanent-magnet synchronous machine with the set rotational speed $\omega = 0$.

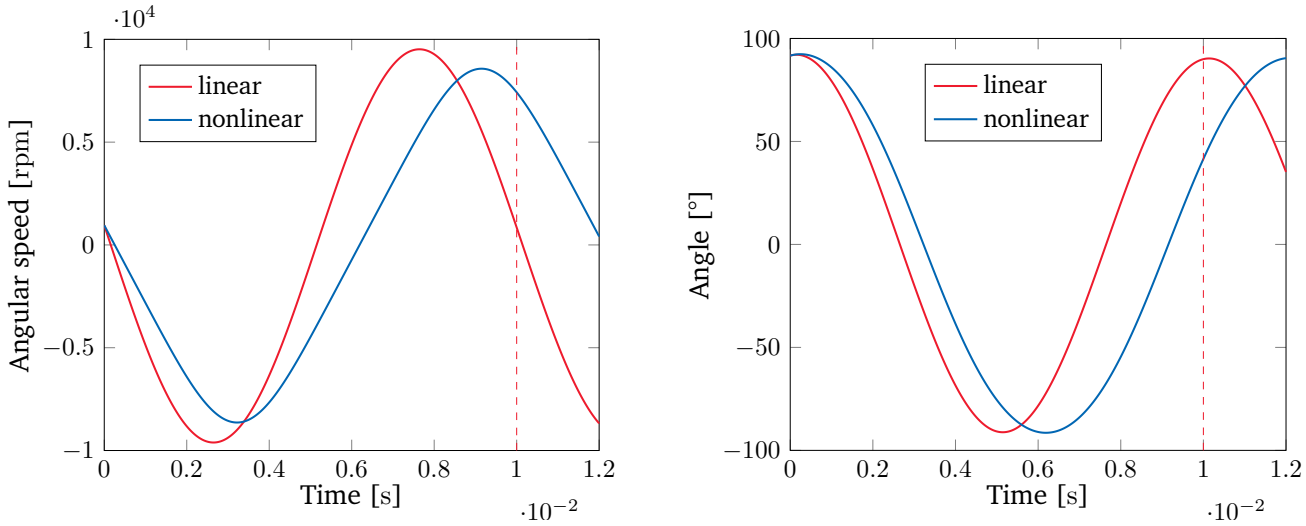

(a) Angular speed ω.

(b) Angular position θ.

Figure 5.16: Solutions of the two oscillator models.

where J is the moment of inertia, and the electromagnetic torque T_{EM} is given by

$$T_{\mathrm{EM}}(\theta, A_z) = -\frac{2\pi p^2 \ell_z \nu_0 \hat{A}_{\mathrm{st}} \hat{A}_{\mathrm{rt}}}{\gamma^{2p} - \gamma^{-2p}} \sin(p\theta), \tag{5.22}$$

with the geometric air gap ratio $\gamma = \sqrt{r_{\mathrm{st}}/r_{\mathrm{rt}}}$ and the reluctivity of vacuum ν_0. The derivation of the formula (5.22) for the torque of the magnetomechanical oscillator is presented in Section 7.1.

For small angles θ, the electromagnetic torque can be approximated as $T_{\mathrm{EM}} \approx -\kappa\theta$ with the *electromagnetic torsion spring constant*

$$\kappa = \frac{2\pi p^2 \ell_z \nu_0 \hat{A}_{\mathrm{st}} \hat{A}_{\mathrm{rt}}}{\gamma^{2p} - \gamma^{-2p}}. \tag{5.23}$$

In this case the equation (5.21) becomes

$$J\theta''(t) + \kappa\theta(t) = 0, \tag{5.24}$$

which also models the classical harmonic oscillator or an LC-circuit. The solution of (5.24) is given by

$$\theta(t) = \hat{\theta}\cos(\omega_{\mathrm{osc}} t - \hat{\psi}), \quad \omega_{\mathrm{osc}} = \sqrt{\kappa/J}, \tag{5.25}$$

where the amplitude $\hat{\theta}$ and the phase constant $\hat{\psi}$ can be found by imposing the ICs $\theta(0) = \theta_0$ and $\theta'(0) = \omega_0$. The solution of the equation (5.24) is periodic on the interval $\mathcal{I}_{\mathrm{osc}} = [0, 2\pi/\omega_{\mathrm{osc}}]$. In practice, the second-order ODEs (5.21) and (5.24) are written as a system of two first-order ODEs via introduction of the variable $\omega(t) = \theta'(t)$ as in (2.104)-(2.105).

Setting $p = 1$, $\hat{A}_{\mathrm{st}} = \hat{A}_{\mathrm{rt}} = 2 \cdot 10^{-4}\,\mathrm{Wb/m}$, and $J = 9.4\,\mu\mathrm{g/m^2}$, we calculate the angular frequency $\omega_{\mathrm{osc}} = 630\,\mathrm{rad/s}$, which corresponds to the eigenfrequency $f_{\mathrm{osc}} = \omega_{\mathrm{osc}}/2\pi = 100.2\,\mathrm{Hz}$. The angular speed ω and the angle θ of the linear and the nonlinear oscillator models, obtained using the IE method with the time step $\delta T = 10^{-5}\,\mathrm{s}$ starting from the ICs $\omega_0 = 100\,\mathrm{rad/s}$ and $\theta_0 = 1.6\,\mathrm{rad}$ at $t = 0$, are illustrated in Figure 5.16a and Figure 5.16b, respectively. As expected, the solution of the linear model (5.24) is periodic on $\mathcal{I}_{\mathrm{osc}} = [0, 0.01]\,\mathrm{s}$, while the nonlinear model (5.21) is periodic on a slightly bigger interval

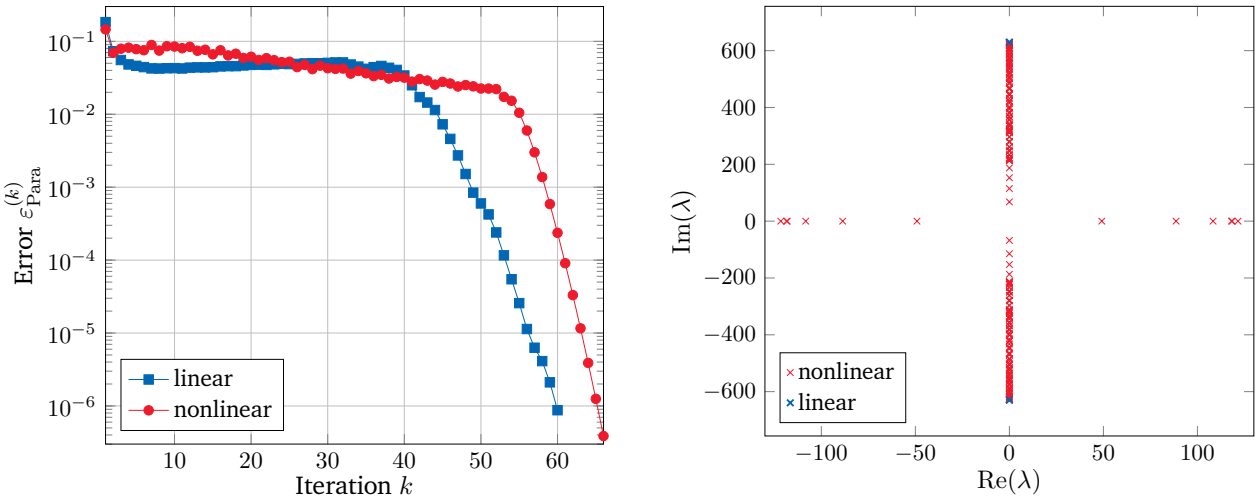

(a) Convergence of Parareal.

(b) Eigenvalues of the Jacobian matrices.

Figure 5.17: Convergence of Parareal and eigenvalues of the two oscillator models.

$[0, 0.012]\,\text{s}$. As already mentioned, the difference between the two models (and between the corresponding periods) becomes smaller for smaller values of θ, which we have observed when setting the IC, e.g., $\theta_0 = \pi/6\,\text{rad}$.

We now apply the Parareal algorithm to the linear and nonlinear oscillator models on $[0, 0.2]\,\text{s}$ with the fine step $\delta T = 10^{-5}\,\text{s}$ and number of subintervals $N = 200$ (which yields the coarse step $\Delta T = 10^{-3}\,\text{s}$). The convergence of the method up to the tolerance $\varepsilon_{\text{tol}} = 10^{-6}$ in terms of the error (5.20) for the two models with the ICs $\omega_0 = 100\,\text{rad/s}$ and $\theta_0 = 1.6\,\text{rad}$ is illustrated in Figure 5.17a. In the linear case, Parareal converged after 60 iterations, while the nonlinear model required 66 iterations. We observe that the errors do not decrease considerably or even slightly increase during the first 40 and 52 iterations in the linear and the nonlinear case, respectively. This indicates that the method has difficulties in error reduction for such a simple example, as shown also in [47, 55]. To understand the nature of the slow convergence, we consider the eigenvalues of the Jacobian matrices for the linear and nonlinear models, which are given for the ODE systems with respect to $[\omega, \theta]^\top$ by

$$\mathbf{J}_{\text{lin}} = \begin{bmatrix} 0 & -\kappa/J \\ 1 & 0 \end{bmatrix} \quad \text{and} \quad \mathbf{J}_{\text{nlin}}(\theta, A_z) = \begin{bmatrix} 0 & T'_{\text{EM}}(\theta, A_z)/J \\ 1 & 0 \end{bmatrix}, \tag{5.26}$$

respectively. The value of κ is defined in (5.23), while the derivative of $T_{\text{EM}}(\theta, A_z)$ from (5.22) (with respect to θ) is calculated as

$$T'_{\text{EM}}(\theta, A_z) = -\frac{2\pi p^3 \ell_z \nu_0 \hat{A}_{\text{st}} \hat{A}_{\text{rt}}}{\gamma^{2p} - \gamma^{-2p}} \cos(p\theta). \tag{5.27}$$

The eigenvalues calculated at each time step starting from $t = 0$ are illustrated in Figure 5.17b. We see that most of the eigenvalues λ are located on the imaginary axis with $|\text{Im}(\lambda)| \leq 630$, and some of the eigenvalues are purely real. We thus conclude that the presence of purely imaginary eigenvalues makes it tough for Parareal to converge, which is in agreement with [9, 40]. With this idea in mind, we investigate two circuit schemes describing induction machines in the following section.

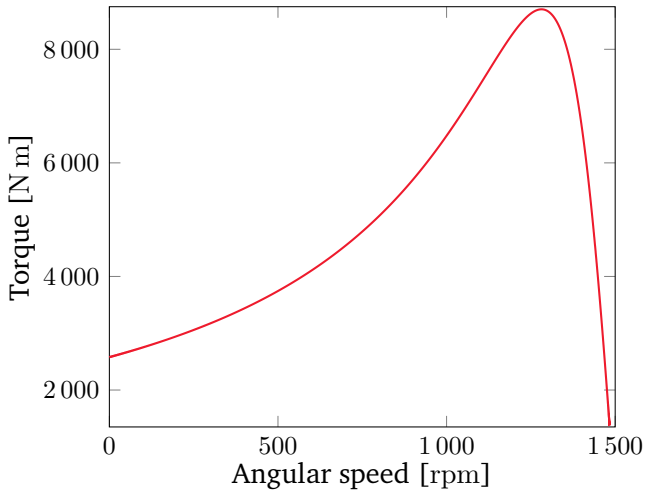

(a) Torque for Steinmetz model.

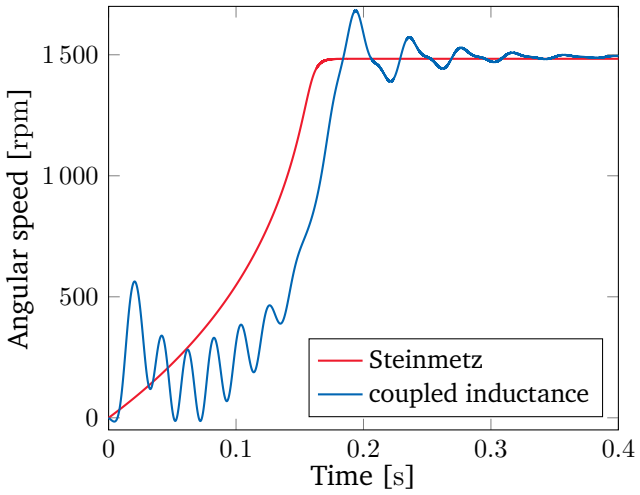

(b) Angular speed ω.

Figure 5.18: Solutions of the induction motor's equivalent schemes.

5.3.2 Equivalent schemes of an induction machine

We now consider the two equivalent schemes of an induction motor from Section 2.4.3: the Steinmetz model and the coupled inductance model. The stator of the $p = 2$ pole-pair induction machine is supplied by a 3ph voltage source of frequency $f = 50\,\mathrm{Hz}$ and amplitude $U_{\mathrm{peak}} = 1401.1\,\mathrm{V}$ given by

$$u_k^{\mathrm{st}}(t) = U_{\mathrm{peak}} \cos\big(2\pi f t - (k-1)\cdot 2\pi/3\big), \quad k = 1,2,3. \tag{5.28}$$

The rotor voltages are $u_k^{\mathrm{rt}} = 0$, $k = 1,2,3$. The resistances and inductances of the equivalent circuit, shown in Figure 2.15, are $R_{\mathrm{st}} = 0.06\,\Omega$, $L_{\sigma,\mathrm{st}} = 88.3\,\mathrm{mH}$, $R_{\mathrm{Fe}} = 557.6\,\Omega$, $L_{\mathrm{h}} = 0.075\,\mathrm{H}$, $L_{\sigma,\mathrm{rt}} = 2.3\,\mathrm{mH}$, $R_{\mathrm{rt}} = 0.15\,\Omega$. The rotation of the induction motor is described by

$$J\omega'(t) = T_{\mathrm{EM}}(\omega,\theta) - T_{\mathrm{load}}, \tag{5.29}$$
$$\theta'(t) = \omega(t), \tag{5.30}$$

where $J = 3\,\mathrm{kg/m^2}$, and $T_{\mathrm{load}} = 1372.9\,\mathrm{N\,m}$ is given at half load. In the Steinmetz model the torque $T_{\mathrm{EM}}(\omega)$ is defined in (2.111), while the coupled inductance model defines the torque $T_{\mathrm{EM}}(\theta)$ by (2.117) and couples the equations (5.29)-(5.30) to the system (2.118). For both equivalent schemes we consider homogeneous ICs in all variables.

The torque-speed curve obtained from the IE calculation on $[0, 0.4]\,\mathrm{s}$ with the step size $\delta T = 10^{-5}\,\mathrm{s}$ of the Steinmetz model is illustrated in Figure 5.18a, whose form is in a good agreement with the sketch from the Figure 2.14a. The angular speeds of both Steinmetz and the coupled inductance models are shown in Figure 5.18b. There, we see that the solution of the Steinmetz model reaches the steady state monotonically, while in the coupled inductance model transient oscillations are present. In both cases the same constant speed is obtained eventually.

Using the same parameters (time interval $[0, 0.2]\,\mathrm{s}$, fine step size $\delta T = 10^{-5}\,\mathrm{s}$, number of cores $N = 200$, coarse step size $\Delta T = 10^{-3}\,\mathrm{s}$) as for the magnetomechanical oscillator models, we apply the Parareal method for the two equivalent motor schemes. The convergence of the algorithm up to the tolerance $\varepsilon_{\mathrm{tol}} = 10^{-6}$ in terms of the error (5.20) is illustrated in Figure 5.19a. The Steinmetz and the coupled inductance models

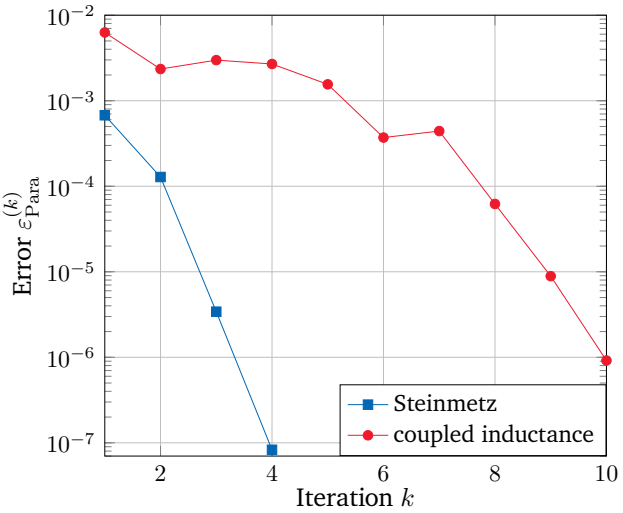

(a) Convergence of Parareal.

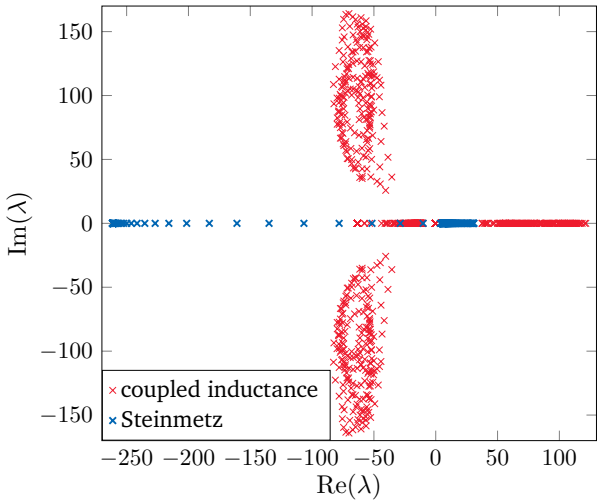

(b) Eigenvalues of the Jacobian matrices.

Figure 5.19: Convergence of Parareal and eigenvalues of the induction motor's equivalent schemes.

required 4 and 10 iterations, respectively. Compared to the magnetomechanical oscillator models (which require 60 and 66 Parareal iterations), this is a considerable reduction of the number of iterations. Looking at the eigenvalues of the numerically calculated Jacobian matrices of the two equivalent motor models in Figure 5.19b, we see that no scheme has purely imaginary eigenvalues.

Based on the investigation performed in this section and the results from [47, 55], we conclude that convergence of the Parareal method depends on the eigenvalues of the considered system. In particular, slower convergence is observed for problems containing a pair of complex conjugate purely imaginary eigenvalues like the harmonic or the magnetomechanical oscillators. On the other hand, for problems with only purely real or complex eigenvalues, whose real parts are non-zeros such as the equivalent schemes of induction motors, Parareal converges quickly. Based on the performed eigenvalue analysis of the equivalent motor schemes, we thus expect no purely imaginary eigenvalues also in a FEM model of an induction motor, which stems from a discretization of parabolic-elliptic PDE with an additional equation of motion, see Section 2.4. Indeed, also an investigation of the induction machine model from Section 5.1.3 in GetDP shows that the eigenvalues of the system matrix are purely real with magnitude of 10^7 in the linear case.

5.4 Steady-state analysis of a coaxial cable model

In this section the results from [82] are presented, where a TP problem for a coaxial cable model is solved using different parallel approaches: PP-IC (4.18)-(4.19), PP-PC with the with the (Jacobi-like) fixed point iteration (4.25), PP-PC with MH coarse grid correction from Section 4.4, as well as the TP discretization (3.95) followed by the MH correction from Section 3.3.2 according to the Remark 4.7. As a reference the sequential time-stepping solution until the steady state is considered.

Figure 5.20 illustrates a 2D sketch of a multi-material domain Ω, similar to the one depicted in Figure 2.1. It consists of a steel tube Ω_{Fe}, a conducting wire Ω_{Cu}, and an air gap Ω_{Air} and represents the cross-section of the coaxial cable. The electromagnetic phenomena in Ω are mathematically described by the eddy current

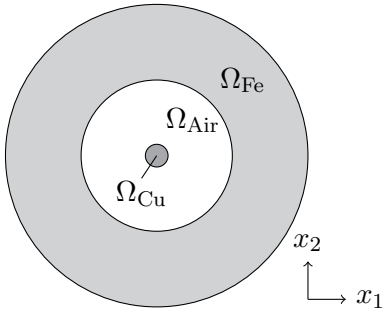

Figure 5.20: 2D model of a coaxial cable[11].

problem in the 2D setting (2.32) when the inner wire is supplied by a sinusoidal current source, i.e., the function f on the RHS in (2.32) is defined by

$$f(\vec{x},t) = \mathbb{1}_{\Omega_{\mathrm{Cu}}}(\vec{x})100\sin(2\pi t/T), \quad (\vec{x},t) \in \Omega \times [0,T], \tag{5.31}$$

where $\mathbb{1}_{\Omega_{\mathrm{Cu}}}$ is the indicator function of the subdomain Ω_{Cu} and $T = 0.02\,\mathrm{s}$. The conductivity $\sigma(\vec{x}) \geq 0$, $\vec{x} \in \Omega$ is defined in (2.8) and gives a parabolic-elliptic character to the PDE. The reluctivity $\nu(\vec{x},|\vec{B}|)$ is defined in (2.9), where $\nu(|\vec{B}|)$ originates from the BH-curve depicted in Figure 2.2 and satisfies the Corollary 2.2.

Including the BC (2.33) we discretize the PDE (2.32) using FEM with $N_{\mathrm{d}} = 2\,269$ and linear shape functions and obtain the system of DAEs (3.30). The time integration is performed with the IE method, where the time step size $\delta T = 10^{-5}\,\mathrm{s}$ is used for the sequential time stepping, for TP MH approach, and also as a fine step size of the considered PinT methods. The coarse propagator solves only one time step per window $[T_{n-1},T_n]$, $n = 1,\ldots,N$, thereby using the step size $\Delta T = T/N$. Convergence of the applied approaches up to the tolerance $\varepsilon_{\mathrm{tol}} = 10^{-3}$ is considered. The error (4.26) is used for PP-IC and PP-PC, while TP MH calculates the error (4.84). The error (5.1) within the sequential time stepping includes the $\|\cdot\|_{\times}$-norm given by

$$\|\mathbf{u}-\mathbf{v}\|_{\times} = \frac{\|\mathbf{u}-\mathbf{v}\|_2}{\varepsilon_{\mathrm{tol}} + \|\mathbf{u}\|_2}, \quad \mathbf{u},\mathbf{v} \in \mathbb{R}^{N_{\mathrm{d}}} \tag{5.32}$$

We point out that the solutions calculated by each of the applied parallel methods deviate from the sequential benchmark solution in the norm (5.32) up to the tolerance of $2.5 \cdot 10^{-2}$. Performance of the solution approaches is investigated for the linear and nonlinear coaxial cable models in the following two sections.

5.4.1 Linear model

Assuming the reluctivity function ν is linear, we obtain a DAE system (4.62) with the constant matrix $\mathbf{K}_\nu$. In this case the PP-PC system (4.23) can be constructed explicitly and diagonalized using the MH transformation, thereby solving N separate N_{d}-dimensional systems in parallel. Alternatively, the MH approach can be applied to the TP IE discretization, as proposed in [17] and described in Section 3.3.2. Since the TP MH method discretizes the interval $[0,T] = [0,0.02]\,\mathrm{s}$ using the fine step size $\delta T = 10^{-5}\,\mathrm{s}$, we have $N_{\mathrm{f}} = T/\delta T = 2 \cdot 10^3$ variables of size N_{d}. In this case $N_{\mathrm{f}} \gg N$ linear systems can be solved in parallel provided N_{f} parallel

[11] `www.femm.info/wiki/tubeexample`.

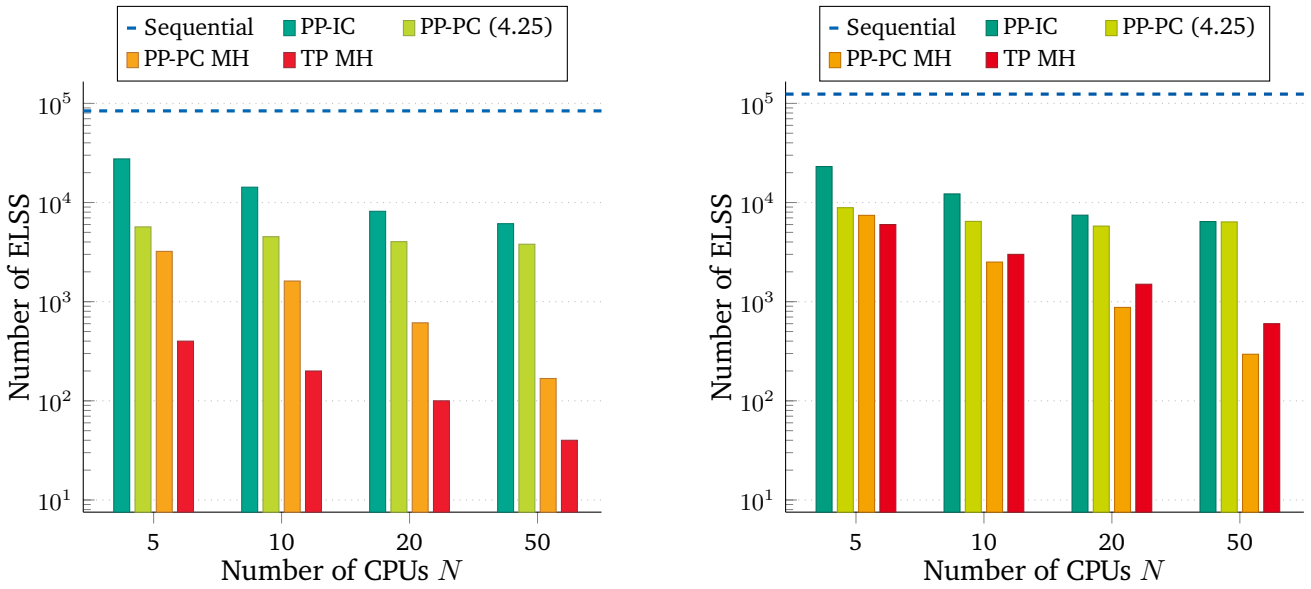

(a) Linear model.

(b) Nonlinear model.

Figure 5.21: Comparison of the computational costs of different approaches for the coaxial cable models and different values of N (strong scaling), presented in a logarithmic scale [82] ©2021 Society for Industrial and Applied Mathematics.

processors are available. However, in our case the parallelization capacity is limited to N central processing units (CPUs), solving N_f/N linear systems each.

Figure 5.21a illustrates the computational costs of the parallel algorithms for different $N \in \{5, 10, 20, 50\}$, when the precision of the fine solution remains unchanged (strong scaling), [82]. Comparing bars of different colors for a fixed N shows the cost reduction due to an applied method, while comparing bars of the same color corresponds to the reduction due to parallelism. The classical time stepping starting from a homogeneous IC $\mathbf{u}_0 = \mathbf{0}$ is performed over $k^* = 42$ periods until the periodicity error (5.1) reached the tolerance $\varepsilon_\mathrm{tol} = 10^{-3}$ in terms of the norm (5.32). This includes the solution of $N_\mathrm{seq} = 84\,000$ linear systems (100%) and is used as a benchmark for comparison to other approaches.

The number of ELSS within PP-IC (4.18)-(4.19) amounts to about 33% $(N = 5)$ and 7.3% $(N = 50)$ of the sequential calculation. The PP-PC method with the Jacobi-like iteration (4.25) solves effectively about 7% of N_seq, already when exploiting only $N = 5$ processing units. However, the disadvantage of this approach is that the computational costs stagnate and there is no further acceleration when applying additional computational power [82]. In contrast to this, the MH approach applied to the PP-PC system (4.23) as in [81] calculates 4% and 0.2% of system solves within the sequential calculation, using $N = 50$ and $N = 5$ cores, respectively. Finally, the TP MH approach [17] requires 0.5% $(N = 5)$ and 0.05% $(N = 50)$ ELSS, which shows that the performance gain of this method scales perfectly linearly as N grows.

5.4.2 Nonlinear model

In the nonlinear case the PP-PC system (4.68) is linearized with the simplified Newton method (4.72), accompanied by the MH coarse grid correction at each Newton iteration. The initial guess (4.75) is cho-

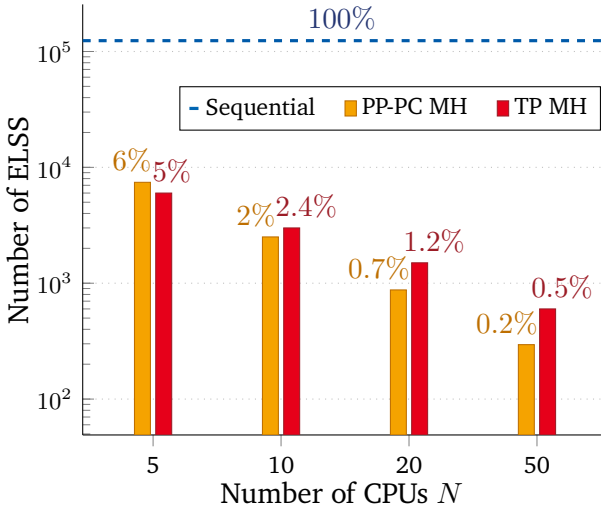

(a) Effective linear solutions (maximum among CPUs).

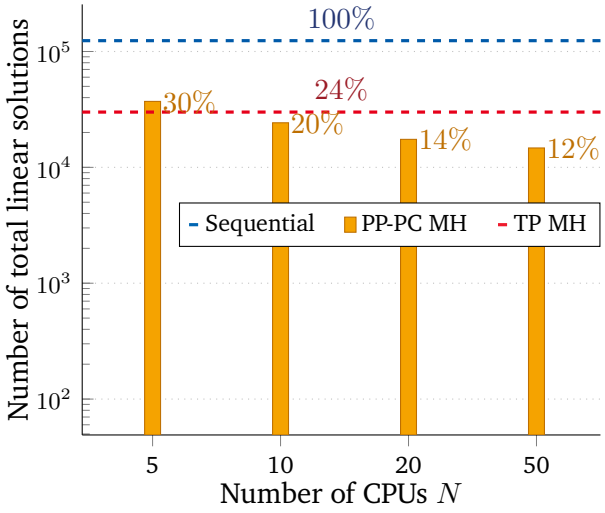

(b) Total linear solutions (sum for all CPUs).

Figure 5.22: Number of linear systems solved within PP-PC MH and TP MH for the nonlinear coaxial cable model (presented in a logarithmic scale) and its comparison to the sequential time stepping in terms of the percentage [82] ©2021 Society for Industrial and Applied Mathematics.

sen

$$\mathbf{U}_{\mathrm{tot}}^{(k+1,0)} := \left[\left(\mathbf{b}_N^{(k)}\right)^\top, \left(\mathbf{b}_1^{(k)}\right)^\top, \ldots, \left(\mathbf{b}_{N-1}^{(k)}\right)^\top \right]^\top, \tag{5.33}$$

i.e., $\mathbf{Z}^{(k)} = \mathbf{0}$, at PP-PC iteration $k+1$. Almost identical results have been obtained for the choice (4.80). The solution with simplified Newton and the MH diagonalization is also applied to the TP system (3.95) with the initial approximation $\mathbf{u}_{\mathrm{tot}}^{(0)} = \mathbf{0}$. Figure 5.21b illustrates the computational efforts of all the previously described methods for the nonlinear coaxial cable model. Sequential time stepping starting from zero IC reached the steady state up to the prescribed tolerance $\varepsilon_{\mathrm{tol}} = 10^{-3}$ after calculation over $k^* = 31$ periods, which corresponds to solution of $N_{\mathrm{seq}} = 124\,000$ linear systems (100%). The number of ELSS within PP-IC amounts to 18.6% for $N = 5$ and to 5.2% for $N = 50$. The PP-PC method with the Jacobi-like linearization (4.25) computes about 7% and 5% of N_{seq} when using $N = 5$ and $N = 50$ CPUs, respectively. Similarly to the linear case, the costs of the PP-PC solution do not significantly decrease with the growth of N and even increase slightly, when comparing the results for $N = 20$ and $N = 50$, [82].

The PP-PC MH approach effectively solves about 6% of N_{seq} for $N = 5$ and 0.2% of N_{seq} for $N = 50$. In contrast to the linear case, the TP MH solution performs worse than PP-PC MH for almost all the considered values of N except $N = 5$. More specifically, for 10, 20, and 50 cores the number of ELSS within TP MH is equal to 2.4%, 1.2%, and 0.5% of the sequential solution, as illustrated in Figure 5.22a. Figure 5.22b shows the total number of linear systems, solved within PP-PC MH and TP MH. Note that TP MH always solves the same number of linear systems, since increasing the number of cores N does not influence the convergence of the simplified Newton iteration but only disctributes the workload among more CPUs. The TP MH method converges in 15 iterations, each solving $N_{\mathrm{f}} = 2 \cdot 10^3$ linear systems, which in total gives $3 \cdot 10^4$ systems solves. In contrast to this, convergence of PP-PC MH becomes faster as N grows due to the increasing accuracy of the coarse solver. We thus see that even when the code is not truly parallelized, both approaches require much less linear solutions compared to the sequential time stepping (due to the method speed up), [82].

We now compare the actual computational time of PP-PC MH and TP MH to the time stepping until the

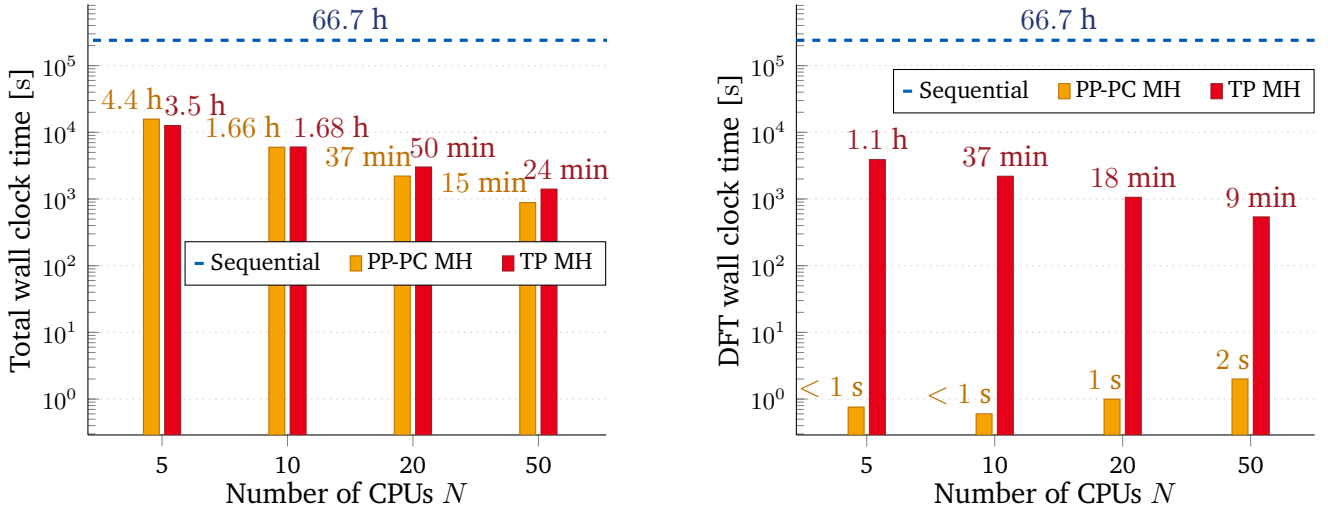

(a) Total computational time.

(b) DFT computational time.

Figure 5.23: Measurement of the wall clock time of PP-PC MH and TP MH, applied to the nonlinear coaxial cable model [82] ©2021 Society for Industrial and Applied Mathematics.

	$N = 5$	$N = 10$	$N = 20$	$N = 50$
Sequential		100%		
PP-PC MH	6.6%	2.5%	0.9%	0.4%
TP MH	5.3%	2.5%	1.3%	0.6%

Table 5.1: Percentage of the wall clock time of PP-PC MH and TP MH with respect to the sequential time stepping, as depicted in Figure 5.23a, [82].

steady state. In particular, the sequential calculation over one period requires 2.15 hours, which extends to a simulation of about 66.7 hours (almost 3 days), when calculating over 31 periods. Analogously to the computation of ELSS, the wall clock time measurements illustrate better performance of PP-PC MH in case of $N = 10$, 20 and 50, and of TP MH when $N = 5$, as illustrated in Figure 5.23a. The corresponding percentages with respect to the sequential execution time are presented in Table 5.1. We note that the values are very close to the estimate in terms of the ELSS in Figure 5.22a.

Figure 5.23b illustrates the computational time of the DFT and its inverse of the two methods. We see that within TP MH the DFT occupies approximately one third of the total computational time for all N (from 33% to 37%), while the DFT cost of PP-PC MH is extremely small (less than 1% of the total execution time). Besides, we see that for TP MH the DFT time decreases with the increase of N, as expected due to the better parallelization capability. The opposite happens within PP-PC MH: although the cost of DFT still remains tiny, it grows together with N, since the size of the DFT matrix $\mathbf{F}$ (3.100) increases. Finally, the communication costs of both approaches are within the range of $14\,\mathrm{s}$ and $48\,\mathrm{s}$ for the considered values of N, [82].

As already mentioned, the more subintervals N are used, the faster convergence of PP-PC is expected due to the increasing precision of the coarse solver. This is seen in Figure 5.24a, which illustrates the error $\varepsilon_{\mathrm{PP}}^{(k)}$ from (4.26) together with the number of the simplified Newton iterations at each iteration k of the PP-PC MH approach. Figure 5.24b shows the percentage of the principal components of PP-PC MH in Algorithm 1

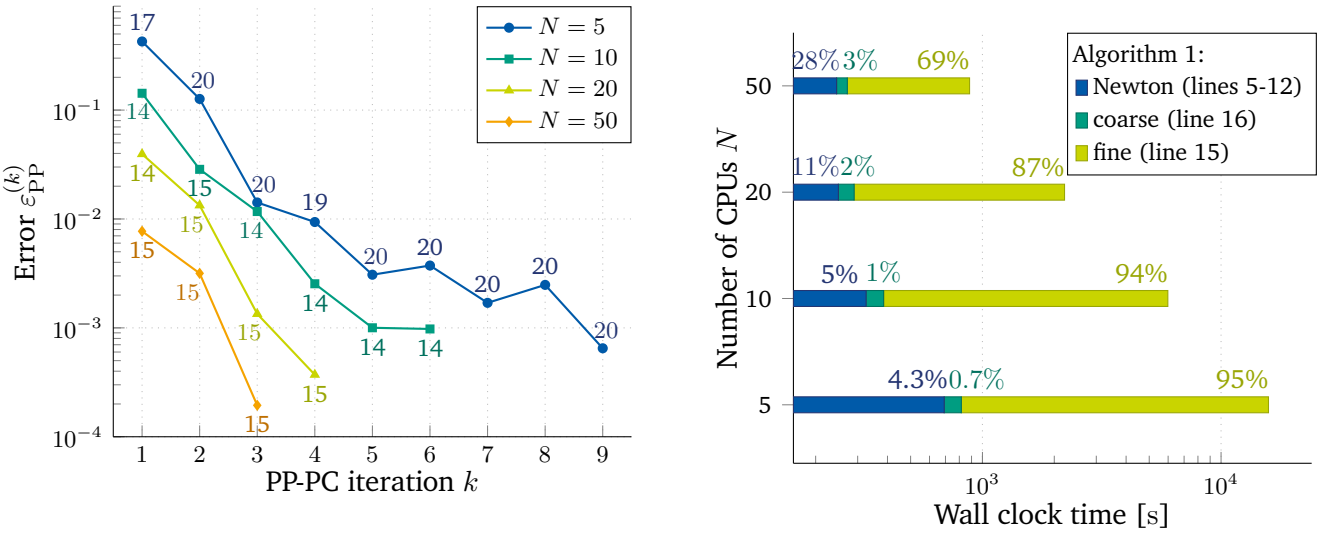

(a) Error and number of the simplified Newton iterations at each PP-PC iteration k.

(b) Contribution of different components of the algorithm to the total computational time.

Figure 5.24: Performance of PP-PC MH for the nonlinear coaxial cable model [82] ©2021 Society for Industrial and Applied Mathematics.

regarding the total calculation time. As expected, the timings of each component decreases with the growth of N and the most time-consuming part is the parallelized fine solution.

5.5 Three-dimensional example: transformer model

Following [82], we consider a 3D model of a transformer, whose cross-section and dimensions are illustrated in Figure 5.25a. The computational domain Ω consists of a steel core and two copper coils, surrounded by air with prescribed homogeneous Dirichlet BC on the outer boundaries. The two coils have 358 and 206 windings, wound around the core, respectively. The purpose of a transformer is to take in electrical power at one voltage and supply it at a different voltage [74, Chapter 7].

The nonlinear magnetic reluctivity ν is given in the ferromagnetic material of the core by the Brauer's curve [20]

$$\nu(\vec{x}, |\vec{B}|) = k_1 \exp(k_2 |\vec{B}|^2) + k_3, \tag{5.34}$$

with parameters $k_1 = 0.3774$, $k_2 = 2.970$, and $k_3 = 388.33$. The reluctivities in the air and the copper regions are given by the reluctivity of vacuum ν_0. The electric conductivity $\sigma(\vec{x})$ is nonzero only in the steel part and is equal to $5 \cdot 10^5\,\mathrm{S/m}$. The coils are supplied by the sinusoidal current input

$$\vec{J}_{\mathrm{s}}(\vec{x}, t) = \vec{\chi}_1(\vec{x}) 10 \sin(2\pi t/T) + \vec{\chi}_2(\vec{x}) 20 \sin(2\pi t/T), \quad (\vec{x}, t) \in \Omega \times [0, T], \tag{5.35}$$

where $\vec{\chi}_i(\vec{x})$, $i = 1, 2$ are the winding functions [117] of the two coils and $T = 0.02\,\mathrm{s}$. The transformer model is described by the eddy current equation (2.28) in the 3D domain, completed by the EBC given in (2.29) and the IC (2.30) or the TP condition (2.31).

The spatial discretization is performed with FIT [134] with $N_{\mathrm{d}} = 48\,417$ DoFs, which leads to a DAE system of the form (3.30) with a prescribed IC or TP condition. We note that although the system size is quite large,

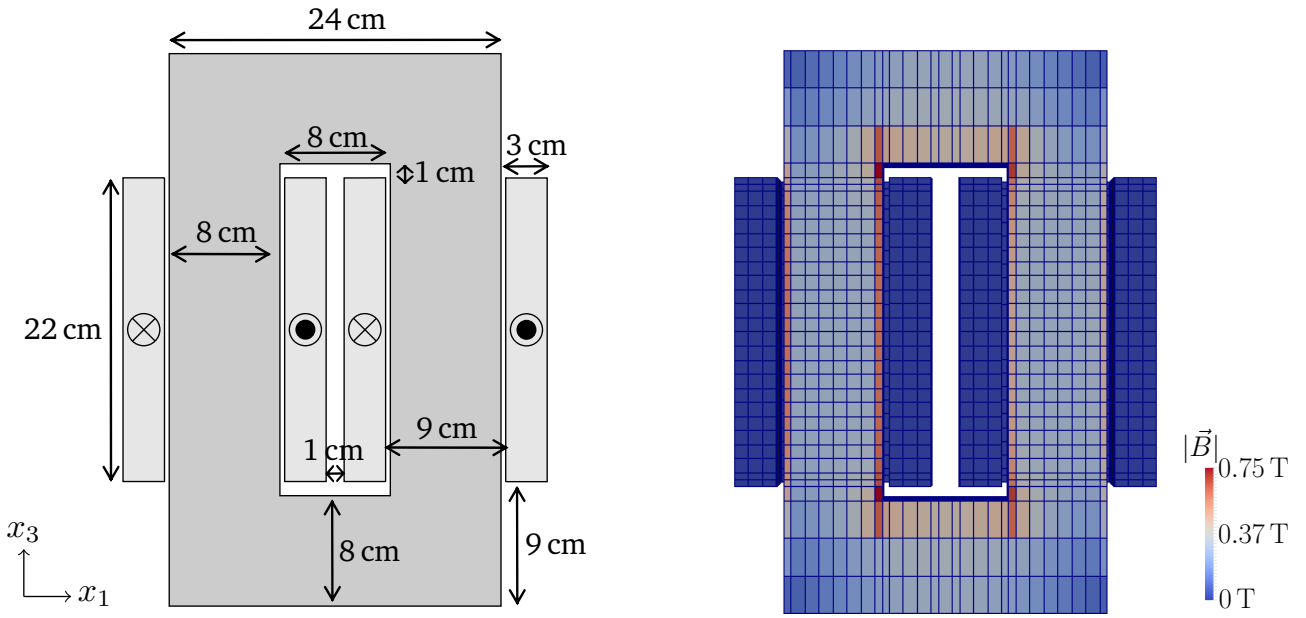

(a) Cross-section of the 3D model. **(b)** Magnetic flux density distribution at $T = 0.02\,\mathrm{s}$.

Figure 5.25: Transformer model discretized with FIT [82] ©2021 Society for Industrial and Applied Mathematics.

the considered grid illustrated in Figure 5.25b is still relatively coarse (i.e., several orders of magnitude larger than the skin depth). The time integration is carried out by the IE method using the (fine) step size $\delta T = 10^{-5}\,\mathrm{s}$. The nonlinear system of equations at each time step is linearized using the so-called *successive substitution method* [82], which can be interpreted as a Newton-like method [30, Section 2.1.3], i.e., for a fixed $n = 1, 2, \ldots$ and for $s = 0, 1, \ldots$ the solution $\mathbf{u}_n^{(s+1)}$ of the linear system

$$\left[\frac{1}{\delta T}\mathbf{M}_\sigma + \mathbf{K}_\nu\left(\mathbf{u}_n^{(s)}\right)\right]\mathbf{u}_n^{(s+1)} = \frac{1}{\delta T}\mathbf{M}\mathbf{u}_{n-1} + \mathbf{f}_n \tag{5.36}$$

is calculated until the error in the solution at two subsequent iterations $s+1$ and s becomes smaller than 10^{-5} in terms of the $\|\cdot\|_\times$-norm, given in (5.12). The sequential solution yields the magnetic flux density distribution at $T = 0.02\,\mathrm{s}$ depicted in Figure 5.25b and the induced TP voltages in the two coils on the period $[0, T]$ depicted in Figure 5.26a.

Within the PP-PC MH approach the coarse step size $\Delta T = 10^{-3}\,\mathrm{s}$ and parallelization among $N = 20$ CPUs is exploited. Linearization of the periodic system (4.68) at the PP-PC iteration $k+1$ is performed using the fixed point iteration (4.83) with the constant matrix [82]

$$\mathbf{H}^{(k)} = \begin{bmatrix} \mathbf{C} + \bar{\mathbf{K}}_\nu & & & -\mathbf{C} \\ -\mathbf{C} & \mathbf{C} + \bar{\mathbf{K}}_\nu & & \\ & \ddots & \ddots & \\ & & -\mathbf{C} & \mathbf{C} + \bar{\mathbf{K}}_\nu \end{bmatrix}, \tag{5.37}$$

where $\mathbf{C} = (1/\Delta T)\mathbf{M}_\sigma$ and $\bar{\mathbf{K}}_\nu$ is obtained for the fixed reluctivity in the steel core $\bar{\nu} = \bar{\nu}_\mathrm{r}\nu_0$ and $\bar{\nu}_\mathrm{r} = 10^{-3}$. Analogously, a fixed point iteration of the form (4.83) is applied also to the TP system (3.95) with the matrix $\mathbf{H}^{(k)}$ from (5.37) and $\mathbf{C} = (1/\delta T)\mathbf{M}$, subsequently applying the MH diagonalization. The PP-PC MH and TP

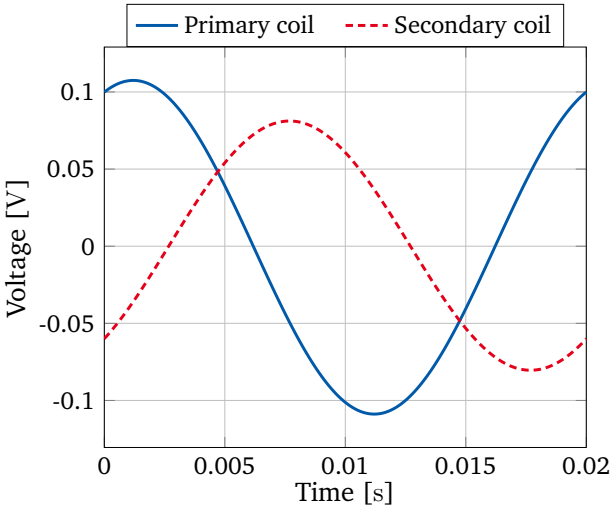

(a) Induced TP voltages in the coils over the period $[0, T]$.

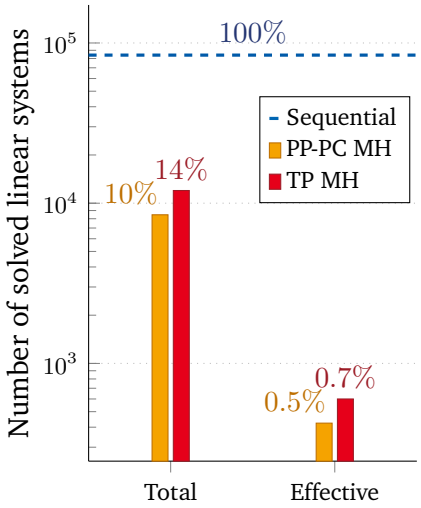

(b) Total and effective linear solutions for $N = 20$.

Figure 5.26: Results for the transformer model [82] ©2021 Society for Industrial and Applied Mathematics.

MH solutions are calculated up to the tolerance $\varepsilon_{\text{tol}} = 10^{-3}$ using the errors (4.26) and (4.84), respectively. Based on [82], we describe the performance of PP-PC MH and TP MH in terms of the effective and total numbers of the solved linear systems, as well as in terms of the wall clock time and compare it to the sequential time stepping.

The sequential time integration with step size $\delta T = 10^{-5}\,\text{s}$ reaches the steady state in terms of the error (5.1) with the $\|\cdot\|_\times$-norm defined in (5.32) up to the tolerance $\varepsilon_{\text{tol}} = 10^{-3}$ after $k^* = 21$ periods, which corresponds to the solution of $84\,000$ linear systems. The TP MH method calculates 600 ELSS until its convergence up to the prescribed tolerance ε_{tol} in terms of the error (4.84) after 6 iterations. It therefore delivers the steady-state solution solving only 0.7% of linear systems, solved within the sequential approach. In turn, PP-PC MH converges in 2 iterations, requiring 6 inner fixed point iterations (4.83) each. It needs 424 ELSS, which is 0.6% of the classical time stepping. The total number of solved linear systems is equal to $6 \cdot 2\,000 = 12\,000$ (14%) for TP MH and $8\,468$ (10%) for PP-PC MH, as illustrated in Figure 5.26b.

Finally, measurements of the wall clock time show that the TP MH calculation lasts slightly more than 9 hours, while PP-PC MH only needs 2.6 hours. The sequential computation over one period takes almost 22 hours, which extends to about 19 days when calculating over 21 periods. The estimated percentage of the classical time stepping are 2% and 0.6% for TP MH and PP-PC MH, respectively. We point out the considerable difference in the percentages of the number of ELSS and of the actual execution time within TP MH (0.7% vs. 2%). This is due to the fact that the linear system solutions take about 60% of the total computational time (while the DFT requires 30%). In contrast, for PP-PC MH, the measure based on the number of ELSS appears to be a much better estimate of the computational effort, since the linear system solutions occupy the major part of the execution time [82].

5.6 Colpitts oscillator model with unknown period

In this section we consider a TP model, where the period T is unknown, in particular, the Colpitts oscillator model [78] with slightly relaxed parameters. It represents a circuit with an inductance $L = 10\,\text{mH}$, a bipolar

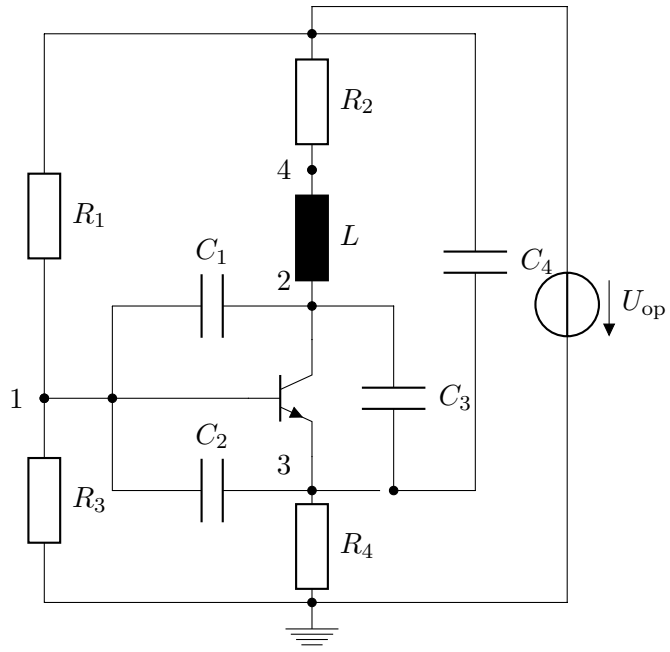

Figure 5.27: Circuit of the Colpitts oscillator model [78].

transistor, as well as with four capacitances $C_1 = 50\,\mathrm{pF}$, $C_2 = 1\,\mathrm{nF}$, $C_3 = 50\,\mathrm{nF}$, and $C_4 = 100\,\mathrm{nF}$, and four resistances $R_1 = 12\,\mathrm{k\Omega}$, $R_2 = 3\,\Omega$, $R_3 = 8.2\,\mathrm{k\Omega}$, and $R_4 = 1.5\,\mathrm{k\Omega}$, see Figure 5.27. This model was also exploited in the multirate context in [108]. In this section we apply the PP-PC UP approach described in Section 4.5 for PinT calculation of the TP solution and the period T. Besides, having calculated the value of T, the TP solution is obtained using the PP-PC approach with the simplified Newton linearization from the Section 4.4.1.

The mathematical model of the circuit is given by an implicit system of ODEs for the unknown four node voltages $\mathbf{U}(t) = \big[U_1(t), U_2(t), U_3(t), U_4(t)\big]^\top$ [78]

$$\begin{bmatrix} 1 & 0 & 0 & 0 \\ 0 & C_1 + C_3 & -C_3 & -C_1 \\ 0 & -C_3 & C_2 + C_3 + C_4 & -C_2 \\ 0 & -C_1 & -C_2 & C_1 + C_2 \end{bmatrix} \mathbf{U}'(t) = \mathbf{f}\big(\mathbf{U}(t)\big), \tag{5.38}$$

with the RHS

$$\mathbf{f}\big(\mathbf{U}\big) = \begin{bmatrix} (U_2 - U_1)R_2/L \\ (U_{\mathrm{op}} - U_1)/R_2 + x_{\mathrm{C}} h(U_4 - U_2) - I_{\mathrm{S}} h(U_4 - U_3) \\ -U_3/R_4 + x_{\mathrm{E}} h(U_4 - U_3) - I_{\mathrm{S}} h(U_4 - U_2) \\ -U_4/R_3 + (U_{\mathrm{op}} - U_4)/R_1 - y_{\mathrm{E}} h(U_4 - U_3) - y_{\mathrm{C}} h(U_4 - U_2) \end{bmatrix}, \tag{5.39}$$

where $U_{\mathrm{op}} = 10\,\mathrm{V}$, $I_{\mathrm{S}} = 1\,\mathrm{mA}$, $y_{\mathrm{C}} = 20\,\mu\mathrm{A}$, $x_{\mathrm{C}} = 1.02\,\mathrm{mA}$, $y_{\mathrm{E}} = 10\,\mu\mathrm{A}$, $x_{\mathrm{E}} = 1.01\,\mathrm{mA}$, and nonlinear function $h(x) = \exp(x/U_{\mathrm{T}}) - 1$, with $U_{\mathrm{T}} = 2.585\,\mathrm{V}$, describes the applied transistor model. Compared to the model introduced in [78], the value of U_{T} is chosen one order of magnitude bigger to ease the convergence of PP-PC using the function h, which due to the presence of the exponential function can easily explode. In practice, this may be avoided using the appropriate homotopy or damping strategies [30]. The transient behavior of the oscillator model (5.38) on $[0, 1.125]\ \mathrm{ms}$ is shown in Figure 5.28a. It is obtained using the IE time stepping with the time step $\delta T = 0.1125\,\mu\mathrm{s}$ starting from the IC $\mathbf{u}_0 = [9.75, 1, 1, 1]^\top$, [83].

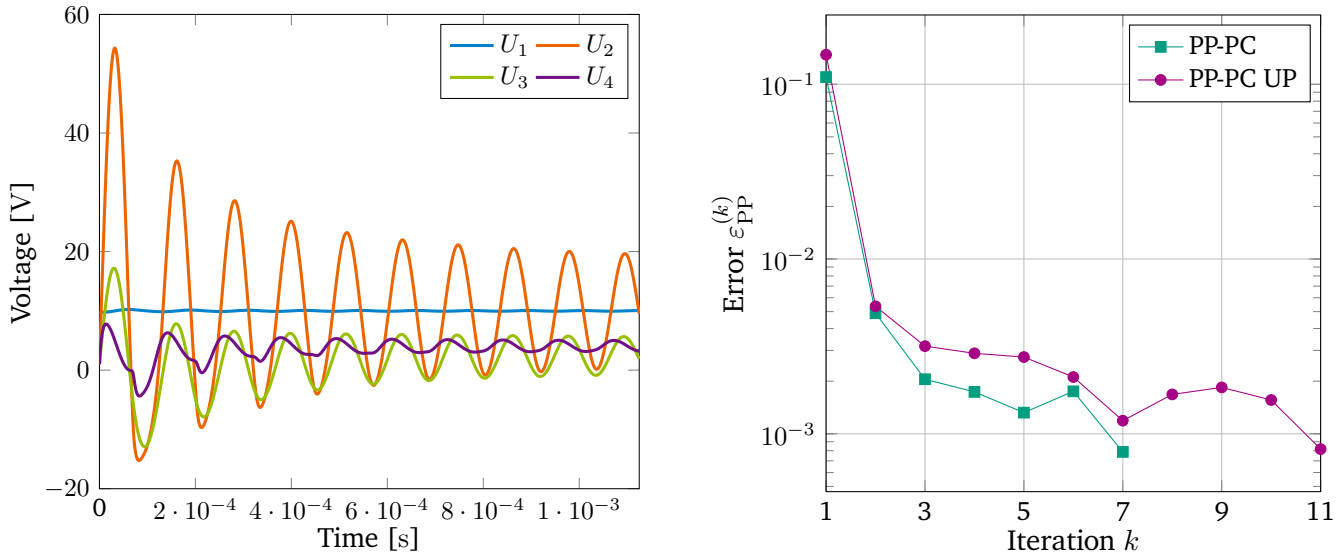

(a) Sequential solution with the IE method.

(b) Convergence of PP-PC and PP-PC UP.

Figure 5.28: Results for the Colpitts oscillator [83].

To find the periodic steady-state solution and the corresponding period T we apply the iteration (4.107). The linearization of the nonlinear TP system on the coarse level is performed using a surrogate linear model, i.e., $\bar{\mathcal{G}}$ solves the problem (4.106) with $\bar{\mathbf{f}}(\mathbf{U}) = \mathbf{A}\mathbf{U} + \mathbf{c}$ given by

$$\mathbf{A} = \begin{bmatrix} -R_2/L & R2/L & & \\ -1/R_2 & -x_{\mathrm{C}}/\bar{U}_{\mathrm{T}} & I_{\mathrm{S}}/\bar{U}_{\mathrm{T}} & (x_{\mathrm{C}} - I_{\mathrm{S}})/\bar{U}_{\mathrm{T}} \\ 0 & I_{\mathrm{S}}/\bar{U}_{\mathrm{T}} & -1/R_4 - x_{\mathrm{E}}/\bar{U}_{\mathrm{T}} & (x_{\mathrm{E}} - I_{\mathrm{S}})/\bar{U}_{\mathrm{T}} \\ 0 & y_{\mathrm{C}}/\bar{U}_{\mathrm{T}} & y_{\mathrm{E}}/\bar{U}_{\mathrm{T}} & -1/R_3 - 1/R_1 - y_{\mathrm{E}}/\bar{U}_{\mathrm{T}} - y_{\mathrm{C}}/\bar{U}_{\mathrm{T}} \end{bmatrix}, \tag{5.40}$$

$$\mathbf{c} = [0, U_{\mathrm{op}}/R_2, 0, U_{\mathrm{op}}/R_1]^{\top}, \tag{5.41}$$

with the original value $\bar{U}_{\mathrm{T}} = 0.2585\,\mathrm{V}$. The unit interval $[0, 1]$ is split into $N = 10$ windows, giving the coarse time step $\Delta\tau = 0.1$, while the fine step is chosen $\delta\tau = 10^{-4}$. The PP-PC UP method converges in 11 iterations and calculated the period $T = 0.1125\,\mathrm{ms}$. For the given period T the PP-PC method with the simplified Newton linearization from the Section 4.4.1 converges in 7 iterations. Both results are obtained up to the tolerance of $\varepsilon_{\mathrm{tol}} = 10^{-3}$ in terms of the error (4.26), whose values at each iteration are illustrated in Figure 5.28b. Comparing the computational cost in terms of the number of ELSS, we have that PP-PC and PP-PC UP deliver the TP solution solving 4 and 3 times less linear systems than the sequential time stepping, respectively, [83].

5.7 Conclusion

This chapter began with a numerical convergence study of the multirate Parareal algorithm for an RL-circuit with pulse-width modulated input, which was in agreement with the theoretical estimate derived in Section 4.3.1. The method was also applied to a buck converter model with two choices of the coarse solver: the first one using a sinusoidal low-frequency input and the second one using the multirate partial differential equation approach. The multirate Parareal and multirate PP-IC methods were then applied to a four-pole

induction machine model. Moreover, time-parallelization of the steady-state analysis of an induction motor used in an electric vehicle drive was performed, due to incorporation of PP-IC into an industrial solver EDYSON of the Robert Bosch GmbH. The speed up of factor 28 compared to the classical sequential time stepping was obtained when exploiting $N = 80$ cores. Besides, we investigated the efficiency of Parareal for an induction motor simulation based on an eigenvalue study of two equivalent motor schemes.

Computation of the steady-state solution of a coaxial cable model shows superiority of the PP-PC MH and TP MH methods over the other considered PinT approaches such as PP-IC and PP-PC with the Jacobi-like fixed point iteration from [50]. In the linear case, the computational cost of the TP MH method was the lowest in terms of effective linear systems solutions, as it required calculation only from 0.05% to 0.5% of the sequential time stepping, when exploiting $N = 50$ and $N = 5$ cores, respectively. In the nonlinear case, PP-PC MH outperformed TP MH for the numbers of cores $N = 10, 20, 50,$ calculating the periodic solution only in 25 minutes, when using $N = 50$ cores, in contrast to almost 3 day long sequential calculations. Application of the PP-PC MH and the TP MH approaches to a transformer model gives the speed up of factors 176 and 51, respectively, compared to the sequential time integration, whose duration was estimated to be approximately 19 days. Finally, the PP-PC UP approach, proposed in Section 4.5, was exploited to calculate a periodic solution of a Colpitts oscillator model.

6 Conclusion and outlook

In this thesis new parallel-in-time methods were proposed for engineering applications and analyzed mathematically. In particular, a multirate Parareal algorithm [51], suitable for problems with pulse-width modulated excitations, was developed and investigated in Section 4.3. The method was extended to time-periodic problems by the author in [52] and tested for an RL-circuit model, a buck converter, and an induction machine in Section 5.1.

The application of the PP-IC method to the steady-state analysis of an induction motor, incorporated into an electric vehicle drive, in Section 5.2 showed superiority of the approach compared to several other existing methods such as the simplified TP-EEC [128] and the calculation of a suitable IC [12]. As a result, a possible speed up of factor 28 compared to the sequential time stepping was observed when exploiting 80 cores [11]. This result is a great aid to industry, as it allows to accelerate the computational design workflow significantly. PP-PC is especially attractive due to its non-intrusiveness, as it allows to exploit possibly already existing (black-box) time-domain solvers.

The convergence of Parareal for induction motors was investigated via eigenvalue-based analysis of two analytical motor models in Section 5.3. Using 200 subintervals a fast convergence (4 and 10 iterations for the two models) was observed, in contrast to a magnetomechanical oscillator, whose Parareal solution as expected had convergence difficulties (60 and 66 iterations for linear and nonlinear models, respectively) related to the beating phenomenon [40]. Also an initial investigation of a linear GetDP model of an induction machine showed presence of only purely real eigenvalues. We point out that this numerical analysis depends on the particular model and shall provide a basis for a more extensive investigation in the future.

A simplified Newton linearization method was introduced and analyzed in Section 4.4 in order to apply the MH diagonalization approach at each iteration of the PP-PC algorithm based on [82]. The application of the PP-PC MH method to a nonlinear 2D coaxial cable model in Section 5.4 gave the periodic steady-state solution in 15 min when using 50 processors, while the sequential solution until the steady state required 66.7 hours (about 3 days). In case of a 3D transformer model and 20 cores, the PP-PC MH approach needed 2.6 hours, in contrast to about 19 days of the sequential time stepping, see Section 5.5. Finally, the PP-PC UP algorithm was proposed and applied to the Colpitts oscillator model based on [83].

To summarize, we point out that although the approaches, which impose a direct periodic coupling on the solution, such as PP-PC MH, outperform other parallelization methods with a relaxed periodicity constraint such as PP-IC, they are more cumbersome to implement in practice, especially for nonlinear problems. Indeed, in order to apply the MH diagonalization within PP-PC, the system matrix has to be first linearized, e.g., with the simplified Newton method, and then transformed into block-cyclic form. In this case, it might be difficult to find an initial approximation for the linearization method, which should at the same time be suitable for the method's convergence and lead to the desired block-cyclic structure. Besides, this approach is excessively intrusive and it is not straightforward to include the rotation in case of electric motor calculations in its

framework. Thus, we consider the PP-IC algorithm to be the most favorable for the steady-state analysis of industrial applications like induction motors due to its simplicity, independence from the motor configurations as, e.g., particular operating points or rotor types, and the already mentioned non-intrusiveness. We also note that the computational costs of PP-IC are comparable to those of PP-PC with the Jacobi-like iteration from [50], as it has been observed for a nonlinear coaxial cable model, when exploiting, e.g., 20 or 50 cores, see Section 5.4.2.

Future research directions could be based on incorporation of Parareal into further directions of mathematics and engineering, described as follows.

1. Investigation of different problem-specific solvers on the coarse and the fine levels within Parareal as, e.g., in [27], where a surrogate coarse model and the fine solution via waveform relaxation were applied for field-circuit coupled systems.
2. Development of novel multiscale parallel-in-time methods which allow for optimal parallel efficiency based on the micro-macro approach [85]. Construction of appropriate "matching" conditions to eliminate the inconsistencies between the fine and the coarse solutions.
3. Parallelized calculation of existing numerical algorithms, e.g., the Runge-Kutta Chebyshev methods [122], similarly to the ParaStieltjes algorithm proposed in [54] for the Stieltjes procedure.
4. Efficient incorporation of parallel-in-time methods into optimization and control problems, e.g., based on [130].
5. Parallelization of uncertainty quantification approaches such as the multilevel Monte Carlo methods [57]. Integration of the method into robust optimization processes in the presence of uncertainties.

7 Appendix

7.1 Derivation of the magnetomechanical oscillator model

In this section we derive the representation (5.22) of the electromagnetic torque T_{EM} for a magnetomechanical oscillator model from Section 5.3.1. Due to the power balance equation (2.108), we have for the torque

$$T_{\mathrm{EM}} = \frac{P_{\mathrm{mech}}}{\omega_{\mathrm{mech}}} = \frac{P_{\mathrm{st}} - P_{\mathrm{rt}}}{\omega_{\mathrm{mech}}}, \tag{7.1}$$

where P_{st} is the power from stator to the air gap and P_{rt} is the power from the air gap to rotor. The power can be calculated using the Poynting vector $\vec{S} = \vec{E} \times \vec{H}$ [115, Section 5.5], with the electric field strength $\vec{E}$ and the magnetic field strength $\vec{H}$. The MVP representation (2.25) with $\phi = 0$ and $\vec{H} = \nu \operatorname{curl} \vec{A}$ within the 2D setting in cylindrical coordinates gives

$$E_z = -\frac{\partial A_z}{\partial t} \quad \text{and} \quad H_\varphi = -\nu \frac{\partial A_z}{\partial r}.$$

The radial component of $\vec{S}$ is thus defined by

$$S_r(r, \varphi, t) = -E_z(r, \varphi, t) H_\varphi(r, \varphi, t) = -\frac{\partial A_z(r, \varphi, t)}{\partial t} \nu \frac{\partial A_z(r, \varphi, t)}{\partial r}. \tag{7.2}$$

Let the air gap of the oscillator have inner radius r_{rt} and outer radius r_{st}. The power flowing in the radial direction through a cylinder hull of length ℓ_z and radius $r_{\mathrm{rt}} \leq r_{\mathrm{ag}} \leq r_{\mathrm{st}}$ is given by

$$P_r(t) = \ell_z r_{\mathrm{ag}} \int_0^{2\pi} S_r(r_{\mathrm{ag}}, \varphi, t) \mathrm{d}\varphi. \tag{7.3}$$

Since the orientations of the powers P_{st} and P_{rt} are opposite to the radial direction, we have the definitions

$$P_{\mathrm{st}}(t) = -\ell_z r_{\mathrm{ag}} \int_0^{2\pi} S_r(r_{\mathrm{ag}}, \varphi_{\mathrm{st}}, t) \mathrm{d}\varphi_{\mathrm{st}}, \qquad P_{\mathrm{rt}}(t) = -\ell_z r_{\mathrm{ag}} \int_0^{2\pi} S_r(r_{\mathrm{ag}}, \varphi_{\mathrm{rt}}, t) \mathrm{d}\varphi_{\mathrm{rt}}, \tag{7.4}$$

where φ_{st} and φ_{rt} are azimuthal coordinates attached to stator and rotor, respectively. They are related via the rotor angle $\theta(t)$ as in (2.97), see Figure 2.13.

The axial components of the MVP at the outer and the inner circles are (see Figure 5.15)

$$A_z(r_{\mathrm{st}}, \varphi_{\mathrm{st}}) = \hat{A}_{\mathrm{st}} \cos(p\varphi_{\mathrm{st}}) \quad \text{and} \quad A_z(r_{\mathrm{rt}}, \varphi_{\mathrm{rt}}) = \hat{A}_{\mathrm{rt}} \cos(p\varphi_{\mathrm{rt}}), \tag{7.5}$$

respectively, where $p \geq 1$ is the pole pair number and $\hat{A}_{\mathrm{st}}$ and $\hat{A}_{\mathrm{rt}}$ are real-valued amplitudes. The analytical solution for the MVP in the air gap and the BCs (7.5) at $r = r_{\mathrm{st}}$ and $r = r_{\mathrm{rt}}$ lead to an expression

$$A_z(r, \varphi_{\mathrm{st}}, \varphi_{\mathrm{rt}}) = \hat{A}_{\mathrm{st}} f_{\mathrm{st},p}(r) \cos(p\varphi_{\mathrm{st}}) + \hat{A}_{\mathrm{rt}} f_{\mathrm{rt},p}(r) \cos(p\varphi_{\mathrm{rt}}) \tag{7.6}$$

where $f_{\mathrm{st},p}(r)$ and $f_{\mathrm{rt},p}(r)$ are the *annular functions* given by a linear combination of r^p and r^{-p}, i.e.,

$$f_{\mathrm{st},p}(r) = a(r/r_{\mathrm{ag}})^p + b(r/r_{\mathrm{ag}})^{-p}, \qquad f_{\mathrm{rt},p}(r) = b(r/r_{\mathrm{ag}})^p + a(r/r_{\mathrm{ag}})^{-p}, \tag{7.7}$$

with the coefficients

$$a = \frac{-\gamma^{-p}}{\gamma^{2p} - \gamma^{-2p}}, \qquad b = \frac{\gamma^{p}}{\gamma^{2p} - \gamma^{-2p}}, \tag{7.8}$$

the geometric mean air gap radius $r_{\mathrm{ag}} = \sqrt{r_{\mathrm{st}} r_{\mathrm{rt}}}$, and the geometric air gap ratio $\gamma = \sqrt{r_{\mathrm{st}}/r_{\mathrm{rt}}}$. The annular functions satisfy

$$f_{\mathrm{st},p}(r_{\mathrm{st}}) = f_{\mathrm{rt},p}(r_{\mathrm{rt}}) = 1, \qquad f_{\mathrm{st},p}(r_{\mathrm{rt}}) = f_{\mathrm{rt},p}(r_{\mathrm{st}}) = 0. \tag{7.9}$$

Calculating the derivatives we have the Wronskian of the annular functions

$$W_p(r) = f'_{\mathrm{rt},p}(r) f_{\mathrm{st},p}(r) - f_{\mathrm{rt},p}(r) f'_{\mathrm{st},p}(r) = \frac{-2p}{r(\gamma^{2p} - \gamma^{-2p})}. \tag{7.10}$$

Due to the coordinate transformation (2.97), the MVP in the air gap is fully written in terms of the stator and the rotor coordinate systems, i.e.,

$$A_z(r, \varphi_{\mathrm{st}}, t) = \hat{A}_{\mathrm{st}} f_{\mathrm{st},p}(r) \cos(p\varphi_{\mathrm{st}}) + \hat{A}_{\mathrm{rt}} f_{\mathrm{rt},p}(r) \cos\big(p\varphi_{\mathrm{st}} - p\theta(t)\big), \tag{7.11}$$

$$A_z(r, \varphi_{\mathrm{rt}}, t) = \hat{A}_{\mathrm{st}} f_{\mathrm{st},p}(r) \cos\big(p\varphi_{\mathrm{rt}} + p\theta(t)\big) + \hat{A}_{\mathrm{rt}} f_{\mathrm{rt},p}(r) \cos(p\varphi_{\mathrm{rt}}). \tag{7.12}$$

Using (7.11) and considering the reluctivity in the air gap is ν_0, we calculate the radial component of the Poynting vector in the stator coordinates:

$$\begin{aligned} S_r(r, \varphi_{\mathrm{st}}, t) &= -\nu_0 \hat{A}_{\mathrm{rt}} f_{\mathrm{rt},p}(r) p\theta'(t) \sin(p\varphi_{\mathrm{st}} - p\theta) \Big[\hat{A}_{\mathrm{st}} f'_{\mathrm{st},p}(r) \cos(p\varphi_{\mathrm{st}}) + \hat{A}_{\mathrm{rt}} f'_{\mathrm{rt},p}(r) \cos(p\varphi_{\mathrm{st}} - p\theta) \Big] \\ &= -\nu_0 \hat{A}_{\mathrm{rt}} f_{\mathrm{rt},p}(r) p\theta'(t) \Big[\hat{A}_{\mathrm{st}} f'_{\mathrm{st},p}(r) \big(\sin(2p\varphi_{\mathrm{st}} - p\theta) - \sin(p\theta) \big) + \hat{A}_{\mathrm{rt}} f'_{\mathrm{rt},p}(r) \sin(2p\varphi_{\mathrm{st}} - 2p\theta) \Big] /2, \end{aligned}$$

where we have used the trigonometric identities

$$\begin{aligned} \sin(p\varphi - p\theta) \cos(p\theta) &= \big(\sin(2p\varphi - p\theta) - \sin(p\theta) \big)/2, \\ \sin(p\varphi - p\theta) \cos(p\varphi - p\theta) &= \big(\sin(2p\varphi - 2p\theta) \big)/2. \end{aligned}$$

Taking into account the integration rule

$$\int_0^{2\pi} \sin(m\varphi + \beta) \mathrm{d}\varphi = 0, \quad m \in \mathbb{N}, \tag{7.13}$$

we obtain due to (7.4) the stator power

$$P_{\mathrm{st}}(t) = -\ell_z r_{\mathrm{ag}} \nu_0 \pi \hat{A}_{\mathrm{rt}} \hat{A}_{\mathrm{st}} f_{\mathrm{rt},p}(r_{\mathrm{ag}}) f'_{\mathrm{st},p}(r_{\mathrm{ag}}) p\theta'(t) \sin(p\theta). \tag{7.14}$$

Analogously, using the representation (7.12) in the rotor coordinates we have

$$\begin{aligned} S_r(r, \varphi_{\mathrm{st}}, t) &= \nu_0 \hat{A}_{\mathrm{st}} f_{\mathrm{st},p}(r) p\theta'(t) \sin(p\varphi_{\mathrm{rt}} + p\theta) \Big[\hat{A}_{\mathrm{st}} f'_{\mathrm{st},p}(r) \cos(p\varphi_{\mathrm{rt}} + p\theta) + \hat{A}_{\mathrm{rt}} f'_{\mathrm{rt},p}(r) \cos(p\varphi_{\mathrm{rt}}) \Big] \\ &= \nu_0 \hat{A}_{\mathrm{st}} f_{\mathrm{st},p}(r) p\theta'(t) \Big[\hat{A}_{\mathrm{st}} f'_{\mathrm{st},p}(r) \sin(2p\varphi_{\mathrm{rt}} + 2p\theta) + \hat{A}_{\mathrm{rt}} f'_{\mathrm{rt},p}(r) \big(\sin(2p\varphi_{\mathrm{rt}} + p\theta) + \sin(p\theta) \big) \Big] /2, \end{aligned}$$

which using (7.4) and (7.13) gives the rotor power

$$P_{\mathrm{rt}}(t) = -\ell_z r_{\mathrm{ag}} \nu_0 \pi \hat{A}_{\mathrm{rt}} \hat{A}_{\mathrm{st}} f_{\mathrm{st},p}(r_{\mathrm{ag}}) f'_{\mathrm{rt},p}(r_{\mathrm{ag}}) p\theta'(t) \sin(p\theta). \tag{7.15}$$

The mechanical power is defined by the difference between (7.14) and (7.15), i.e.,

$$\begin{aligned} P_{\mathrm{mech}}(t) &= \ell_z r_{\mathrm{ag}} \nu_0 \pi \hat{A}_{\mathrm{rt}} \hat{A}_{\mathrm{st}} p \theta'(t) \sin(p\theta) \left[f_{\mathrm{st},p}(r_{\mathrm{ag}}) f'_{\mathrm{rt},p}(r_{\mathrm{ag}}) - f_{\mathrm{rt},p}(r_{\mathrm{ag}}) f'_{\mathrm{st},p}(r_{\mathrm{ag}}) \right] \\ &= -\frac{2\pi p^2 \ell_z \nu_0 \hat{A}_{\mathrm{rt}} \hat{A}_{\mathrm{st}}}{\gamma^{2p} - \gamma^{-2p}} \theta'(t) \sin(p\theta), \end{aligned} \tag{7.16}$$

where the formula (7.10) was applied. As a result, the electromagnetic torque is determined by (5.22) due to (7.1) and since $\omega_{\mathrm{mech}} = \theta'(t)$.

List of acronyms

2D	two-dimensional
3D	three-dimensional
3ph	three-phase
a.e.	almost every
AC	alternating current
BC	boundary condition
BVP	boundary-value problem
CPU	central processing unit
DAE	differential-algebraic equation
DC	direct current
DFT	discrete Fourier transform
DoFs	degrees of freedom
EBC	electric boundary condition
EE	explicit Euler
ELSS	effective linear systems solutions
FEM	finite element method
FFT	fast Fourier transform
FIT	finite integration technique
HB	harmonic balance
IBVP	initial-boundary-value problem
IC	initial condition
IE	implicit Euler
iff	if and only if
IVP	initial-value problem
KCL	Kirchhoff current law
KVL	Kirchhoff voltage law
LHS	left-hand side
LTE	local truncation error
MBC	magnetic boundary condition
MH	multi-harmonic
MNA	modified nodal analysis
MPDE	multirate partial differential equation
MQS	magnetoquasistatic
MVP	magnetic vector potential
ODE	ordinary differential equation
OP	operating point
PDE	partial differential equation
PinT	parallel-in-time

PP-IC	periodic Parareal algorithm with initial-value coarse problem
PP-PC	periodic Parareal algorithm with periodic coarse problem
PP-PC MH	PP-PC with MH coarse grid correction
PP-PC UP	PP-PC with unknown period
PWM	pulse-width modulated
RHS	right-hand side
TP	time-periodic
TPBVP	TP boundary-value problem
TP-EEC	TP explicit error correction
TR	trapezoidal rule
UP	unknown period

List of symbols

Electromagnetic field quantities

Symbol	Unit	Description
$\vec{B}$	T	Magnetic flux density
$\vec{H}$	$\mathrm{A/m}$	Magnetic field strength
$\vec{D}$	$\mathrm{C/m^2}$	Electric flux density
$\vec{E}$	$\mathrm{V/m}$	Electric field strength
$\vec{J}$	$\mathrm{A/m^2}$	Electric current density
$\vec{J}_\mathrm{s}$	$\mathrm{A/m^2}$	Electric source current density
$\vec{A}$	$\mathrm{Wb/m}$	Magnetic vector potential
ϕ	V	Electric scalar potential
ϱ	$\mathrm{C/m^3}$	Electric charge density
ε	$\mathrm{F/m}$	Electric permittivity
μ	$\mathrm{H/m}$	Magnetic permeability
μ_0	$\mathrm{H/m}$	Magnetic permeability in vacuum
ν	$\mathrm{m/H}$	Magnetic reluctivity
ν_0	$\mathrm{m/H}$	Magnetic reluctivity in vacuum
σ	$\mathrm{S/m}$	Electric conductivity

Electric circuit quantities

Symbol	Unit	Description
R	Ω	Resistance
L	H	Inductance
C	F	Capacitance
v	V	Voltage
i	A	Current

Induction motor quantities

Symbol	Unit	Description
s		Slip
θ	rad	Rotor angle
ω_{sync}	$\mathrm{rad/s}$	Synchronous speed
ω_{mech}	$\mathrm{rad/s}$	Revolution speed
T_{EM}	$\mathrm{N\,m}$	Electromagnetic torque
T_{load}	$\mathrm{N\,m}$	Load (or shaft) torque
P_{mech}	W	Mechanical power
J	$\mathrm{kg/m^2}$	Moment of inertia
R_{st}	Ω	Stator resistance
R_{rt}	Ω	Rotor resistance
R_{Fe}	Ω	Iron loss resistance
$L_{\sigma,\mathrm{st}}$	H	Stator leakage inductance
$L_{\sigma,\mathrm{rt}}$	H	Rotor leakage inductance
L_{h}	H	Magnetizing inductance

Mathematical notations

Symbol	Description
$\imath$	Imaginary unit
$\mathbb{R}$	Set of real numbers
$\mathbb{R}^+$	Set of positive real numbers
$\mathbb{R}_0^+$	Set of non-negative real numbers
$\mathbb{R}^n$	n-dimensional real space
$\mathbb{N}$	Set of natural numbers
$\mathbb{Z}$	Set of integer numbers
$\mathbb{C}$	Set of complex numbers
$\mathbb{C}^-$	Set of complex numbers with non-positive real part
$C^k(U)$	Class of continuously differentiable functions up to order k on an open domain U
$C_0^\infty(U)$	Class of infinitely continuously differentiable functions with compact support in U

Bibliography

[1] R. A. Adams, *Sobolev spaces*, ser. Pure and applied mathematics. New York: Academic Press, 1978.

[2] M. Alexander, A. Kelleter, M. R. De Larramendi, P. Heuser, and M. Herranz Gracia, *Electric machine*, Patent US US 2017 / 0331353, 2017.

[3] A. Alonso Rodríguez and A. Valli, *Eddy Current Approximation of Maxwell Equations*, ser. Modeling, Simulation and Applications. Heidelberg: Springer, 2010, vol. 4. DOI: 10.1007/978-88-470-1506-7.

[4] H. W. Alt, *Linear Functional Analysis: An Application-Oriented Introduction*. Springer-Verlag London, 2016, ISBN: 978-1-4471-7280-2. DOI: 10.1007/978-1-4471-7280-2.

[5] A. Arkkio, *Finite element analysis of cage induction motors fed by static frequency converters*, *IEEE Transactions on Magnetics*, vol. 26, no. 2, pp. 551–554, 1990, ISSN: 0018-9464. DOI: 10.1109/20.106376.

[6] A. Arkkio, *Analysis of induction motors based on the numerical solution of the magnetic field and circuit equations*, PhD Thesis, Helsinki University of Technology, 1987, ISBN: 951-22-6076-X. urn: urn:nbn:fi:tkk-001267.

[7] F. Assous, P. Ciarlet, and S. Labrunie, *Mathematical foundations of computational electromagnetism*. Springer, 2018, ISBN: 978-3-319-70841-6.

[8] F. Bachinger, U. Langer, and J. Schöberl, *Numerical analysis of nonlinear multiharmonic eddy current problems*, *Numerische Mathematik*, vol. 100, no. 4, pp. 593–616, 2005. DOI: 10.1007/s00211-005-0597-2.

[9] G. Bal, *On the convergence and the stability of the parareal algorithm to solve partial differential equations*, R. Kornhuber, R. Hoppe, J. Périaux, O. Pironneau, O. B. Widlund, and J. Xu, Eds., ser. Lecture Notes in Computational Science and Engineering, vol. 40, Berlin: Springer, 2005, pp. 425–432, ISBN: 978-3-540-22523-2. DOI: 10.1007/b138136.

[10] A. Bartel, S. Baumanns, and S. Schöps, *Structural analysis of electrical circuits including magnetoquasistatic devices*, *Applied Numerical Mathematics*, vol. 61, pp. 1257–1270, 2011, ISSN: 0168-9274. DOI: 10.1016/j.apnum.2011.08.004.

[11] D. Bast, I. Kulchytska-Ruchka, S. Schöps, and O. Rain, *Accelerated steady-state torque computation for induction machines using parallel-in-time algorithms*, *IEEE Transactions on Magnetics*, vol. 56, no. 2, pp. 1–9, 2020, ISSN: 0018-9464. DOI: 10.1109/TMAG.2019.2945510. arXiv: 1902.08277.

[12] A. Bermúdez, D. Gómez, M. Piñeiro, and P. Salgado, *A novel numerical method for accelerating the computation of the steady-state in induction machines*, *Computers and Mathematics with Applications*, vol. 79, no. 2, pp. 274–292, 2020, ISSN: 0898-1221. DOI: 10.1016/j.camwa.2019.06.032.

[13] G. Bertotti, *Hysteresis in Magnetism: For Physicists, Materials Scientists, and Engineers*, 1st ed. New York: Academic Press, 1998, ISBN: 9780080534374.

[14] A. Binder, *Elektrische Maschinen und Antriebe*. Berlin Heidelberg: Springer, 2012, ISBN: 978-3-540-71850-5. DOI: 10.1007/978-3-540-71850-5.

[15] B. K. Bose, *Power Electronics And Motor Drives*. Burlington: Academic Press, 2006, ISBN: 978-0-12-088405-6.

[16] A. Bossavit, *Computational Electromagnetism: Variational Formulations, Complementarity, Edge Elements*. San Diego, CA, USA: Academic Press, 1998, ISBN: 978-0-12-118710-1. DOI: 10.1016/B978-0-12-118710-1.X5000-4.

[17] O. Bíró and K. Preis, *An efficient time domain method for nonlinear periodic eddy current problems*, *IEEE Transactions on Magnetics*, vol. 42, no. 4, pp. 695–698, 2006, ISSN: 0018-9464. DOI: 10.1109/TMAG.2006.871666.

[18] H. G. Brachtendorf, G. Welsch, and R. Laur, *Fast simulation of the steady-state of circuits by the harmonic balance technique*, in *Proceedings of ISCAS 95 - International Symposium on Circuits and Systems*, IEEE, 1995. DOI: 10.1109/iscas.1995.520406.

[19] H. G. Brachtendorf, G. Welsch, R. Laur, and A. Bunse-Gerstner, *Numerical steady state analysis of electronic circuits driven by multi-tone signals*, *Electrical Engineering (Archiv für Elektrotechnik)*, vol. 79, no. 2, pp. 103–112, 1996. DOI: 10.1007/BF01232919.

[20] J. R. Brauer, *Simple equations for the magnetization and reluctivity curves of steel*, *IEEE Transactions on Magnetics*, vol. 11, no. 1, p. 81, 1975, ISSN: 0018-9464. DOI: 10.1109/TMAG.1975.1058555.

[21] K. E. Brenan, S. L. Campbell, and L. R. Petzold, *Numerical Solution of Initial-Value Problems in Differential-Algebraic Equations*. Philadelphia, PA, USA: Society for Industrial and Applied Mathematics, 1995, ISBN: 978-0-89871-353-4. DOI: 10.1137/1.9781611971224.

[22] S. C. Brenner and L. R. Scott, *The mathematical theory of finite element methods*, 3. ed., ser. Texts in applied mathematics. New York: Springer, 2008, vol. 15, ISBN: 9780387759333.

[23] H. Brezis, *Functional Analysis, Sobolev Spaces and Partial Differential Equations*, ser. Universitext (Berlin. Print). Springer, 2010, ISBN: 978-0387709130.

[24] R. Bulirsch, *Die Mehrzielmethode zur numerischen Lösung von nichtlinearen Randwertproblemen und Aufgaben der optimalen Steuerung*, Carl-Cranz-Gesellschaft, Technical Report, 1971.

[25] K. Burrage, *Parallel and sequential methods for ordinary differential equations*. Oxford: Oxford University Press, 1995, ISBN: 978-0198534327.

[26] I. Cortes Garcia, H. De Gersem, and S. Schöps, *A structural analysis of field/circuit coupled problems based on a generalised circuit element*, *Numerical Algorithms*, vol. 83, no. 1, pp. 373–394, 2020, ISSN: 1017-1398. DOI: 10.1007/s11075-019-00686-x. arXiv: 1801.07081.

[27] I. Cortes Garcia, I. Kulchytska-Ruchka, and S. Schöps, *Efficient simulation of field/circuit coupled systems with parallelised waveform relaxation*, *IEEE Transactions on Magnetics*, vol. 56, no. 2, pp. 1–4, 2020, ISSN: 0018-9464. DOI: 10.1109/TMAG.2019.2952695. arXiv: 1909.08895.

[28] I. Cortes Garcia, S. Schöps, C. Strohm, and C. Tischendorf, *Generalized elements for a structual analysis of circuits*, T. Reis, S. Grundel, and S. Schöps, Eds., ser. Differential-Algebraic Equations Forum, Berlin: Springer, 2020, ISBN: 978-3-030-53904-7. DOI: 10.1007/978-3-030-53905-4. arXiv: 1912.05199.

[29] G. De Luca, P. Bolcato, and W. H. A. Schilders, *Proper Initial Solution to Start Periodic Steady-State-Based Methods*, *IEEE Transactions on Circuits and Systems I: Regular Papers*, vol. 66, no. 3, pp. 1104–1115, 2019. DOI: 10.1109/TCSI.2018.2874570.

[30] P. Deuflhard, *Newton methods for nonlinear problems: affine invariance and adaptive algorithms*. Berlin: Springer, 2004.

[31] P. Deuflhard and F. Bornemann, *Scientific Computing with Ordinary Differential Equations*, 1st ed. New York: Springer, 2002, ISBN: 978-1441930118.

[32] C. Di, I. Petrov, J. J. Pyrhönen, and J. Chen, *Accelerating the Time-Stepping Finite-Element Analysis of Induction Machines in Transient-Magnetic Solutions*, *IEEE Access*, vol. 7, pp. 122 251–122 260, 2019. DOI: 10.1109/ACCESS.2019.2938269.

[33] V. Dolean, P. Jolivet, and F. Nataf, *An Introduction to Domain Decomposition Methods*. Philadelphia, PA: Society for Industrial and Applied Mathematics, 2015. DOI: 10.1137/1.9781611974065.

[34] D. Estévez Schwarz, *A step-by-step approach to compute a consistent initialization for the MNA*, *International Journal of Circuit Theory and Applications*, vol. 30, no. 1, pp. 1–6, 2002.

[35] ——, *Consistent initialization for index-2 differential algebraic equations and its application to circuit simulation*, Dissertation, Humboldt-Universität Berlin, Berlin, 2000.

[36] D. Estévez Schwarz and R. Lamour, *The computation of consistent initial values for nonlinear index-2 differential-algebraic equations*, *Numerical Algorithms*, vol. 26, no. 1, pp. 49–75, 2001, ISSN: 1017-1398. DOI: 10.1023/A:1016696413810.

[37] D. Estévez Schwarz and C. Tischendorf, *Structural analysis of electric circuits and consequences for MNA*, *International Journal of Circuit Theory and Applications*, vol. 28, no. 2, pp. 131–162, 2000. DOI: 10.1002/(SICI)1097-007X(200003/04)28:2<131::AID-CTA100>3.0.CO;2-W.

[38] L. C. Evans, *Partial Differential Equations*. Oxford: Oxford University Press, 1998.

[39] C. Farhat and M. Chandesris, *Time-decomposed parallel time-integrators: theory and feasibility studies for fluid, structure, and fluid–structure applications*, *International Journal for Numerical Methods in Engineering*, vol. 58, no. 9, pp. 1397–1434, 2003, ISSN: 0029-5981. DOI: https://doi.org/10.1002/nme.860.

[40] C. Farhat, J. Cortial, C. Dastillung, and H. Bavestrello, *Time-parallel implicit integrators for the near-real-time prediction of linear structural dynamic responses*, *International Journal for Numerical Methods in Engineering*, vol. 67, no. 5, pp. 697–724, 2006, ISSN: 0029-5981. DOI: https://doi.org/10.1002/nme.1653. eprint: https://onlinelibrary.wiley.com/doi/pdf/10.1002/nme.1653.

[41] A. F. Filippov, *Differential equations with discontinuous righthand sides: control systems*, ser. Mathematics and Its Applications. Springer, Dordrecht, 1988, vol. 18, ISBN: 978-90-481-8449-1. DOI: 10.1007/978-94-015-7793-9.

[42] F. N. Fritsch and R. E. Carlson, *Monotone piecewise cubic interpolation*, *SIAM Journal on Numerical Analysis*, vol. 17, no. 2, pp. 238–246, 1980. DOI: 10.1137/0717021.

[43] H. R. Fudeh and C. M. Ong, *Modeling and Analysis of Induction Machines Containing Space Harmonics Part I: Modeling and Transformation*, *IEEE Transactions on Power Apparatus and Systems*, vol. PAS-102, no. 8, pp. 2608–2615, 1983. DOI: 10.1109/TPAS.1983.317781.

[44] M. J. Gander and S. Vandewalle, *Analysis of the parareal time-parallel time-integration method*, *SIAM Journal on Scientific Computing*, vol. 29, no. 2, pp. 556–578, 2007, ISSN: 1064-8275. DOI: 10.1137/05064607X.

[45] M. J. Gander, *50 years of time parallel time integration*, T. Carraro, M. Geiger, S. Körkel, and R. Rannacher, Eds., ser. Contributions in Mathematical and Computational Sciences, vol. 9, Springer, 2015, pp. 69–113, ISBN: 978-3-319-23320-8. DOI: 10.1007/978-3-319-23321-5_3.

[46] ——, *Analysis of the Parareal Algorithm Applied to Hyperbolic Problems Using Characteristics*, *Boletín de la Sociedad Española de Matemática Aplicada*, vol. 42, pp. 21–35, 2008.

[47] M. J. Gander and E. Hairer, *Analysis for Parareal Algorithms Applied to Hamiltonian Differential Equations*, *Journal of Computational and Applied Mathematics*, vol. 259, 2–13, 2014, ISSN: 0377-0427. DOI: 10.1016/j.cam.2013.01.011.

[48] ——, *Nonlinear Convergence Analysis for the Parareal Algorithm*, in *Domain Decomposition Methods in Science and Engineering XVII*, U. Langer, M. Discacciati, D. E. Keyes, O. B. Widlund, and W. Zulehner, Eds., Berlin, Heidelberg: Springer, 2008, pp. 45–56, ISBN: 978-3-540-75199-1. DOI: 10.1007/978-3-540-75199-1_4.

[49] M. J. Gander and L. Halpern, *Time Parallelization for Nonlinear Problems Based on Diagonalization*, in *Domain Decomposition Methods in Science and Engineering XXIII*, C.-O. Lee, X.-C. Cai, D. E. Keyes, H. H. Kim, A. Klawonn, E.-J. Park, and O. B. Widlund, Eds. Cham: Springer International Publishing, 2017, pp. 163–170, ISBN: 978-3-319-52389-7. DOI: 10.1007/978-3-319-52389-7_15.

[50] M. J. Gander, Y.-L. Jiang, B. Song, and H. Zhang, *Analysis of two parareal algorithms for time-periodic problems*, *SIAM Journal on Scientific Computing*, vol. 35, no. 5, A2393–A2415, 2013, ISSN: 1064-8275. DOI: 10.1137/130909172.

[51] M. J. Gander, I. Kulchytska-Ruchka, I. Niyonzima, and S. Schöps, *A new parareal algorithm for problems with discontinuous sources*, *SIAM Journal on Scientific Computing*, vol. 41, no. 2, B375–B395, 2019, ISSN: 1064-8275. DOI: 10.1137/18M1175653. arXiv: 1803.05503.

[52] M. J. Gander, I. Kulchytska-Ruchka, and S. Schöps, *A new parareal algorithm for time-periodic problems with discontinuous inputs*, in *Domain Decomposition Methods in Science and Engineering XXV*, R. Haynes, S. MacLachlan, X.-C. Cai, L. Halpern, H. H. Kim, A. Klawonn, and O. Widlund, Eds., ser. Lecture Notes in Computational Science and Engineering, vol. 138, Springer, 2020, ISBN: 978-3-030-56749-1. DOI: 10.1007/978-3-030-56750-7_27. arXiv: 1810.12372.

[53] M. J. Gander, J. Liu, S.-L. Wu, X. Yue, and T. Zhou, *ParaDiag: Parallel-in-Time Algorithms Based on the Diagonalization Technique*, 2020. arXiv: 2005.09158.

[54] M. J. Gander and T. Lunet, *ParaStieltjes: Parallel computation of Gauss quadrature rules using a Parareal-like approach for the Stieltjes procedure*, *Numerical Linear Algebra with Applications*, e2314, 2020. DOI: 10.1002/nla.2314.

[55] M. J. Gander and M. Petcu, *Analysis of a Krylov subspace enhanced parareal algorithm for linear problems*, *ESAIM: Proc.*, vol. 25, pp. 114–129, 2008. DOI: 10.1051/proc:082508.

[56] C. Geuzaine, *GetDP: A general finite-element solver for the de Rham complex*, in *Proceedings in Applied Mathematics and Mechanics*, vol. 7, Wiley, 2007, pp. 1 010 603–1 010 604. DOI: 10.1002/pamm.200700750.

[57] M. B. Giles, *Multilevel Monte Carlo methods*, *Acta Numerica*, vol. 24, pp. 259–328, 2015, ISSN: 1474-0508. DOI: 10.1017/S096249291500001X.

[58] D. F. Griffiths, *Introduction to Electrodynamics*. Upper Saddle River, NJ, USA: Prentice-Hall, 1999, ISBN: 978-0-13-805326-0.

[59] J. Gyselinck, P. Dular, C. Geuzaine, and W. Legros, *Harmonic-balance finite-element modeling of electromagnetic devices: A novel approach*, *IEEE Transactions on Magnetics*, vol. 38, no. 2, pp. 521–524, 2002, ISSN: 0018-9464. DOI: 10.1109/20.996137.

[60] J. Gyselinck, C. Martis, and R. V. Sabariego, *Using dedicated time-domain basis functions for the simulation of pulse-width-modulation controlled devices – application to the steady-state regime of a buck converter*, in *Electromotion 2013*, Cluj-Napoca, Romania, 2013.

[61] J. Gyselinck, L. Vandevelde, P. Dular, C. Geuzaine, and W. Legros, *A general method for the frequency domain FE modeling of rotating electromagnetic devices*, *IEEE Transactions on Magnetics*, vol. 39, no. 3, pp. 1147–1150, 2003, ISSN: 0018-9464. DOI: 10.1109/TMAG.2003.810381.

[62] J. Gyselinck, L. Vandevelde, and J. Melkebeek, *Multi-slice FE modeling of electrical machines with skewed slots-the skew discretization error*, *IEEE Transactions on Magnetics*, vol. 37, no. 5, pp. 3233–3237, 2001, ISSN: 0018-9464. DOI: 10.1109/20.952584.

[63] W. Hackbusch, *Parabolic multi-grid methods*, in *Computing methods in applied sciences and engineering VI*, R. Glowinski and J.-L. Lions, Eds., ser. Lecture Notes in Computational Science and Engineering, vol. 55, Amsterdam: North-Holland, 1984, 189—197.

[64] E. Hairer, S. P. Nørsett, and G. Wanner, *Solving Ordinary Differential Equations I: Nonstiff Problems*, 2nd ed., ser. Springer Series in Computational Mathematics. Berlin, Germany: Springer, 2000, ISBN: 978-3-540-56670-0.

[65] ——, *Solving Ordinary Differential Equations II: Stiff and Differential-Algebraic Problems*, 2nd ed., ser. Springer Series in Computational Mathematics. Berlin, Germany: Springer, 2002, ISBN: 978-3-642-05220-0.

[66] B. Hannon, P. Sergeant, and L. Dupré, *Time- and spatial-harmonic content in synchronous electrical machines*, *IEEE Transactions on Magnetics*, vol. 53, no. 3, 2017, ISSN: 0018-9464. DOI: 10.1109/TMAG.2016.2637316.

[67] T. Hara, T. Naito, and J. Umoto, *Time-periodic finite element method for nonlinear diffusion equations*, *IEEE Transactions on Magnetics*, vol. 21, no. 6, pp. 2261–2264, 1985. DOI: 10.1109/tmag.1985.1064193.

[68] H. A. Haus and J. R. Melcher, *Electromagnetic Fields and Energy*. Prentice-Hall, 1989, ISBN: 978-0-13-249020-7.

[69] B. He, C. Lu, N. Chen, D. Lin, and P. Zhou, *An Efficient Parallel Computing Method for the Steady-State Analysis of Electric Machines Using the Woodbury Formula*, *IEEE Transactions on Magnetics*, vol. 56, no. 2, pp. 1–4, 2020, ISSN: 0018-9464. DOI: 10.1109/TMAG.2019.2953600.

[70] B. Heise, *Analysis of a fully discrete finite element method for a nonlinear magnetic field problem*, *SIAM Journal on Numerical Analysis*, vol. 31, no. 3, pp. 745–759, 1994.

[71] C.-W. Ho, A. E. Ruehli, and P. A. Brennan, *The modified nodal approach to network analysis*, *IEEE Transactions on Circuits and Systems*, vol. 22, no. 6, pp. 504–509, 1975. DOI: 10.1109/TCS.1975.1084079.

[72] D. G. Holmes and T. A. Lipo, *Pulse Width Modulation For Power Converters*. Canada: Wiley-IEEE Press, 2003, ISBN: 0-471-20814-0.

[73] A. Hughes, *Electric Motors and Drives: Fundamentals, Types and Applications*, 3rd ed. Newnes, 2005, ISBN: 978-0-7506-4718-2.

[74] T. J. R. Hughes, J. A. Cottrell, and Y. Bazilevs, *Isogeometric analysis: CAD, finite elements, NURBS, exact geometry and mesh refinement*, *Computer Methods in Applied Mechanics and Engineering*, vol. 194, pp. 4135–4195, 2005, ISSN: 0045-7825. DOI: 10.1016/j.cma.2004.10.008.

[75] N. Ida and J. P. A. Bastos, *Electromagnetics and calculation of fields*, 2nd ed. New York: Springer, 1997, ISBN: 978-0-387-94877-5.

[76] J. D. Jackson, *Classical Electrodynamics*, 3rd. New York, NY, USA: Wiley & Sons, 1998, ISBN: 978-0-471-30932-1. DOI: 10.1017/CBO9780511760396.

[77] B. Kaltenbacher, M. Kaltenbacher, and S. Reitzinger, *Identification of nonlinear B–H curves based on magnetic field computations and multigrid methods for ill-posed problems*, *European Journal of Applied Mathematics*, vol. 14, pp. 15–38, 2003. DOI: 10.1017/S0956792502005089.

[78] W. Kampowsky, P. Rentrop, and W. Schmidt, *Classification and numerical simulation of electric circuits*, *Surveys on Mathematics for Industry*, vol. 2, no. 1, pp. 23–65, 1992.

[79] H. Katagiri, Y. Kawase, T. Yamaguchi, T. Tsuji, and Y. Shibayama, *Improvement of convergence characteristics for steady-state analysis of motors with simplified singularity decomposition-explicit error correction method*, *IEEE Transactions on Magnetics*, vol. 47, no. 5, pp. 1458–1461, 2011, ISSN: 0018-9464. DOI: 10.1109/CEFC.2010.5481752.

[80] H. B. Keller, *Numerical Methods for Two Point Boundary Value Problems*. New York: Blaisdell, 1968.

[81] I. Kulchytska-Ruchka, H. De Gersem, and S. Schöps, *An efficient steady-state analysis of the eddy current problem using a parallel-in-time algorithm*, in *The Tenth International Conference on Computational Electromagnetics (CEM 2019)*, Edinburgh, UK, 2019, ISBN: 978-1-83953-066-1. DOI: 10.1049/cp.2019.0113. arXiv: 1905.13076.

[82] I. Kulchytska-Ruchka and S. Schöps, *Efficient parallel-in-time solution of time-periodic problems using a multi-harmonic coarse grid correction*, *SIAM Journal on Scientific Computing*, vol. 43, no. 1, pp. C61–C88, 2021, ISSN: 1064-8275. DOI: 10.1137/20M1314756. arXiv: 1908.05245.

[83] ——, *Towards a parallel-in-time calculation of time-periodic solutions with unknown period*, in *Scientific Computing in Electrical Engineering SCEE 2020*, W. Schilders, M. van Beurden, and N. Budko, Eds., ser. Mathematics in Industry, Berlin: Springer, 2020. arXiv: 2004.01612, forthcoming.

[84] I. Kulchytska-Ruchka, S. Schöps, I. Niyonzima, and M. J. Gander. (2019). *A GNU Octave Implementation of a new Parareal Algorithm for Problems with Discontinuous Sources*, [Online]. Available: http://www.github.com/temf/parareal.

[85] F. Legoll, T. Lelièvre, and G. Samaey, *A micro-macro parareal algorithm: Application to singularly perturbed ordinary differential equations*, *SIAM Journal on Scientific Computing*, vol. 35, no. 4, A1951–A1986, 2013, ISSN: 1064-8275. DOI: 10.1137/120872681.

[86] E. Lelarasmee, *The waveform relaxation method for time domain analysis of large scale integrated circuits: Theory and applications*, PhD Thesis, EECS Department, University of California, Berkeley, 1982.

[87] D. Linaro, D. del Giudice, A. Brambilla, and F. Bizzarri, *Application of Envelope-Following Techniques to the Shooting Method*, *IEEE Open Journal of Circuits and Systems*, vol. 1, pp. 22–33, 2020. DOI: 10.1109/OJCAS.2020.2987973.

[88] J.-L. Lions, Y. Maday, and G. Turinici, *A parareal in time discretization of PDEs*, *Comptes Rendus de l'Académie des Sciences – Series I – Mathematics*, vol. 332, no. 7, pp. 661–668, 2001, ISSN: 0764-4442. DOI: 10.1016/S0764-4442(00)01793-6.

[89] P. Maponi, *The solution of linear systems by using the Sherman–Morrison formula*, *Linear Algebra and its Applications*, vol. 420, no. 2, pp. 276–294, 2007, ISSN: 0024-3795. DOI: https://doi.org/10.1016/j.laa.2006.07.007.

[90] J. C. Maxwell, *A dynamical theory of the electromagnetic field*, *Royal Society Transactions*, vol. CLV, pp. 459–512, 1864.

[91] N. Mohan, T. M. Undeland, and W. P. Robbins, *Power electronics: converters, applications and design*, 3rd ed. Wiley, 2003, ISBN: 9780471226932.

[92] P. Monk, *Finite Element Methods for Maxwell's Equations*. Oxford: Oxford University Press, 2003.

[93] D. D. Morrison, J. D. Riley, and J. F. Zancanaro, *Multiple shooting method for two-point boundary value problems*, *Communications of the Association for Computing Machinery*, vol. 5, no. 2, 613–614, 1962.

[94] M. Nakhla and J. Vlach, *A piecewise harmonic balance technique for determination of periodic response of nonlinear systems*, *IEEE Transactions on Circuits and Systems*, vol. 23, no. 2, pp. 85–91, 1976. DOI: 10.1109/TCS.1976.1084181.

[95] J. C. Nédélec, *Mixed finite elements in R^3*, *Numerische Mathematik*, vol. 35, no. 3, pp. 315–341, 1980, ISSN: 0945-3245. DOI: 10.1007/BF01396415.

[96] A. Nicolet and F. Delincé, *Implicit Runge-Kutta methods for transient magnetic field computation*, *IEEE Transactions on Magnetics*, vol. 32, no. 3, pp. 1405–1408, 1996, ISSN: 0018-9464. DOI: 10.1109/20.497510.

[97] J. Nievergelt, *Parallel methods for integrating ordinary differential equations*, *Communications of the Association for Computing Machinery*, vol. 7, pp. 731–733, 1964.

[98] K. Niyomsatian, P. Vanassche, R. V. Sabariego, and J. Gyselinck, *Systematic control design for half-bridge converters with LCL output filters through virtual circuit similarity transformations*, in *2017 IEEE Energy Conversion Congress and Exposition (ECCE)*, 2017, pp. 2895–2902. DOI: 10.1109/ECCE.2017.8096535.

[99] C. Pechstein, *Multigrid-Newton-methods for nonlinear-magnetostatic problems*, Master's Thesis, Universität Linz, Linz, Austria, 2004.

[100] C. Pechstein and B. Jüttler, *Monotonicity-preserving interproximation of b-h-curves*, *Journal of Computational and Applied Mathematics*, vol. 196, no. 1, pp. 45–57, 2006, ISSN: 0377-0427. DOI: 10.1016/j.cam.2005.08.021.

[101] A. Pels, H. De Gersem, R. V. Sabariego, and S. Schöps, *Multirate PWM balance method for the efficient field-circuit coupled simulation of power converters*, *Journal of Mathematics in Industry*, vol. 9, no. 8, 2019, ISSN: 2190-5983. DOI: 10.1186/s13362-019-0065-8. arXiv: 1907.03719.

[102] A. Pels, J. Gyselinck, R. V. Sabariego, and S. Schöps, *Efficient simulation of DC-DC switch-mode power converters by multirate partial differential equations*, *IEEE Journal on Multiscale and Multiphysics Computational Techniques*, vol. 4, no. 1, pp. 64–75, 2019, ISSN: 2379-8793. DOI: 10.1109/JMMCT.2018.2888900. arXiv: 1707.01947.

[103] A. Pels, I. Kulchytska-Ruchka, and S. Schöps, *Parallel-in-time simulation of power converters using multirate PDEs*, in *Scientific Computing in Electrical Engineering SCEE 2020*, W. Schilders, M. van Beurden, and N. Budko, Eds., ser. Mathematics in Industry, Berlin: Springer, 2020. arXiv: 2006.06544, forthcoming.

[104] A. Pels, R. V. Sabariego, and S. Schöps, *Efficient simulation of DC-AC power converters using multirate partial differential equations*, *International Journal of Numerical Modelling: Electronic Networks, Devices and Fields*, 2019, ISSN: 0894-3370. DOI: 10.1002/jnm.2683. arXiv: 1907.12626.

[105] L. Perko, *Differential Equations and Dynamical Systems*, 3rd ed. Springer-Verlag New York, 2001, vol. 7, ISBN: 978-1-4613-0003-8. DOI: 10.1007/978-1-4613-0003-8.

[106] Y. Pinchover and J. Rubinstein, *An Introduction to Partial Differential Equations*. Cambridge: Cambridge University Press, 2005. DOI: 10.1017/CBO9780511801228.

[107] A. Preumont, *Mechatronics – Dynamics of Electromechanical and Piezoelectric Systems*, ser. Solid Mechanics and its Applications. Springer, 2006, vol. 136, ISBN: 978-1402046957.

[108] R. Pulch, *Multi time scale differential equations for simulating frequency modulated signals*, *Applied Numerical Mathematics*, vol. 53, no. 2–4, pp. 421–436, 2005, ISSN: 0168-9274. DOI: 10.1016/j.apnum.2004.08.013.

[109] J. Pyrhönen, T. Jokinen, and H. Valéria, *Design of Rotating Electrical Machines*. John Wiley & Sons, Ltd., 2008, ISBN: 978-0470695166.

[110] A. Quarteroni and A. Valli, *Numerical Approximation of Partial Differential Equations*, ser. Springer Series in Computational Mathematics. Berlin, Germany: Springer, 2008, vol. 23, ISBN: 978-3-540-85267-4. DOI: 10.1007/978-3-540-85268-1.

[111] J. C. Rautio, *The Long Road to Maxwell's Equations*, *IEEE Spectrum*, vol. 51, no. 12, pp. 36–56, 2014, ISSN: 0018-9235. DOI: 10.1109/MSPEC.2014.6964925.

[112] T. Reis, *Mathematical Modeling and Analysis of Nonlinear Time-Invariant RLC Circuits*, in *Large-Scale Networks in Engineering and Life Sciences*, P. Benner, R. Findeisen, D. Flockerzi, U. Reichl, and K. Sundmacher, Eds. Cham: Springer International Publishing, 2014, pp. 125–198, ISBN: 978-3-319-08437-4. DOI: 10.1007/978-3-319-08437-4_2.

[113] J. Roychowdhury, *Analyzing circuits with widely separated time scales using numerical PDE methods*, *IEEE Transactions on Circuits and Systems Part I: Fundamental Theory and Applications*, vol. 48, no. 5, pp. 578–594, 2001, ISSN: 1057-7122. DOI: 10.1109/81.922460.

[114] R. V. Sabariego and J. Gyselinck, *Eddy-current-effect homogenization of windings in harmonic-balance finite-element models*, *IEEE Transactions on Magnetics*, vol. 53, no. 6, 2017, ISSN: 0018-9464. DOI: 10.1109/TMAG.2017.2675962.

[115] S. J. Salon, *Finite Element Analysis of Electrical Machines*. Kluwer, 1995.

[116] S. Salsa, *Partial Differential Equations in Action: From Modelling to Theory*, 1st ed. Milan: Springer-Verlag Mailand, 2009, ISBN: 978-88-470-0752-9. DOI: 10.1007/978-88-470-0752-9.

[117] S. Schöps, H. De Gersem, and T. Weiland, *Winding functions in transient magnetoquasistatic field-circuit coupled simulations*, *COMPEL: The International Journal for Computation and Mathematics in Electrical and Electronic Engineering*, vol. 32, no. 6, pp. 2063–2083, 2013. DOI: 10.1108/COMPEL-01-2013-0004.

[118] S. Schöps, I. Niyonzima, and M. Clemens, *Parallel-in-time simulation of eddy current problems using parareal*, *IEEE Transactions on Magnetics*, vol. 54, no. 3, pp. 1–4, 2018, ISSN: 0018-9464. DOI: 10.1109/TMAG.2017.2763090. arXiv: 1706.05750.

[119] J. Sherman and W. J. Morrison, *Adjustment of an Inverse Matrix Corresponding to a Change in One Element of a Given Matrix*, *The Annals of Mathematical Statistics*, vol. 21, no. 1, pp. 124 –127, 1950. DOI: 10.1214/aoms/1177729893.

[120] W. Shockley, *The theory of p-n junctions in semiconductors and p-n junction transistors*, *The Bell System Technical Journal*, vol. 28, no. 3, pp. 435–489, 1949. DOI: 10.1002/j.1538-7305.1949.tb03645.x.

[121] P. P. Silvester and R. L. Ferrari, *Finite Elements for Electrical Engineers*, 2nd ed. Cambridge, UK: Cambridge University Press, 1996, ISBN: 978-0-521-44505-4.

[122] B. Sommeijer, L. F. Shampine, and J. G. Verwer, *RKC: An explicit solver for parabolic PDEs*, *Journal of Computational and Applied Mathematics*, vol. 88, no. 2, pp. 315–326, 2 1998, ISSN: 0377-0427. DOI: 10.1016/S0377-0427(97)00219-7.

[123] C. P. Steinmetz, *The Alternating Current Induction Motor*, *Transactions of the American Institute of Electrical Engineers*, vol. XIV, no. 1, pp. 183–217, 1897. DOI: 10.1109/T-AIEE.1897.5570186.

[124] J. Stoer and R. Bulirsch, *Introduction to numerical analysis*, 3rd ed., ser. Texts in applied mathematics. Springer-Verlag New York, 2002, vol. 12, ISBN: 978-0-387-21738-3. DOI: 10.1007/978-0-387-21738-3.

[125] J. Sun, *Pulse-Width Modulation*, in *Dynamics and Control of Switched Electronic Systems: Advanced Perspectives for Modeling, Simulation and Control of Power Converters*. London: Springer-Verlag London, 2012, pp. 25–61, ISBN: 978-1-4471-2885-4. DOI: 10.1007/978-1-4471-2885-4.

[126] Y. Takahashi, K. Fujiwara, T. Iwashita, and H. Nakashima, *Parallel finite-element method based on space-time domain decomposition for magnetic field analysis of electric machines*, *IEEE Transactions on Magnetics*, vol. 55, no. 6, pp. 1–4, 2019, ISSN: 0018-9464. DOI: 10.1109/tmag.2019.2895590.

[127] Y. Takahashi, T. Tokumasu, K. Fujiwara, T. Iwashita, and H. Nakashima, *Parallel TP-EEC method based on phase conversion for time-periodic nonlinear magnetic field problems*, *IEEE Transactions on Magnetics*, vol. 51, no. 3, 2015, ISSN: 0018-9464. DOI: 10.1109/TMAG.2014.2356193.

[128] Y. Takahashi, T. Tokumasu, A. Kameari, H. Kaimori, M. Fujita, T. Iwashita, and S. Wakao, *Convergence acceleration of time-periodic electromagnetic field analysis by singularity decomposition-explicit error correction method*, *IEEE Transactions on Magnetics*, vol. 46, no. 8, pp. 2947–2950, 2010, ISSN: 0018-9464. DOI: 10.1109/TMAG.2010.2043721.

[129] L. N. Trefethen, *Finite Difference and Spectral Methods for Ordinary and Partial Differential Equations*. Cornell University, 1996.

[130] S. Ulbrich, *Generalized SQP methods with "parareal"time-domain decomposition for time-dependent PDE-constrained optimization*, in *Real-Time PDE-Constrained Optimization*, L. T. Biegler, O. Ghattas, M. Heinkenschloss, D. Keyes, and B. v. Bloemen Waanders, Eds. SIAM, 2007, pp. 145–168, ISBN: 978-0-89871-621-4. DOI: 10.1137/1.9780898718935.ch7.

[131] M. Urabe, *Galerkin's procedure for nonlinear periodic systems*, *Archive for Rational Mechanics and Analysis*, vol. 20, no. 2, pp. 120–152, 1965, ISSN: 0003-9527. DOI: 10.1007/BF00284614.

[132] F. Vasca and L. Iannelli, Eds., *Dynamics and Control of Switched Electronic Systems*, Advances in Industrial Control, Berlin: Springer, 2012. DOI: 10.1007/978-1-4471-2885-4.

[133] T. Weiland, *A discretization method for the solution of Maxwell's equations for six-component fields*, *International Journal of Electronics and Communications*, vol. 31, pp. 116–120, 1977.

[134] ——, *Time domain electromagnetic field computation with finite difference methods*, *International Journal of Numerical Modelling: Electronic Networks, Devices and Fields*, vol. 9, no. 4, pp. 295–319, 1996, ISSN: 0894-3370. DOI: 10.1002/(SICI)1099-1204(199607)9:4<295::AID-JNM240>3.0.CO;2-8.

[135] D. E. Womble, *A time-stepping algorithm for parallel computers*, *SIAM Journal on Scientific Computing*, vol. 11, no. 5, 824—837, 1990, ISSN: 1064-8275. DOI: 10.1137/0911049.

[136] S.-L. Wu, *Towards Parallel Coarse Grid Correction for the Parareal Algorithm*, *SIAM Journal on Scientific Computing*, vol. 40, no. 3, A1446–A1472, 2018, ISSN: 1064-8275. DOI: 10.1137/17M1141102.

[137] S.-L. Wu, H. Zhang, and T. Zhou, *Solving time-periodic fractional diffusion equations via diagonalization technique and multigrid*, *Numerical Linear Algebra with Applications*, vol. 25, no. 5, e2178, 2018. DOI: 10.1002/nla.2178.

[138] K. S. Yee, *Numerical solution of initial boundary value problems involving Maxwell's equations in isotropic media*, *IEEE Transactions on Antennas and Propagation*, vol. 14, no. 3, pp. 302–307, 1966, ISSN: 0018-926X. DOI: 10.1109/TAP.1966.1138693.

[139] E. Zeidler, *Nonlinear Functional Analysis and its Applications II/A. Linear Monotone Operators*. Springer-Verlag, New York Inc., 1990.

[140] ——, *Nonlinear Functional Analysis and its Applications II/B. Nonlinear Monotone Operators*. Springer-Verlag, New York Inc., 1990.

Acknowledgments

The work on this thesis was accompanied by the priceless support of many people, whose contribution is highly appreciated and acknowledged in the following.

First of all, I would like to express my greatest gratitude to my supervisor Prof. Dr. Sebastian Schöps for the opportunity to work in this interesting research field, to develop my scientific qualifications and soft skills; as well as for making the work conditions comfortable, guiding and assisting me during the years of my doctoral studies.

Secondly, I thank Prof. Dr. Martin Gander for the collaboration on parallel-in-time methods, for many inspirational scientific conversations and organization of my visits to Geneva.

I am also very grateful to Prof. Dr. Herbert De Gersem for his help with understanding of the rotating field theory and electric machines, for the multiple fruitful discussions on the multi-harmonic approach, and for providing the Octave-code for the calculation of the equivalent induction motor schemes and the magnetomechanical oscillator models.

I thank Dr. Oliver Rain for being our industrial partner and engineering advisor, providing us with practical engineering insights as well as with new technological applications. My gratitude is expressed to Denys Bast for incorporating Parareal and PP-IC into the in-house solver Edyson of the Robert Bosch GmbH, which led to a joint publication of academia and industry. Also the contribution of the academic project parties within the PASIROM project is appreciated: thanks to the colleagues from the University of Wuppertal, the University of Koblenz-Landau, the mathematics department at TU Darmstadt for the common publications and collaboration meetings.

The work of Dr. Idoia Cortes García and Dr. Andreas Pels is appreciated: thank you for the multiple mathematical and engineering discussions, which resulted in interesting publications. I also thank Prof. Dr. Roland Pulch for providing the code for calculation of the Colpitts oscillator model.

Thanks to the colleagues from the CEM group and the TEMF institute and the former PhD students of the Graduate School CE for the fun during the lunch and tea meetings, even in the uneasy COVID-19 times. Also for the free time activities like the GSC events, visits to the Christmas market, and diverse afterwork- or weekend-reunions.

I acknowledge the assistance of the Welcome Centre at TU Darmstadt, especially Sabrina Glindmeyer, with the immigration issues, thanks for offering German language courses and foreign researchers meetings. Thanks to the administration offices of TEMF and the Centre for Computational Engineering for their assistance in sometimes delicate administrative issues.

Besides, this research was supported by the Graduate School CE within the Centre for Computational Engineering at Technische Universität Darmstadt, as well as by the BMBF grant 05M2018RDA (PASIROM) and the European High-Performance Computing Joint Undertaking (JU) under the grant agreement No 955701.

The JU receives support from the European Union's Horizon 2020 research and innovation programme and Belgium, France, Germany, Switzerland.

Finally, many thanks to Fernando for becoming my (not only dance) companion, for your constant support and understanding. Last but not least, I thank my loving family for believing in me and supporting me, even being more than a thousand kilometers away.